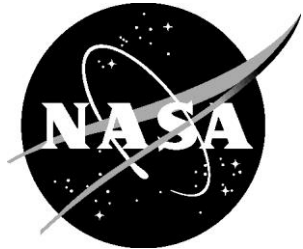


NASA/CR-2015-218792



# Novel Control Effectors for Truss Braced Wing

*Edward V. White*

*The Boeing Company, St. Louis, Missouri*

*Rakesh K. Kapania*

*Virginia Polytechnic Institute and State University, Blacksburg, Virginia*

*Shiv Joshi*

*NextGen Aeronautics, Inc., Torrance California*

---

August 2015

## NASA STI Program . . . in Profile

Since its founding, NASA has been dedicated to the advancement of aeronautics and space science. The NASA scientific and technical information (STI) program plays a key part in helping NASA maintain this important role.

The NASA STI program operates under the auspices of the Agency Chief Information Officer. It collects, organizes, provides for archiving, and disseminates NASA's STI. The NASA STI program provides access to the NTRS Registered and its public interface, the NASA Technical Reports Server, thus providing one of the largest collections of aeronautical and space science STI in the world. Results are published in both non-NASA channels and by NASA in the NASA STI Report Series, which includes the following report types:

- **TECHNICAL PUBLICATION.** Reports of completed research or a major significant phase of research that present the results of NASA Programs and include extensive data or theoretical analysis. Includes compilations of significant scientific and technical data and information deemed to be of continuing reference value. NASA counter-part of peer-reviewed formal professional papers but has less stringent limitations on manuscript length and extent of graphic presentations.
- **TECHNICAL MEMORANDUM.** Scientific and technical findings that are preliminary or of specialized interest, e.g., quick release reports, working papers, and bibliographies that contain minimal annotation. Does not contain extensive analysis.
- **CONTRACTOR REPORT.** Scientific and technical findings by NASA-sponsored contractors and grantees.

- **CONFERENCE PUBLICATION.** Collected papers from scientific and technical conferences, symposia, seminars, or other meetings sponsored or co-sponsored by NASA.
- **SPECIAL PUBLICATION.** Scientific, technical, or historical information from NASA programs, projects, and missions, often concerned with subjects having substantial public interest.
- **TECHNICAL TRANSLATION.** English-language translations of foreign scientific and technical material pertinent to NASA's mission.

Specialized services also include organizing and publishing research results, distributing specialized research announcements and feeds, providing information desk and personal search support, and enabling data exchange services.

For more information about the NASA STI program, see the following:

- Access the NASA STI program home page at <http://www.sti.nasa.gov>
- E-mail your question to [help@sti.nasa.gov](mailto:help@sti.nasa.gov)
- Phone the NASA STI Information Desk at 757-864-9658
- Write to:  
NASA STI Information Desk  
Mail Stop 148  
NASA Langley Research Center  
Hampton, VA 23681-2199

NASA/CR-2015-218792



# Novel Control Effectors for Truss Braced Wing

*Edward V. White*

*The Boeing Company, St. Louis, Missouri*

*Rakesh K. Kapania*

*Virginia Polytechnic Institute and State University, Blacksburg, Virginia*

*Shiv Joshi*

*NextGen Aeronautics, Inc., Torrance, California*

National Aeronautics and  
Space Administration

Langley Research Center  
Hampton, Virginia 23681-2199

Prepared for Langley Research Center  
under Contract NNL10AA00B

---

August 2015

## Acknowledgments

The authors would like to thank NASA for funding the research and the valuable insights by Drs. Ruben Del Rosario and Richard Wahls. The authors would like to thank the Boeing team, which is comprised of Mr. Brian Foist, Program Manager; Mr. Daniel Chen, loads, aeroelasticity, structural sizing, and finite element modeling; Mr. David Hyde, guidance and control requirements and analysis; Dr. Yueping Guo, noise assessment; Mr. Timothy Allen, loads requirements and finite element modeling; Mr. Antonio Gonzales, mass properties; Mr. Christopher Droney, conceptual design; and Mr. Brent Whiting, assistant Program Manager. The authors also appreciate the assistance at Virginia Polytechnic Institute and State University (Virginia Tech) and Next Gen Aeronautics, Inc. In addition to Dr. Kapania, the Virginia Tech (VT) team was made up of Dr. Joseph Schetz, Mr. Wrik Mallik, Dr. John Coggin, and Mr. David Jingoleski. Additional support from Next Gen Aeronautics, Inc. was provided by Dr. Jay Kudva, Mr. Robert Bortolin, Mr. Adam Propst, and Mr. Gerald Andersen.

Available from:

NASA STI Program / Mail Stop 148  
NASA Langley Research Center  
Hampton, VA 23681-2199  
Fax: 757-864-6500

## TABLE OF CONTENTS

Executive Summary .....	1
1. INTRODUCTION .....	3
2. Background and Assumptions .....	4
2.1 Scope of Work Summary.....	4
2.2 Flight Vehicle Assumptions .....	6
3. Concept Development.....	8
3.1 Requirements Development.....	8
3.2 SUGAR VGRWT Concept Development .....	15
3.2.1 Load Path Assessment Criteria .....	18
3.2.2 Skin Assessment Criteria .....	21
3.2.3 Final Concept Selection .....	23
4. Aircraft/NCE Configuration Multidisciplinary Optimization (MDO) .....	31
4.1 Introduction.....	31
4.2 Design Methodology .....	33
4.2.1 Development of new structural model .....	33
4.2.2 Aeroelastic Analysis of the Lateral Motion of the Vehicle .....	34
4.2.2.1 Aerodynamic Analysis .....	34
4.2.2.2 Analysis of Control Effectiveness.....	35
4.2.2.3 Analysis of Rolling Motion.....	36
4.3 Multidisciplinary Optimization Problem Statement.....	37
4.4 Results.....	39
4.4.1 Cantilever Designs .....	39
4.4.1.1 Optimization results .....	39
4.4.1.2 Performance of the New Structural Model .....	41
4.4.2 Truss-braced Wing Designs .....	41
4.4.2.1 Optimization Results .....	41
4.5 Summary and Conclusion.....	45
5. Subsystem Layout, Finite Element, and Kinematic Models.....	47
5.1 Kinematic Model .....	47
5.2 Initial Structural Sizing.....	51
5.3 Actuation and Routing.....	53

5.4	Summary of NCE for Dual Aisle Aircraft .....	54
5.5	MDO Output for Dual Aisle Aircraft .....	55
5.5.1	Skin Moment of Inertia.....	57
5.6	NCE Model Design for Dual Aisle Aircraft .....	60
5.6.1	CAD Design.....	60
5.7	Discussion of NCE Design for Dual Aisle Aircraft.....	66
6.	Subsystem Study .....	68
6.1	System Description .....	68
6.2	Subsystem Integration .....	70
7.	Aerodynamic Analysis.....	71
7.1	Introduction.....	71
7.2	Methods and Models.....	72
7.2.1	Vortex Lattice Method.....	72
7.2.2	Computational Fluid Dynamics .....	73
7.2.3	Design of VGRWT/NCE Tip.....	73
7.2.4	Clean Wing Models .....	76
7.2.4.1	Tornado Models .....	77
7.2.4.2	Fluent Models .....	79
7.2.5	Wing Models with Strut and Jury .....	81
7.3	Results and Discussion .....	84
7.3.1	Clean Wing Results.....	84
7.3.1.1	Tornado Results .....	85
7.3.1.2	Fluent Results.....	85
7.3.1.3	Comparison of Results .....	92
7.3.1.4	Viscous Drag Estimation.....	92
7.3.2	Force and Moment Results on the Various Wingtips .....	93
7.3.2.1	Wingtip Results for All Configurations .....	93
7.3.2.2	Wingtip Performance Deltas .....	98
7.3.2.3	Wingtip Viscous Drag Estimation .....	100
7.3.3	Drag Estimation of Flow over Wing/VGRWT/NCE Tip Joint .....	101
7.4	Conclusions.....	104
8.	Noise Assessment for Baseline and Novel Control Effectors .....	106
8.1	Summary of Acoustic Results .....	106

8.2 Configuration and Performance.....	107
8.3 Overall Method of Analysis.....	108
8.3.1 CFD Analysis for Noise.....	110
8.3.2 Airframe Noise.....	113
8.3.3 Engine Noise.....	118
8.3.4 Total Aircraft (System Noise).....	122
9. Novel Control Effector Aeroelastic Finite Element Model .....	124
9.1 Develop SUGAR VGRWT Finite Element Model .....	124
9.1.1 Integration with Baseline SUGAR Model .....	124
9.1.2 Overall NCE FEM Design .....	125
9.1.3 Material and Element Selection.....	127
9.1.4 Component Interfaces .....	128
9.1.5 FEM Analysis .....	132
10. Airplane Aeroelastic/Controllability Validation.....	134
10.1 SUGAR VGRWT Aeroelastic Analysis.....	134
10.1.1 Finite Element Model .....	134
10.1.2 Flutter Analysis .....	136
10.1.2.1 Full-Fuel Results .....	137
10.1.2.2 Reserve-Fuel Results.....	137
10.1.2.3 Mass Sensitivity Study .....	152
10.1.3 Lateral Trim Analysis .....	154
10.1.4 Conclusions.....	159
10.2 Dual Aisle Aircraft MDO Configuration Aeroelastic Analysis .....	159
10.2.1 Half Span Model .....	160
10.2.2 Flutter Analysis with strut pre-load for Half Span Model .....	162
10.2.3 Full Span Model.....	162
10.2.4 Modeling NCE Configurations .....	164
10.2.5 Flutter Analysis .....	165
10.2.6 Novel Control Effector Effectiveness Analysis .....	166
10.2.7 Sizing Analysis .....	167
10.3 Airplane Controllability Analysis.....	168
11. Quantitative Analysis System of Technical Performance .....	176
12. Conclusions.....	177

13. Recommendations.....	180
14. References.....	182
Appendix A. VGRWT Mechanization Concepts Summary .....	185
Appendix B. Aeroelastic Analysis Equations of Motion.....	201
Appendix C. Structural Modes Comparison for SUGAR VGRWT .....	204
<b>REPORT DOCUMENTATION PAGE .....</b>	<b>236</b>

## LIST OF FIGURES

Figure 1	Novel Control Effector Program Plan.....	4
Figure 2	Variable Geometry Raked Wing Tip (VGRWT) Concept .....	6
Figure 3	SUGAR Phase 2 N+3 Vehicle Configuration.....	7
Figure 4	Baseline Wing – SUGAR 765-095-RC, C210b.....	16
Figure 5	SUGAR Wing with VGRWT Geometry Selected to Maintain Effective Span .....	17
Figure 6	Load Path evaluation matrix (green desirable/red undesirable) .....	21
Figure 7	Skin Evaluation Matrix (Green Desirable/Red Undesirable) .....	22
Figure 8	VGRWT Tornado Model, Wingtip Unswept (Dimensions in Meters).....	24
Figure 9	VGRWT Tornado Model, Wingtip Swept at 35°, Pivot at Trailing Edge (Dimensions in meters) .....	24
Figure 10	Twist per Unit Span .....	25
Figure 11	Force vs. Aileron Deflection, Single Wingtip .....	26
Figure 12	Moment about Wing Elastic Axis vs. Aileron Deflection, Single Wingtip.....	26
Figure 13	Multi-Pivot Geometry for Effective Pivot at Trailing Edge .....	27
Figure 14	Aft Spar Pivot/Forward Spar Track/Rail Geometry .....	28
Figure 15	Shear cell used in previous NextGen morphing program with silicone skin removed to show flexible support blades.....	29
Figure 16	Flexible trailing edge fairing concept for VGRWT in unswept (left) and swept (right) conditions. ....	29
Figure 17	Sketch of Boeing NCE wingtip concept .....	32
Figure 18(a)	Previous VT MDO Structural Model Suitable for Weight Estimation.....	34
Figure 18(b)	New VT MDO Structural Model for Improved Torsional Stiffness Evaluation .....	34
Figure 19	Control Effectiveness measurement envelope for "777-like" aircraft .....	36
Figure 20	"777-like" vehicle flight mission .....	37
Figure 21	"Boeing 777-like" vehicle flight envelope and flutter boundary .....	38
Figure 22	Cantilever Designs Obtained without NCE Tip.....	39
Figure 23	Minimum Fuel Cantilever: Design 1 .....	40
Figure 24	Bank Angles Achieved by Design 1 at Various Altitudes and Mach Numbers along Flight Path .....	40
Figure 25	Bending and torsional stiffness distribution for a cantilever design with old and new structural models .....	41

Figure 26	Minimum Fuel Optimized TBW designs with Flutter as a Constraint .....	42
Figure 27	Selected TBW designs: TBW Design 1(left) and TBW Design 2(right).....	42
Figure 28	Bank Angles Achieved by TBW Design 1 And TBW Design 2 In 2.0 Seconds With Conventional Aileron .....	43
Figure 29	TBW Design1. From left: (a)NCE forward 5 deg (TBWdes1sf5), (b) NCE unswept (TBWdes1as-is), (c) NCE back 10 deg (TBWdes1sb10).....	44
Figure 30	TBW Design 2. From left: (a)NCE forward 5 deg (TBWdes2sf5), (b) NCE unswept (TBWdes2as-is), (c) NCE back 10 deg (TBWdes2sb10).....	44
Figure 31	Bank angle achieved by TBW Design 1 and Design 2 in 2.0 seconds with the NCE tip at various altitudes but only at cruise Mach numbers and flutter Mach numbers at these altitudes. ....	45
Figure 32	Overview of cutline geometry showing the axis of rotation (Axis 1), the fixed root wing (green), variable wingtip (yellow), and rear fairing clearance cut (white). ....	48
Figure 33	Overview of kinematic model in the unswept (left) and swept (right) positions. ....	49
Figure 34	Overhead view of track and beam mechanism with track structure set to transparent showing overlap between track and beam at full sweep. ....	49
Figure 35	Forward track and beam structure looking in from the wingtip with the wingtip fairing hidden. ....	50
Figure 36	Cross section of nested track and beam structure showing the fixed structures (wing root track, blue; root wing skin, green) and moving structures (wingtip beam, red; wingtip forward fairing, yellow)....	51
Figure 37	Rear spar pivot block (left) and cross spar (right). ....	51
Figure 38	Tornado generated wingtip force and moment values with respect to aileron deflection. ....	52
Figure 39	Component Level Sizing of Wingtip Forward Spar and Track .....	53
Figure 40	Finite element analysis of full wingtip structure with skin and fairings hidden showing structural margin greater than unity. ....	53
Figure 41	Representative actuator in the extended/swept (left) and retracted/unswept (right) positions. ....	54
Figure 42	Space for electrical and hydraulic line routing with representative flexible line (black). ....	54
Figure 43	Example of MDO Output (Image split into 2 lines for ease of viewing) .....	55
Figure 44	MDO Output Explanation Graphic Provided by VT and Edited by NextGen to Correct Errors and Improve Understanding. Spar Caps and Stiffeners (stringers) have the Same Area in Calculations .....	56

Figure 45	Sketch of Fuselage and Wing around Model of NCE / Wing Joint Showing Different Coordinate Systems used in MDO Output File .....	57
Figure 46	Graphic from MDO Paper Explaining Wing Box Geometry .....	57
Figure 47	Sketch of the MDO Cross Section Used to Calculate Cross-Sectional Properties of Components.....	58
Figure 48	Sketch of Wing Box and Skin at node 27. The Wing Box is Highlighted. ....	59
Figure 49	Wingtip with NCE at Zero Sweep .....	61
Figure 50	Close-up of NCE Skin 'Bump' at Wing Joint.....	62
Figure 51	Wingtip with NCE Swept Forward 15° .....	63
Figure 52	Wingtip with NCE Swept Aft 10° .....	63
Figure 53	View of the NCE-Wing Joint Area with NCE Swept Forward 15° .....	64
Figure 54	View of NCE-Wing Joint Showing Actuator Connection to NCE Rib and End of NCE Spar Visible in Slider Joint with Wing. NCE Swept Forward 15° . ....	65
Figure 55	NCE-Wing Joint Showing Actuator Attachment to Wing Rib. Left - NCE Swept Forward 15°; Right - NCE Swept Aft 10° .....	66
Figure 56	VGRWT minimum (0 deg) and maximum sweep (35 deg) .....	68
Figure 57	Mechanization concept details (aft fairing not shown).....	69
Figure 58	Forward spar track and beam mechanism (notional actuator shown).....	69
Figure 59	Early Sketch of VGRWT/NCE Tip Pivot Concept.....	74
Figure 60	Geometry Sketch of Fully-Swept VGRWT/NCE Tip .....	75
Figure 61	Wing Thickness and Twist per Span for SUGAR and VGRWT/NCE Tip .....	76
Figure 62	Boeing Aircraft Company J airfoil [33].....	77
Figure 63	Tornado Clean Wing Models (Half Span Only, dimensions in meters) .....	79
Figure 64	Fluent Clean Wing Models before Adaptation Top: Baseline SUGAR Main Wing Middle: SUGAR Wing with Unswept VGRWT/NCE Tip Bottom: SUGAR Wing with Fully-Swept VGRWT/NCE Tip.....	81
Figure 65	Full Configuration with Strut and Jury .....	82
Figure 66	Details of Strut (Top) and Jury (Bottom) Tornado Models (? = taper ratio).....	83
Figure 67	Baseline SUGAR (Left) and Unswept (Right) VGRWT/NCE Tip Details, Dimensions in meters, tip areas for comparison are shaded .....	83
Figure 68	Quarter-Sweep (Left) and Half-Sweep (Right) VGRWT/NCE Tip Details, Dimensions in meters, tip areas for comparison are shaded .....	84
Figure 69	Three-Quarter (Left) and Full-Sweep (Right) VGRWT/NCE Tip Details, Dimensions in meters, tip areas for comparison are shaded.....	84

Figure 70	Adaptive Gridding Convergence for Unswept VGRWT/NCE Tip Case (CL in red) .....	86
Figure 71	Grids at the Wing Root for Unswept VGRWT/NCE Tip Case (Top – Original Grid; Bottom – Final Adapted Grid) .....	87
Figure 72	Fluent Prediction of Top Surface Pressure Contours of Baseline SUGAR Main Wing .....	88
Figure 73	Fluent Prediction of Top Surface Pressure Contours of SUGAR Wing with Unswept VGRWT/NCE Tip.....	89
Figure 74	Fluent Prediction of Top Surface Pressure Contours of SUGAR Wing with Fully-Swept VGRWT/NCE Tip .....	90
Figure 75	Fluent Prediction of Velocity Profile at Wing Root (Left) and Main Wing/VGRWT Junction (Right).....	91
Figure 76	Fluent Prediction of Streamlines over SUGAR Wing with Fully-Swept VGRWT/NCE Tip .....	91
Figure 77	Baseline SUGAR Tip (Left) and Unswept VGRWT/NCE Tip (Right) Force Location (Dimensions in meters).....	94
Figure 78	Quarter-Sweep VGRWT/NCE Tip (Left) and Half-Sweep VGRWT/NCE Tip (Right) Force Location (Dimensions in meters).....	94
Figure 79	Three-Quarter Sweep VGRWT/NCE Tip (Left) and Full-Sweep VGRWT/NCE Tip (Right) Force Location (Dimensions in meters).....	95
Figure 80	Wingtip Resultant Force as a Function of Sweep and Aileron Deflection .....	96
Figure 81	Wingtip Moment as a Function of Sweep and Aileron Deflection.....	97
Figure 82	Wingtip Force Coefficient Deltas for VGRWT/NCE Tip as a Function of Sweep and Aileron Deflection.....	99
Figure 83	Wingtip Moment Coefficient Deltas for VGRWT/NCE Tip as a Function of Sweep and Aileron Deflection .....	100
Figure 84	Fluent Prediction of Streamlines over Step for Fully-Swept VGRWT/NCE Tip (Step drawn in red) .....	102
Figure 85	Fluent Prediction of Pressure Contours of Unswept (Left) and Fully-Swept (Right) VGRWT/NCE Wingtip at Main Wing/Wingtip Junction .....	104
Figure 86	FAR 36 Noise Profile.....	108
Figure 87	Overall Noise Analysis Process .....	109
Figure 88	SUGAR Unstructured Geometry at Approach .....	110
Figure 89	SUGAR Unstructured Geometry at Takeoff.....	111
Figure 90	CFD++ Solution Convergence.....	111
Figure 91	CFD++ Computed Mach Cuts .....	112

Figure 92	Post-Processing of CFD++ Data for Computing Sectional Lift Coefficient .....	112
Figure 93	SUGAR Free vs. SUGAR Total Gear Noise Comparison at Approach .....	114
Figure 94	SUGAR Slat System Deployment for Approach/Cutback/Sideline .....	114
Figure 95	SUGAR Slat System Definition for Noise Analysis.....	115
Figure 96	SUGAR Free vs. SUGAR Slat Noise Comparison at Approach .....	116
Figure 97	SUGAR Flap System Deployment at Approach.....	116
Figure 98	SUGAR Flap System Deployment at Cutback/Sideline .....	116
Figure 99	SUGAR Flap System Definition for Noise Analysis.....	117
Figure 100	SUGAR Free vs. SUGAR Flap Noise Comparison at Approach .....	118
Figure 101	GE Noise-Power-Distance (NPD) Predictions for Hardwall Engine .....	119
Figure 102	GE Hardwall Engine System Noise Assessment (without airframe and acoustic liners) .....	120
Figure 103	Process for Derivation of SUGAR Treated Engine Noise.....	121
Figure 104	SUGAR/RGWRT Sideline Aircraft Noise .....	122
Figure 105	SUGAR/RGWRT Cutback Aircraft Noise .....	122
Figure 106	SUGAR/RGWRT Approach Aircraft Noise.....	123
Figure 107	Simplified kinematic model of the variable geometry raked wingtip kinematic developed in Task 3.0 in fully unswept 0° (left) and fully swept 35° (right) sweep positions.....	124
Figure 108	Top-level view of the baseline SUGAR PATRAN model (top) and integrated VGRWT/SUGAR model in the unswept 0 degree (middle) and fully swept 35 degree (bottom) positions.....	127
Figure 109	NCE wingtip internal structural mesh showing element basic layout with 2-D beam element dimensions displayed .....	128
Figure 110	Kinematic model of variable sweep mechanisms showing rear spar pinned hinge pivot joint (left) and forward track and beam (right) with bearing blocks highlighted (light blue) and track structure set to be transparent (clear blue). .....	129
Figure 111	MPC elements used to model the track and beam interface, track and beam attachment points, rear pivot joint, and wingtip sweep actuator attachment points. Constrained degrees of freedom are listed for each element group and are referenced to the local coordinate system defining the wing sweep pivot axis.....	130
Figure 112	Track and beam interface for 26 degree sweep case. MPC elements (pink) are located at the upper and lower ends of the track and the upper and lower ends of the beam which nests inside the track. Solid elements show on top for clarity. Skeleton view on bottom shows the internal	

connection between the end of the beam and inside of the track. Note that the MPC on far left is used to rigidly attach the upper beam cap to the wingtip upper spar cap.....	131
Figure 113 RBE2 Elements (pink) Modeling the Aileron Hinges (top, bottom left) and the Local Coordinate System Defining the Hinge Axis and MPC Constraints .....	132
Figure 114 The structural FEM of the NCE equipped aircraft was developed by NextGen and provided to VT. The 26-degree, or $\frac{3}{4}$ sweep configuration is shown here. ....	135
Figure 115 The important nonstructural masses were added to the FEM. The total planform weight of the NCE wingtip (structural + non-structural) was similar to the baseline sugar (10 psf).....	135
Figure 116 A new aero-mesh (left) was developed for the 0-degree NCE FEM (right). .....	136
Figure 117 A new aero-mesh (left) was developed for the 26-degree NCE FEM (right). .....	136
Figure 118 Box-by-box aerodynamic weight factors (NASTRAN WFACT) were applied to the NCE. These values were approximated from the baseline SUGAR aircraft (Boeing Overflow #'s @ Mach 0.82).....	138
Figure 119 The V-G plot of the critical flutter mode for the full fuel case. Results are shown for the 0-degree and 26-degree NCE configurations as well as the baseline SUGAR aircraft. ....	139
Figure 120 Critical flutter mode for 0-degree NCE full fuel case. 320 KEAS and 2.68 Hz.....	140
Figure 121 V-F plot for NCE 0-degree full fuel case.....	141
Figure 122 V-G plot for NCE 0-degree full fuel case.....	142
Figure 123 Critical flutter mode for 26-degree NCE full fuel case. 363 KEAS and 2.72 Hz.....	143
Figure 124 V-F plot for NCE 26-degree full fuel case.....	144
Figure 125 V-G plot for NCE 26-degree full fuel case.....	145
Figure 126 The V-G plot of the critical flutter mode for the reserve fuel case. Results are shown for the 0-degree and 26-degree NCE configurations as well as the baseline SUGAR aircraft. ....	146
Figure 127 Critical flutter mode for 0-degree NCE reserve fuel case. 296 KEAS and 2.66 Hz.....	147
Figure 128 V-F plot for NCE 0-degree reserve fuel case.....	148
Figure 129 V-G plot for NCE 0-degree reserve fuel case.....	149
Figure 130 Critical flutter mode for 26-degree NCE full fuel case. 327 KEAS and 2.69 Hz.....	150

Figure 131	V-F plot for NCE 26-degree reserve fuel case.....	151
Figure 132	V-G plot for NCE 26-degree reserve fuel case.....	152
Figure 133	A study was conducted to evaluate the effect of an aft shift in the wing center of gravity on flutter speed. Ballast weight was added along the aileron hingeline. ..	153
Figure 134	The effect on flutter velocity by adding weight to the aft portion of the wing. Results are shown for the baseline SUGAR wing, the baseline NCE wing, and a minimum gauge structure NCE wing. The trend seen is that flutter speed increases with the addition of aft weights. This result is contrary to typical behavior seen in a traditional cantilever wing (i.e., not a TBW). ..	154
Figure 135	Locations and names of the various control surfaces on the NCE equipped aircraft. For comparison the original SUGAR wing is shown in the inset picture upper left. ....	155
Figure 136	E/R $C_{L\delta}$ vs. dynamic pressure for 0-degree and 26-degree NCE aircraft. Results are provided for control configurations using NCE aileron only, or SUGAR aileron only. Zero crossings indicate the dynamic pressure at which aileron reversal occurs. The desired value to achieve sufficient roll control at cruise condition, acting in aileron reversal, is -0.6. ....	157
Figure 137	Various control surface arrangements were considered for their ability to achieve the desired aileron reversal control. These variations included ailerons of different sizes, full-flying aileron wingtips with fore (or aft) hinge points, and a point force controller located at the very distal end of the wing.....	158
Figure 138	Several variations on the original NCE FEM were evaluated with the goal to achieve the desired role-rate acting in roll reversal. ....	158
Figure 139	Boeing Process for Modeling and Analyzing Virginia Tech MDO Vehicle .....	160
Figure 140	Half Span Structural Model .....	161
Figure 141	Half Span Doublet Lattice Aero Model .....	161
Figure 142	V-G Diagram of Half Span Model.....	162
Figure 143	Full Span Structural Model.....	163
Figure 144	Full Span Doublet Lattice Aero Model.....	163
Figure 145	Mass Property Table in Nastran.....	164
Figure 146	Model of NCE in 3 Different Configurations .....	164
Figure 147	NCE to Wing Connectivity .....	165
Figure 148	NCE Control Surface .....	165
Figure 149	V-G Diagram for Dual Aisle Aircraft with Unswept, 5° Forward Swept, and 10° Aft Swept Novel Control Effector Wing Tip .....	166

Figure 150	Aeroelastic Trim Results from Nastran .....	167
Figure 151	TBW Design 2 Bank Angle Change in 2.3 sec.....	171
Figure 152	TBW Design 2 Time for 30 deg Bank Angle Change. ....	172
Figure 153	TBW Design 2 Roll Mode Time Constant. ....	173
Figure 154	TBW Design 2 Representative Climb and Cruise Roll Performance. ....	174
Figure 155	Key VT MDO Summarized Results for Dual-Aisle TBW Configuration.....	178
Figure C-1	Full-fuel: Structural mode 7 for baseline SUGAR (0.92 Hz) and 0-deg NCE (0.94) Hz. ....	204
Figure C-2	Full-fuel: Structural mode 8 for baseline SUGAR (1.14 Hz) and 0-deg NCE (1.14) Hz. ....	204
Figure C-3	Full-fuel: Structural mode 9 for baseline SUGAR (1.20 Hz) and 0-deg NCE (1.21) Hz. ....	205
Figure C-4	Full-fuel: Structural mode 10 for baseline SUGAR (1.66 Hz) and 0-deg NCE (1.64) Hz. ....	205
Figure C-5	Full-fuel: Structural mode 11 for baseline SUGAR (1.95 Hz) and 0-deg NCE (2.11) Hz. ....	206
Figure C-6	Full-fuel: Structural mode 12 for baseline SUGAR (2.26 Hz) and 0-deg NCE (2.26) Hz. ....	206
Figure C-7	Full-fuel: Structural mode 13 for baseline SUGAR (2.28 Hz) and 0-deg NCE (2.29) Hz. ....	207
Figure C-8	Full-fuel: Structural mode 14 for baseline SUGAR (2.66 Hz) and 0-deg NCE (2.65) Hz. ....	207
Figure C-9	Full-fuel: Structural mode 15 for baseline SUGAR (2.71 Hz) and 0-deg NCE (2.81) Hz. ....	208
Figure C-10	Full-fuel: Structural mode 16 for baseline SUGAR (3.06 Hz) and 0-deg NCE (3.13) Hz. ....	208
Figure C-11	Full-fuel: Structural mode 17 for baseline SUGAR (3.20 Hz) and 0-deg NCE (3.23) Hz .....	209
Figure C-12	Full-fuel: Structural mode 18 for baseline SUGAR (3.54 Hz) and 0-deg NCE (3.56) Hz. ....	209
Figure C-13	Reserve-fuel: Structural mode 10 and 11 for 0-deg NCE.....	210
Figure C-14	Reserve-fuel: Structural mode 15 and 16 for 0-deg NCE.....	210
Figure C-15	Full-fuel: Structural mode 10 and 11 for 26-deg NCE. ....	211
Figure C-16	Full-fuel: Structural mode 15 and 16 for 26-deg NCE. ....	211
Figure C-17	Reserve-fuel: Structural mode 10 and 11 for 26-deg NCE.....	212
Figure C-18	Reserve-fuel: Structural mode 15 and 16 for 26-deg NCE.....	212



## LIST OF TABLES

Table 1	NASA Subsonic Fixed Wing Metrics/Goals .....	3
Table 2	Roll Performance Requirements for Class III Aircraft .....	14
Table 3	Roll Performance Requirements for Class III Aircraft .....	14
Table 4	Lateral Axis Flying Qualities and Maneuver Requirements.....	15
Table 5	Comparison of SUGAR Wing Planforms.....	23
Table 6	Tornado Output for Various Planforms .....	24
Table 7	Initial Load Cases Considered .....	39
Table 8	Selected MDO designs.....	42
Table 9	Given Cross Section $I_{tr}$ Compared with Calculated Wing Box Skin $I_{tr}$ (Leading Edge and Trailing Edge Skins Not Included).....	58
Table 10	Comparison of Cross Sectional Area and Moment of Inertia for Different Levels of Design Detail.....	59
Table 11	Comparison of SUGAR Main Wing Planforms .....	78
Table 12	Comparison of Tornado Wing Models .....	78
Table 13	Geometry of Strut and Jury.....	82
Table 14	Tornado Results for Clean Wing Configurations .....	85
Table 15	Fluent Results for Clean Wing Configurations.....	88
Table 16	Comparison of Tornado and Fluent Results for Clean Wing Cases .....	92
Table 17	Viscous Drag Estimation for Each Configuration .....	93
Table 18	Viscous Drag Estimation on Various Wingtip Configurations Configuration Baseline SUGAR Tip .....	101
Table 19	Drag Due to Wing/VGRWT/NCE Joint .....	103
Table 20	Noise levels (EPNL dB) of the baseline SUGAR aircraft and their margins to regulatory limits .....	106
Table 21	Comparison of Moise Levels (EPNL dB) between the Baseline SUGAR Aircraft and that with VGRWT Implemented .....	106
Table 22	Effects of VGWRT Raking on Noise Levels (EPNL dB) .....	106
Table 23	FlightPerformance Parameters for Noise Analysis.....	108
Table 24	Main Gear and Nose Gear Noise Prediction Input Parameters.....	113
Table 25	Slat Noise Prediction Input Parameters .....	115
Table 26	Flap Noise Prediction Input Parameters at Approach.....	117
Table 27	Flap Noise Prediction Input Parameters at Cutback .....	117

Table 28	Flap Noise Prediction Input Parameters at Sideline .....	117
Table 29	GE Noise Modeling Assumptions for the SUGAR Volt Engine .....	118
Table 30	NCE FEM Groups.....	125
Table 31	Summary of flutter speeds for the baseline SUGAR aircraft and the NCE equipped aircraft. ....	137
Table 32	Dynamic derivatives for the lateral trim analysis of the 0-degree NCE configuration. Results for the baseline SUGAR are also provided in the highlighted rows. ....	156
Table 33	Dynamic derivatives for the lateral trim analysis of the 26-degree NCE configuration.....	156
Table 34	Summary of Quantitative Technical Performance Measures.....	178

## LIST OF SYMBOLS, ABBREVIATIONS, AND ACRONYMS

$\text{AAW}$	active aeroelastic wing
$\text{AR}$	aspect ratio
$b$	reference span
$\tilde{b}$	span of the wing (ft)
$c$	chord of the wing
$c_{\text{cs}}$	chord of the control surface
$C_D$	drag coefficient
$C_{D\text{step}}$	drag coefficient of step
$C_{D\text{tip}}$	drag coefficient of wingtip only
$c_D$	independent drag coefficient
$C_{D0}$	zero lift drag coefficient
$C_L$	lift coefficient
$\text{Cl}$	coefficient of roll moment
$\text{Cl}_\delta$	roll control power
$\text{Cl}_p$	roll damping
$Cl_p$	coefficient of roll moment due to roll rate
$C_{Mc/4}$	moment coefficient about quarter chord
$\text{CAD}$	computer aided design
$\text{CFD}$	computational fluid dynamics
$\text{C.G.}$	center of gravity
$\text{COTS}$	commercial off-the-shelf
$\text{dB}$	decibels
$e$	Oswald efficiency factor
$e$	distance between aerodynamic center of the wing and the elastic axis of the wing
$e_{\text{cs}}$	distance between aerodynamic center of the control surface and the elastic axis of the wing
$\text{EI}_{xx}$	bending stiffness about X axis
$\text{EI}_{yy}$	bending stiffness about Y axis
$\text{EI}_{zz}$	bending stiffness about Z axis
$\text{EI}_{\text{tr}}$	bending stiffness along the local transverse or out-of-plane direction of the beam
$\text{EPN}$	effective perceived noise
$\text{EPNL}$	effective perceived noise level
$\text{ERA}$	Environmentally Responsive Aircraft
$\text{FEM}$	finite element model
$g$	force of gravity
$\text{GJ}$	torsional stiffness

$h$	step height
$I_{m-xx}$	second moment of area about the local x axis
$I_{xx}$	rolling moment of inertia
$K_{a-wing}$	aerodynamic stiffness of the wing
$K_{\text{flex},\delta}$	roll effector flex-to-rigid ratio
$K_{\text{flex},p}$	roll damping flex-to-rigid ratio
$K_s$	structural stiffness of the wing
$K_{e/r,\delta}$	elastic to rigid ratio due to control surface deflection
$K_{e/r,p}$	elastic to rigid ratio due to roll rate
$L$	lift on the wing
$L_{r-\text{cs}}$	rigid lift due to the control surface
$L_{r-\text{wing}}$	rigid lift due to the angle of attack of the wing
$l_r$	rigid roll moment of the wing
$l_e$	elastic roll moment of the wing
LE	leading edge
$M$	pitching moment of the wing
$M_{r-\text{cs}}$	rigid pitching moment due to the control surface
$M_{r-\text{wing}}$	rigid pitching moment due to the initial angle of attack of the wing
MDO	multi-disciplinary optimization
NCE	novel control effector
NMAS	NextGen Morphing Aircraft Structures
OML	outer mold line
P	roll rate as a function of time
$p$	roll rate (rad/s)
$p_{cmd}$	roll rate commanded (rad/s)
$P_{ss}$	steady-state (maximum) roll rate
$p_{ss}$	steady-state roll rate (rad/s)
PNL	perceived noise level
PNLT	tone corrected perceived noise level
$\dot{p}_{max}$	maximum roll acceleration (rad <sup>2</sup> /s)
qbar	dynamic pressure
$Q_{r-\text{wing}}$	rigid aerodynamic forces due to initial angle of attack of the wing; represent a matrix if shown in bold
$Q_{r-\text{cs}}$	rigid aerodynamic forces due to control surface: represent a matrix if shown in bold
q	generalized degrees of freedom
$q_d$	dynamic pressure
S	reference area of the wing (ft <sup>2</sup> )

$S_{tip}$	area of wingtip
S&C	stability and control
sb	swept back
sf	swept forward
SOW	statement of work
SUGAR	Subsonic Ultra-Green Aircraft Research
t	time
TBW	truss braced wing
TE	trailing edge
TM	technical monitor
$x$	distance from leading edge to step
$V_d$	dive airspeed
$V_t$	true airspeed
$V_T$	true airspeed (ft/s)
VGRWT	variable geometry raked wing tip
VLM	vortex lattice method
VT	Virginia Tech
WBS	work breakdown structure
$\alpha$	angle of attack of the wing
$\alpha_r$	initial angle of attack of wing
$\beta$	step incidence angle
$\beta_r$	control surface deflection
$\Delta C_{Force}$	change in resultant force
$\Delta C_{Moment}$	change in moment
$\delta$	roll effector deflection
$\delta_{max}$	max aileron deflection allowed (degrees or rads)
$\frac{\partial C_L}{\partial \alpha}$	change in lift coefficient with the angle of attack of the wing
$\frac{\partial C_M}{\partial \alpha}$	change in pitching moment coefficient with the angle of attack of wing
$\frac{\partial C_L}{\partial \beta}$	change in lift coefficient with control surface deflection
$\frac{\partial C_M}{\partial \beta}$	change in pitching moment with control surface deflection
$\Lambda$	sweep
$\Lambda_{LE}$	leading edge sweep angle
$\tau$	time constant (sec)
$\tau$	roll mode time constant (RMTC)

## ABSTRACT

At cruise flight conditions very high aspect ratio/low sweep truss braced wings (TBW) may be subject to design requirements that distinguish them from more highly swept cantilevered wings. High aspect ratio, short chord length and relative thinness of the airfoil sections all contribute to relatively low wing torsional stiffness. This may lead to aeroelastic issues such as aileron reversal and low flutter margins. In order to counteract these issues, high aspect ratio/low sweep wings may need to carry additional high speed control effectors to operate when outboard ailerons are in reversal and/or must carry additional structural weight to enhance torsional stiffness.

The novel control effector evaluated in this study is a variable sweep raked wing tip with an aileron control surface. Forward sweep of the tip allows the aileron to align closely with the torsional axis of the wing and operate in a conventional fashion. Aft sweep of the tip creates a large moment arm from the aileron to the wing torsional axis greatly *enhancing* aileron reversal. The novelty comes from using this enhanced and controllable aileron reversal effect to provide roll control authority by acting as a servo tab and providing roll control through intentional twist of the wing. In this case the reduced torsional stiffness of the wing becomes an advantage to be exploited.

The study results show that the novel control effector concept does provide roll control as described, but only for a restricted class of TBW aircraft configurations. For the configuration studied (long range, dual aisle, Mach 0.85 cruise) the novel control effector provides significant benefits including up to 12% reduction in fuel burn.

## EXECUTIVE SUMMARY

The proposed study was based on the following hypothesis: for very high aspect ratio/low sweep truss braced wings (TBW) the short chord length and relative thinness of the airfoil sections may combine to produce low wing torsional stiffness leading to aeroelastic issues such as outboard aileron reversal and low flutter margins. The NASA/AFRL/Boeing X-53 aircraft demonstrated flight control in full aileron reversal was possible and even advantageous. But for a fixed wing planform there will be some range of dynamic pressures where aileron effectiveness is going through zero while transitioning from no reversal to full reversal. In that range of dynamic pressure the aileron has insufficient authority to provide roll control and other means of roll control must be provided. Usually this is done with the added weight and complexity of a separate high speed aileron. The proposed novel control effector enables the outboard aileron to be effective throughout the flight envelope by providing the ability to control the level of aileron reversal. At moderate speeds the wing tip can be either swept forward to maximize the normal mode operating dynamic pressure or swept aft to minimize the reversal (active aeroelastic wing) mode of operation. This enables adequate roll authority throughout the flight envelope.

The novel control effector addressed in this study is an aileron on a variable sweep raked wing tip. The concept is the subject of US patent number 8,651,431. The original study plan was to develop a Variable Geometry Raked Wing Tip (VGRWT) for the Subsonic Ultra-Green Aircraft Research (SUGAR) truss-braced wing configuration (765-095-200) developed for the Phase 1 NASA Environmentally Responsive Aircraft (ERA) N+3 program. At the time of the proposal for this project, the Phase 1 ERA N+3 effort was complete and the Phase 2 was beginning. Phase 1 developed the aircraft configuration but left development of structural models for Phase 2. The Phase 2 development of structural models was conducted in parallel with the early phases of this program. The program plan was to design the VGRWT design for the SUGAR vehicle and then use structural models when they became available. When these models became available it was found that the wing structure was unexpectedly stiff in torsion and the VGRWT could not operate as intended. Further, the flutter speed of the SUGAR wing structural model was found to be extremely sensitive to small changes such that integration of the VGRWT induced drastic drops in flutter speed. A substantial effort was undertaken to develop a VGRWT configuration that would function as intended without producing unacceptable reduction of flutter speed (i.e., reduction that cannot be accommodated even with active flutter control). This effort was unsuccessful leading to the conclusion that the existing SUGAR aircraft configuration was not suitable for the novel control effector. This conclusion left open the possibility that a different configuration may exist that would accommodate and benefit from the proposed VGRWT novel control effector. An extension to the program was implemented to conduct a search for suitable configuration(s).

The approach for suitable configurations needed to optimize the aircraft configuration subject to certain additional constraints: that the wing torsional stiffness be sufficiently low to allow the VGRWT to function in both normal and aileron reversal modes; and that the flutter speed remained sufficiently high that active flutter control could reasonably be expected to be feasible for an N+3 aircraft. This required enhancements to Virginia Tech's (VT) MDO capability so as to accommodate these additional constraints. The enhancements included:

- Improved structural model for the wing box to accurately represent torsional stiffness.
- Ability to calculate roll control authority (roll rate and time to bank)
- Addition of flutter speed calculation

VT completed addition of these capabilities and exercised the MDO first looking at a conventional tube and wing configuration. After some searching of the design space no obvious candidate was found for a configuration that could benefit from the novel control effector (VGRWT). This seems to be due in large part to the effective torsional stiffness of the higher sweep wings of conventional tube and wing configurations. Next attention was turned to Truss Braced Wing (TBW) configurations. One of the lessons learned from study of the SUGAR configuration was that the relatively high torsional stiffness may have been necessitated by the unusual aeroelastic response of the low sweep in the SUGAR TBW which was optimized for cruise at Mach = 0.7. It was desired to examine a TBW design optimized for cruise at higher Mach. This study then optimized for cruise at Mach = 0.84. The genetic algorithm optimizer found that configurations fell into three groups: 1) designs with positive flutter margins with relatively stiff wings that did not benefit from the VGRWT; 2) designs with substantially improved fuel burn but negative flutter margins; and 3) a transition group. The Group 2 configurations had a highly variable level of flutter margin but nearly a constant level of best fuel burn. The Group 3 transition showed designs with variable fuel burn at fairly modest levels of negative flutter margin (within the capability expected for active flutter suppression). Further, the transition group showed torsional characteristics that were suitable for operation of the VGRWT. A design was selected from this transition group that had fuel burn essentially as good as the Group 2 designs, had a torsional stiffness such that the VGRWT was needed to provide roll control across the flight envelope and had a level of negative flutter margin within the capabilities expected for active flutter suppression. Further, there were indications the VGRWT could also affect the flutter characteristics in a positive way.

## 1. INTRODUCTION

The report documents trade study research into Novel Control Effectors (NCE). The report is organized in the same way as the program tasks and Statement of Work (SOW). The Subsonic Fixed Wing Project (SFW) is performing research into concepts, technologies, and tools that will enable dramatic reductions in noise and emissions, and increase the performance (fuel burn and reduced field length) characteristics of subsonic/transonic fixed wing aircraft. The major metrics/goals are illustrated in Table 1. The NCE development will be performed to be consistent with the N+3 goals.

During execution of this contract, NNL10AA00B-NNL11AC32T “Novel Control Effector for Truss Braced Wing.” it was determined that the potential applicability of the initial research would be substantially enhanced by opening the design domain slightly to permit a wider range of target aircraft for application of the effector than was originally specified. By doing so, the value of work to the Government, and to the United States' aircraft industry, was greatly improved.

**Table 1. NASA Subsonic Fixed Wing Metrics/Goals**

CORNERS OF THE TRADE SPACE	N+1 (2015)*** Technology Benefits Relative to a Single Aisle Reference Configuration	N+2 (2020)*** Technology Benefits Relative to a Large Twin Aisle Reference Configuration	N+3 (2025)** Technology Benefits
Noise (cum below Stage 4)	-32dB	-42 dB	-71 dB
LTO NOx Emissions (below CAEP 6)	-60%	-75%	better than -75%
Performance: Aircraft Fuel Burn	-33%**	-50%**	better than -70%
Performance: Field Length	-33%	-50%	exploit metroplex* concepts

\*\*\* Technology Readiness Level for key technologies = 4-6  
\*\* Additional gains may be possible through operational improvements  
\* Concepts that enable optimal use of runways at multiple airports within the metropolitan areas

This research addresses the following objectives:

1. Design a Variable-Geometry Raked Wingtip (VGRWT) for a truss-braced wing. Design a wingtip with one or more high-rate control effectors that can be raked in flight to modify the location of the surface's aerodynamic center as a function of flight condition. The wingtip's high-rate control effectors will have sufficient bandwidth for stabilization and control of aeroelastic wing dynamics, load alleviation, and suppression of wing buffet.
2. Design and analyze the actuation system for the VGRWT. Define a set of actuators to meet the goals of Objective 2.1 with minimum weight, and analyze its mass properties, kinematics, structural dynamics, and power consumption.
3. Perform a vehicle-level analysis of the impact of the VGRWT on a vehicle with a truss-braced wing. Provide an analysis to quantify the impact of the VGRWT on vehicle weight, drag, noise, and power consumption, comparing the VGRWT against a baseline truss-braced wing.
4. Develop a dynamical model of a vehicle with VGRWT and truss-braced wing and assess the performance of the vehicle when equipped with VGRWT.

## 2. BACKGROUND AND ASSUMPTIONS

The final report is organized similar to Scope of Work (SOW) for this program as shown in Figure 1. Technical sections discuss each major task in the program plan. Technical Memoranda were generated and delivered at the conclusion of the major tasks.

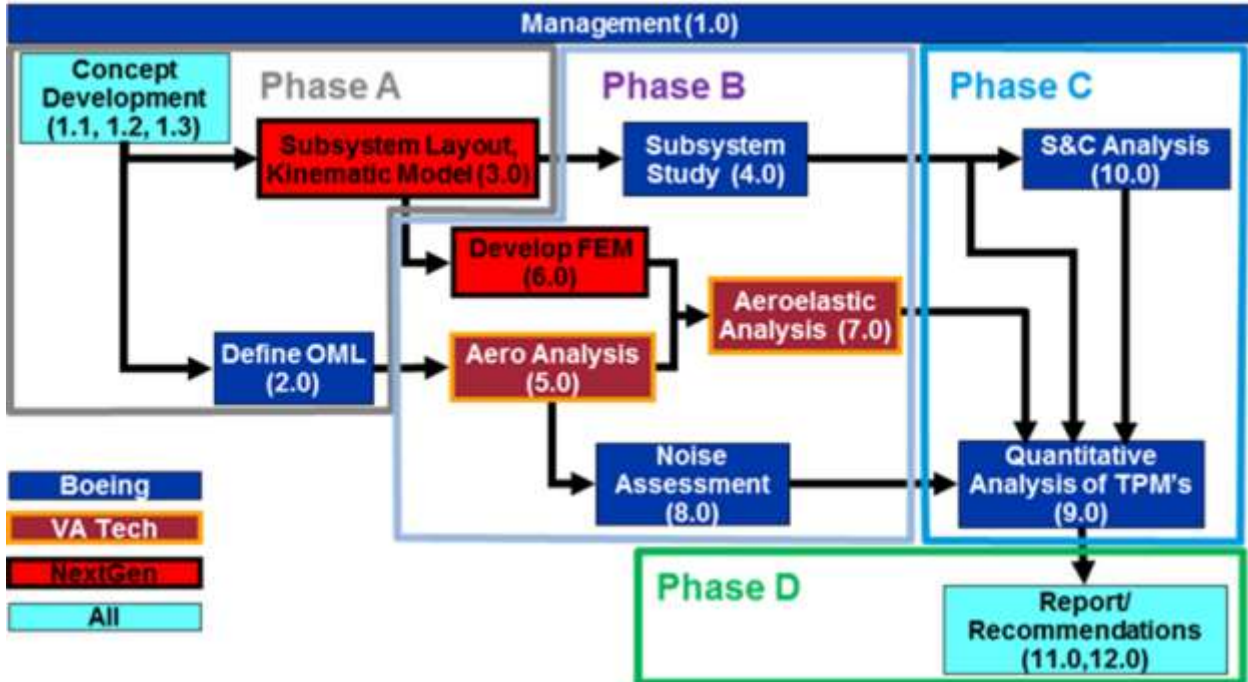


Figure 1. Novel Control Effector Program Plan

### 2.1 SCOPE OF WORK SUMMARY

The primary objectives of Task 1 were the identification of requirements and development of the concepts for the VGRWT. Subtasks included: Task 1.1 "Collaboration Workshop and Concept Development: Define Loads and Requirements," Tasks 1.2 "Develop Mechanization Concepts," Task 1.2 Subtask Revision 1 "Aircraft/NCE Configuration Multidisciplinary Optimization (MDO) Definition," Task 1.3 "Select Single Concept and Define Key Characteristics," and Task 1.3 Sub-task Revision 2 "Aircraft/NCE Configuration Selection."

The original approach to Tasks 1.2 and 1.3 were to conduct a brainstorming exercise, down-select to a few high payoff concepts, then conduct a trade study to select the best concept for the this program. The concepts were categorized according to the means of providing the variable geometry primary load path and the means of providing the skin closeouts needed by the variable geometry. The trade study on load path did not indicate a clear winner and the detailed examination of the options lead to selection of a hybrid approach as described in the Technical Memorandum. This approach uses a simple pivot hinge point near the aft wing spar and a sliding tracked mechanism located near the forward wing spar.

Likewise the decision was made to hybridize the approach to the skins. The forward skin area was selected as a rigid nesting fairing that is contained within the swing outer mold line (OML) when the tip is unswept. The smaller closeout area aft of the pivot was selected to be a flexible skin concept. This selection was made due to the reflex geometry of the airfoil which would require

considerable out of plane flexibility of a more conventional stiff fairing as is used on the leading edge. Details of this design are documented in "Concept Development."

Task 2 defined the outer mold line of the VGRWT and was transmitted to NASA in IGES format. Transmittal of the OML was documented in the Task 2 Technical Memorandum.

Task 3 and Task 3 Revision 3 refined the design of the selected concept as described in "Subsystem Layout, Finite Element, and Kinematic Models." The structure was sized based on loads provided by Virginia Tech using low fidelity aerodynamics (vortex lattice methods) and was updated using higher fidelity loads data by Boeing. The effort, including definition of the conformal trailing edge fairing design, is documented in the Task 3 Technical Memorandum.

Task 4 defines the specific subsystem components for the VGRWT and in particular the characteristics of the actuators used for both the wing sweep and tip aileron. The requirements for the subsystem components were found to be modest. The primary system components are the sweep and aileron actuators. The sweep motion occurs in reaction to flight condition and is not used for primary control of the vehicle. As a result, the rate, bandwidth and power requirements for this actuator are quite modest and an electro-mechanical actuator (EMA) was selected. Commercial off-the-shelf (COTS) actuators are available with capabilities very close to what is required and the weight of the actuator was estimated from similarity to existing COTS actuators. The VGRWT aileron is used for primary flight control and hence must have a bandwidth capable of vehicle flight control. However, the aileron area is smaller than the baseline SUGAR outer wing aileron and the requirements on the NCE aileron actuator will be less stringent than those on the baseline SUGAR wing aileron. Again an EMA actuator is easily capable of the required motion and weight was estimated from similarity to existing COTS actuators.

Task 5 defines the aerodynamic data base to be used for the final evaluation. The effort is documented in "Aerodynamic Analysis" and disseminated to the aerospace community in technical paper AIAA-2013-2403.

Task 6 defines the finite element model of the complete SUGAR aircraft with the added VGRWT. Task 6 is documented in the "Subsystem Layout, Finite Element, and Kinematic Models" section and is documented in the Task 6 Technical Memorandum.

Task 7 is the aeroelastic analysis of the complete vehicle. The Task 7 analyses have uncovered two significant findings for the original configuration:

1. The SUGAR wing structural design which was structurally optimized to meet a flutter speed requirement has a flutter speed that is highly sensitive to structural changes. The addition of the VGRWT significantly lowers the flutter speed, even beyond what could reasonably be corrected by active flutter suppression.
2. The SUGAR wing structure is substantially stiffer in torsion than expected; to the point where the VGRWT cannot achieve aileron reversal and as a result cannot function as intended.

Substantial effort was put into correcting both these deficiencies and the overall conclusion is that the existing SUGAR vehicle is simply the wrong airplane to take advantage of the VGRWT concept. It is judged that there is limited value to continue the development effort using the current SUGAR airplane as the target application airplane. An effort is currently in the planning stages to

identify airplane configuration(s) that may benefit most from VGRWT. The Task 7 effort has been documented in the Task 7 Technical Memorandum.

Task 8 defined the acoustics impact of the VGRWT on the SUGAR vehicle. The overall conclusion is that the VGRWT adds a negligible amount of acoustical noise (approx. 0.1 dB) to the vehicle's overall noise level.

Task 9 Subtask Revision 5 is a quantitative analysis of the VGRWT's impact on weight, drag, noise, and power consumption.

Task 10 Subtask Revision 4 validated the aeroelastic performance (flutter speed and elastic/rigid ratios and controllability) of the aircraft combined with the refined VGRWT finite element model from Task 3, Subtask Revision 3. Performance discrepancies between those calculated by the finite element approach and the MDO analyses were identified.

Tasks 11 and 12 documented recommendations and findings of this program.

## 2.2 FLIGHT VEHICLE ASSUMPTIONS

The proposed novel control effector for this program is a variable geometry raked wing tip as illustrated in Figure 2.

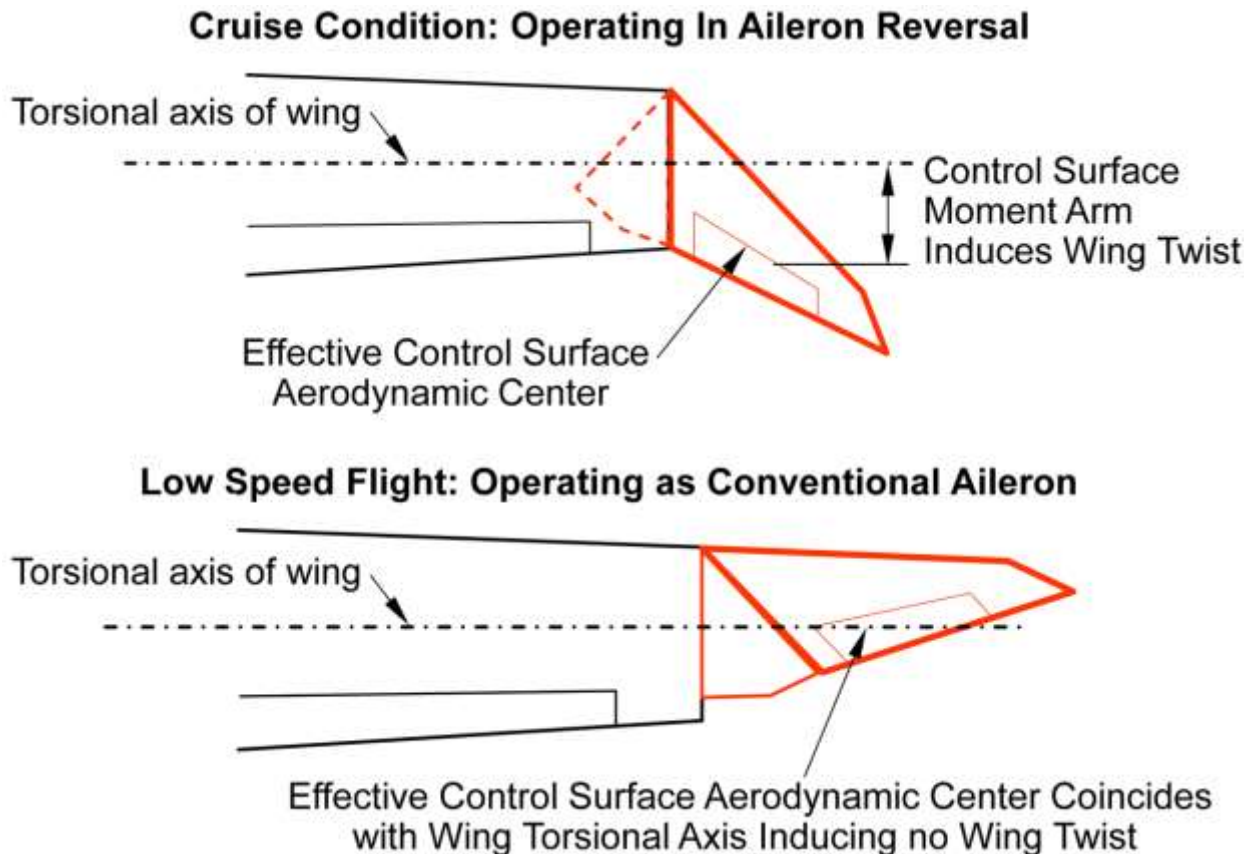


**Figure 2. Variable Geometry Raked Wing Tip (VGRWT) Concept**

The concept offers an approach by which wing twist can be modified in flight through aileron reversal forces also known as active aeroelastic wing. For a fixed geometry, aileron reversal forces

are dependent upon dynamic pressure and at the actual aileron reversal speed render the control surface completely unable to effect any control. The variable geometry allows the aileron to create controllable wing twist across the entire flight envelope. The actual utility of this approach needs to be studied in detail through application to a specific airplane design. Many aspects of the design such as weight, effect on control and handling, effect on drag and lift/drag need to be assessed for a specific baseline wing. Initially, this study used the SUGAR Phase II truss braced wing configuration 765-095-RD illustrated in Figure 3 as the platform for evaluation of the VGRWT concept and operations.



**Figure 3. SUGAR Phase 2 N+3 Vehicle Configuration**

By the end of Contract Year 2 (September 2013), the following conclusions were apparent.

- SUGAR wing is torsionally stiffer than anticipated
  - Torsional stiffness is largely not due to truss-brace system
  - Wing structure was weight optimized with flutter as a hard constraint
- As designed the NCE tip cannot induce aileron reversal – for the SUGAR 095 vehicle wing:
  - Variable sweep offers no or minimal benefit
  - Various design changes reduce E/R ratio, but not enough
- Small changes to wing (such as addition of NCE tip) have a larger than expected impact on flutter speed
- Softening of wing to facilitate aileron reversal result in extremely low flutter speeds
- The NCE concept is not viable for the present SUGAR aircraft configuration

As results became available, the study planform switched to a long range, larger, dual aisle commercial aircraft.

### 3. CONCEPT DEVELOPMENT

#### 3.1 REQUIREMENTS DEVELOPMENT

In order to define a viable configuration for the novel control effector, a set of requirements was established.

**Task 1.1 Requirements and Loads.** The SOW for Task 1.1 reads: "The contractor shall define requirements for aeroelastic and stability and control (S&C) performance to size the VGRWT control effector. The contractor shall base the performance requirements on the Subsonic Ultra Green Aircraft Research (SUGAR), truss-braced wing, and will estimate expected loads on the effector. The SUGAR PHASE I wing model was developed by Boeing under the NASA Contract "SUGAR for Subsonic Fixed Wing", NNL08AA16B - NNL08AD01T. The contractor shall provide the NASA Technical Monitor (TM) with a technical memorandum describing the requirements and their rationale."

Detailed requirements for Task 1.1:

- Loads conditions shall be derived from the SUGAR design load conditions and at a minimum include the following load conditions:
  - Symmetric pull-up of 2.5g
  - Symmetric push over of -1.0g
  - Flaps Down symmetric pull-up of 2.0g
  - 1.67 and 0G initial roll, steady roll, and checked rolls
  - 2G Taxi Bump
  - FAR Part 25 1-Cos gust criteria will be used for dynamic gust. Critical dynamic gust loads will be phased to produce force cards which will be used for static strength sizing. The VGWRT is assumed to move slow enough as to not appreciably effect gust loads, therefore gust conditions will be run open loop.
- A sufficient survey of airplane weight, C.G., fuel loading, speed, and altitude shall be analyzed to guarantee maximum loads on the structure being sized.
- Loads definition fidelity will be sufficient to support sizing of the major load paths of the Variable Geometry Raked Wing Tip (VGWRT) design to provide conceptual level weight and volumetric estimates

**Task 1.2 Mechanization Concepts Requirements.** The SOW for Task 1.2 reads: "The contractor shall define three or more mechanization concepts for the VGRWT and select one for further development. The contractor shall define requirements for actuator output power, displacements, and rates for the VGRWT actuators. The contractor shall survey commercial off-the-shelf (COTS) and advanced technology actuators that meet or exceed the defined requirements. If an advanced technology actuator appears promising, but falls just short of meeting the requirements, the contractor shall identify the key technology advances needed for that actuator."

Detailed requirements for Task 1.2:

- Concepts defined shall be consistent with the SUGAR outer wing geometry and structural load paths.

- Concepts may exceed the wing OML locally at the variable geometry location, but will minimize the extent to which wing profiles are modified
- Concepts will provide load paths sufficient withstand the design load conditions defined in Task 1.1 above
- Actuation of the VGRWT control surface(s) will be required at rates commensurate with primary flight control and will require dynamic response analyses of the structure and actuator.
- Rate of change of the large scale variable geometry actuation is expected to vary with changes in flight conditions (Mach, altitude, dynamic pressure) such that quasi-static loads and design analyses are likely to be sufficient for the large scale geometry change of the VGRWT. In the event that high rate variable geometry change is required, dynamic structural response analyses will be required.

**Task 1.2, Subtask Revision 1 Aircraft/NCE Configuration Multidisciplinary Optimization (MDO) Definition.** The SOW for Task 1.2 Subtask Revision 1 reads: "The contractor shall perform an MDO study selecting at least three candidate aircraft configurations which incorporate the Variable Geometry Raked Wing Tip (VGRWT) concept to provide a performance advantage. The design space of the MDO study shall include the following parameters at a minimum:

- Aircraft wing planform geometry (aspect ratio, sweep, area, taper)
- Aircraft wing torsional and bending stiffness and twist-bend coupling
- Variable geometry raked wing tip planform (tip span, spanwise/chordwise location of pivot, sweep range, area, taper)
- Variable geometry raked wing tip torsional and bending stiffness

The contractor shall define the MDO objective function/constraints as a weighted combination of parameters that shall include at a minimum:

- Minimum wing weight including VGRWT weight
- Minimum aerodynamic drag
- Maximum flutter speed (up to a specific value)
- Maximum roll control authority through VGRWT aileron reversal (E/R ratios)
- Maximum wing fuel volume (dry VGRWT)

The aircraft dynamic models used in the MDO analyses will be based on existing dynamic model information and may be limited to beam-rod representations of the aircraft structure. The contractor shall define for each of the three optimized configurations values of key performance metrics as compared to a representative baseline aircraft design. The three optimized configurations may be selected as the top three configurations resulting from the MDO analysis using a single objective function or the top performer from different MDO analyses using different weighting parameters in the objective function."

Detailed requirements for Task 1.2 Subtask Revision 1:

- No additional requirements over that required by the SOW.

**Task 1.3 Concept Selection Requirements.** The SOW for Task 1.3 reads: "The contractor shall down select a single mechanization concept from Task 1.2, and define the down selected concept's key characteristics. This shall include range of motion, rate limits, delay for control system latency, bandwidth, and weight and volume of major components. The contractor shall deliver a technical memorandum to the TM that describes the mechanization concepts from Task 1.2, the rationale for the downselection, the key characteristics demanded of the down selected concept, and any technology shortfalls and required actuator technology advancements that may be identified in Task 1.2."

Detailed requirements for Task 1.3:

- No additional requirements over that required by the SOW.

**Task 1.3 Subtask Revision 2 Aircraft/NCE Configuration Selection.** The SOW for Task 1.3 Subtask Revision 2 reads: "In consultation with NASA, the contractor shall review the configurations defined in the MDO analyses in Task 1.2, Subtask Revision 1 and select one configuration to use for the remainder of the study. The selection shall be based on best estimated performance as measured against NASA N+3 performance goals and other factors as decided in consultation with NASA. The selection and its supporting rationale will be informally communicated to the Government via a teleconference meeting between the Contractor and the Government technical monitor, and will be added to the progress report that follows completion of Task 1.3."

Detailed requirements for Task 1.3 Subtask Revision 2:

- No additional requirements over that required by the SOW.

**Task 2 OML Definition.** The SOW for Task 2 reads: "The contractor shall generate an electronic representation of the vehicle and control effector Outer Mold Line (OML) with a watertight geometry. The baseline vehicle OML shall be the SUGAR vehicle. The contractor shall modify the baseline OML to include the OML for the VGRWT. The contractor shall deliver baseline and modified OMLs to the Technical Monitor in electronic format."

Detailed requirements for Task 2:

- No additional requirements over that required by the SOW.

**Task 3 Subsystem Layout.** The SOW for Task 3 reads: "The contractor shall design the VGRWT concept's mechanization. This layout shall include the required mechanical and electrical subsystems, and shall indicate load bearing structural members, mechanical linkages and joints, and actuation components. The mechanization shall also include the electrical subsystem needed to drive the actuator or actuators."

The contractor shall develop a kinematic model of the VGRWT mechanization system, and shall perform kinematic simulations of the mechanization to verify proper actuator motion. The contractor shall develop a finite element model of the novel control effector using MSC PATRAN and MSC NASTRAN. The model shall be of medium fidelity, and the contractor shall use it to analyze structural loads, linear aeroelasticity, and to perform modal analyses in Task 7. The contractor shall apply the expected aerodynamic loadings defined in Task 1.1 to verify that the structural design is adequate.

The contractor shall deliver the PATRAN, NASTRAN, and kinematic models to the TM, with a technical memorandum that documents the models. This documentation shall include all assumptions made in deriving the models, definitions of variables, coordinate systems, and units."

Detailed requirements for Task 3:

- Subsystem layout will identify any protrusions beyond the wing OML and will minimize those protrusions.

**Task 3, Subtask Revision 3 NCE Subsystem Layout, Kinematic and Finite Element Model.** The SOW for Task 3 Subtask Revision 3 reads: "The contractor shall define a conceptual design for the selected variable geometry raked wing tip in sufficient detail to validate the feasibility of the MDO defined configuration in Task 1.3, Subtask Revision 2. Contractor shall create kinematic CAD and 3-D finite element model of the VGRWT design in sufficient detail to assure that structural requirements are met and structural weight is as estimated by the MDO."

Detailed requirements for Task 3 Subtask Revision 3:

- No additional requirements over that required by the SOW.

**Task 4 Subsystem Study.** The SOW for Task 4 reads: "Using the models developed in WBS 4, the contractor shall define the detailed functional requirements for the VGRWT, including range of motion, maximum and minimum rate limits, bandwidth, and time delays. The contractor shall also define the subsystem weight and power requirements. The contractor shall provide the TM with a technical memorandum that describes the proposed requirements and their rationale."

Detailed requirements for Task 4:

- No additional requirements over that required by the SOW.

**Task 5 Aerodynamics Analysis.** The SOW for Task 5 reads:

#### **"Task 5.1 Aerodynamic Analysis**

The contractor shall deliver the aerodynamic database developed under WBS 6 to the TM upon completion of its development, and all Computational Fluid Dynamics (CFD) input decks and output files, along with a technical memorandum that documents the data.

#### **Task 5.2 Develop Aerodynamic Model**

The contractor shall use CFD methods to compute the vehicle aerodynamics for the VGRWT OML developed in Task 2.

#### **Task 5.3 Aero Database to Define Drag and Support 6-DOF Simulations**

The contractor shall use CFD methods to develop an aerodynamic database of coefficients, including overall vehicle force and moment coefficients, S&C coefficients, control effector force and moment coefficients.

Detailed requirements for Task 5.1, 5.2, 5.3:

- Boeing will develop a baseline vehicle computational fluid dynamics (CFD) model for the OML defined in WBS 3.0 using CFD methods with levels of analysis fidelity appropriate to the flight regime, but not less than the one specified by NASA in the RFP requirements.
- Virginia Tech shall modify the baseline vehicle computational fluid CFD model with novel control effectors (NCE) and conduct studies over a suitable range of NCE parameters to document performance. The approach will involve detailed simulations of the outer portion of the wing deemed to be strongly influenced by the presence of the NCE. This will result in prediction of "deltas" to the baseline model results. This task will culminate in an aerodynamic database of coefficients including overall vehicle aerodynamic force and moment coefficients, stability and control coefficients, control effector force and moment coefficients, and surface pressure distributions suitable for flying qualities simulation and structural loads analyses. Supplementary baseline vehicle CFD database to match level of fidelity and breadth of novel control effector database will be developed.

#### **Task 5.4 Aero Database for Aeroelastic Analysis**

The contractor shall use CFD methods to develop an aerodynamic database of surface pressures suitable for aeroelastic analysis."

Detailed requirements for Task 5.4:

- Aerodynamic database for aeroelastic analysis shall be of equivalent fidelity as the baseline SUGAR database.
- Aerodynamic model for aeroelastic analysis will be doublet lattice corrected to match available CFD results.
- Drag loads from CFD will be applied to the loads conditions for strength sizing.

**Task 6 Aeroelastic FEM Development.** The SOW for Task 6 reads: "The contractor shall modify the baseline vehicle finite element model to include the VGRWT. The combined model shall have sufficient fidelity to perform aeroelastic simulations in MSC NASTRAN. The contractor shall perform static loading and modal analyses of the model to ensure the overall integrity of the model. The model shall be suitable for loads analysis and for determining elastic to rigid ratios and dynamic derivatives, to be used in vehicle simulations for determining flying qualities. The contractor shall deliver this finite element model to the TM upon completion of its development, along with a technical memorandum that describes it. This documentation shall include all assumptions made in deriving the models, definitions of variables, coordinate systems, and units."

Detailed requirements for Task 6:

- No additional requirements over that required by the SOW.

**Task 7 Aeroelastic FEM Analyses.** The SOW for Task 7 reads: "The contractor shall conduct finite element analysis to size the aeroelastic structural model with VGRWT control effectors using the same structural design criteria as used in the baseline vehicle defined in the SUGAR Phase II contract, NNL08AA16B-NNL11AA00T. The sizing analysis shall constrain the wing stiffness to be above a S&C-defined minimum consistent with the criteria used to size the VGRWT in Task 1.1. The contractor's analysis shall include calculation of elastic-to-rigid ratios to be used in the

S&C analysis of Task 10. The contractor's sizing analysis shall determine the structural weight increment due to the VGRWT. The analysis shall size the finite element model for linear aeroelastic loads, flutter, buckling, and stiffness. The contractor shall deliver a technical memorandum to the TM that documents the aeroelastic analysis' assumptions, technical approach, and results upon completion of this analysis. The contractor shall also deliver all of the relevant model input decks and output files to the TM."

Detailed requirements for Task 7:

- To obtain a valid weight increment due to VGRWT the Aeroelastic FEM Analysis shall be equivalent to baseline SUGAR including:
  - Structural optimization including strength, buckling, flutter, and any stiffness requirements.
  - Size all structure impacted by internal load changes due to the VGRWT.
  - Strength sizing will be done to the baseline SUGAR ultimate strain allowables and minimum gauges. All skin panels will be assumed unbuckled at ultimate load.
  - No global buckling at ultimate load including the strut and jury.
  - No flutter at 1.15 Vd
  - The large scale geometry change of the VGRWT is expected to move slowly enough to not appreciably affect flutter, therefore flutter analyses will be performed at representative fixed positions of the VGRWT. Sufficient intermediate positions will be analyzed to assure flutter requirements are met at all VGRWT positions.
  - Vehicle and control surface E/R ratios for use in S&C analysis will be determined

**Task 8 Noise Assessment.** The SOW for Task 8 reads: "The contractor shall assess the noise of the baseline SUGAR wing and VGRWT-equipped wing, with the control effector in different positions. The contractor shall use the method described in Guo, Y., "Airframe Noise Prediction by Acoustic Analogy" Contract NAS1-00086, February 2004 to assess noise from the VGRWT components. The contractor shall use the results of this analysis and the NASA Aircraft Noise Prediction Program (ANOPP) to compute relevant noise metrics, including spectrum, far field directivity, overall levels, and perceived levels. The contractor shall deliver a technical memorandum documenting the noise analysis' assumptions, technical approach, and results upon completion of this analysis."

Detailed requirements for Task 8:

- No additional requirements over that required by the SOW.

**Task 9 Subtask Revision 5 Quantitative Analysis System of Technical Performance Measures (TPMs).** The SOW for Task 9 Subtask Revision 5 reads: "The contractor shall perform a quantitative analysis of the VGRWT's impact on weight, drag, noise, and power consumption. This analysis shall quantify the differences in these metrics between the baseline aircraft control effectors, and those of the vehicle equipped with VGRWT. The contractor shall identify any deficiencies in meeting typical commercial aircraft design requirements and the approach for meeting requirements. For example, if flutter speed is less than current design requirements would dictate contractor shall identify the need for and expected performance penalties, if any, of incorporating active flutter suppression."

Detailed requirements for Task 9 Subtask Revision 5:

- No additional requirements over that required by the SOW.

**Task 10 Subtask Revision 4 Airplane Aeroelastic/Controllability Validation.** The SOW for Task 10 reads: "The contractor shall create an aircraft level finite element model that includes the 3-D finite element model of the VGRWT defined in Task 3, Subtask Revision 3. The aircraft mode other than the VGRWT shall be based on existing information and models and may be the same simplified beam-rod representation of the aircraft used in the Task 1.2 Subtask Revision 1 MDO analyses. The contractor shall validate the aeroelastic performance (flutter speed and elastic/rigid ratios and controllability) of the aircraft combined with the refined VGRWT finite element model from Task 3, Subtask Revision 3. The contractor shall identify any performance deficiencies relative to the MDO analyses and define modifications to address these deficiencies."

Detailed requirements for Task 10:

- For the purposes of this evaluation the SUGAR vehicle is treated as a Class III (large transport) vehicle in flight phase categories B (non-terminal, gradual maneuvering) and C (terminal maneuvering) as defined in MIL-STD-1797A.
- Required bank angle change in a given period of time from MIL-STD-1797A is summarized in Table 2. Medium speed range requirements are used for category A flight phases, high speed for category B, and low speed for category C flight phases. These requirements are noted by the bolded, italicized values in Table 2.

**Table 2. Roll Performance Requirements for Class III Aircraft**

Time to Achieve 30° Bank Angle Change (seconds)			
Speed Range	Cat A	Cat B	Cat C
Low	1.8	2.3	<b>2.5</b>
Medium	<b>1.5</b>	2.0	2.5
High	2.0	<b>2.3</b>	2.5

- The roll mode time constant requirements are summarized in Table 3. Boeing experience from the High Speed Civil Transport program was referenced to determine the time constant requirements in Table 3.

**Table 3. Roll Performance Requirements for Class III Aircraft**

Level	$\tau_R$ (sec)
1	1.4
2	3.0
3	10.0

- The remaining roll axis flying qualities parameters and maneuver requirements are summarized in Table 4.

**Table 4. Lateral Axis Flying Qualities and Maneuver Requirements**

All Categories	
<b>Target Roll Mode Time Constant</b>	<ul style="list-style-type: none"> <li>• 1.0*(100/equivalent airspeed in knots)           <ul style="list-style-type: none"> <li>– Upper Limit of 1.0</li> <li>– Lower Limit of 0.4</li> </ul> </li> </ul>
<b>Maneuver Requirements</b>	<ul style="list-style-type: none"> <li>• Time to Bank Demonstration Maneuver           <ul style="list-style-type: none"> <li>– Low Speed (L) Requirements for Cat C</li> <li>– Med Speed (M) Requirements for Cat A</li> <li>– High Speed (H) Requirements for Cat B</li> <li>– Perform at 1 g</li> <li>– Step input for maximum roll performance, roll through 30 deg bank angle, no capture</li> </ul> </li> </ul>
<b>Atmospheric Disturbance Requirements</b>	<ul style="list-style-type: none"> <li>• Survive MIL-STD-1797A Severe Lateral Gust           <ul style="list-style-type: none"> <li>– Using All Available Control Effectors</li> </ul> </li> <li>• Maintain Control in Moderate Turbulence           <ul style="list-style-type: none"> <li>– Using Dedicated Cruise Control Effectors (if applicable)</li> </ul> </li> </ul>

- Control power requirements will be determined by converting handling qualities requirements to angular rate and acceleration requirements at specific flight conditions. Appropriate conditions have not yet been identified.

**Task 11 Future Recommendations.** The SOW for Task 11 reads: "The contractor shall develop a strategic roadmap for future analysis, hardware development, and/or wind tunnel tests to improve the VGRWT technical readiness level. The contractor shall deliver these recommendations in the final report."

Detailed requirements for Task 11:

- No additional requirements over that required by the SOW.

### 3.2 SUGAR VGRWT CONCEPT DEVELOPMENT

The development of the Task 1.2 Mechanization Concepts requires a suitable baseline design to permit valid assessment of the Variable Geometry Raked Wing Tip (VGRWT) benefits and penalties. For the assessments of the VGRWT performance benefits to be valid, the baseline must have reasonably good performance without the VGRWT devices. The aircraft selected for this is the Boeing Subsonic Ultra Green Aircraft Research (SUGAR) 765-095-RC design. This design was the subject of a Multi-Disciplinary Optimization (MDO) study to identify the optimum span and jury strut configuration. The Novel Control Effectors program will take this optimized vehicle as its baseline to ensure that the performance comparisons will be made against a high performing design. This study led to the selection of wingspan of 170 feet and a truss braced wing configuration with a single jury strut. The specific configuration is designated C210b. The baseline wing has no tip treatment and is shown in Figure 4.

The next step was to select the wing tip geometry. The major choices were to choose the VGRWT span, sweep change extremes, and spanwise location for interface to the C210b wing. Three approaches were considered, 1) no change to the C210b wing (set the wing pivot point at some distance inboard of the tip resulting in no extension of span), 2) add a VGRWT to the wing at the existing tip (increases the span by the span of the VGRWT, and 3) create a planform in between these extremes.

A group of subject matter experts very familiar with the SUGAR configuration was consulted and formed a consensus that the best approach to be able to assess the VGRWT benefits and penalties was option 3. A wing tip span of 120 inches and a leading edge (LE) sweep range of 15 degrees (wing LE straight) to a maximum sweep of 50 degrees (VGRWT LE swept 35 degrees relative to wing LE). The location of the pivot and tip planform was selected to give an effective span equal to the baseline SUGAR wing. The selected configuration is shown in Figure 5. Further it was decided to maintain the same airfoil over the entire wing tip.

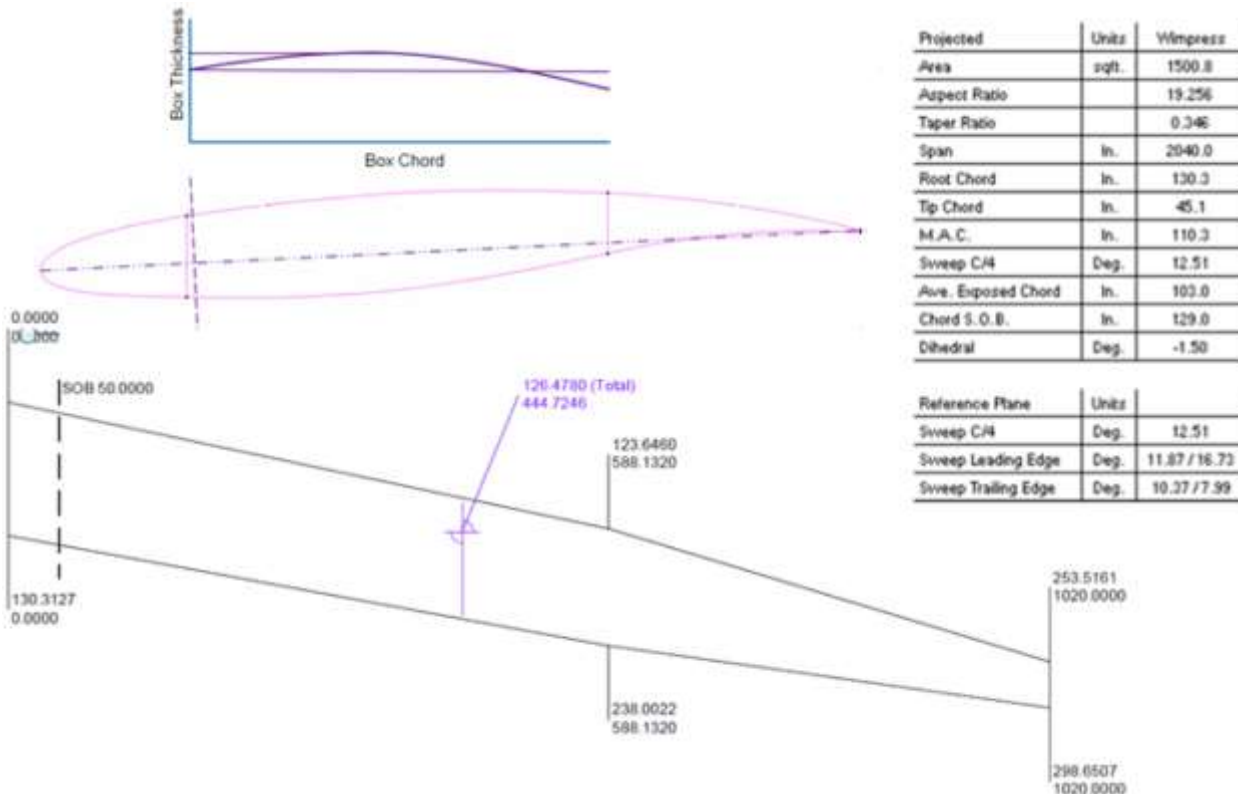


**Figure 4. Baseline Wing – SUGAR 765-095-RC, C210b**

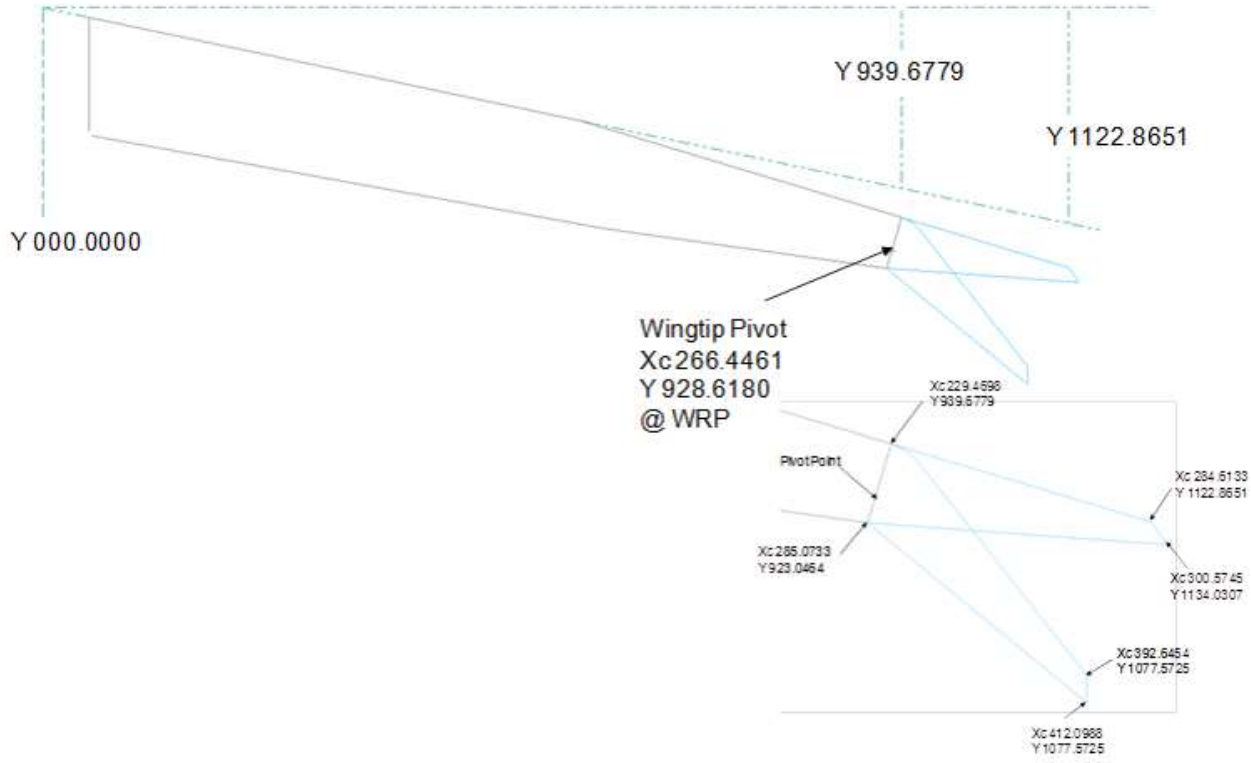


**Figure 5. SUGAR Wing with VGRWT Geometry Selected to Maintain Effective Span**

With the definition of the VGRWT planform the mechanization concepts could then be developed. The primary mechanical goal of the mechanization study was to minimize weight added to the wing. The primary aerodynamic/noise goals were to minimize drag and noise impacts. Specifically the following guidelines were adopted.

- Minimize additional weight
- Efficiently transfer tip loads to wing Forward/Aft spars
- Provide desirable twist-bend coupling (adjust load introduction point)
- No steps/snags in LE or TE for any position of the VGRWT
- Keep mechanization and actuation within the wing moldline (goal)
- Expected life consistent with commercial aircraft wing/control surface structures
- Assumes cycling rake angle no more than a few times per flight
- Wing tip control surface operates similar to existing control surfaces

The next step was to perform a brainstorming exercise which resulted in a large number of concepts. The concepts were compiled for review by NASA. The compilation is shown in Appendix A. The concepts included many ideas from a simple pivot (similar to existing variable sweep aircraft wings, e.g., B-1, F-111, F-14) ranging all the way to full morphing designs with flexible wing spars and flexible skins where the planform of the wing changed smoothly without any specifically identifiable effective pivot point.

A review/assessment of the concepts was conducted. The concepts generally included a concept for the primary load carrying structure and a concept(s) for the skin needed to achieve the geometry change. It was evident skin concepts were largely separable from the primary load path concepts and that it would be possibly advantageous to inter-mix the concepts. To reduce the resulting large matrix of solutions, the approaches to variable geometry primary load path and variable geometry skin were considered separately. Many of the load path and skin concepts were similar and so were grouped into a tractable number of options.

For the load path, each of the proposed concepts was classified into one of five categories:

- Single pivot (within the planform of the wing)
- Multiple pivot (may have a single effective pivot point within or outside of the wing planform)
- Tracked (rail and track concept similar to what is currently used on leading edge slats)
- Flexible spars/load carrying structure (the flexible spar may be limited to an area close to the joint, providing a flexible joint between a rigid wing and rigid wing tip, or a completely flexible wing tip)
- Fore/aft translation of the tip (rather than sweep)

Skin concepts were broadly categorized into:

- Flexible skins that undergo large strains to accommodate the required planform change)
- Rigid surface which telescopes into the wing as a single piece
- Sliding/telescoping skin panels

The mechanization concepts of Task 1.3 were grouped as shown above and put through an evaluation process. The structural load path and skins concepts were assessed separately. Although there were some differences in the evaluation criteria between the groups, most assessment criteria were common. All criteria were assessed on a five level scale designated low, medium-low, medium, medium-high, high - with low being the most desirable. There was not absolute baseline rating available for the VGRWT because of its novelty. Consequently rating levels were assigned as relative ratings amongst the concept.

### 3.2.1 Load Path Assessment Criteria

**Weight** – Since a detailed weight estimate for each of the concepts was not possible without a detailed design, weight was estimated based on engineering judgment. Direct load paths are favored. The SUGAR wing design, two spars with forward spar at 25% chord and aft spar at 66% chord was used.

**Complexity** – This was used as a surrogate estimation of cost and was primarily related to parts count but also was scored based on any need for high cost materials or manufacturing processes that would be used in production. Development costs of any technologies needed to implement the concept were also considered.

**Maturity (technical risk)** – Because the NCE is to be designed to support an N+3 aircraft, it was assumed that there would be sufficient time to buy down the technology risk, if sufficient funding were made available. It is assumed that sufficient funding would be made available if this

program quantifies large benefits that would justify the required funding. The estimated scale of that funding was addressed under the previous criteria. The primary objective of this criterion was an estimate of risk to this program that there would be insufficient program resources to develop a concept to the level of detail where reliable weights could be quantified and reliable structural models could be built to support the aeroelastic analyses later in the program. As a result, concepts built around pivoting rigid structure scored well while highly advanced concepts involving continuous deformation of load carrying structures scored poorly. It is believed that the aerodynamic, aeroelastic, noise and stability and control analyses done on the program will reveal opportunities for significant performance enhancement of highly advanced adaptive structures.

**Pivot Chordwise Location Limitations** – The initial definition of the concept did not identify any optimum location of the pivot or effective pivot point. Definition of an optimum, or even just a desirable pivot location requires the level of detailed analyses that will be completed by the end of the program but is not available now. Consequently, some advantage was given to concepts that permitted a wider range of pivot locations.

**Actuation Requirements** – Assessments under this criterion were based primarily on whether conventional COTS actuators are sufficient for the design or development of a new actuator concept was required. One of the underlying assumptions developed in Task 1.1 was that the variable geometry motion (sweep) would be conducted at a relatively slow speed, with time constant measured in seconds. That is, there would be no attempt to perform primary flight control (roll) or alleviate aeroelastic instability by varying the tip sweep. Roll control and control of aeroelastic response will be provided the trailing edge aileron on the wing tip which will function as a common aileron. As a result, COTS actuators should be sufficient.

For the sweep actuation, the force required by the actuation system is driven from two sources, the force required to overcome aerodynamic loads, and the force required to internally deform the load path. For the concepts involving kinematics of quasi-rigid structures (pivots and tracks/rails) the second load source was considered negligible at this level of design. The assessment would primarily consider number of independent degrees of freedom that may require actuators. For example the simple pivot and track concepts are both strictly single degree of freedom mechanical systems that would require only one actuator. The multi-pivot concept may or may not need two or more actuators if the multiple degrees of freedom could not be tied together to produce a single degree of freedom motion.

The flexible/deforming spar concepts that derive from morphing structures research will require additional force (and therefore power) capability than the concepts based on conventional kinematics. Also there is the potential that conventional actuators would not be able to produce the desired motion and new technology actuators would be required.

These assessments indicate that the primary benefit of advanced actuation technology would be to reduce weight of the actuation system (power per unit mass) and reduce its power requirements (power efficiency). Smart material actuators have an inherent advantage of high power density and have the potential to enable lighter weight actuators. However, the actuator weights are not expected to be extreme and there is no reason to assume the need for smart material actuation with the exception of the flexible spar where they may be needed to provide distributed actuation.

**Requires bumping OML** – Having parts of the actuation system protruding out of the wing skin, even with fairings, will be highly undesirable from both an aerodynamic drag and a noise

perspective. However, none of the load path concepts from the brainstorming appear to require significant protrusions from the wing profile with the exception of the translating aileron concept.

**Design for Desired Torsional Stiffness** – The criterion estimates the difficulty of obtaining sufficient torsional stiffness at the VGRWT to wing interface. The flexible spar concept requires significant anisotropy of its stiffness to reduce actuation power while carrying bending loads. The need to additionally achieve required torsion stiffness adds to the complexity of the flexible spar concept.

**Difficulty of Integrating Aileron and actuator** – This criterion was used to assess any restrictions placed on the size (spanwise or chordwise) of the aileron on the VGRWT. Most concepts required minimal restrictions on the aileron dimensions. Except that the pivot location affects the inboard end of the aileron slightly. A more forward pivot has the effect of making the inboard end of the aileron need to be moved outboard away from the pivot. Only the flexible spar had a potential for significantly restricting the aileron dimensions.

The Load Path assessment matrix is shown in Figure 6. The final selection was based on this matrix, however matrix criteria (columns) were not all weighted equally. The following criteria were highly weighted:

- Weight
- Complexity
- Maturity
- Requires protruding through the wing Outer Mold Line (OML)
- Design for torsional stiffness

The Difficulty of Integrating Aileron and actuator criterion was weighted low primarily because it did not appear to be a strong differentiator. Actuation requirements were likewise weighted low. Challenges with integration of actuation into the flexible spar concept were not strongly considered to be a differentiator because recent morphing aircraft programs (e.g., NextGen Aeronautics NMAS-1/2) have shown good potential for integrating conventional and smart material actuation into such designs.

Concept (Load Path)	Rank	Weight (load carrying structure)	Complexity (parts count)	Maturity (technical risk)	Pivot Chordwise Location Limitations	Actuation Requirements	Requires Bumping OML	Design for Desired Torsional Stiffness	Difficulty of Integrating Aileron (incl. actuator)
Single Pivot	3	Medium (single primary load path)	Low	Low	Medium (rotation point must be within wing box)	Low	Low-Medium (requires bumping OML if pivot outside wing box)	Low	Low
Multiple Pivot (4 bar)	1	Low-Medium (Larger number of moving parts and joints require additional stiffening)	Low-Medium	Low	Low (Pivot may be located at any location, even outside wing)	Low-Medium (may require additional actuators)	Low	Low-Medium	Low
Tracked	2	Medium	Medium	Low (variation on existing flap tracks)	Low (Pivot may be located at any location, even outside wing)	Low	Low	Medium	Low
Flexible Spar	X	Low-Medium (may require additional stabilizing structure)	Medium-High	High	Medium (restricted by spar)	High (Requires actuation energy to deform structure)	Low	Medium-High	Medium
Translating Aileron/Wing Tip	X	Medium	Medium-High	Low-Medium	No Sweep Change but drivers really need sweep change?	Medium (translation actuator housed in tip)	Medium	Medium-High (actuator must move with surface or extend)	Low

Figure 6. Load Path Evaluation Matrix (green desirable/red undesirable)

The multiple pivot concepts seemed to have a slight edge over the other concepts and were initially selected. However, all three of the kinematic concepts were very close in the rankings and none were immediately ruled out because of significant potential advantages for hybrid combinations.

### 3.2.2 Skin Assessment Criteria

**Weight** – An assessment was performed similar to that done for the load paths. Assessments of the skin weight for the flexible skin concept were heavily influenced by Boeing's long experience with Continuous Moldline Technology (CMT, now often called Continuous MoldLine (CML) technology. This technology has been highly successful at producing highly deformable skins that withstand out of plane local pressure loads. However, the weight of such skins is quite high relative to conventional composite or metallic skins. And the additional power requirements for actuators to drive the skin can be large. Both depend strongly on how close dimensionally the skin needs to stay relative to the desired shape. It was expected that the penalties for imperfect skin shape in this application would be high.

**Complexity** – This is largely driven by parts count, but also includes a complexity factor for both manufacturing and technology development.

**Maturity (technical risk)** – This criterion was assessed on the same basis as for the load path assessment.

**Impact of skin smoothness** – This assessment was primarily based on the need for skin joints and sliding seals.

**Impact on Actuation Requirements** – This assessment was based on the degree to which additional actuators or actuator power would be needed.

**Impact on Integrating Aileron** – Similar to the load path assessment, this criterion assessed whether the skin concept would reduce the aileron dimensions by requiring internal volume that would otherwise be used for the aileron.

The Skin assessment matrix is shown in Figure 7. The final selection was based on this matrix, however matrix criteria (columns) were not all weighted equally. The following criteria were highly weighted:

- Weight
- Complexity
- Maturity

Based on inputs from aerodynamics members of the team, the skin smoothness criterion was weighted relatively low. The initial engineering judgment assessment is that the small joints will likely not have a large impact on drag. This initial assessment will be validated during the program by assessing drag for both perfectly smooth skin geometry and for geometry with small steps and joints. If it is found that the difference is in fact large, we will be able to assess benefits with a perfectly smooth skin and can recommend development of flexible skin technology for this kind of application.

The following criteria received a relatively low weighting:

- Impact on Actuation Requirements
- Impact on Integrating Aileron - did not seem to be a strong discriminator

Concept (Skin)	Rank	Weight	Complexity (parts count)	Maturity (technical risk)	Impact on skin smoothness	Impact on actuation requirements Requirements	Impact on Integrating Aileron (incl. actuator)
Reinforced flexible skin - no steps (eg, CMT)	X	Medium-High	High	Medium-High (depending on strain levels required)	Low	Medium-High	Medium
Rigid surface structure	1	Low-Medium	Low	Low	Medium-High	Low	Low
Sliding/ telescoping covers	2	Low-Medium	Medium (covers require additional supports, guides, seals, etc.)	Low-Medium	Medium-High	Medium (covers may need their own actuators)	Medium

Figure 7. Skin Evaluation Matrix (Green Desirable/Red Undesirable)

The flexible skin was not selected in large part because of the Boeing experience with CML regarding weight and actuation requirements. Certainly such skins will have a drag/noise performance advantage, but unless we evaluate the stepped skin concepts we will not be able to assess the degree to which future development of flexible skins is justified. The approach described above yields both answers, stepped and smooth, and will enable quantification of the value of smooth, flexible skins.

Further, the approach outlined above, that will also obtain the performance benefits for a smooth skin, lead to the conclusion that if we fail to evaluate a sliding, rigid skin concept with steps, we would not be able to assess the need for future development of such skins.

The two other skin concepts involving small steps in the skin were ranked very closely and the actual selection will be an engineering tradeoff between number of step joints used and amount of internal volume required. A single rigid skin surface that telescopes into the wing, the tip or both appears to be the best selection due to minimum number of steps. This approach will be adopted unless the detailed layout shows the VGRWT is better served by multiple skin fairings.

### 3.2.3 Final Concept Selection

A preliminary aerodynamic analysis of the Variable Geometry Raked Wing Tip (VGRWT) was conducted using a vortex lattice method (VLM) to provide basic loads data to support the concept selection. A MATLAB code, Tornado, was selected due to ease of use and familiarity with the programming language. However, this code, as with all VLM codes, only calculates inviscid drag. This was not seen to be a problem at this stage of the project, as only low fidelity results are necessary at this time. A baseline planform was needed to compare and evaluate any performance enhancements or penalties of the VGRWT. The baseline selected was that of the Boeing Subsonic Ultra Green Aircraft Research (SUGAR) 765-095-RC design, specifically the planform designated C210b. This planform was modeled with Tornado, and the results showed good convergence. The pertinent data is shown below as Table 5.

**Table 5. Comparison of SUGAR Wing Planforms**

	C210b Planform	Tornado Model
<b>Area (ft<sup>2</sup>)</b>	1477.11	1476.69
<b>Span (in)</b>	2039.3	2039.29
<b>Aspect Ratio</b>	19.552	19.557
<b>Mean Aerodynamic Chord</b>	110.286	110.256
<b>Lift Coefficient</b>	0.7	0.708

Next, the VGRWT was added to the planform in accordance with the conventions agreed upon by the team. An aileron was also added to the VGRWT, taken to be 25% of chord. Only the extreme wingtip sweep cases of 0° and 35° were modeled for these preliminary analyses. These models were made assuming the pivot point of the wingtip is located at the trailing edge. The Tornado models of the wingtips in both sweep positions are shown in Figures 8 and 9, respectively. In order to maintain the same lift coefficient as the C210b planform, the main wing twist was altered slightly using Tornado. Also, in order to better facilitate the meshing of the retractable skin fairing into the leading edge of the wing, an area of constant twist was maintained near the pivot point. This twist distribution is shown in Figure 10. With these changes in place, the new planforms were

re-evaluated. With the wingtip swept  $35^\circ$  in the cruise configuration, the performance is quite comparable to the SUGAR C210b. This data is summarized below in Table 6.

**Table 6. Tornado Output for Various Planforms**

	C210b Planform	Planform with VGRWT	Planform with VGRWT
<b>Wingtip Sweep (deg)</b>	N/A	0	35
<b>Root Chord AoA (deg)</b>	3	3	3
<b>Area (ft<sup>2</sup>)</b>	1476.69	1511.33	1517.45
<b>Span (in)</b>	2039.29	2268.86	2186.02
<b>Aspect Ratio</b>	19.557	23.653	21.869
<b>Total Lift (lb)</b>	116048.4	117750.7	116234.3
<b>C<sub>L</sub></b>	0.708	0.703	0.691
<b>C<sub>D</sub></b>	0.0087	0.0075	0.0076
<b>C<sub>M</sub></b>	-0.72	-0.73	-0.71

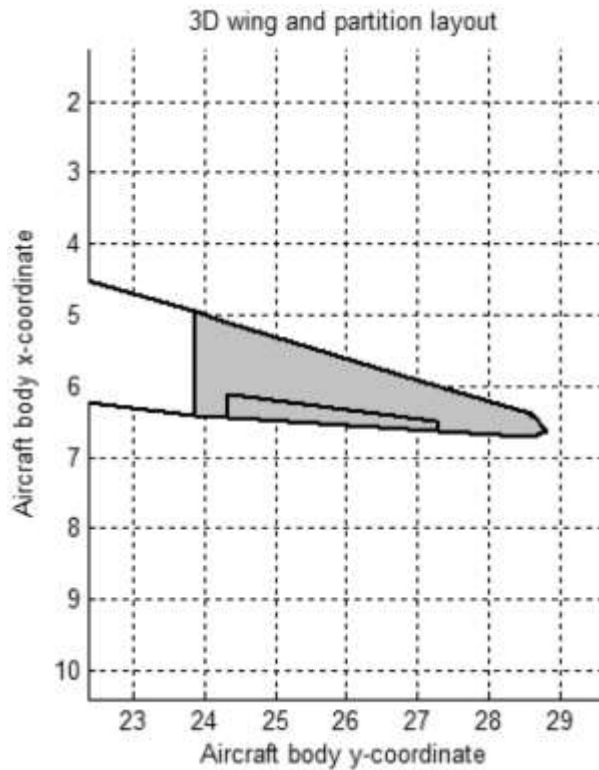


**Figure 8. VGRWT Tornado Model,  
Wingtip Unswept  
(Dimensions in Meters)**

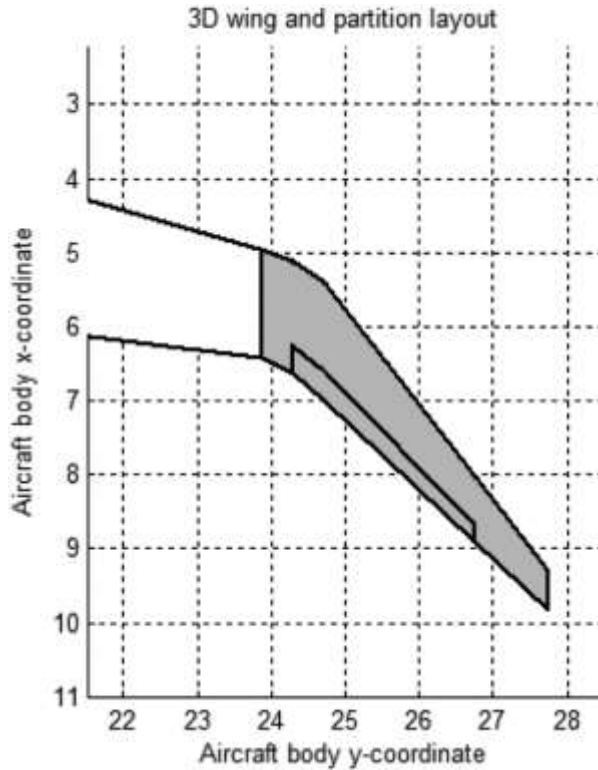


**Figure 9. VGRWT Tornado Model,  
Wingtip Swept at  $35^\circ$ ,  
Pivot at Trailing Edge  
(Dimensions in meters)**

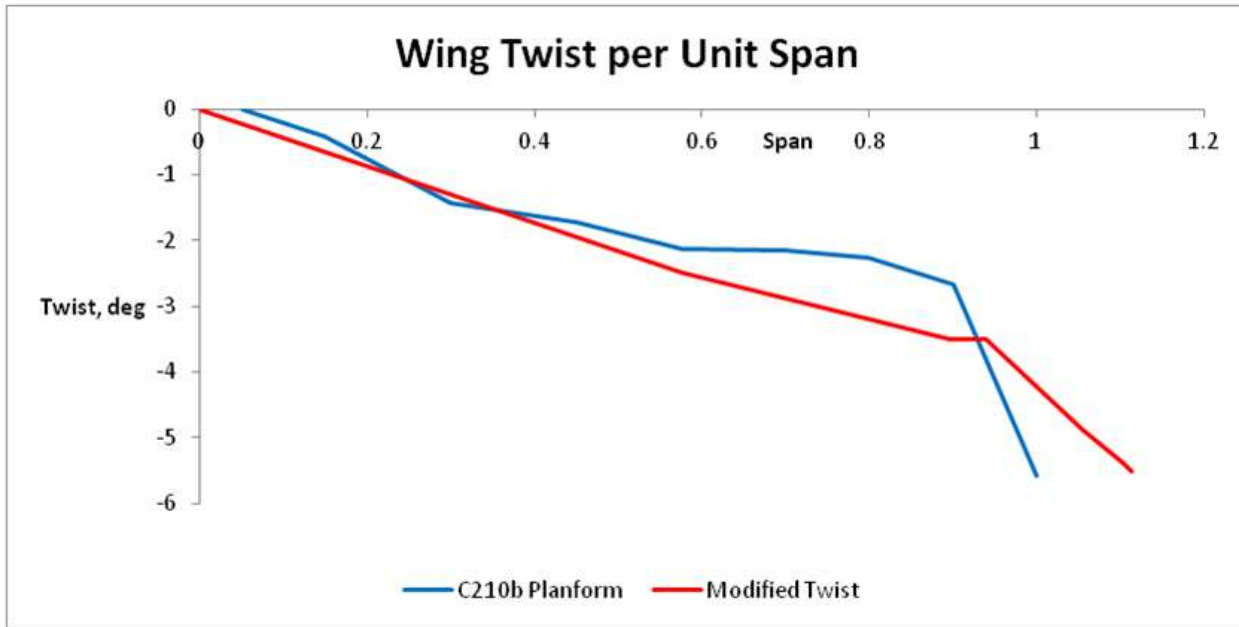


**Figure 10. Twist per Unit Span**

The forces and moments generated due to aileron deflection were studied. The aileron was deflected  $\pm 20^\circ$ . Tornado defines a downward deflection as positive, and this convention was maintained throughout the analysis. The resultant force over the wingtip (lift, drag, and side force) was calculated and plotted against deflection angle. The values plotted are for a single wingtip only and are shown in Figure 11. Using this resultant force, the twisting moment was calculated about the main wing elastic axis, taken to be 40% of the main wing chord. It was also plotted against the deflection angle. The values are also for a single wingtip only and are shown in Figure 12. This data shows that a large force and moment can be generated with the VGRWT in the fully swept position.

A simple viscous drag correction is being investigated in order to give more realistic drag coefficients. We also hope to interrogate the Tornado output to infer surface streamline patterns to aid in the wing/wingtip junction design. Finally, the structural implications of the VGRWT on the wing, such as deflection and torsional stiffness, will be investigated as the project continues.

### Resultant Force vs Aileron Deflection, Single VGRWT

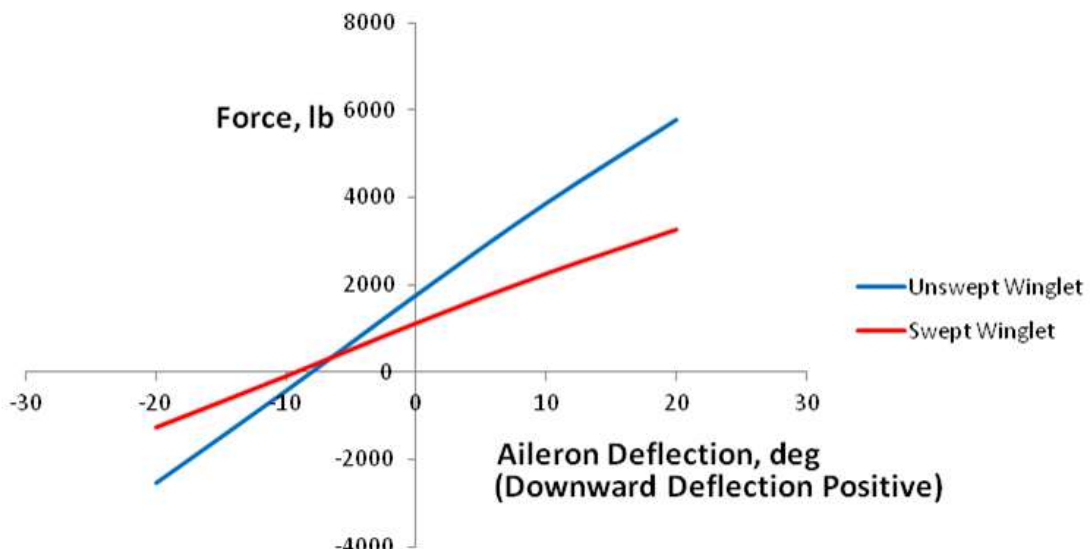


Figure 11. Force vs. Aileron Deflection, Single Wingtip

### Moment about Wing Elastic Axis vs Aileron Deflection, Single VGRWT

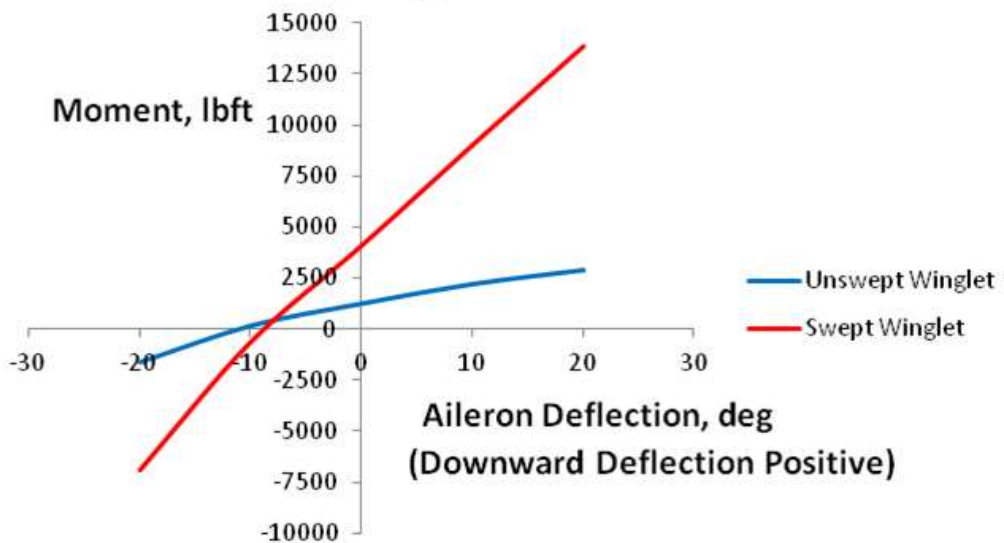
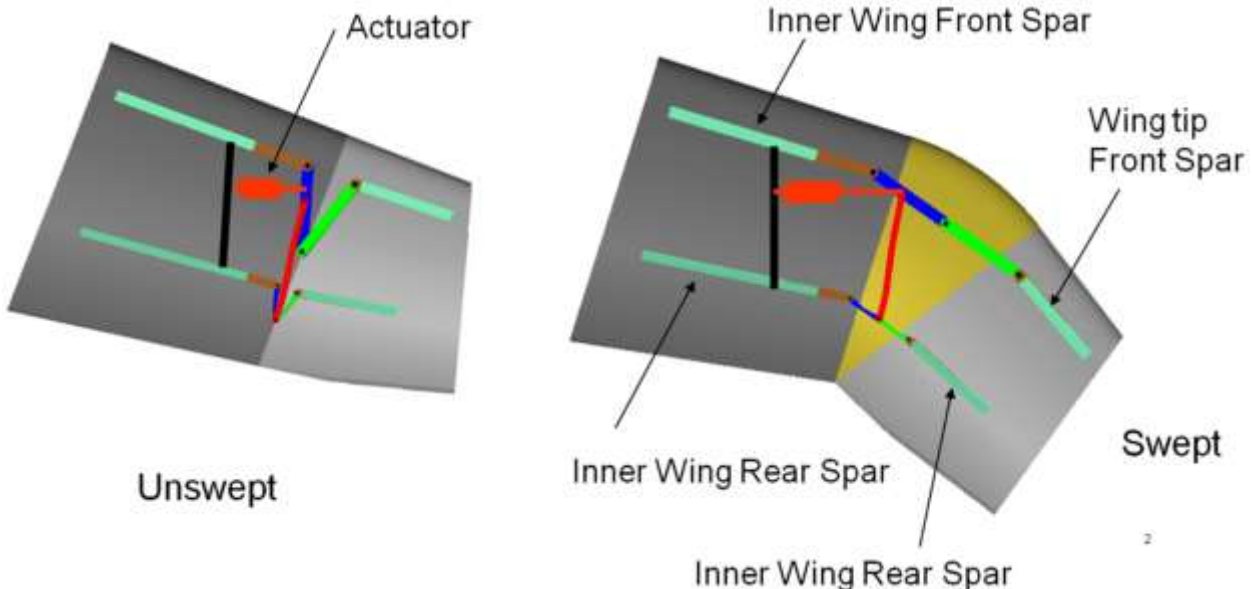


Figure 12. Moment about Wing Elastic Axis vs. Aileron Deflection, Single Wingtip

Additional conceptual layout work was required to differentiate between the options identified in the concept evaluation; specifically, the location of the pivot point and integration of the skin concept. An effective pivot point at the trailing edge reduces the number of skin fairing parts, potentially to just one. However, this one fairing would be quite large. The kinematic geometry for an effective pivot point at the trailing edge can only be achieved with the multiple pivot concept shown in Figure 13, or with a track and rail concept.



**Figure 13. Multi-Pivot Geometry for Effective Pivot at Trailing Edge**

This concept has two perceived shortcomings. First, a fairly large area (yellow) must be filled in with the retractable skin fairing. Second, when the tip is at its most forward sweep, the load path from the tip forward spar to the wing forward spar is highly indirect. Moving the pivot forward to the rear spar reduces the area of the forward skin fairing significantly, provides a very short and direct load path for the aft spar and reduces the length of the linkage that must be folded to provide the load path for the forward spar. Additional layout work indicated that the forward multi-pivot linkage could be replaced with a track and rail system as illustrated in Figure 14.

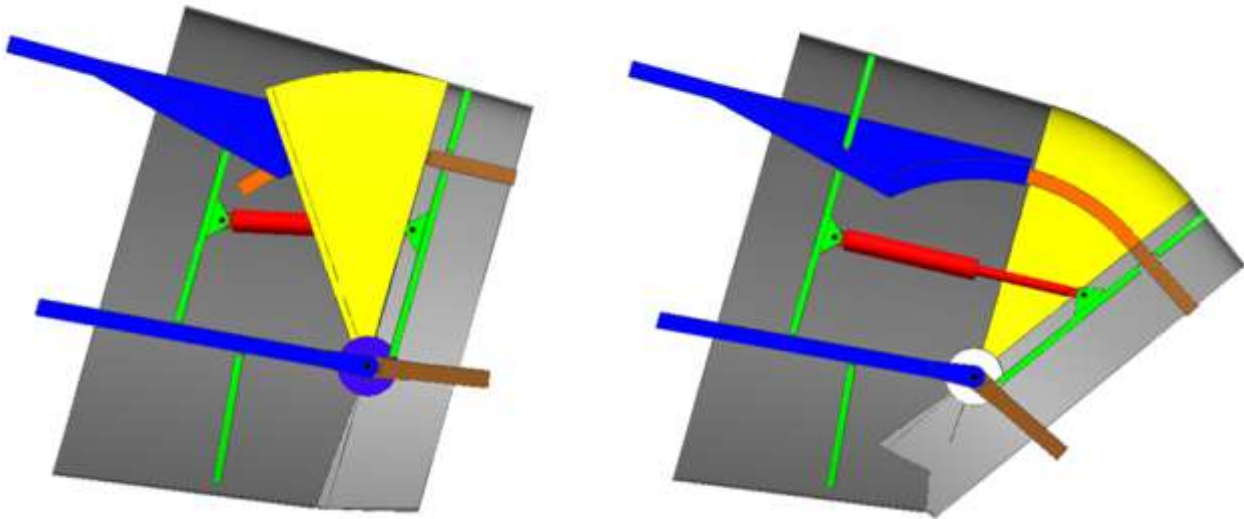


**Figure 14. Aft Spar Pivot/Forward Spar Track/Rail Geometry**

The Figure 14 mechanization concept has been selected for the NCE program. System layout and structural sizing are now underway. Small changes to location of actuator and details of the skin fairings will occur during system layout. The key features of this concept include:

- Short, direct load paths for both the forward and aft spar
- Reduced size of the skin fairing which must nest into the wing
- Easy integration of actuator
- Easy integration of electrical, hydraulic or other lines through the joint

A concept for the flexible trailing edge fairing located aft of the wingtip pivot point was developed based upon previous experience with morphing wing structures. Shear cell elements with rigid edges, flexible support blades, and a thin silicone membrane skin (0.080" thickness) have been shown to provide substantial changes in area while supporting out-of-plane skin loads without wrinkling or distortion (Figure 15). NextGen wind tunnel tests [1] have demonstrated that this concept is capable of withstanding Mach numbers as high as 0.9 and dynamic pressures of 400 psf with minimal out-of-plane deflection.



**Figure 15. Shear cell used in previous NextGen morphing program with silicone skin removed to show flexible support blades.**

The NCE trailing edge fairing concept utilizes four long trapezoidal shear cell pairs (Figure 16, red and white segments) attached to fixed points along the rear spar. The outermost edges are attached to the adjacent rigid trailing edge surfaces on the root wing and wingtip. The use of trapezoidal shear cells allows the trailing edge length to be reduced in the swept case without needing the leading edge spacing to change significantly. Triangular areas (orange) would be filled with a negative Poisson's Ratio material similar to that used for the DARPA/NASA/NextGen Morphing Aircraft Structures (NMAS) program under AFRL Contract F33615-02-C-3257 and NASA Contract NNL06AA26C. Floating thin rigid fairings (blue) cover the uneven leading edge of the shear cells.

The estimated weight of the complete flexible fairing is approximately 6-7 lbs, however a value of 15 lbs will be used to be conservative. In order to compress the fairing, a maximum torque of 339 ft-lbs may be required about the pivot point, however it is anticipated that the actual value required will be reduced by pre-stressing the skin membrane.

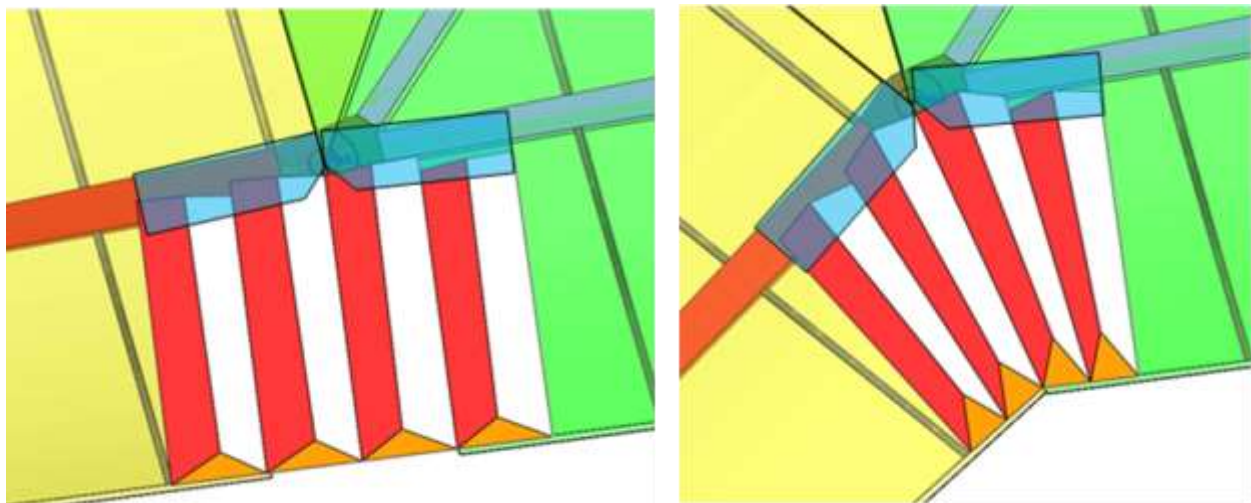


**Figure 16. Flexible trailing edge fairing concept for VGRWT in unswept (left) and swept (right) conditions.**

The range of motion of the selected concept is a sweep change of 35 degrees in the plane of the wing. The unswept position has the tip leading edge parallel to the outer wing leading edge which has a 15 degree sweep. The actuation system is reported upon in Task 4, Subsystem Study. It will be either a linear actuator or a rack and pinion type actuator driving the track and rail at the forward spar. The Task 4 study will choose the specific type of actuator for the sweep mechanism and for the aileron. Candidate actuators included hydraulic, electric motor driven electromechanical actuator (EMA), electrohydraulic actuator (EHA) or other motor driving a ball screw type of pushrod. Other candidate actuators were also considered. Because the sweep actuator is not be used for primary flight control, the rate of actuation for the sweep mechanism is low such that other advanced actuators such as shape memory alloy (SMA) may also be considered to minimize weight and volume. In general, the requirements for the sweep actuator are modest and a wide variety of existing actuator types is expected to easily provide the required motion.

The requirements on the aileron actuator are no different than is typical for ailerons on this class of aircraft. However, the aileron actuator will be used for primary flight control and so bandwidth and control system latency requirements are similar to existing aileron actuators. Again it is expected that the conventional technology actuators will be adequate for the VGRWT aileron.

The key potential technology shortcoming may be the skins. The planned approach of analyzing both perfectly smooth and stepped skins will provide the basis for assessing the importance of the flexible skins.

## 4. AIRCRAFT/NCE CONFIGURATION MULTIDISCIPLINARY OPTIMIZATION (MDO)

In order to observe the aeroelastic effects of the NCE wingtip, a trial design was developed and applied to the FEM developed for the SUGAR TBW aircraft and analyzed for flutter and lateral roll control performance. Flutter analyses were performed for full-fuel and reserve fuel mass cases, as well as for the 0 degree and 26 degree sweep cases of the NCE wing-tip. The addition of the NCE wingtip caused a reduction in flutter speed when compared to the baseline SUGAR wing. The baseline SUGAR aircraft was optimized to have a flutter speed of 401 KEAS. The worst case NCE flutter analysis was for the 0-degree sweep NCE, reserve fuel mass case, and it showed a flutter speed of 296 KEAS. The flutter speed dependence on ballast weight was also examined. The trend shown for this TBW aircraft is for the flutter speed to increase with the addition of ballast, which is counter to the behavior typically seen for a cantilever wing.

The lateral control analysis indicated that sufficient roll-control authority was achieved for the 0-degree sweep configuration at cruise, but that the wing was not acting in control reversal. Sweeping the NCE to 26 degrees moved operation closer to the reversal point but did not achieve reversal and also lacked sufficient roll authority. Several alternative aileron and structural designs were considered for their ability to achieve the goal of adequate roll-control acting in aileron reversal. The results indicated that designs which used a more flexible wing (“minimum gauge structure”) increased the aileron reversal effect. Similarly, aileron designs whose Center of Pressure (CP) moved aft of the baseline, such as the “long aileron” and “extra-long aileron” also improved the aileron reversal effect. Designs which did not change the aileron CP (“2x effectiveness”) had no effect on the reversal effect while designs that moved the CP forward (“Full flying NCE”) were actually detrimental to achieving aileron reversal. These results indicate that the magnitude of the aileron force does not influence the E/R, but rather it is the location of the force that is important. This behavior is best illustrated by the “tip controller” variation which demonstrates an E/R value which is closest to the desired goal of -0.6.

Since the NCE wingtip could not be applied desirably on the torsionally stiff TBW SUGAR wing, the focus was instead shifted to more flexible aircraft for longer-range mission. It was also planned that the concept should be tried on new designs obtained from the VT MDO environment. The new phase of the VT NCE research has been published as an AIAA paper as shown below.

### 4.1 INTRODUCTION

The rising cost of fuel has been a major concern to the commercial aerospace community over the past few decades. This has led the National Aeronautics and Space Administration (NASA) to select minimizing fuel burn and increasing energy efficiency as their main long-term research objectives for subsonic fixed wing commercial aircraft [2]. In order to meet these requirements, TBW configurations have been studied extensively at Virginia Tech over the past 15+ years in comparison with the conventional cantilever wing designs. The designs are optimized for minimum fuel burn with the help of the MDO tools developed at Virginia Tech [3] employing future technologies and concepts to benefit the aerodynamic performance [4]. Results obtained for a long-range mission similar to a Boeing 777-200 LR for a cruise Mach of 0.85, showed that the optimized cantilever vehicle was able to reduce fuel burn by up to 21% and the optimized TBW by up to 35% compared to existing designs [5]. These designs resulted in much larger lift to drag ratio and much larger span than the existing configuration. The overall effect is aircraft designs with flexible wings

whose aeroelastic behavior was not studied while performing MDO simulations in the past. Some recent investigations of TBW designs for a medium-range mission like a Boeing 737-800NG at a cruise Mach of 0.7 performed through the VT MDO environment, predicted that these configurations could undergo flutter within the flight envelope [6]. To prevent flutter, a flutter constraint was applied which stiffened the structure by either increasing the thickness of the wing sections or reducing the span or both and hence reduced lift to drag ratios. The overall effect was an increase in fuel burn caused by the flutter constraint.

Recently, concerns about the control effectiveness of these flexible aircraft at or around cruise conditions have been considered. An analysis of control effectiveness is necessary to predict control reversal and the roll control authority of an airplane at various flight conditions. It is expected that for very flexible designs, control reversal may occur at or around the cruise conditions or even much earlier leading to a region of dynamic pressure around cruise conditions where very little control effectiveness is provided by the aileron. Such instances for flexible wings have been mentioned in the past [7]. This problem has been addressed in the past in several ways. The most notable of these being the smart aileron stiffness approach [8] or using a combination of leading-edge and trailing-edge ailerons with their motion controlled using active mechanisms [9, 10, 11]. All of these methods use conventional aileron control in pre-reversal conditions or until the control effectiveness drops below a specified value. Beyond such dynamic pressures, the active mechanism tries to suppress control reversal or control the aircraft in post-reversal conditions by changing the sign of the control forces. While these alternatives seem productive, the weight associated with multiple control surfaces and the related mechanisms and the risk associated with the failure of the active control mechanisms are significant drawbacks. Thus, the alternative proposed by Boeing considered here is to employ a wing-tip which will have a mechanism to sweep forward and back as required within the flight envelope and provide the necessary roll control and possibly bring about flutter mitigation of the designs. This wing-tip shown in Figure 17 is termed as the Novel Control Effector (NCE) wing-tip. If successful, it will prove a simpler, lighter and more robust system than the conventional mechanism as it obviates the additional control surface or wing stiffening or active flutter suppression mechanisms. These observations motivated the present investigation into the benefits of using the NCE tip both for roll control and for flutter avoidance.

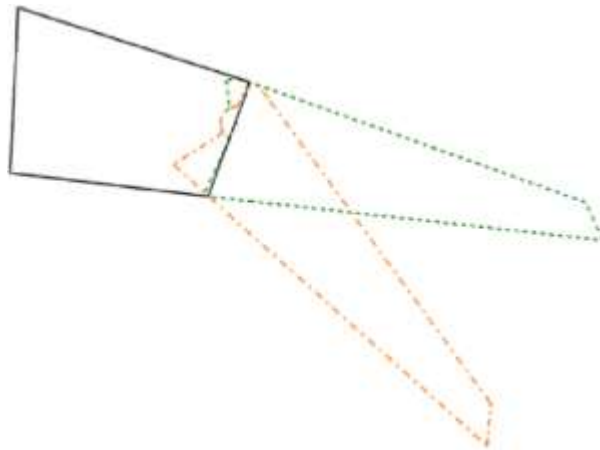


**Figure 17. Sketch of Boeing NCE Wingtip Concept**

Some modifications were made in the structural modeling in the VT MDO code for a more accurate computation of the torsional stiffness of the wing which is considered to be a very important part of the study. An analysis was developed to evaluate the control effectiveness of the aileron as well as the steady-state roll rates, maximum roll accelerations and bank angles achieved over a prescribed time. Constraints were also formulated based on the values of bank angles required of the aircraft over a certain time at cruise flight conditions. Results given later in the article show that the NCE tip is able to meet the requirements to sustain desirable roll motion and also provide significant increase in flutter margin by changing the sweep of the tip relative to the wing.

## 4.2 DESIGN METHODOLOGY

The VT MDO design methodology developed previously [3] was used mostly for the MDO process except for a new structural model that was developed for the structural analysis. The aeroelastic analysis module was also updated by adding the capability to evaluate the control effectiveness due to control surfaces and for evaluating steady-state roll rate, roll acceleration of the aircraft and bank angles as a function of time for a single degree-of-freedom lateral motion of the aircraft.

### 4.2.1 Development of new structural model

The structural analysis in all the previous MDO studies [5, 12, 13] was carried out using the double plate idealization of the aircraft wing-box as shown in Figure 18(a). It was assumed that the wing-box would act as a beam with the bending stiffness provided by the upper and lower skins and the spars and the ribs carrying the shear loads. It is understood, that this leads to much thicker upper and lower skins than in an actual aircraft wing-box where the spars and the stiffeners provide most of the bending stiffness and the skins just form very thin panels carrying shear. The simple model is adequate for estimating the load-bearing weight but the thicker skins would result in an over estimation of the torsional stiffness of the wing sections thereby leading to inaccurate aeroelastic analysis, especially while measuring the control effectiveness of the wing. This problem has been addressed in this study by introducing an updated, higher-fidelity wing-box model as shown in Figure 18(b).

The wing-box is designed as a combination of spars, skin panels and stiffeners. The skin panels formed by the network of the spars, the stiffeners and the ribs, are designed against panel buckling due to shear loads. The wing-box may have multiple stiffeners. For this study, we have chosen three stiffeners based on the type of aircraft and the wing span and chord lengths. Simply supported boundary conditions are assumed for the plate. The shear stresses developed in the skin panels due to external transverse forces and torques are compared against critical shear buckling stresses of the skin panels. Thus, the skin panels are sized iteratively by increasing their thickness starting from a minimum value of 0.1 in. until the stresses meet the buckling constraint. The spar webs do not contribute to bending but are designed against shear stresses generated from the shear flow due to both transverse lift forces and those generated due to twisting loads. The spar webs are sized by comparing the shear stresses against yielding due to shear. The spar caps and the stiffeners are the major contributors towards bending stiffness. Their areas are sized by comparing the direct stresses developed from the bending moment at the various sections against yielding.

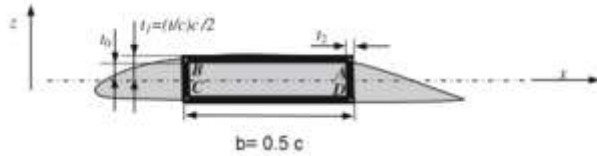


**Figure 18(a). Previous VT MDO Structural Model Suitable for Weight Estimation**

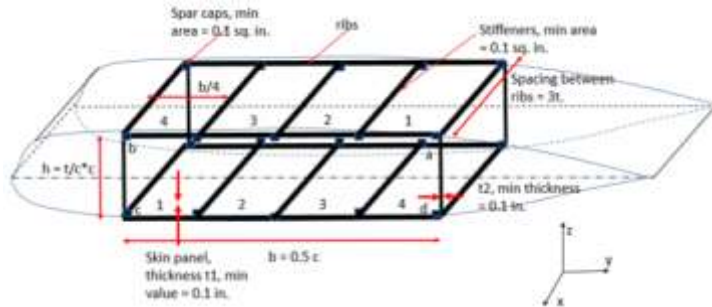


**Figure 18(b). New VT MDO Structural Model for Improved Torsional Stiffness Evaluation**

Standard methods from Megson [14] are used to evaluate the shear flow in the wing section as shown in Figure 18(b). The shear stresses are obtained by dividing the shear flow by the thickness of the member. The highest stresses are obtained at the end panels. These are then used for skin buckling check against the critical buckling stresses obtained from Timoshenko and Gere [15], where tabulated values are provided for various ratios of panel dimensions when these panels are subjected to uniform loads on all the sides.

The shear stresses at the spar webs are obtained by dividing the total shear flow due to transverse forces and those due to twisting moments by the thickness of the spar webs. The total shear stress is then compared to the allowable yield stress in shear for the ductile material. Finally, the direct stresses due to bending are obtained using conventional analysis and compared with the allowable yield stress of the material in tension/compression. The material properties are available in [5].

#### 4.2.2 Aeroelastic Analysis of the Lateral Motion of the Vehicle

##### 4.2.2.1 Aerodynamic Analysis

It is well-known that using thin airfoil theory with Prandtl-Glauert corrections for compressibility of the flow is not sufficient for representing the transonic flow experienced by the vehicle. Thus, an attempt to incorporate some measure of transonic effects has been included here by varying the location of the aerodynamic center of the airfoil from quarter chord to around 40% of the airfoil chord as the flow accelerates from Mach 0.5 to 0.9, both for the main wing as well as for the aileron. Such effects due to the formation of normal shock waves in transonic flow are well known and have been observed in experimental results for a varied class of airfoils [16]. Although, due to lack of CFD simulations, the simple model used in the present study cannot claim highly accurate values of the shift in aerodynamic center, the results will certainly be a closer representation of the reality.

Since the flutter analysis described later in the article uses a Prandtl-Glauert based compressibility correction for the aerodynamics, a Mach number of 0.96 is considered as the maximum Mach

number up to which reasonably accurate predictions can be performed even with the simple aerodynamic center shift mentioned above.

#### 4.2.2.2 Analysis of Control Effectiveness

The control effectiveness is measured by evaluating the ratio of elastic to rigid rolling moments developed on a wing due to a unit deflection of the control surface. Usually, such studies are performed for the outboard aileron mainly because of the large moment arm associated to it to generate rolling moments of larger magnitude. If the wing was perfectly rigid, the aileron would produce an additional lift force when it is deflected at positive angles of attack. However, for an elastic wing, the negative pitching moment generated by the aileron would develop negative angles of attack in the main wing due to the wing twist associated with a flexible wing. Thus, negative normal force is generated which counter-acts the lift generated by the aileron thereby reducing its effectiveness. For certain flight conditions and given structural stiffness of the wing, the effective stiffness of the wing maybe such that large twist is generated on the main wing thereby developing an overall negative normal force for the wing-aileron system leading to control reversal. Such a situation may occur well before divergence and would adversely affect the flight handling capabilities as well as flight safety.

The control effectiveness was calculated for a range of flight conditions based on the flight envelope of the long-range mission of Boeing 777-200ER as shown in Figure 19. The red line represents the cruise Mach number of the flight at various altitudes, and the two blue dotted lines on either side of it represents the upper and lower limits of Mach number at which control effectiveness is being evaluated.

It is clear that using thin airfoil theory with Prandtl-Glauert corrections for compressibility of the flow is not sufficient for representing the transonic flow experienced by the vehicle. Thus, an attempt to incorporate some measure of the transonic effects has been attempted by varying location of the aerodynamic center of the airfoil from quarter chord to around 40% of the airfoil as the flow accelerated form Mach 0.5 to Mach 0.9, both for the main wing and the aileron. Such effects due to formation of normal shock waves in transonic flow are well known and have been observed in experimental results for a varied class of airfoils [10]. Although, due to lack of CFD simulations, the simple model used in the present study cannot claim accurate values of the shift in aerodynamic center, the results will certainly be a closer representation of the reality.

The main aeroelastic equation used for the analysis of control effectiveness is as shown below. The detailed derivation for the aeroelastic system and the analyses for control effectiveness have been provided in Appendix.

$$[K_s]\{q\} = [K_{a-wing}]\{q\} + \mathbf{Q}_{r-wing} + \mathbf{Q}_{r/cs} \quad (1)$$

In the absence of any elastic deformation, the rigid rolling moment can be obtained by using just the rigid aerodynamic forces,

$$l_r = (.)(\mathbf{Q}_{r-wing} + \mathbf{Q}_{r/cs}) \quad (2)$$

Where  $(.)$  represents an operator which converts the lift and pitching moment to the roll moment by multiplying with a moment arm or via coordinate transformation. In order to evaluate the

elastic roll moment, we must first solve Equation 9 to obtain  $q$ . Then, we can obtain the elastic roll moment as,

$$l_e = (.)([K_{a-wing}]\{q\} + \mathbf{Q}_{r-wing} + \mathbf{Q}_{r-cs}) \quad (3)$$

The ratio  $l_e$  to  $l_r$  gives the value of the control effectiveness.

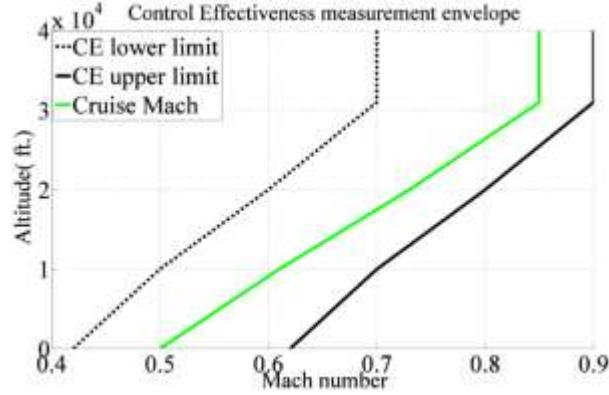


**Figure 19. Control Effectiveness measurement envelope for "777-like" aircraft**

#### 4.2.2.3 Analysis of Rolling Motion

One of the major goals of this study was to investigate the effect of the sweeping mechanism of the NCE tip on the roll motion of the vehicle. Thus, analysis of the roll motion is required to perform this study. A roll control requirement of long-range transport flight is the capability to roll through 30 degrees bank angle in 2.0 seconds using the outboard aileron [17]. For this study, all of the outboard aileron is placed on the NCE tip and it will be observed if the sweep of the NCE tip can be used to meet to bank angle requirement whenever the conventional wing-aileron system fails to do so.

Assuming a single degree of freedom and small angle approximation, the 1st order kinematics for the roll rate  $p$  of the vehicle can be written as,

$$\dot{p} = (p_{cmd} - p)/\tau \quad (4)$$

Integrating Equation 4 and assuming  $p_{cmd} = p_{ss}$  as the initial condition, we have the following equation for the roll rate of the vehicle,

$$p(t) = p_{ss} \left( 1 - e^{t/\tau} \right) \quad (5)$$

The bank angle  $\phi$  can be derived using Equation 5 as follows,

$$\begin{aligned} \phi(\Delta t) &= \int_0^{\Delta t} p(t) dt \\ &= \int_0^{\Delta t} p_{ss} \left( 1 - e^{t/\tau} \right) dt \end{aligned}$$

$$= \int_0^{\Delta t} p_{ss} \left(1 - e^{t/\tau}\right) dt \quad (6)$$

Again, in Equation 4, if it is assumed that at initiation  $p_{cmd} = p_{ss}$  and  $p = 0$ ,

$$\dot{p}_{t=0} = \dot{p}_{max} = \frac{p_{ss}}{\tau} \quad (7)$$

Thus, if we know  $p_{ss}$  and  $\dot{p}_{max}$ , we can find out  $\tau$ . This can be used in Equation 6 to find out bank angle  $\phi$  achieved in the time interval  $\Delta t$ . This can be employed as a constraint in the MDO for the roll control requirement for the vehicle. The roll rate and roll acceleration can be evaluated by using the equilibrium of rolling motion as,

$$\begin{aligned} \dot{p} &= \frac{l}{I_{m-xx}} = \frac{q_d \tilde{s} b}{I_{m-xx}} \sum Cl \\ \dot{p} &\approx \frac{q_d \tilde{s} b}{I_{m-xx}} \left( Cl_{\delta} \delta + Cl_p \frac{pb}{2V_T} \right) \end{aligned} \quad (8)$$

Thus, for maximum roll acceleration when  $p = 0$ , from Equation 8 we have

$$\dot{p}_{max} \approx \frac{q_d \tilde{s} b}{I_{m-xx}} K_{e/r,\delta} Cl_{\delta} \delta_{max} \quad (9)$$

Again, after a very long time when steady-state roll rate is achieved and  $\dot{p} = 0$ , we have

$$\dot{p}_{ss} \approx \frac{2V_T}{b} \frac{K_{e/r,\delta} Cl_{\delta}}{K_{e/r,p} Cl_p} \delta_{max} \quad (10)$$

Thus, Equations 9, 10, 7 and 6 can be used to obtain the bank angle  $\phi$  as explained before.

### 4.3 MULTIDISCIPLINARY OPTIMIZATION PROBLEM STATEMENT

The vehicle flight mission is shown in Figure 20. The vehicle takes off from an 11,000 ft. runway, climbs to an initial cruise altitude for a range of 7730 NM at a Mach number of 0.85. The landing takes place on an 11,000 ft. field located at sea level with reserve fuel for an additional 350 NM.

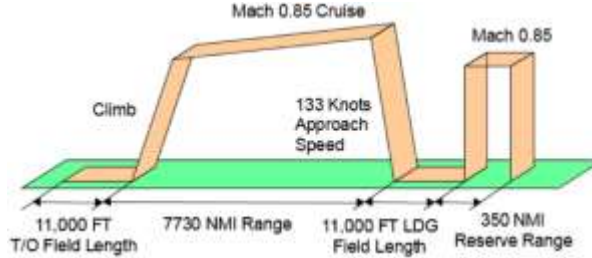


**Figure 20. "777-like" Vehicle Flight Mission**

The objective for the mission is to minimize fuel burn and emissions. The optimization process is a search algorithm which traverses the design parametric space to search for designs which satisfy all the required design constraints and at the same time gives the minimum value for the

objective function. The optimization algorithm used here is a Genetic Algorithm, Darwin, which uses an evolutionary method to search for feasible designs.

The design parametric space is made up of design variables which include geometric design variables like span, aspect-ratio, sectional chords and sectional thicknesses at various locations along the span, as well as non-geometric variables like fuel weight, design altitude and maximum required thrust for the aircraft. These design variables have been chosen carefully based on previous studies [3, 5] as they provide a sufficient parametric definition of the aircraft configurations as well as their performance.

The design constraints include maximum tip deflection at landing, maximum sectional 2D lift coefficient constraint for transonic flow, range of the vehicle, fuel capacity of the wings as well as constraints on landing, take-off and approach as per FAA regulations. These have been discussed in detail in a previous study [6]. There are additional constraints on flutter and now on roll control. The flutter constraint used here is similar to the one described in [6] except that the flutter boundary  $M_F$ , is as defined in Figure 21. This boundary is either 1.15 times the dive speed of the aircraft or a Mach number of 0.96 whichever is lowest. A Mach number of 0.96 is considered as the maximum Mach number up to which reasonably accurate predictions can be performed.

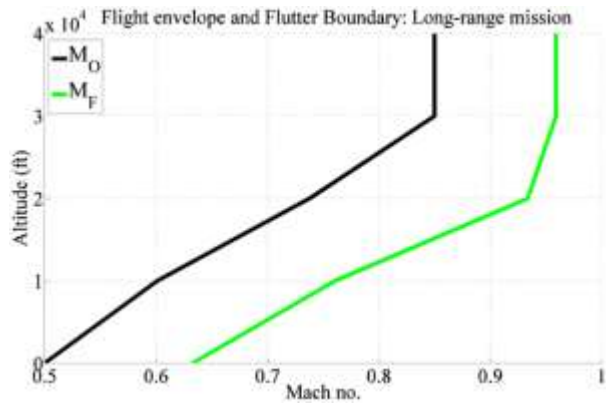


**Figure 21. "Boeing 777-like" Vehicle Flight Envelope and Flutter Boundary**

The new addition in this study is the constraint on bank angle achieved by the aircraft with the outboard aileron in a specified time. This is evaluated at several cruise flight conditions along the flight envelope, and the lowest value is considered as the most critical case. The prescribed value is 30 degrees bank angle rotated in 2.0 seconds due to an outboard aileron and this is set as the constraint. If the most critical value passes this requirement, the constraint for the desired roll motion will be satisfied.

The entire MDO study is carried out in ModelCenter [18] framework, which serves as an interface between the various custom analysis modules also known as analysis nodes, and the optimizer termed as the optimization node. ModelCenter provides the necessary link between the various nodes which are required to perform the multidisciplinary study. Details about the ModelCenter environment and its functionalities have been discussed before [3, 6, 12] and will not be restated here.

The initial study was performed with a reduced set of load cases, as certain gust load cases were not considered relevant at least for the preliminary simulations. The loads cases are shown in Table 7.

**Table 7. Initial Load Cases Considered**

Load Case #	Load Factor	Fuel (%)	Altitude (kft.)	Flutter Analyses
1	+2.5g	100	-	Mach 0.5 to Flutter boundary
2	+2.5g	20	-	Mach 0.5 to Flutter boundary
3	-1.0g	100	-	Mach 0.5 to Flutter boundary
4	-1.0g	0	-	Mach 0.5 to Flutter boundary
5	2.0g Taxi Bump	100	0	-

## 4.4 RESULTS

### 4.4.1 Cantilever Designs

The whole analysis was performed in a two-step process. First the designs were obtained with the MDO tool without an NCE tip, and all the constraints other than the bank-angle constraint were satisfied. Then, based on the performance of the designs to achieve the roll requirement without the NCE tip, a second set of analyses were made outside the MDO framework with the NCE tip set at various sweep angles to observe if the tip provides benefits for roll motion and/or flutter.

#### 4.4.1.1 Optimization results

The MDO tool was applied to cantilever designs and the feasible designs which satisfied all the applied constraint other than the bank-angle constraint are shown in Figure 22. From these designs, Design 1 was chosen as the most attractive design for having the minimum fuel burn as well as relatively low take-off weight. Cantilever Design 1 is illustrated in Figure 23, and the design parameters are shown in the first column of Table 8.

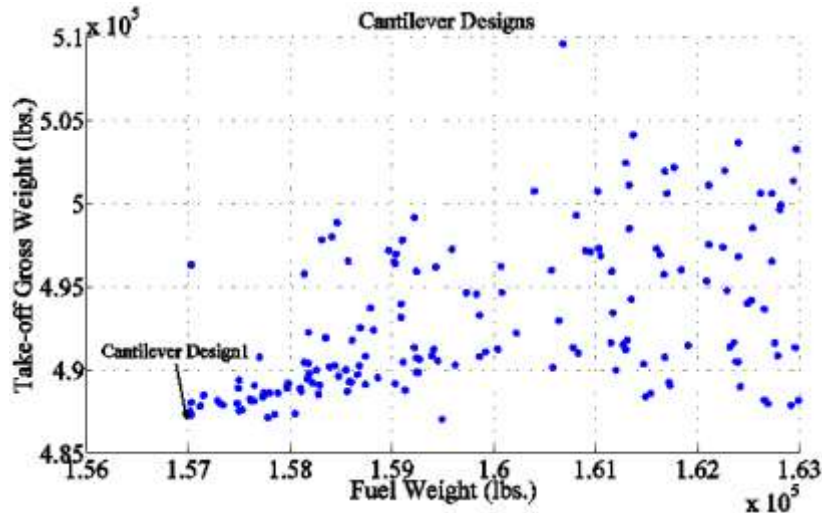


**Figure 22. Cantilever Designs Obtained without NCE Tip**



**Figure 23. Minimum Fuel Cantilever: Design 1**

To understand the capacity of the conventional aileron to provide sufficient roll control for cantilever designs, the bank angle achieved by the aircraft in 2.0 seconds with a conventional aileron for various Mach numbers at various altitudes are shown in Figure 24. One can see that at the cruise Mach numbers at each of the different altitudes depicted in Figure 24 by small black squares on each of the lines, the conventional aileron easily meets the requirement for bank angle to be achieved in 2.0 seconds. Thus, we can conclude that for the best cantilever designs obtained by minimizing fuel burn, the NCE tip is not required for the vehicle to achieve the required roll control.

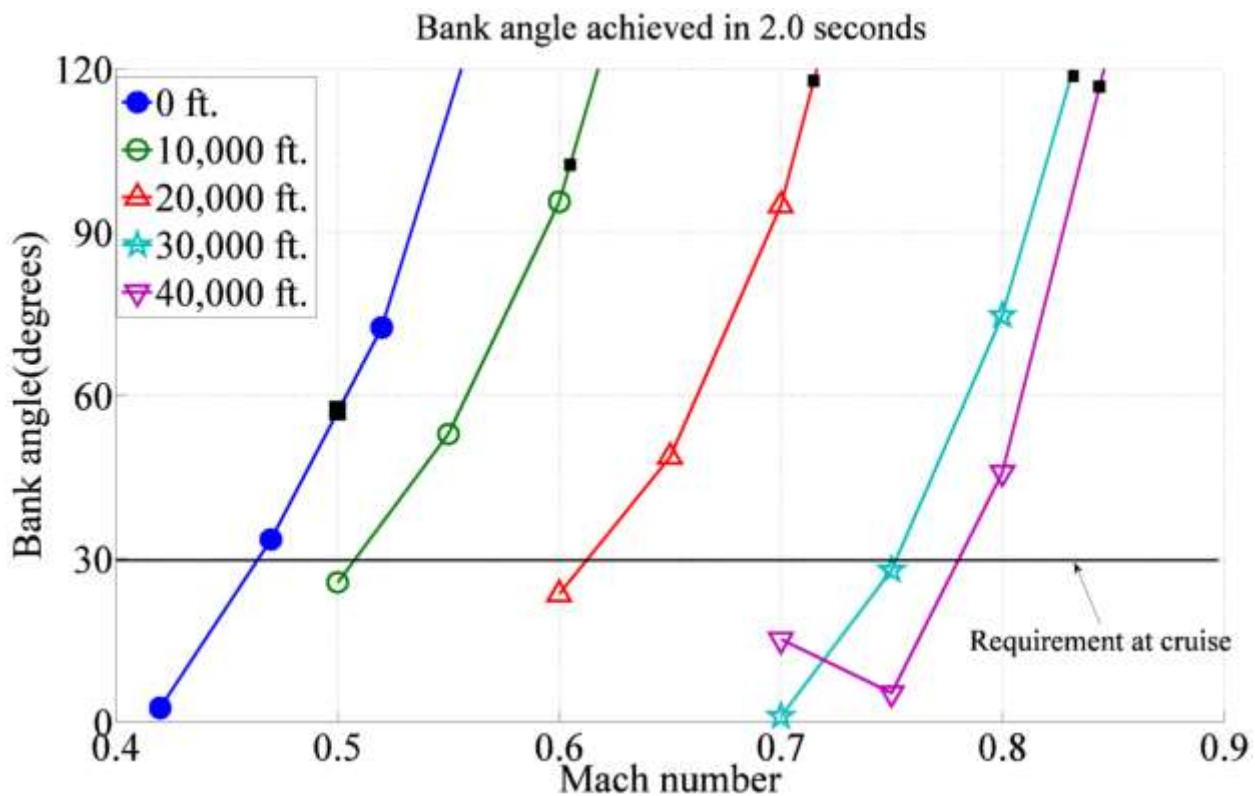


**Figure 24. Bank Angles Achieved by Design 1 at Various Altitudes and Mach Numbers along Flight Path**

#### 4.4.1.2 Performance of the New Structural Model

All the results shown so far have been obtained with the new model. To show some of the validation efforts performed for the new model (see Figure 18(b)) and to also show that the new model correctly predicts lower torsional stiffness, the same design was resized using the old model (see Figure 18(a)) and the distribution for the bending and torsional stiffness are compared for the two sets of models in Figure 25. The results indicate that with a more accurate representation of the wing box, a lower value of torsional stiffness is obtained which results in a more accurate aeroelastic analysis.

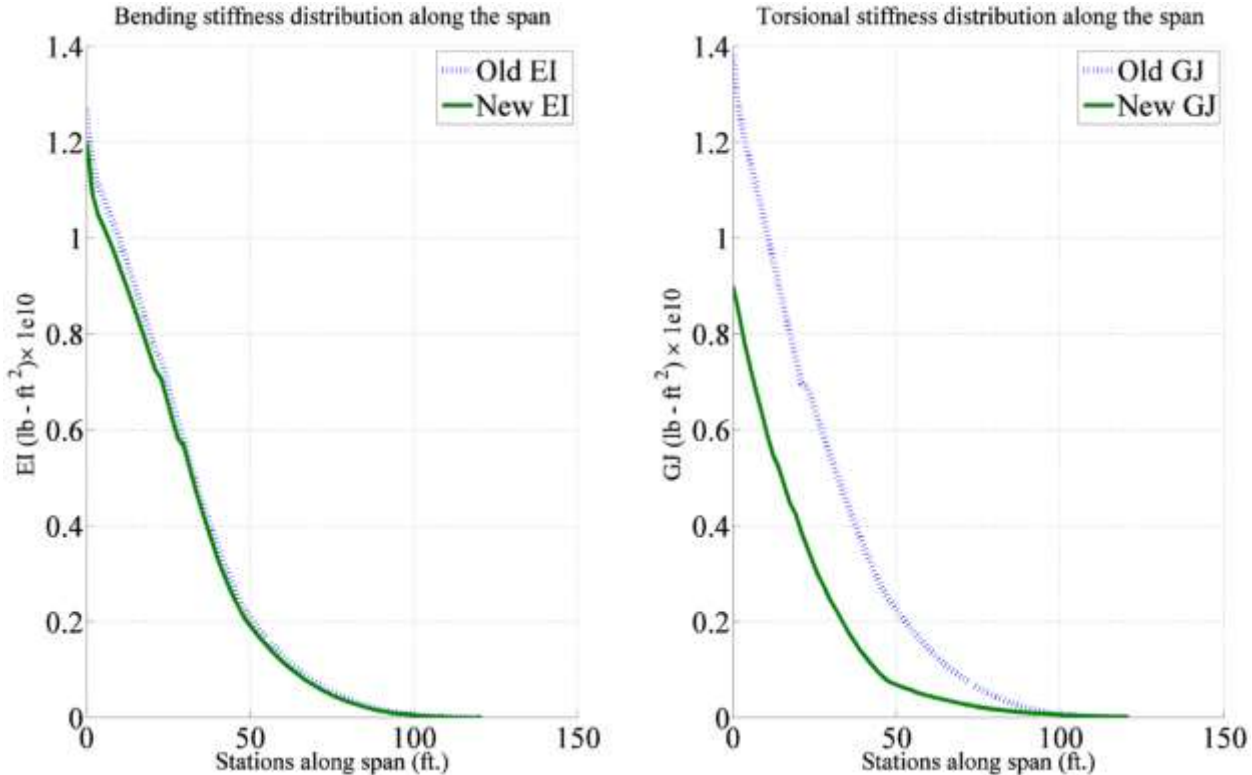


**Figure 25. Bending and Torsional Stiffness Distribution for a Cantilever Design with Old and New Structural Models**

#### 4.4.2 Truss-braced Wing Designs

Since the cantilever designs proved flexible enough to be able to achieve the required bank angle at cruise conditions without the NCE tip, we now investigate the TBW designs to observe potential applicability of the NCE tip to such aircraft configurations.

##### 4.4.2.1 Optimization Results

Previous studies [6] have shown that the truss-braced designs obtained from the VT MDO tool undergo flutter. Hence, they were stiffened within the MDO framework by a flutter constraint to prevent flutter. Thus, at first, the MDO results for the TBW designs are obtained here by applying flutter as a constraint but without applying any constraint for bank angle. These results are shown in Figure 26. As one can see, the flutter constraint imposes a penalty on fuel burn of the TBW designs. Two selected designs, TBW Design 1 and TBW Design 2 are shown in Figure 27, and

their design parameters are listed in Table 8. The results in the table show that going from TBW Design 1 to TBW Design 2, the flutter constraint stiffens the wing by reducing the semi-span by 10% which increases fuel burn by 7% if the increase in fuel burn is measured with respect to the Cantilever Design 1 which is now considered as the baseline.

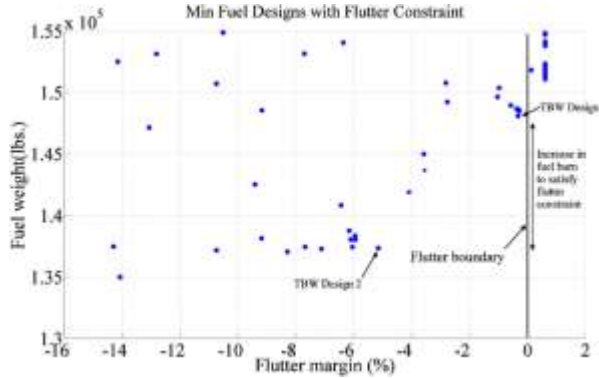


**Figure 26. Minimum Fuel Optimized TBW Designs with Flutter as a Constraint**

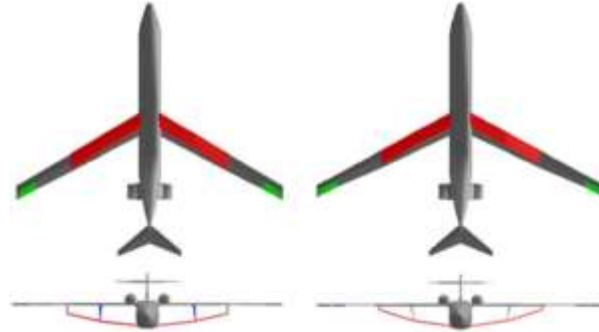


**Figure 27. Selected TBW Designs: TBW Design 1(left) and TBW Design 2(right)**

**Table 8. Selected MDO Designs**

Design Parameters	Cant Design 1	TBW Design 1	TBW Design 2
Fuel Weight (lbs)	157,000 (Baseline)	149,000 (-5:1%)	138,000 (-12:1%)
TOGW (lbs)	482,000	479,000	476,700
Wing/strut semi-span (ft)	130.3	121.35/71.68	130.64/71.39
Wing ¼ chord sweep (degrees)	29.6	27.7	26.2
Root chord (ft)	37.38	20.69	20.89
Tip chord (ft)	7.47	15.35	11.00
Strut chord (ft)	-	11.98	13.00
Jury chord (ft)	-	3.00	3.03
Root t/c	0.100	0.113	0.114
Tip t/c	0.080	0.091	0.085
Strut t/c	-	0.100	0.110
Jury t/c	-	0.077	0.078
Flutter Margin (%)	Does not flutter	-0.33	-5.53

The bank angles achieved by the two TBW designs with the conventional aileron are shown in Figure 28. Results indicate that at the cruise Mach numbers for the various altitudes represented

by black squares on the different lines, both the TBW designs fail to meet the requirement for the bank angle achieved in 2.0 seconds. TBW Design 1 cannot be used due to lack of roll control authority and TBW Design 2 cannot be used due to both flutter and lack of roll control authority although it has significantly lower fuel burn. Thus, to solve the problem for the TBW designs, the NCE tip is applied to TBW Design 1 and TBW Design 2 by using a variable-sweep mechanism through a joint at approximately 85% of the span of the wing. Thus, the 15% of the span towards the tip of the wing serves as the NCE wing-tip, and it contains all of the outboard aileron.

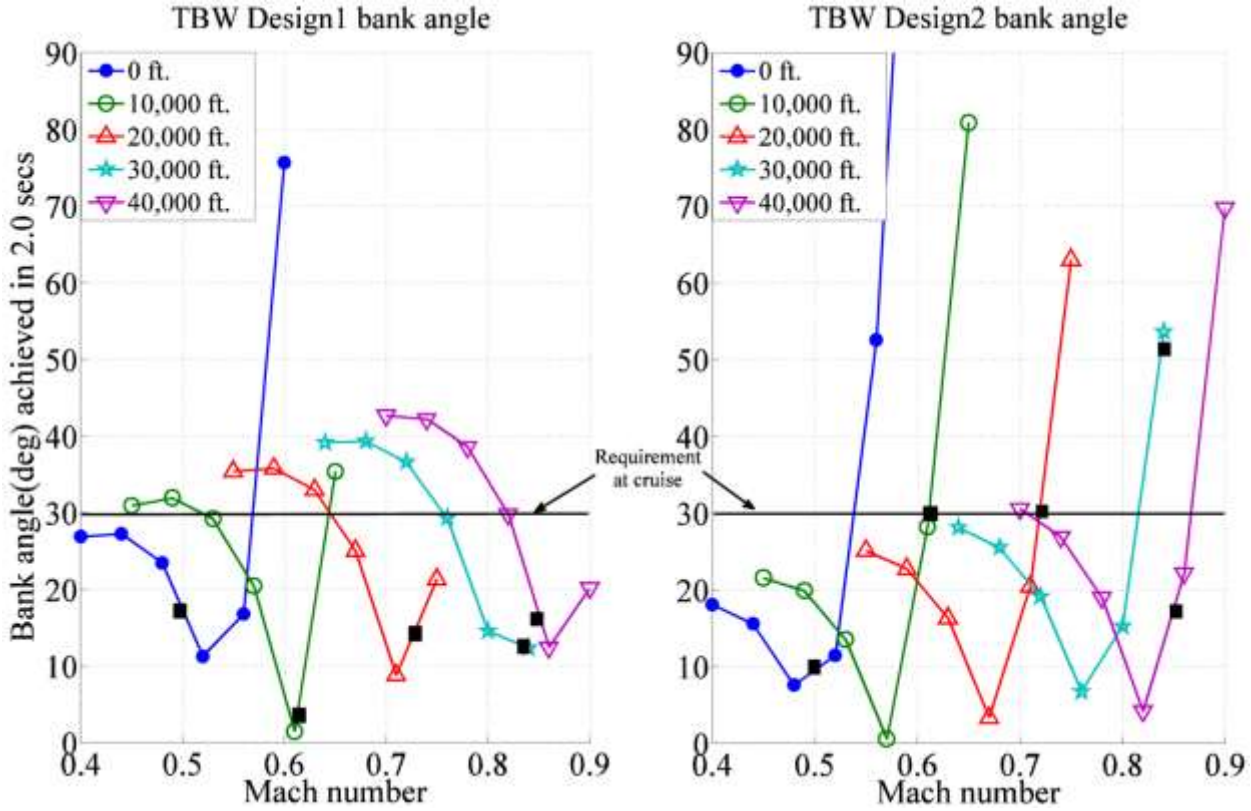
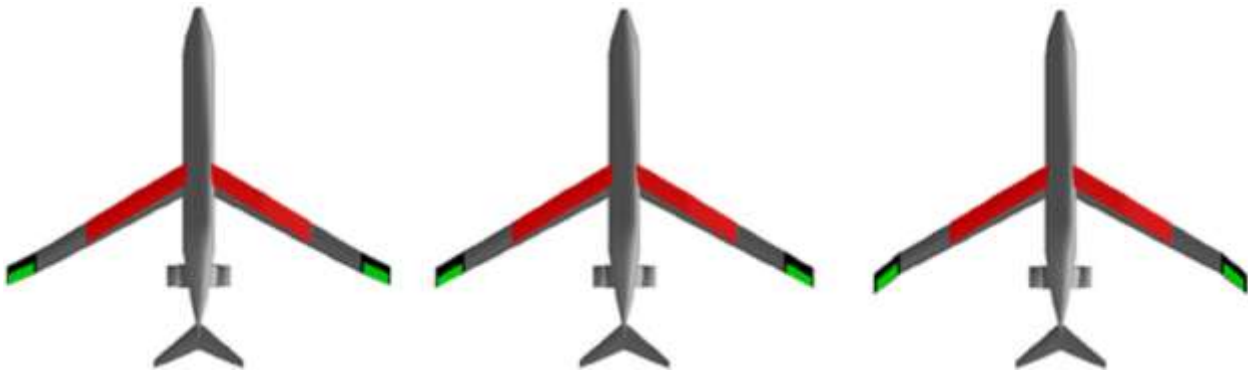


Figure 28. Bank Angles Achieved by TBW Design 1 and TBW Design 2 In 2.0 Seconds with Conventional Aileron

Figures 29 and 30 show the various configurations of TBW Design 1 and TBW Design 2 respectively, with the wing-tip swept at different angles. The forward and aft sweep angles shown are represented by acronyms such as sf- for swept forward and sb- for swept back followed by the value of the sweep of the NCE-tip relative to the wing in degrees. The configuration where the tip is not swept relative to the wing is termed as the 'as-is' configuration. The three configurations shown were studied, and their flutter Mach numbers at various altitudes and the bank angles achieved at cruise Mach numbers for various altitudes have been compared against one another in Figure 31. The results show several important aspects of using a variable-sweep NCE-tip. For TBW Design 1, the 10 degrees swept back NCE-tip was able to meet the requirement of the bank angle at the cruise Mach numbers at 10,000-30,000 ft., whereas the 5 degrees swept forward NCE tip was able to meet the bank angle requirements at the cruise conditions at sea-level and 40,000 ft. Thus, a movable NCE tip with forward and back sweep is able to meet the roll control requirements whereas the 'as-is' configuration, which would behave similar to a wing without the NCE tip, failed to meet the requirement on its own.



**Figure 29. TBW Design 1. From Left: (a) NCE Forward 5 deg (TBWdes1sf5), (b) NCE Unswept (TBWdes1as-is), (c) NCE Back 10 deg (TBWdes1sb10)**



**Figure 30. TBW Design 2. From Left: (a) NCE Forward 5 deg (TBWdes2sf5), (b) NCE Unswept (TBWdes2as-is), (c) NCE Back 10 deg (TBWdes2sb10)**

The other important result was that the forward and aft sweeping NCE tip is able to increase the flutter margin whenever appropriate sweep is used to achieve the required bank angle. Thus, at 20,000 ft., a positive flutter margin is achieved by the 10 degrees swept-back configuration, whereas the 'as-is' configuration would have a -0.33% flutter margin. For TBW Design 2, the behavior of the tip is different, but still the movable NCE tip is able to meet the goals. For this design, the combination of the 5 degrees forward swept, the 'as-is' and the 10 degrees swept back configuration is required to meet the requirement of the bank angle achieved in 2.0 seconds and to avoid flutter. The 10 degrees swept back configuration proves useful at sea-level to come close to 30 degrees bank angle requirement. At 10,000 ft., the 'as-is' unswept configuration proves useful for both the bank angle as well as for providing higher flutter margin. From 20,000-40,000 ft., the 5 degrees swept forward NCE tip proves useful for achieving 30 degrees bank angle and to increase the flutter margin sufficiently to meet the requirement for flutter. Thus, for both TBW Design 1 and TBW Design 2, the movable NCE tip can be used to meet the required bank angle in 2.0 seconds as well as avoiding the onset of flutter within the flutter boundary. For this to happen, the NCE tip has to be swept forward or aft or kept un-swept relative to the wing depending on which of these configurations proves useful at that specific flight condition.

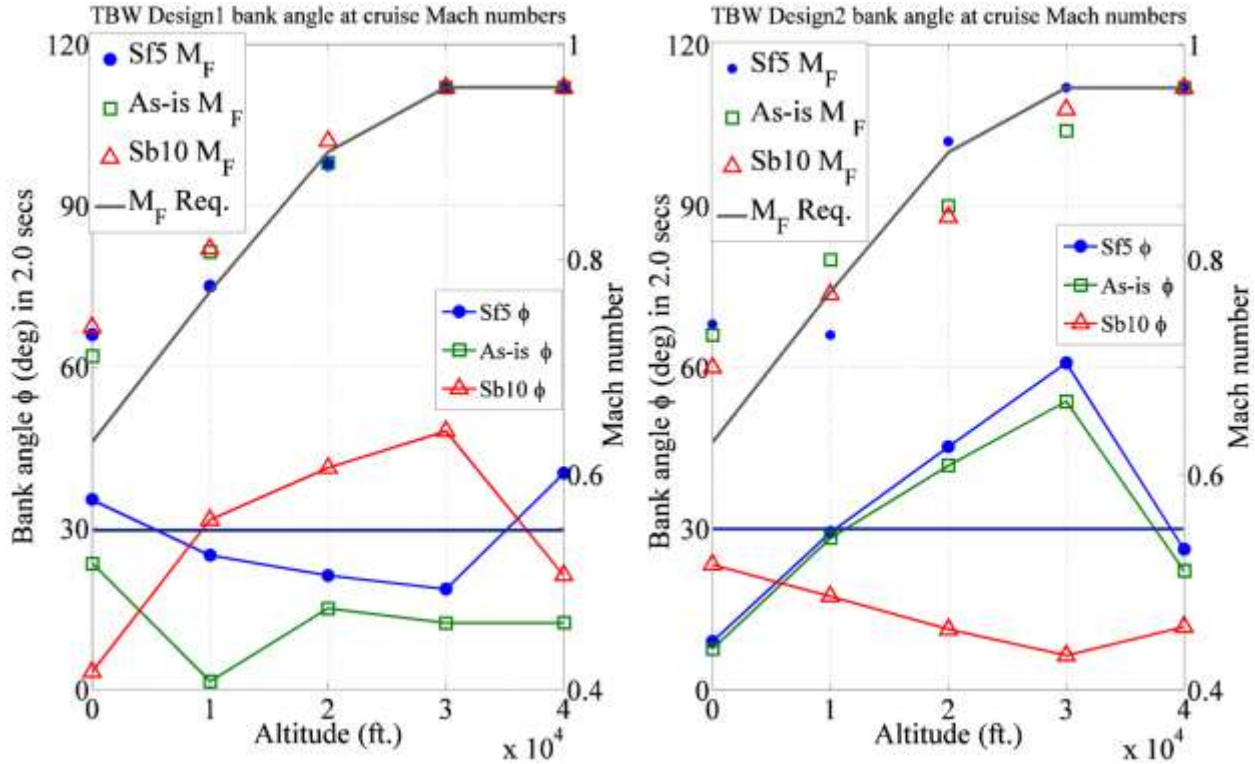


**Figure 31. Bank angle achieved by TBW Design 1 and Design 2 in 2.0 seconds with the NCE tip at various altitudes but only at cruise Mach numbers and flutter Mach numbers at these altitudes.**

#### 4.5 SUMMARY AND CONCLUSION

The present study was aimed at investigating the aeroelastic effects of a novel variable-sweep wing-tip (NCE) mechanism on flexible wing aircraft designed for a flight mission similar to Boeing 777-200 LR. It was expected that both cantilever and truss-braced wing configurations optimized for minimum fuel burn for such a mission would be very flexible. Conventional procedures for obtaining sufficient roll control authority may not be applicable to such designs. Thus, it was decided that instead of increasing weight by stiffening the wing or incorporating additional control surfaces, the roll control for these designs might be achieved by enhancing control reversal by the NCE to have sufficient negative control effectiveness and then using that for obtaining sufficient roll control capability. The NCE tip can be swept fore and aft as required and the effectiveness of such an idea to achieve the required roll control authority was studied. The roll requirement is measured as the ability of the wing-aileron system to achieve 30.0 degrees of bank angle in 2.0 seconds at cruise conditions.

To achieve this goal, first a new wing structural model was developed which replaces the earlier double-plate model of the wing-box with a combination of ribs, spar-caps, spar-webs and stringers. This was performed to produce a better estimation of torsional stiffness compared to the old model. Secondly, the capability of computing steady-state roll rate, maximum roll acceleration and the bank angle achieved as a function of time was developed within the aeroelastic analysis module of the MDO.

Results obtained after the implementation of the new model show that a cantilever wing configuration optimized for minimum fuel burn turns out to be flexible enough to meet the bank angle requirement without the application of the NCE tip. However, the same is not true for the TBW

designs as they turn out to be stiffer once the flutter constraint is applied, and they fail to achieve the required bank angle at cruise conditions with just a conventional aileron. Furthermore, the necessary stiffening of the TBW designs to prevent flutter leads to some loss of aerodynamic efficiency of the designs and results in higher fuel burn. If TBW designs are constrained to prevent flutter within the flutter boundary, a penalty of about 8% increase in fuel burn is imposed upon them. Further stiffening of these designs to prevent/delay control reversal and meet the roll requirement via conventional methods would increase fuel burn further, thereby nullifying most of their benefits over an optimized cantilever. Thus, applying the NCE tip seems a suitable option.

Results show that when the TBW designs include the NCE tip, they are able to achieve the bank angle required at cruise conditions by a combination of sweeping the tip back by 10 degrees, or forward by 5 degrees or having no sweep at all relative to the wing at various conditions within the flight envelope. It was also observed that as the NCE tip changed the configuration of the wing due to its sweep to achieve the required bank angle in 2.0 seconds, the new configuration also turned out to be one with higher flutter margin. Thus, for certain conditions, a swept NCE tip would prevent flutter within the flutter boundary and simultaneously provide sufficient capability for roll control. The NCE tip helps to avoid this penalty. Another way to avoid this penalty is active flutter suppression mechanism, which is a complicated method and is more prone to malfunctioning than the simpler route of sweeping the NCE tip to prevent flutter. The NCE tip helps the TBW designs meet sufficient roll control capability and also avoid the 7-8% penalty on fuel burn imposed by the flutter constraint. Thus, the final TBW design with the NCE tip is predicted to have 12% lower fuel burn than its optimized cantilever counterpart. The NCE tip is thus an enabling technology for truss-braced wing aircraft.

## **5. SUBSYSTEM LAYOUT, FINITE ELEMENT, AND KINEMATIC MODELS**

A technical memorandum, dated June 29, 2012, documents the completion of Task 3 development of the kinematic and finite element modes for the Concept Development for the Novel Control Effectors (NCE) contract. The SOW for Task 3 is found in Section 3.1 "Requirements Development".

This section documents the transmission of the kinematic and finite element models VGRWT for a SUGAR single aisle aircraft. The kinematic model is in the form of a Solidworks CAD model. The finite element model is in ANSYS. The conversion of this model to PATRAN/NASTRAN is in work and the all up model will be delivered in PATRAN/NASTRAN.

### **5.1 KINEMATIC MODEL**

An aft spar pivot/forward track and beam layout was previously selected. The key features of this design included:

- Short, direct load paths for both the forward and aft spar
- Reduced size of the skin fairing which must nest into the wing
- Easy integration of actuator
- Easy integration of electrical, hydraulic or other lines near the aft joint

The range of motion of the selected concept is a sweep change of 35 degrees in the plane of the wing. In order to minimize disruptions at wing leading edge (LE), the forward cut line between the root wing and the variable wingtip was set perpendicular to the local LE. The axis of rotation was placed 37.5 inches from the LE and perpendicular to the local chord line. Finally, the cut line aft of the axis was set perpendicular to the local trailing edge (TE) with 17.5 degree cuts on either side to allow the trailing edges to meet when swept and to make room for a flexible rear fairing when unswept. The axis was placed forward of the SUGAR rear spar to utilize the greater wing box thickness for the rear pivot components while remaining close to the existing rear spar location. Setting the axis normal to the chord line and the cut lines normal to the LE and TE reduces the difficulty of designing the required fairings, as shown in Figure 32.

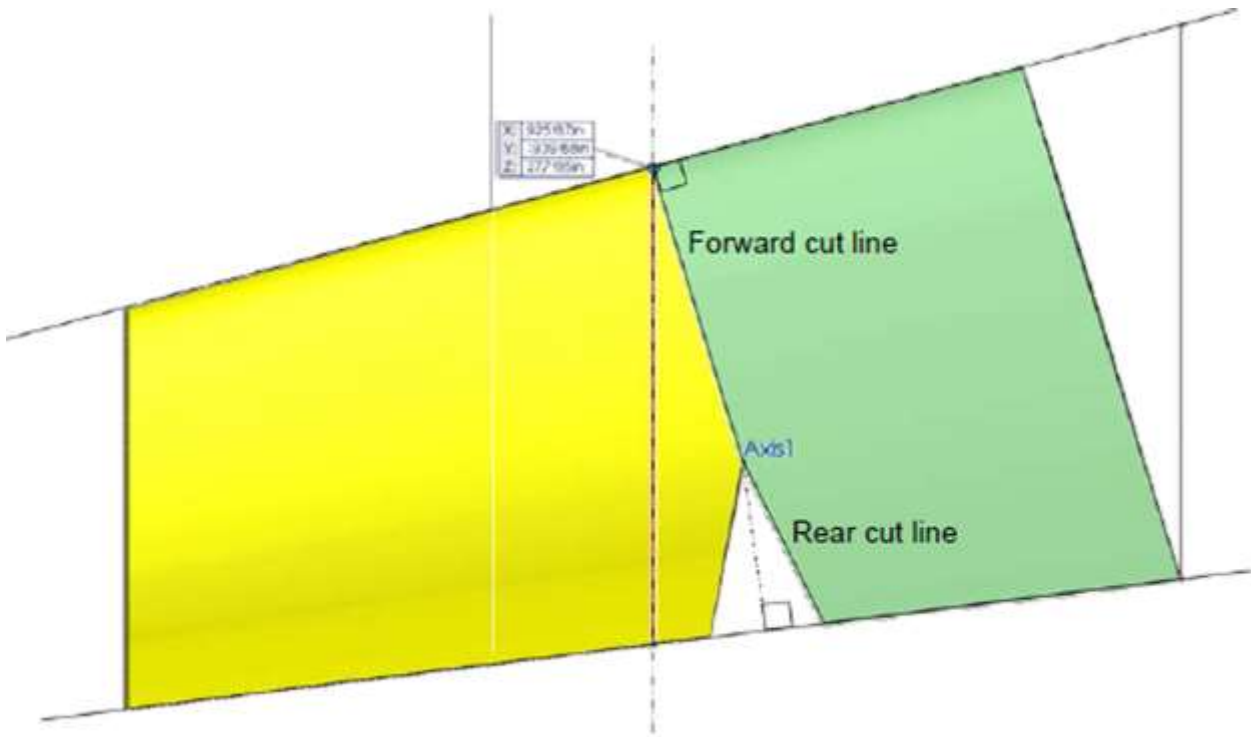


**Figure 32. Overview of cutline geometry showing the axis of rotation (Axis 1), the fixed root wing (green), variable wingtip (yellow), and rear fairing clearance cut (white).**

The track and beam system for the forward spar were designed and sized to fit entirely within the forward wingtip fairing. Figure 33 shows the entire structure at the limits of motion. Both the track and the beam are I-beam/box-beam hybrids to help resist both bending and torsion loads due to the large shift in the wingtip center of lift. Figures 34 and 35 show a cross section of the structure looking in from the wingtip. The wingtip beam nests within the fixed track and has a minimum of 15 degrees overlap at all times to transfer loads. Bearing blocks fit inside the outer flanges of the wingtip beam and serve to transfer load and maintain alignment between the two structures. Clearance is maintained between the wingtip beam (red) and the forward fairing (yellow) such that the fixed track (blue) can nest between them (Figure 36), while further clearance is maintained between the fixed track and the fixed root wing skin (green), allowing the wingtip fairing to nest inside when the wingtip is unswept.

The rear pivot block is a simple pinned hinge (Figure 37). A diagonal cross spar serves to transfer loads from the wingtip to the front spar as well as to stabilize the track/beam structure and support actuator loads. Thin ribs serve to transfer pressure loads from the skin to the spar structures.

The rear fairing requires further development work. The current concept calls for a flexible membrane skin over rib-like supports which radiate from the axis of rotation. These supports will be nested together when the wingtip is swept while the skin material will stretch over top of them while the wing is swept forward. Details of the expected pressure loads in this area are needed to further detail this concept.

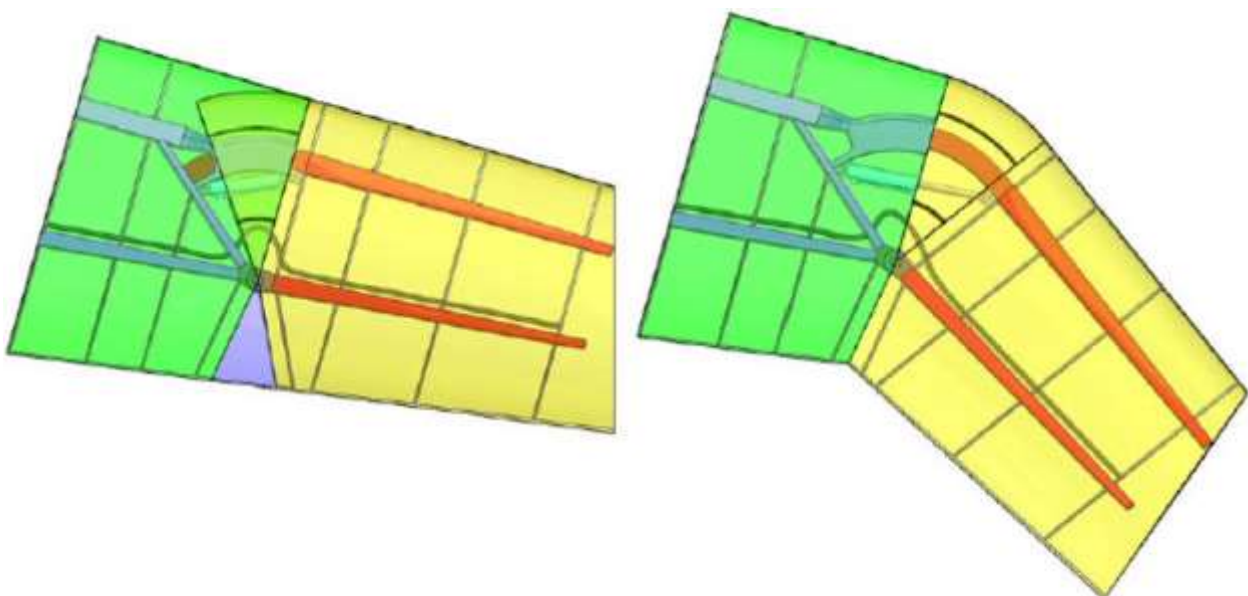


Figure 33. Overview of kinematic model in the unswept (left) and swept (right) positions.

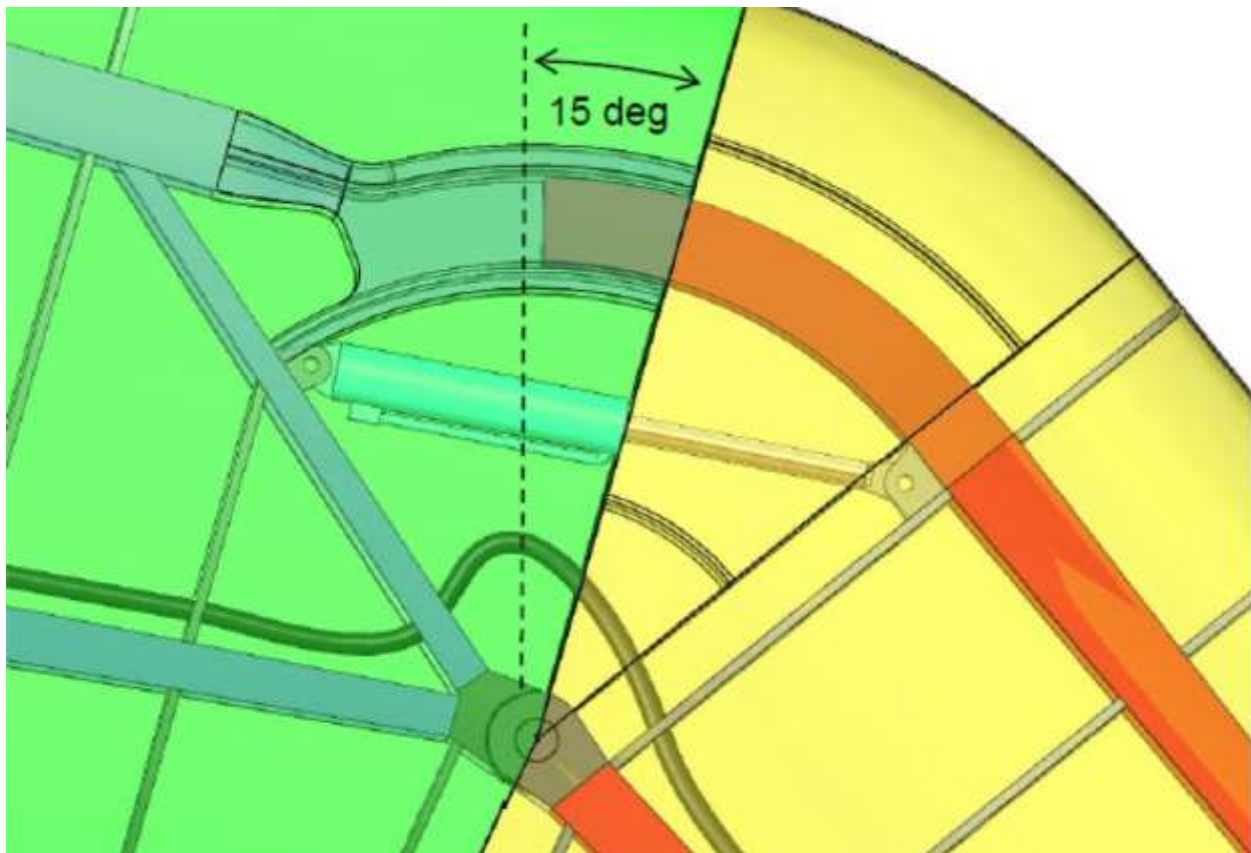
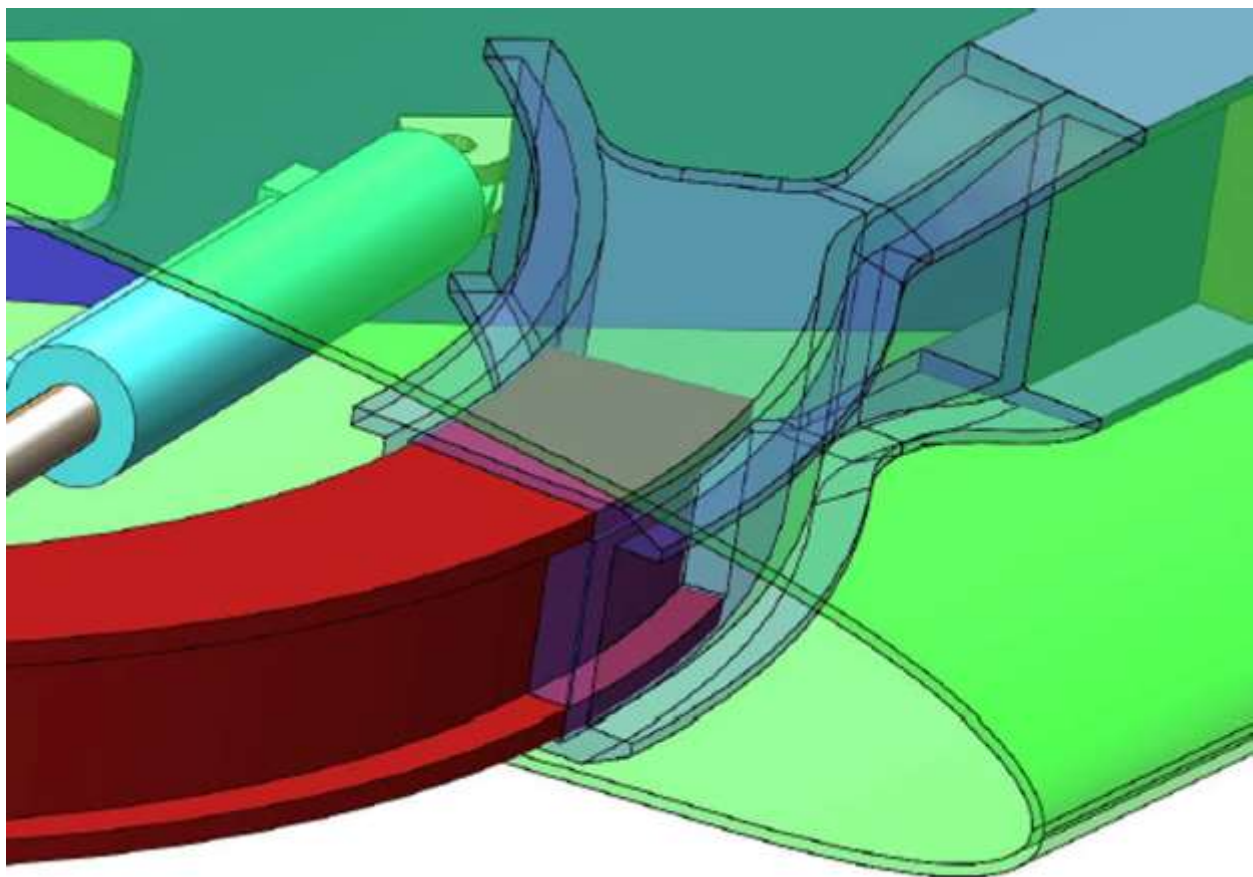


Figure 34. Overhead view of track and beam mechanism with track structure set to transparent showing overlap between track and beam at full sweep.



**Figure 35. Forward track and beam structure looking in from the wingtip with the wingtip fairing hidden.**

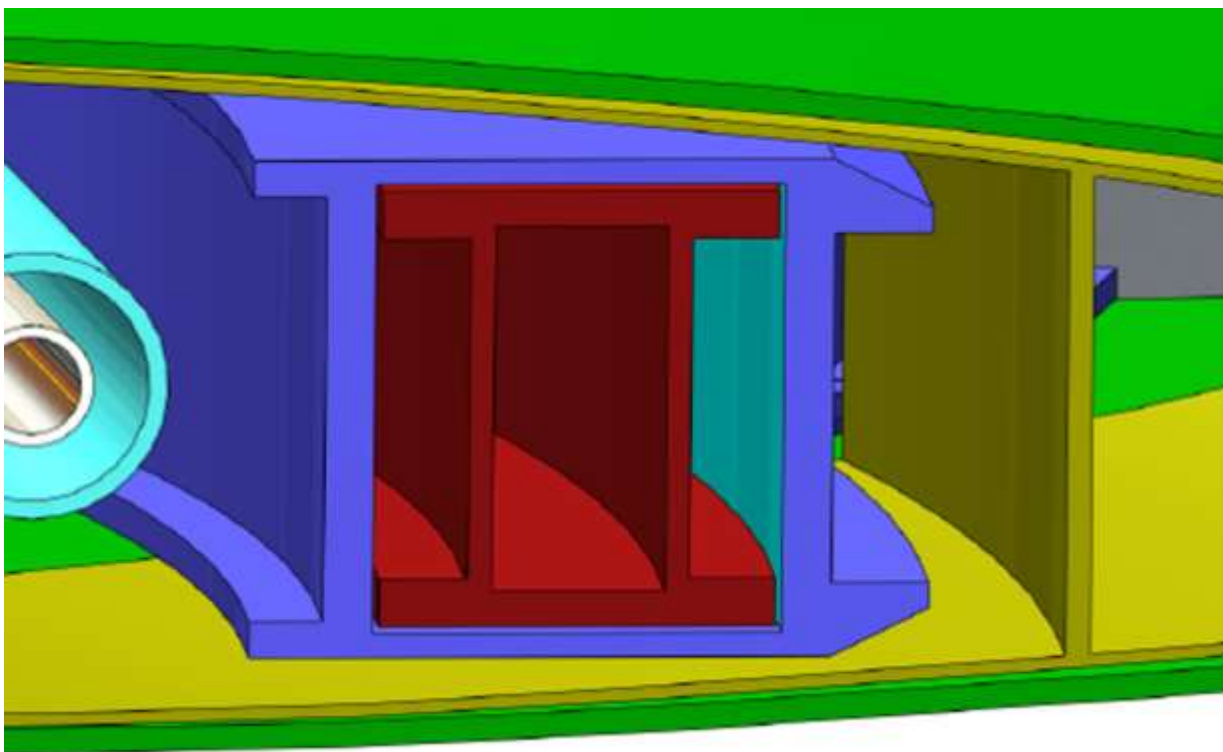


Figure 36. Cross section of nested track and beam structure showing the fixed structures (wing root track, blue; root wing skin, green) and moving structures (wingtip beam, red; wingtip forward fairing, yellow).

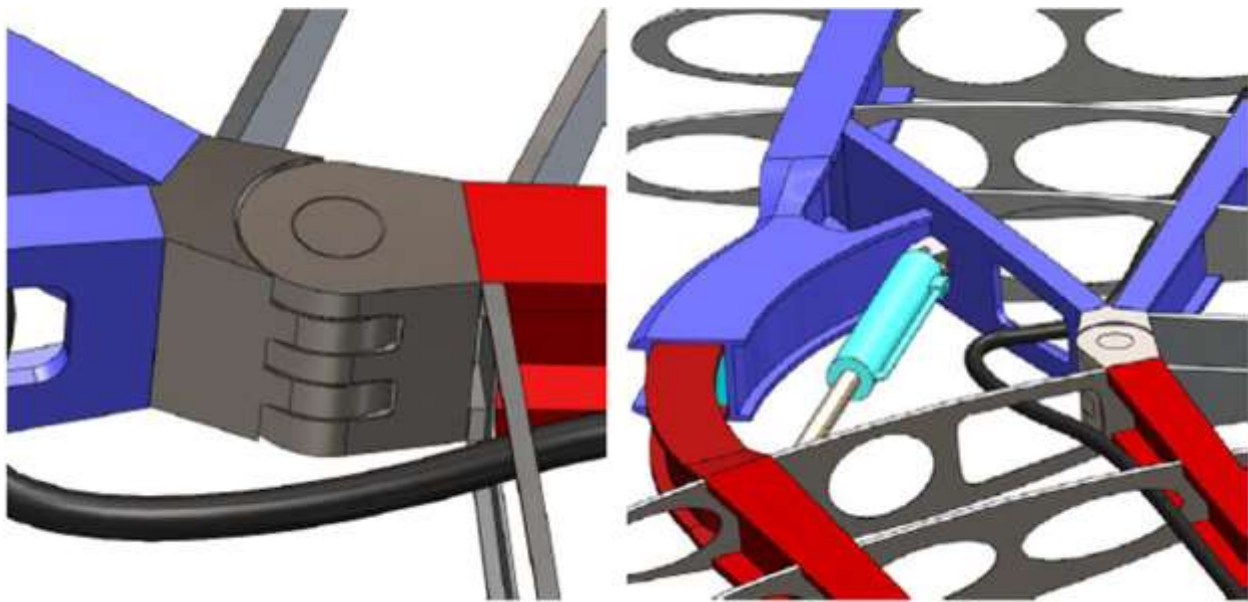


Figure 37. Rear spar pivot block (left) and cross spar (right).

## 5.2 INITIAL STRUCTURAL SIZING

Initial component sizing was completed using preliminary force and moment data from Tornado provided by Virginia Tech (Figure 38). These inputs were described as point lift forces at the

wingtip center of lift and moments about the wing aeroelastic axis at 40% chord. Loading cases were established for both swept and unswept positions with and without aileron loads. A design load of  $\pm 2.5G$ 's was used with an additional 1.5 safety factor. Rough sizing was completed on the primary load bearing structures (front and rear spars, rear pivot blocks, and front track and rail) by applying the highest expected loads on a component by component basis using ANSYS finite element models, as shown in Figure 39. Refinements to the sizing were made using assembly-level models in ANSYS with point loads on the wingtip spars (Figure 40); however, final sizing will require the application of distributed pressure loads on the skin, which is not yet available.

Materials used in the model were based upon standard high strength titanium and aluminum alloys, as well as approximations for quasi-isotropic woven carbon fiber laminates and high modulus directional carbon fiber. Titanium was used for the rear pivot blocks and actuator mounts, while aluminum was used for the rib structures. Quasi-isotropic carbon fiber was used for the skin panels, while directional carbon fiber was modeled for the spar and track/beam structures.

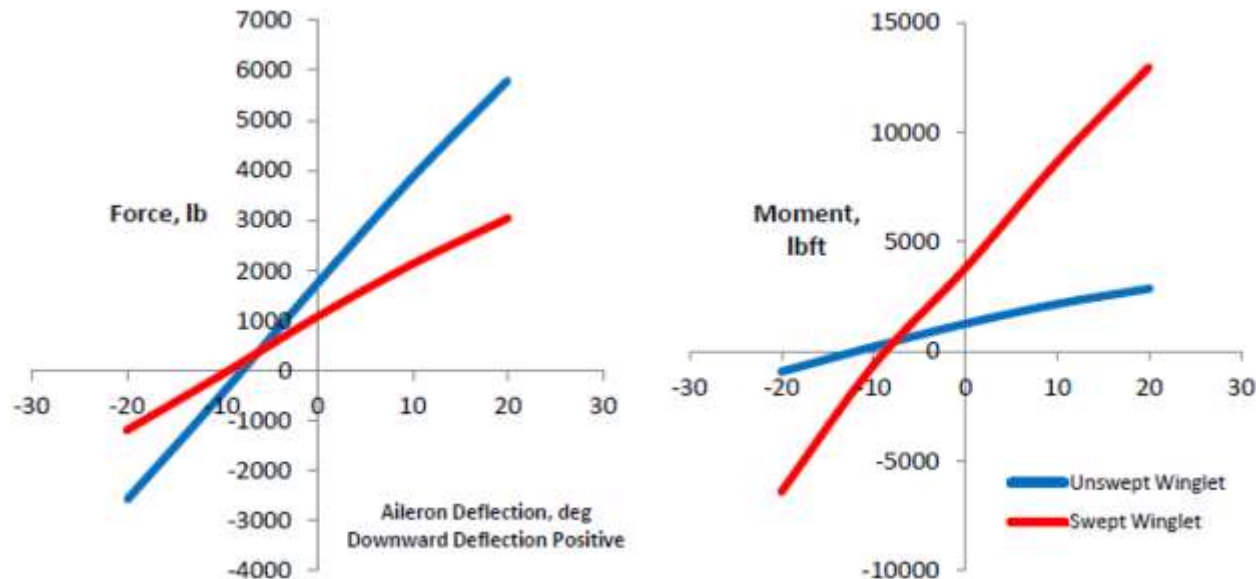


**Figure 38. Tornado generated wingtip force and moment values with respect to aileron deflection.**

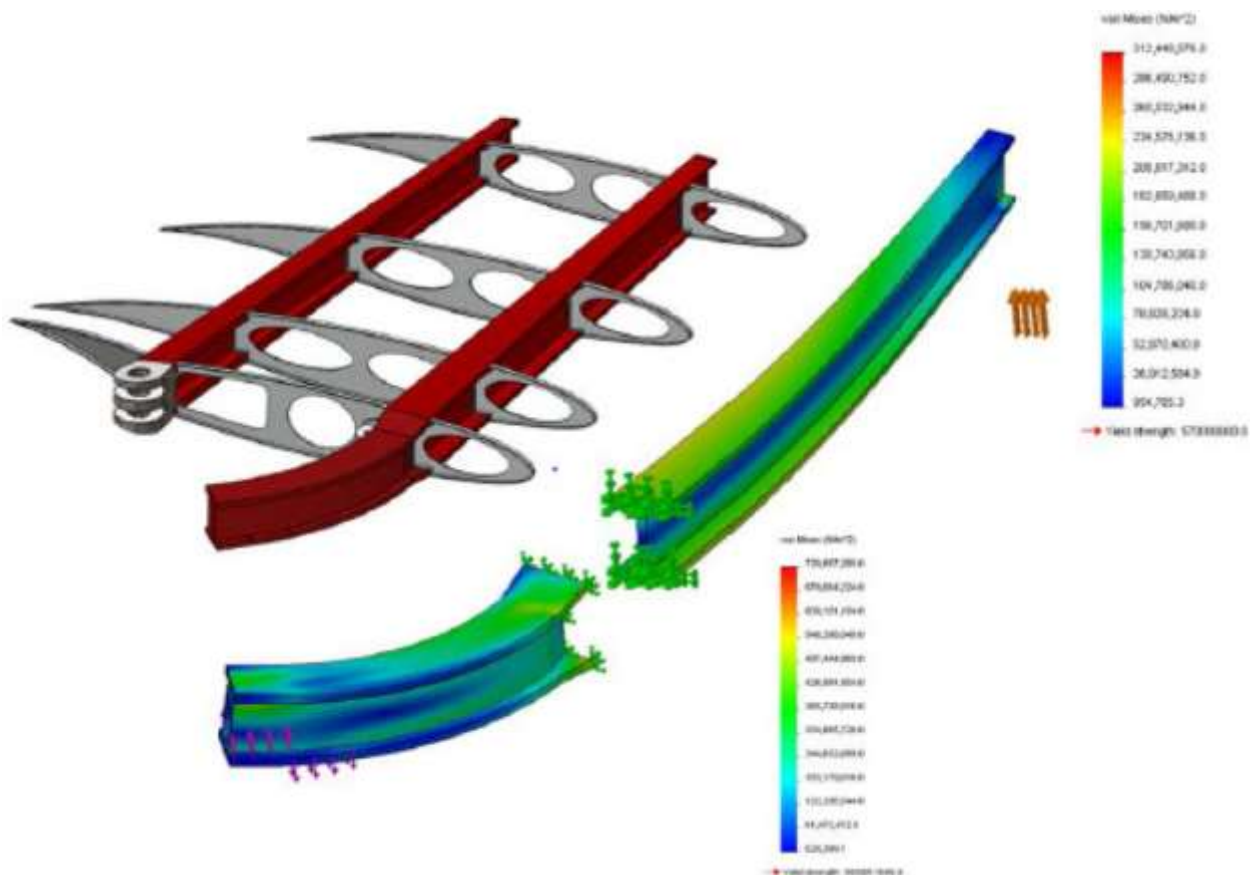


**Figure 39. Component Level Sizing of Wingtip Forward Spar and Track**

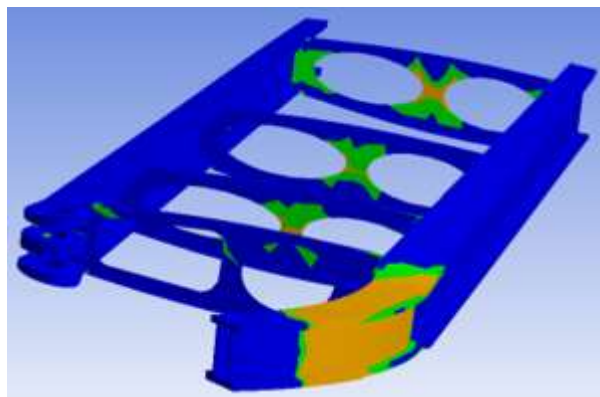


**Figure 40. Finite element analysis of full wingtip structure with skin and fairings hidden showing structural margin greater than unity.**

### 5.3 ACTUATION AND ROUTING

At the time of this report, actuator type and requirements had not been identified. Therefore, a representative actuator was integrated into the kinematic model in order to visualize a likely means of actuating the variable wingtip mechanism. A 2.75 inch diameter hydraulic cylinder was modeled (Figure 41), which could provide over 20,000 pounds of actuation force using a 5,000 psi hydraulic system, although an electric or electro-hydraulic actuator system could easily be substituted. As shown, the actuator has a length of 18.0 inches when retracted and a stroke of 11.0 inches. The

space in which the actuator resides is capable of accepting significantly larger actuators, with only adjustments to the mounting blocks required to maintain clearance with other structures.

Additionally, a clear routing path for electrical and hydraulic lines is provided in front of the rear spar and pivot block. Sufficient room for cable flexion and extension is available near the rear pivot throughout the range of wingtip motion. A one inch flexible hose was used in the model as seen in Figure 42.

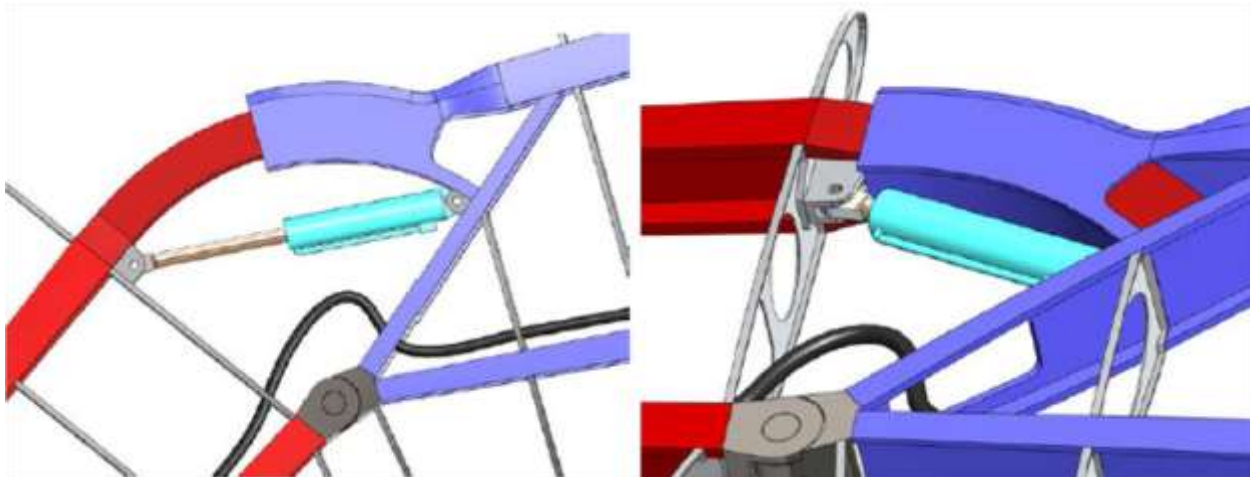


Figure 41. Representative actuator in the extended/swept (left) and retracted/unswept (right) positions.

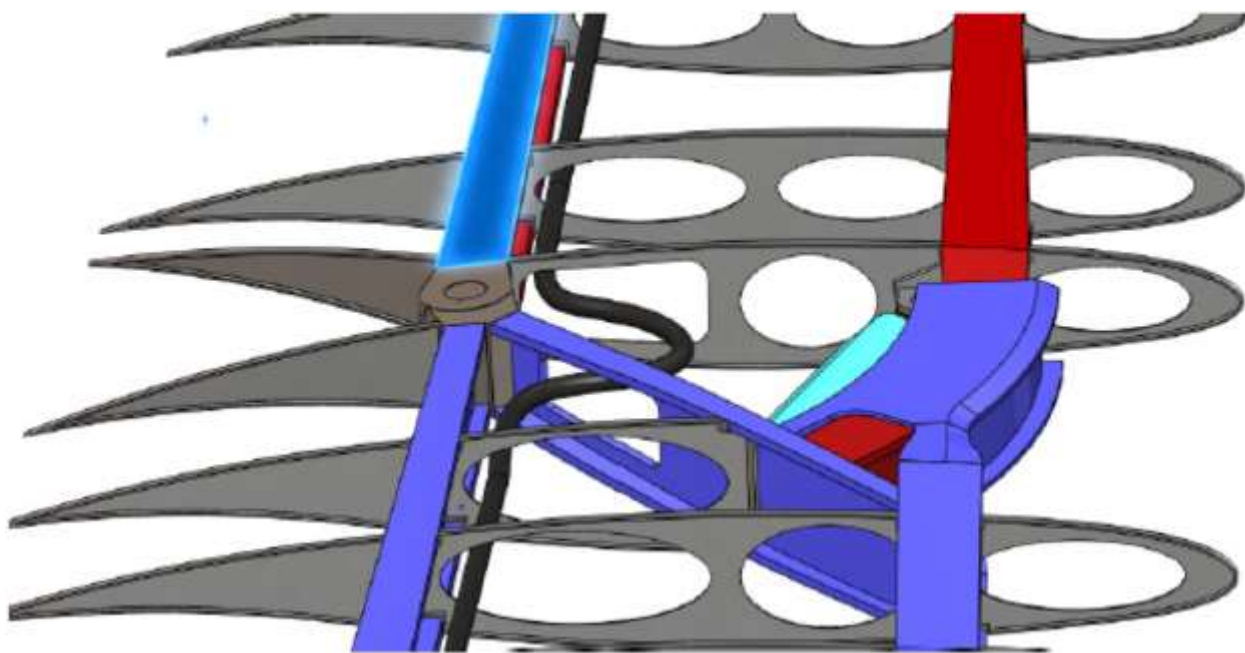


Figure 42. Space for electrical and hydraulic line routing with representative flexible line (black).

#### 5.4 SUMMARY OF NCE FOR DUAL AISLE AIRCRAFT

During the work we were to design a novel control effector (NCE) outboard wing segment, based upon properties produced by Virginia Tech's (VT) multidisciplinary optimization (MDO)

module. The inputs to the MDO model were guided by Boeing, with a goal of a 777 sized vehicle with a rapid roll rate, induced by a variable sweep NCE with a tuned structure that allows the roll reversal phenomenon typically avoided in aircraft design. The MDO output details on wing geometry and specific span stations, including central axis, chord, thickness, skin thickness (broken into 4 segments), spar/stringer area, spar web thickness, and smeared properties for EI and GJ. The intent was to use the output to guide the structural design of the wing.

Crucial to the performance of the variable sweep NCE is the joint attaching the NCE to the bulk of the wing. The joint must be able to carry the aerodynamic loads generated by the NCE and transfer them into the main structure while allowing a range of motion for sweep. Due to the limited volume available for the structure the design must provide rigidity in a small package, while limiting any 'gap' between the NCE and wing skins that could harm efficiency. Our work focused on translating the output of the MDO file into a practical structural layout, focusing on the design of the hinge area where the load will be transferred from the NCE to the main wing.

## 5.5 MDO OUTPUT FOR DUAL AISLE AIRCRAFT

The MDO output provides geometry information for the wing box as well as smeared properties for the cross sectional area, producing GJ, and either  $EI_{xx}$ , and  $EI_{zz}$ , or  $EI_{tr}$  for a given span station. The first 10 points of the provided data is seen in Figure 43. After requesting an explanation of the data and definitions of the column headings [2] was provided, along with a version of Figure 44.

Node #	Xea[ft]	Yea[ft]	Zea[ft]	t11(ft.)	t12(ft.)	t13(ft.)	t14(ft.)
<b>Wing:</b>							
1	6.753	0	0	3.73E-02	2.11E-02	2.02E-02	3.65E-02
2	8.17624	2.77867	0	3.30E-02	1.95E-02	1.91E-02	3.27E-02
3	9.59947	5.55733	0	3.16E-02	2.45E-02	1.61E-02	2.20E-02
4	11.02271	8.336	0	2.94E-02	2.37E-02	1.67E-02	2.01E-02
5	12.44594	11.11467	0	2.74E-02	2.29E-02	1.71E-02	1.84E-02
6	13.86918	13.89333	0	2.45E-02	2.18E-02	1.84E-02	1.58E-02
7	15.29241	16.672	0	2.44E-02	2.08E-02	1.90E-02	1.62E-02
8	16.71565	19.45067	0	2.24E-02	2.00E-02	1.94E-02	1.83E-02
9	18.13889	22.22933	0	2.09E-02	1.94E-02	1.96E-02	1.82E-02
10	19.56212	25.008	0	1.97E-02	1.88E-02	1.79E-02	1.89E-02
<b>Wing:</b>							
Node #	t2(ft.)	spar-cap/ Stringer Area (ft <sup>2</sup> )	b(ft.)	h (ft.)	$EI_{tr}(\text{lb-ft}^2)$	GJ (\text{lb-ft}^2)	
1	1.46E-02	6.09E-02	10.3023	2.3392	1252484080	1194897058	
2	1.43E-02	5.83E-02	10.2171	2.3005	1159630899	1067501859	
3	1.25E-02	5.58E-02	10.1319	2.2622	1073352445	928374580.3	
4	1.25E-02	4.98E-02	10.0467	2.2242	926063478.8	868126541.3	
5	1.25E-02	4.35E-02	9.9615	2.1865	782054453.5	810741868	
6	1.25E-02	3.80E-02	9.87627	2.1491	659962571.8	736771607.1	
7	1.25E-02	2.85E-02	9.79105	2.112	478670034.5	730264225.1	
8	1.25E-02	2.08E-02	9.70583	2.0753	336888475.5	697096901	
9	1.25E-02	1.46E-02	9.62061	2.0389	228634489.7	643927405.5	
10	1.25E-02	1.00E-02	9.53538	2.0028	150791330.7	611199194.7	

Figure 43. Example of MDO Output (Image split into 2 lines for ease of viewing)

After attempting to map the Spar-cap / Stringer Area to a physical geometry based upon the wingbox layout to input into the model without success additional details on the output file were requested. The results of those exchanges are summarized by stating that the areas are not a specific geometry, but are rather abstract areas centered in the skin panel thickness at the specified chord locations.

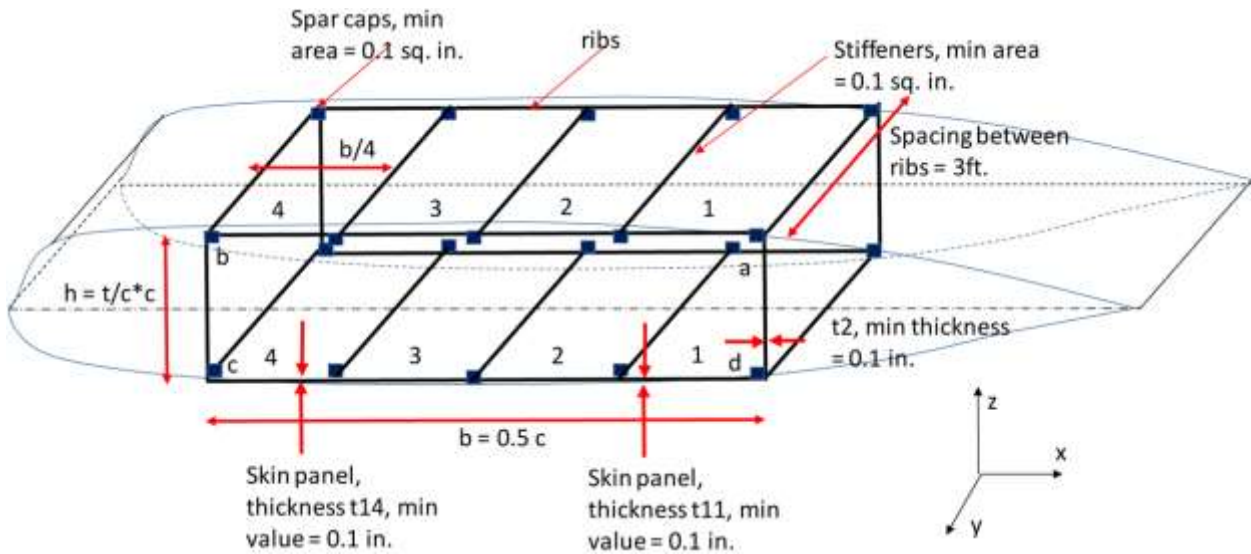


**Figure 44. MDO Output Explanation Graphic Provided by VT and Edited by NextGen to Correct Errors and Improve Understanding. Spar Caps and Stiffeners (stringers) have the Same Area in Calculations**

In order to obtain a geometry for the abstract areas we calculated the moments of inertia of the wingbox and subtracted that from the given moment of inertia for the areas and would come up with unlikely values for most of the points. Further inquiries about the output file eventually found the culprit – the MDO simplifies shear calculations by assuming zero skin contribution. While useful for a first guess, this assumption was used for the final moment of inertia calculations as well, which produces a very conservative value for much of the wing, as will be discussed below.

Once provided with the simplified equations used by the MDO we were able to match some of the outputs. Further analysis of the output file where multiple inconsistencies between specified equations and provided data were identified resulted in a new MDO file being provided, which is shown in Figure 43. The previous output files had all presented  $EI_{xx}$  and  $EI_{yy}$  data, while the new one provided  $EI_{tr}$  data. After another prolonged back and forth it was finally discerned that the  $EI_{tr}$  data is provided in 'structural axis' perpendicular to the leading edge of wing, while the wing geometry data was all provided in the standard 'body axis' system. These two coordinate systems are shown in Figure 45, with planes in the structural system shown in red and planes in the global system in blue.

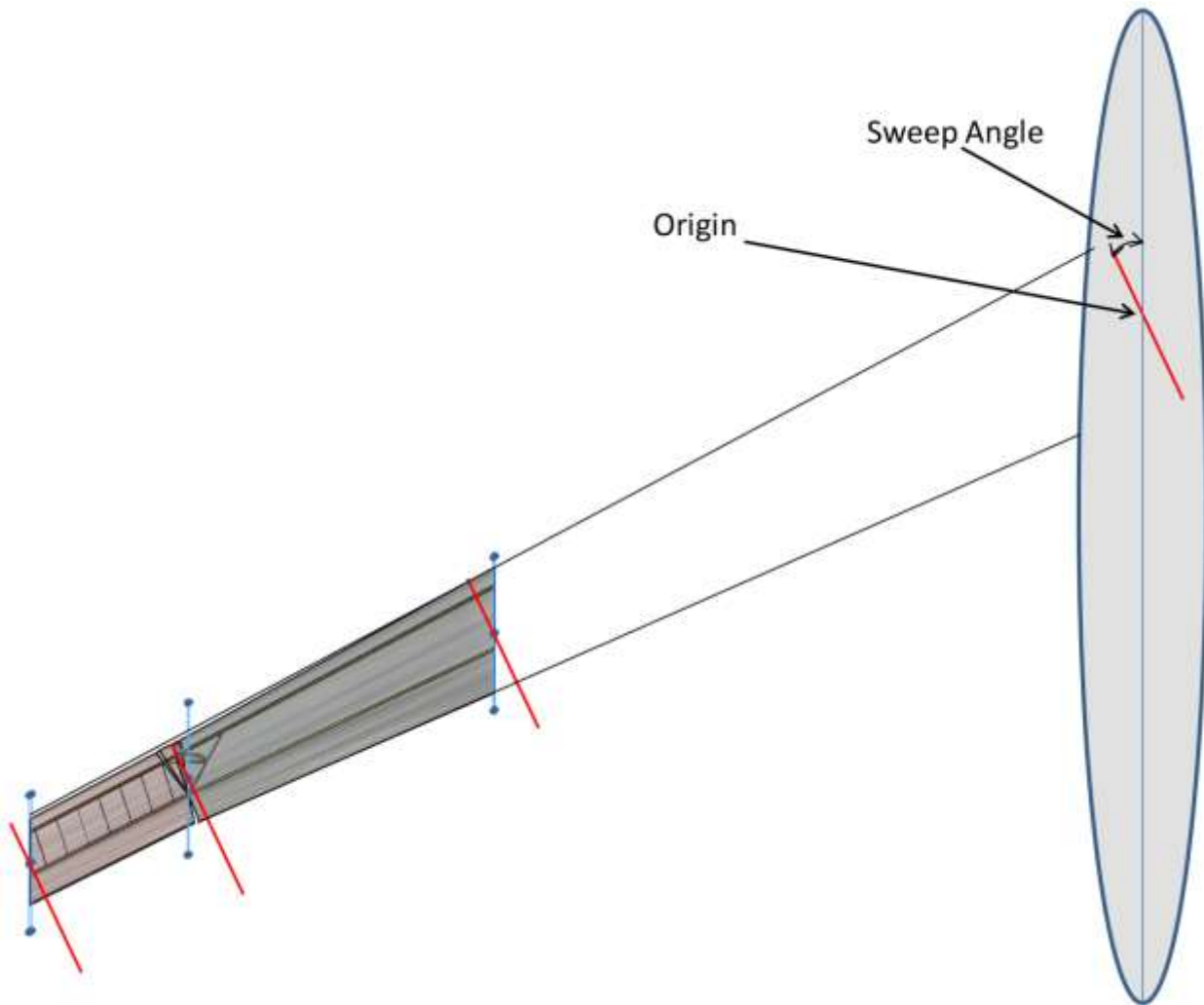


**Figure 45. Sketch of Fuselage and Wing around Model of NCE / Wing Joint Showing Different Coordinate Systems used in MDO Output File**

### 5.5.1 Skin Moment of Inertia

The first step to developing a structural design based upon the output is to understand the breakdown of the properties to define geometry for the 'abstract areas' used for the spars and stringers in the MDO. Before any explanation of the data was provided we worked to calculate the geometry of the spar areas to include the proper cross-section in the physical design.

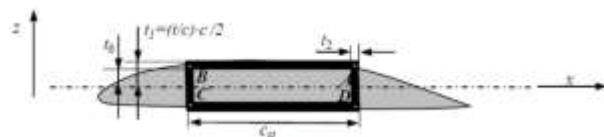


**Figure 46. Graphic from MDO Paper Explaining Wing Box Geometry**

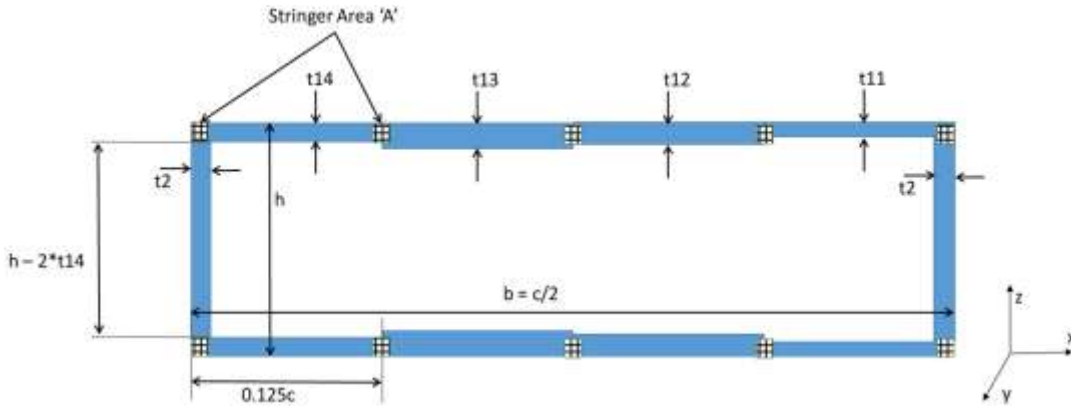


**Figure 47. Sketch of the MDO Cross Section Used to Calculate Cross-Sectional Properties of Components**

To calculate the section properties the MDO simplifies the cross section with the assumption that the skins are negligible. While this greatly simplifies the calculations necessary for shear flow and moment of inertia, it leads to a large error. The skin can provide a large contribution to the moment of inertia of the wing, especially with such thick skins. Table 9 provides a comparison of the MDO calculated  $I_{tr}$  (moment of inertia in the translated, or body coordinate system, that the skin thickness and spar car sizing is given in) and the calculated moment of inertia for just the skin of the wing box (upper and lower skin panels and the webs for the fore and aft spars). Comparing the numbers it is easy to see that the skin contribution is at least as much as the spar / stringer area contribution for most of the nodes beyond the strut attachment. In fact, looking at the full wing the skins can contribute over 3 times the moment of inertia as the areas. The smallest wing contribution is still 1/3 of the area contribution, or 25% of the total for that cross section. Contributions of the leading edge and trailing edge skins were not taken into account for this estimate.

**Table 9. Given Cross Section  $I_{tr}$  Compared with Calculated Wing Box Skin  $I_{tr}$  (Leading Edge and Trailing Edge Skins Not Included)**

Node #	$I_{tr}$	Skin $I_{tr}$
34	1.36E-01	9.22E-02
35	1.08E-01	8.39E-02
36	7.92E-02	7.61E-02
37	5.77E-02	6.89E-02
33	4.26E-02	6.23E-02
39	2.74E-02	5.62E-02
40	2.60E-02	4.65E-02
41	2.46E-02	4.22E-02
42	2.38E-02	3.49E-02
43	2.35E-02	3.32E-02
44	2.32E-02	3.27E-02
45	2.30E-02	3.21E-02
46	2.27E-02	3.16E-02
47	2.25E-02	3.11E-02
43	2.22E-02	3.06E-02
49	2.20E-02	3.00E-02

A sketch of the cross section at Node #27 is seen in Figure 48, with the wing box highlighted in orange. The primary structural members at any given cross section will look similar, though with a slightly different relationship between the chord length and spar cap size. Node 27 is where the strut joins the wing, so the spars just outboard of the joint, as seen below, are at their largest area since they are taking their largest load. This is also the point where the skin of the idealized rectangular wingbox (Figure 47) provides the smallest percentage contribution to the moment of inertia for any of the nodes – 26%.

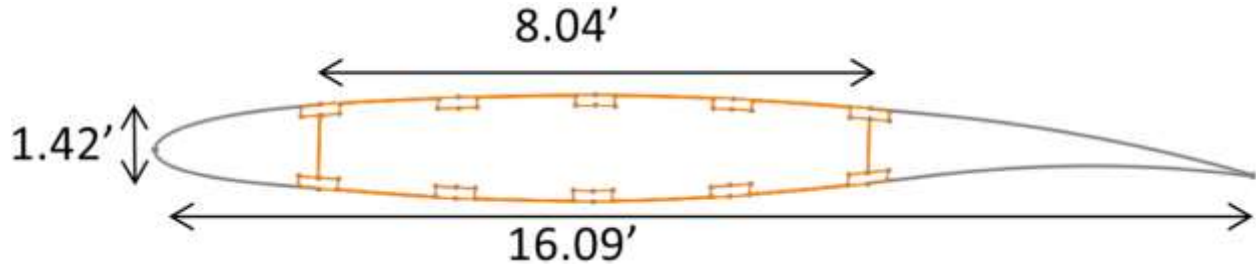


**Figure 48. Sketch of Wing Box and Skin at node 27. The Wing Box is Highlighted.**

Node 39 is more representative of the majority of the structure, having the skin provide 67% of the total moment of inertia of the cross section, slightly more than the average of 57%. Table 10 provides a comparison of the calculated area and area moment of inertia for these two cross sections for the MDO output, and three levels of detail in the design - just the spar/stringer areas, the wing box, and the whole wing. From Node #27 it appears that while the total area of the design is nearly double the MDO output, the moment of inertia is very similar. This is due to the abnormally low skin contribution at this point and the curved nature of the wing compared to the idealized rectangular case output from the MDO. Looking at Node #39 where the skin has only a slightly larger contribution than average for all the nodes given the MDO output is only 1/3 of the actual moment of inertia of the whole wing when including the skin thicknesses specified in the MDO output.

**Table 10. Comparison of Cross Sectional Area and Moment of Inertia for Different Levels of Design Detail**

	Node 27		Node 39	
	$I_{tr}$ [in <sup>4</sup> ]	Area [ft <sup>2</sup> ]	$I_{tr}$ [in <sup>4</sup> ]	Area [ft <sup>2</sup> ]
MX	0.317	0.625	0.027	0.100
Areas	0.192	0.628	0.018	0.100
Wing Box	0.274	0.842	0.060	0.289
Wing	0.308	1.083	0.075	0.478

Since Node #39 is similar to the average relationship between the MDO output (idealized area only) moment of inertia and the actual full wing or wing box moment of inertia the MDO is largely inaccurate. The upside is that the MDO provides a very conservative structure geometry so the final structure may actually be lighter than the output, but it will require a significant amount of effort iterating the structural design to arrive there meaning the MDO may not actually be saving much time or effort compared to the standard design process without this tool.

## **5.6 NCE MODEL DESIGN FOR DUAL AISLE AIRCRAFT**

The design for the NCE joint was based upon the joint designed for an earlier iteration of the concept, on a smaller vehicle. Conceptual models of that design were presented in previous summary reports. This design is more complicated by the fact that the NCE is moving both forward and aft, while the previous design it was only swept aft of the wing.

### **5.6.1 CAD Design**

Since the rear spar carries the majority of the load it was chosen as the hinge point, with the smaller load being carried by a slider joint linking the NCE forward spar to the wing forward spar.

All images presented below show the wing beyond the jury connection, with the NCE in red. The spanwise lines on the wing are a result of the different skin thicknesses output from the MDO in the wingbox. Ribs were only added in the NCE and near the joint in the wing, as the focus of this design effort was on the joint area, not design a layout of the wing. As the ribs pertain to the joint, the MDO locates ribs at a 3 foot spacing. Due to the forward sweep of the NCE no closeout rib can be added in front of the aft spar, so the 3 foot spacing starts at the outermost possible location for a full rib – 52 inches from the end of the aft spar.

Figure 49 shows the NCE at zero sweep. There is a small section of wing that overlaps the NCE forward of the hinge joint. The LE of this 'glove' sits at the LE of the NCE through the full range of sweep limiting any potential gap that could otherwise appear between the sliding skins. Due to the requirements for both forward and aft sweep there is a minor bump on the NCE skin at the joint, seen in Figure 50, which ensures the LE is a constant radius from the hinge so it meets cleanly with the LE of the 'glove' from the wing. At its maximum this bump extends approximately 1.1 inches beyond the straight line LE, producing minimal impact on the aerodynamics of the straight wing, while ensuring no gap at the joint to add drag when the NCE is articulated in either direction.

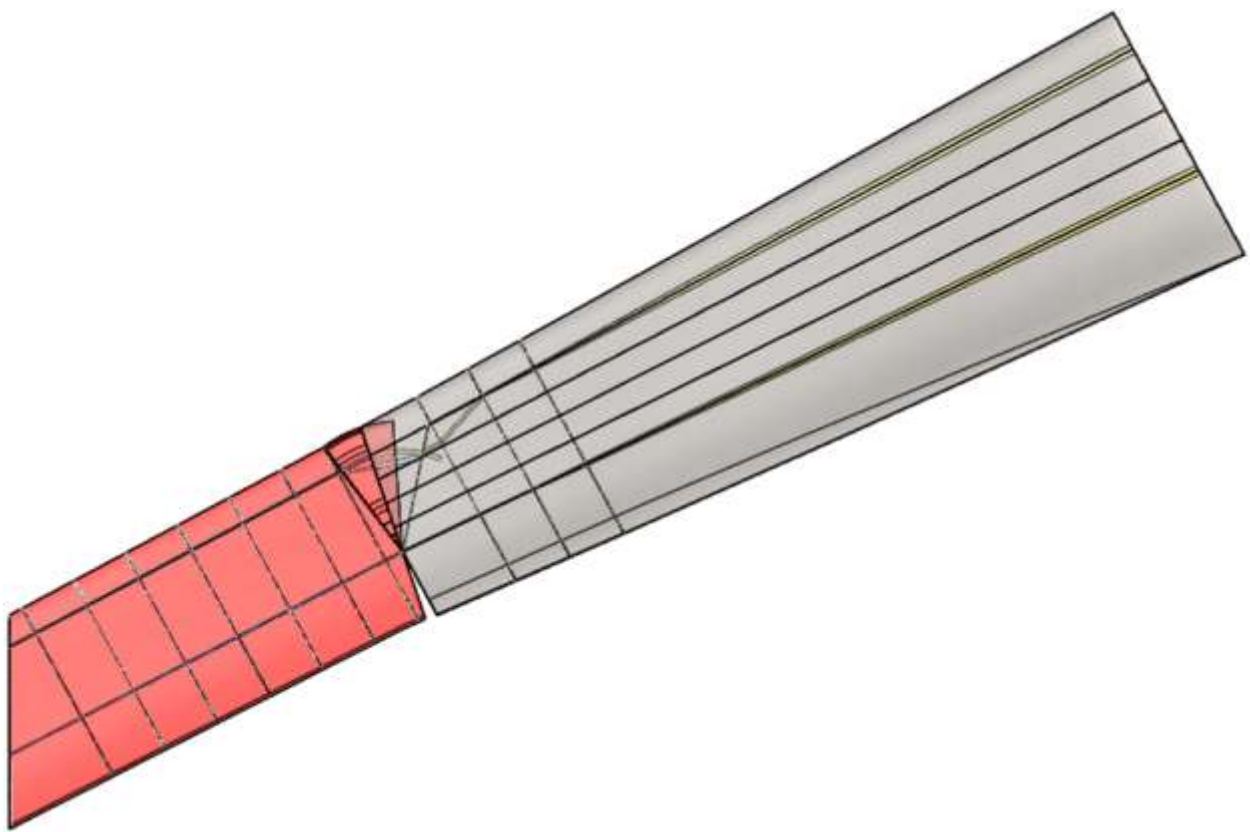


**Figure 49. Wingtip with NCE at Zero Sweep**

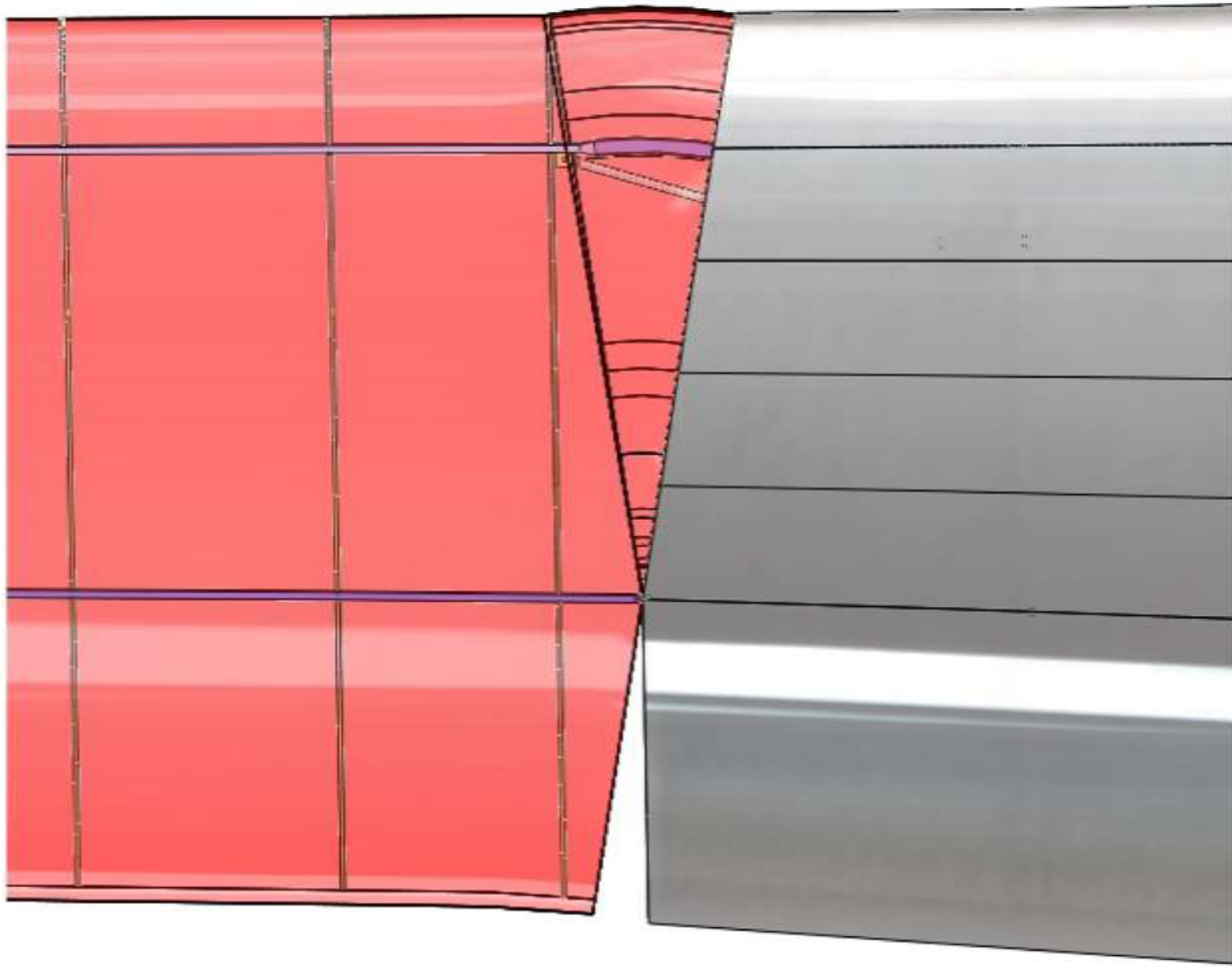


**Figure 50. Close-up of NCE Skin 'Bump' at Wing Joint**

Figure 51 and Figure 52 show the NCE at maximum forward ( $15^\circ$ ) and aft ( $10^\circ$ ) sweep. Just as the interface shape and location of the 'glove' LE wing skin and NCE LE were designed to minimize any potential gap between the two components, the trailing edge interface was designed so that when the NCE is fully swept aft the skins are continuous. A similar sliding skin glove-and-hand configuration could be implemented here. If more detailed studies indicate it is necessary to remove the gap that occurs when the NCE is swept forward the NCE cord can be slightly reduced so the TE can fit within the wing with a similar curvature as seen at the LE joint.

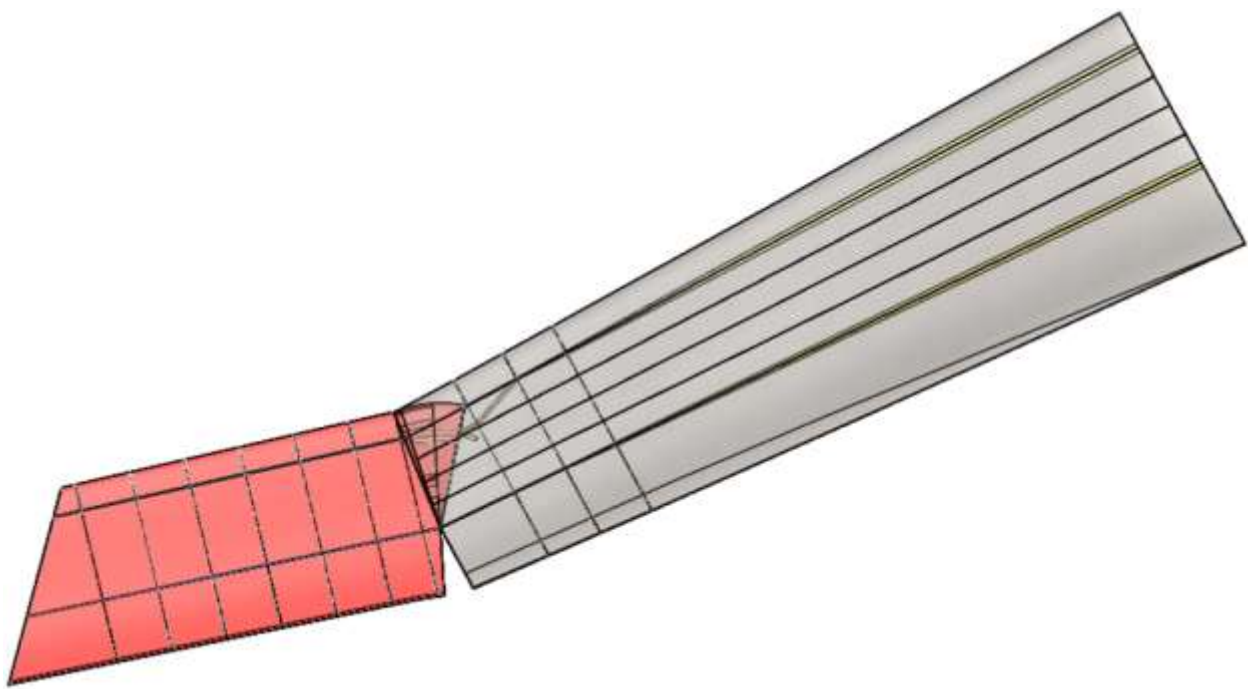


**Figure 51. Wingtip with NCE Swept Forward 15°**

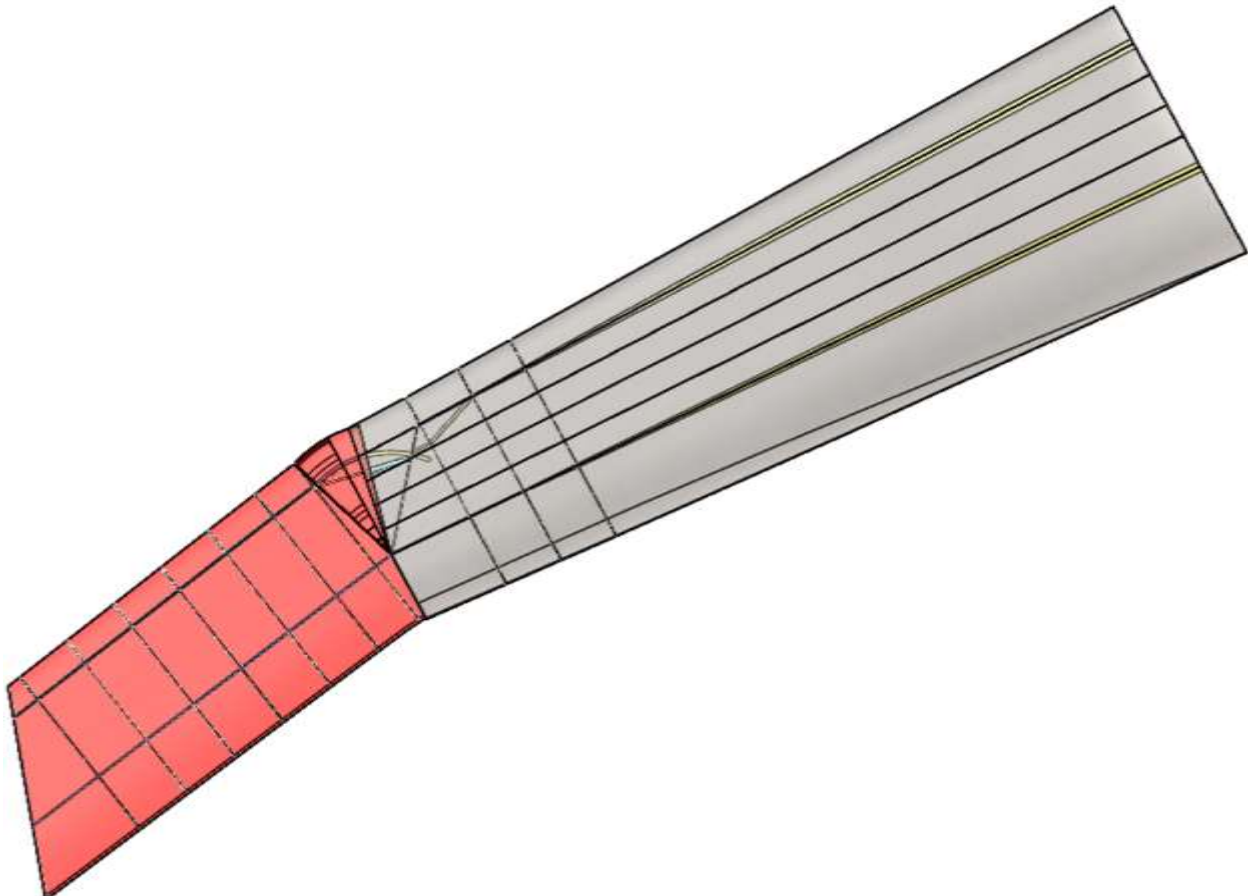


**Figure 52. Wingtip with NCE Swept Aft 10°**

Figure 53 and Figure 54 provide a better look at the joint between the NCE and the wing, and the associated structure to transfer loads from the NCE into the wing spars. Due to the forward sweep in this design the forward spar in the wing cannot run all the way out to the end of the wing skin - it would interfere with the forward sweep motion as seen in Figure 53. With the spar ending 40" before the skin the loads coming from the NCE need to be carried back to the wing structure, and ideally directly to the spar. An angled rib is included that follows the location the NCE at maximum forward sweep, from the hinge at the aft spar to the first full rib in the wing. This angled rib holds the outer section of the sliding mechanism for the forward spar, into which the NCE forward spar loads get transferred. The angled rib is supported at the joint with the sliding mechanism, with the support structure going back to the first full rib, then angling up to meet the spar at the second rib. This support structure is of a box beam geometry to increase torsional rigidity. Once a more defined maximum load case is obtained based upon this geometry the rib a support design will be updated, with potentially removing some of the current load transfer structure and adding support in different locations, such as from the after spar/first rib joint up to the angled rib and potentially other support for the sliding mechanism to improve load transfer to the spar.

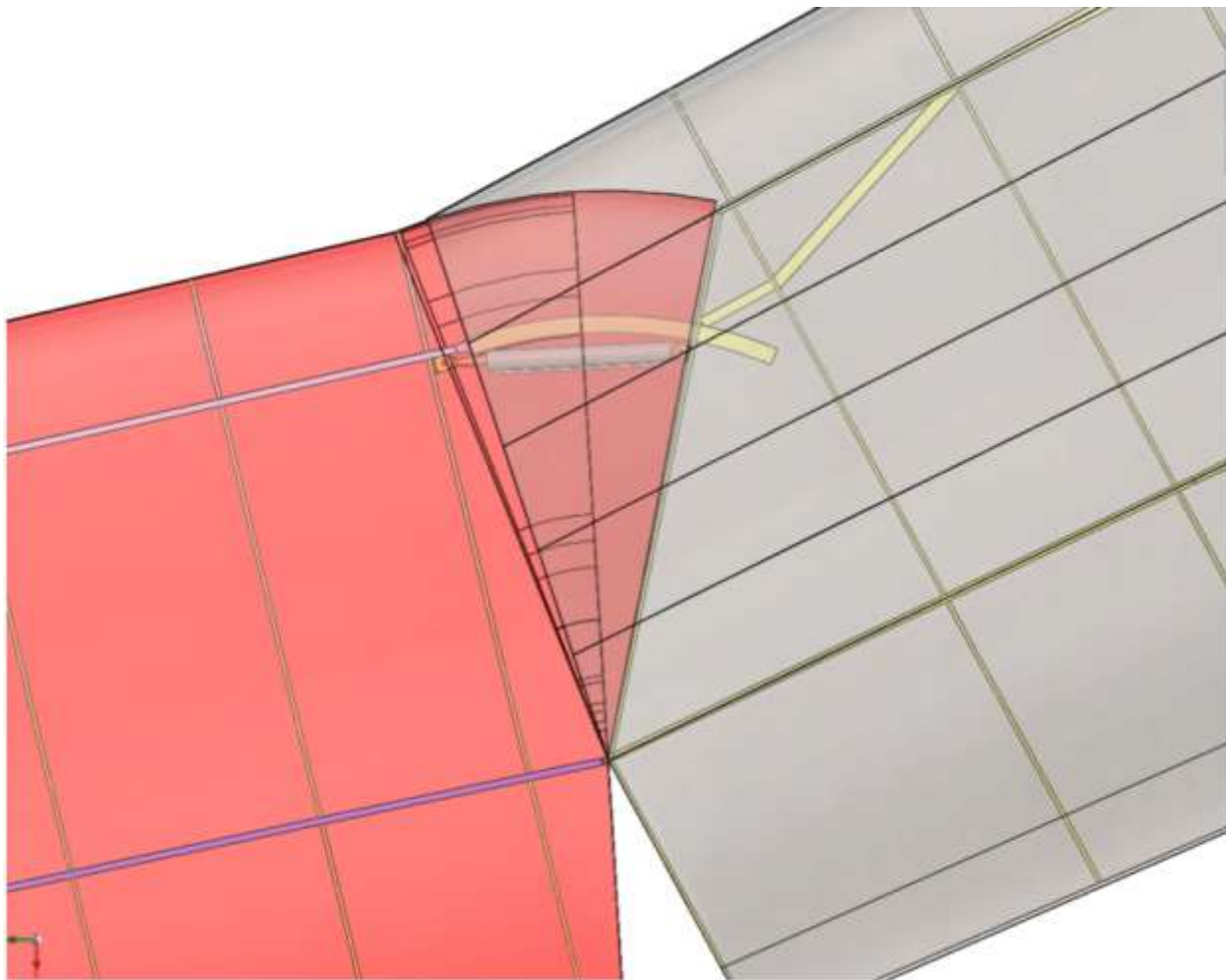


**Figure 53. View of the NCE-Wing Joint Area with NCE Swept Forward 15°**

Since full loadings on the NCE have not been finalized the actuation loads for it cannot be reliably estimated to size and select an actuator. Additionally, the detail design of the sliding mechanism and its support structure will impact the actuation requirements, resulting in a few iterations needed on the structural design before it is practical to size the actuator. Since the actuator cannot be determined a basic hydraulic actuator was added to the model to approximate the sizing and location of the actuator. In Figure 54 the actuator is visible under the overlap between the NCE and wing. The attachment to the NCE rib is also visible at the forward spar. Figure 55 shows the actuator cylinder in light blue (cyan) in both the forward and aft swept configurations, along with its attachment to the angled rib at the sliding mechanism.

The actuator is attached with a pin joint at both ends, as far away as practical from the hinge on the NCE, and as high as possible on the angled rib so the direction of loading on the NCE is as close to perpendicular as the geometry allows. Slight adjustments to the pin location will likely be necessary with the final design, dependent on the actual diameter of the selected actuator, to ensure that the actuator does not contact the sliding mechanism. The current design provides approximately 0.5" gap, for a 2.75" diameter actuator (which requires a 14.5" stroke for the actuation).

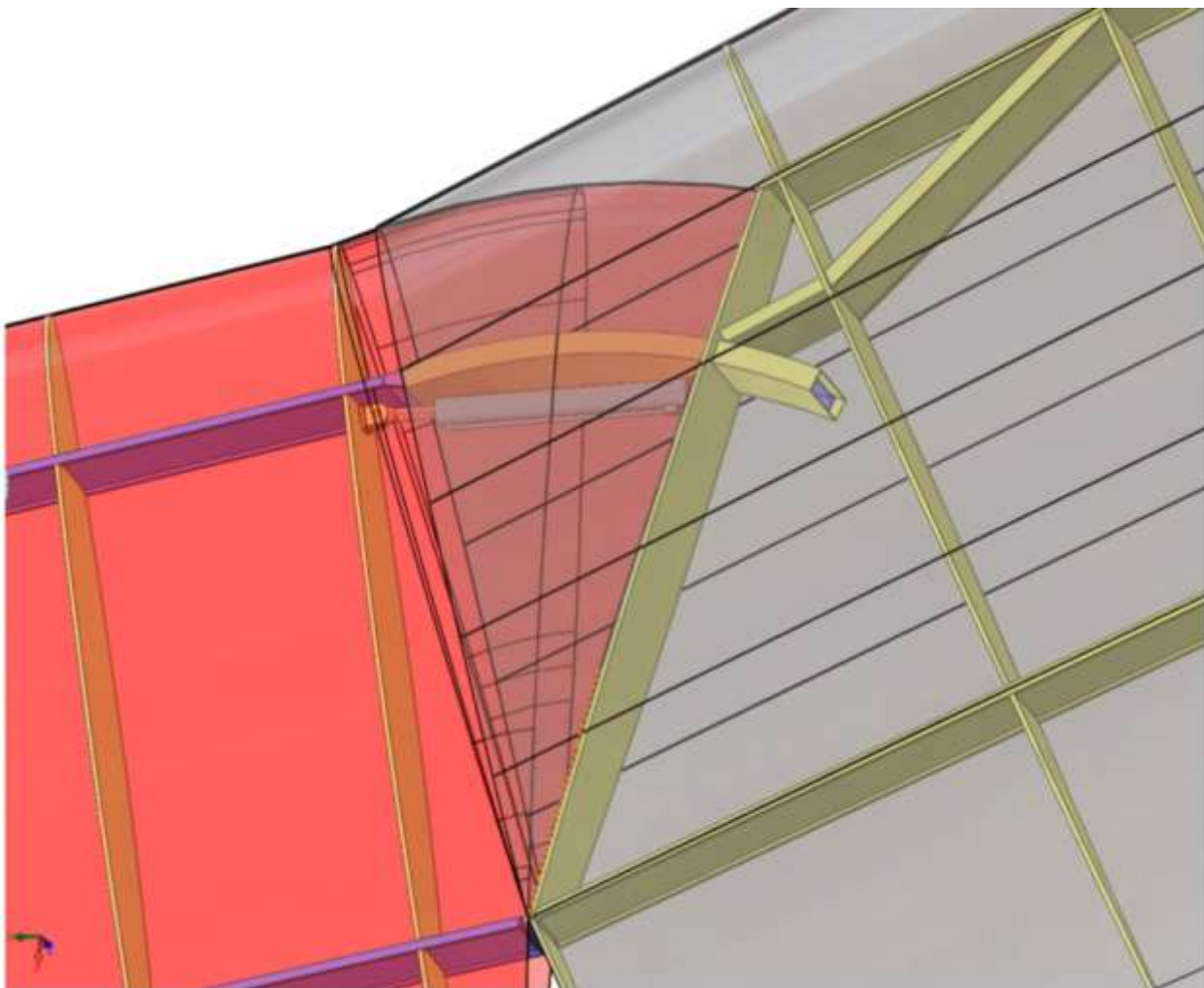


**Figure 54. View of NCE-Wing Joint Showing Actuator Connection to NCE Rib and End of NCE Spar Visible in Slider Joint with Wing. NCE Swept Forward 15°.**

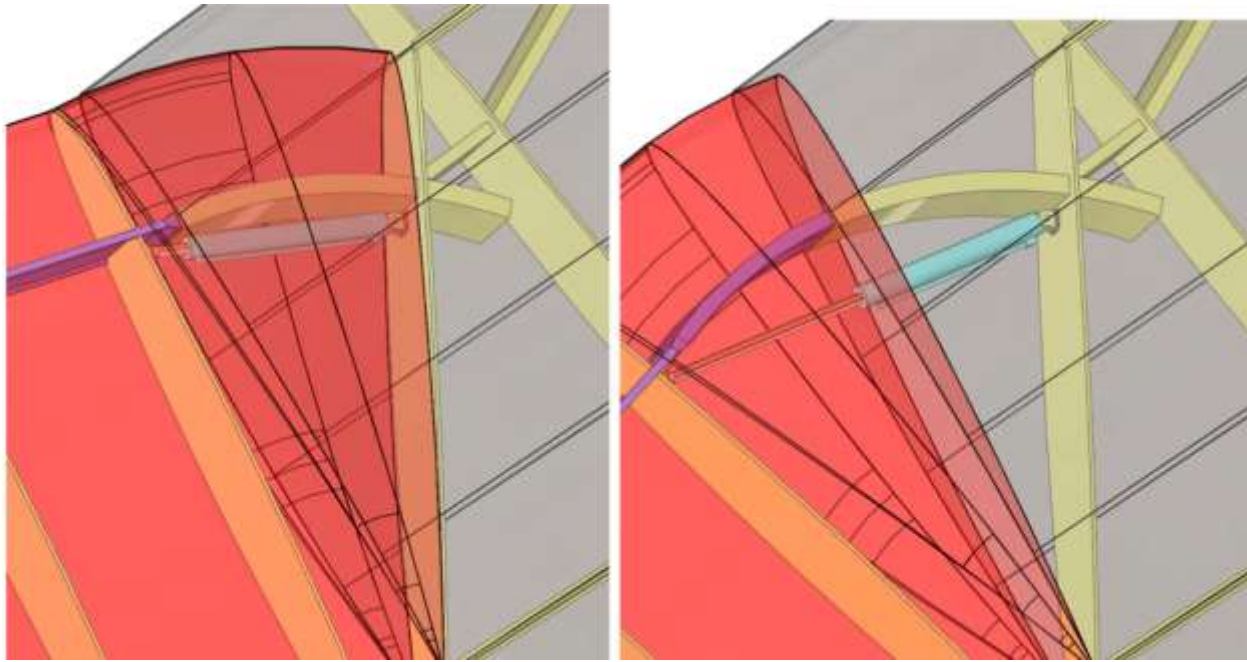


**Figure 55. NCE-Wing Joint Showing Actuator Attachment to Wing Rib. Left - NCE Swept Forward 15°; Right - NCE Swept Aft 10°**

## 5.7 DISCUSSION OF NCE DESIGN FOR DUAL AISLE AIRCRAFT

The MDO output was successfully transferred into a preliminary physical design, including conceptual design of the joint / interface between the NCE and the wing. This includes hinge location and design, basic mechanics of the NCE sliding into the wing during actuation, internal structural layout of the wing and NCE and load transfer mechanism to bring the NCE loads to the wing spars.

While we were able to successfully able to translate the specified parameters from numerical results to a physical design, much improvement can be done to the MDO results to streamline the design process and more rapidly advance the initial design. Some of the noted problem areas that require improvement for the tool to be truly useful include:

1. Producing a functional user manual based upon the existing MDO tool description in a published paper. While much of the content exists, reformatting it into a user manual and correcting the errors is necessary (i.e. Equation 6 in [21]).
2. Generate a document that provides a explanation of the MDO output content along with necessary information to enable its transformation into a physical design (i.e. assumptions and geometrical simplifications, which coordinate system different components are in)
3. Improving geometry from a basic rectangle to allow for a cleaner and more accurate wing shape.
4. We also recommend updating the spar / stringer area calculations so the spars are not the same size as the stringers

Beyond the MDO, the structural design and layout can be further studied to improve the overall layout and structural weight.

1. Determine the load path from NCE to wing, and if it can be controlled. The hinge joint is currently at the aft spar, resulting in less vertical clearance and limited space behind aft of the spar to allow for ailerons and their control and actuation hardware. If the majority of the load is primarily on the aft spar, the sliding spar and load transfer mechanism of the forward spar can be improved.
2. Study the effect of a gap in the TE behind the joint to determine the full impact on the aerodynamics of the vehicle. A fully enclosed TE is possible, though it may not produce a noticeable impact on the vehicle performance.
3. Investigate more LE configurations. If we are able to extend the LE of the wing farther (not with respect to reducing the span of the NCE, but advancing it beyond the hinge - as viewed perpendicular to the LE) we can reduce the impact of the NCE LE on the internal structure of the wing. If the NCE LE does not cross the forward spar the spar can be extended to the sliding joint, for a cleaner load transfer, simpler design, and likely reduced weight. This may also include aerodynamic analysis of the joint, with slightly different planforms necessitated to accommodate the sweeping motion, like the 'bump' at the LE in the current design.

## 6. SUBSYSTEM STUDY

The Task 1 mechanization development resulted in a VGRWT system with modest subsystem functional requirements. This report describes A) the overall system, B) the subsystems elements that will be integrated into the VGRWT. The subsystem study was done for the SUGAR single aisle aircraft. A subsystem study was not performed for the NCE on a larger, dual aisle aircraft.

### 6.1 SYSTEM DESCRIPTION

The Task 1 Technical Memorandum describes the selection of the variable geometry raked wing tip (VGRWT) configuration in detail. The mechanization approach was selected to provide short, direct load paths for the wing tip aerodynamic loads. This selection was primarily driven by minimizing weight. The mechanization approach for the Variable Geometry Raked Wing Tip (VGRWT) illustrated in Figures 56 and 57. The tip sweeps about a pivot point located at the wing aft spar. The wing forward spar incorporates a track and slide mechanism to accommodate the motion and carry wing loads.

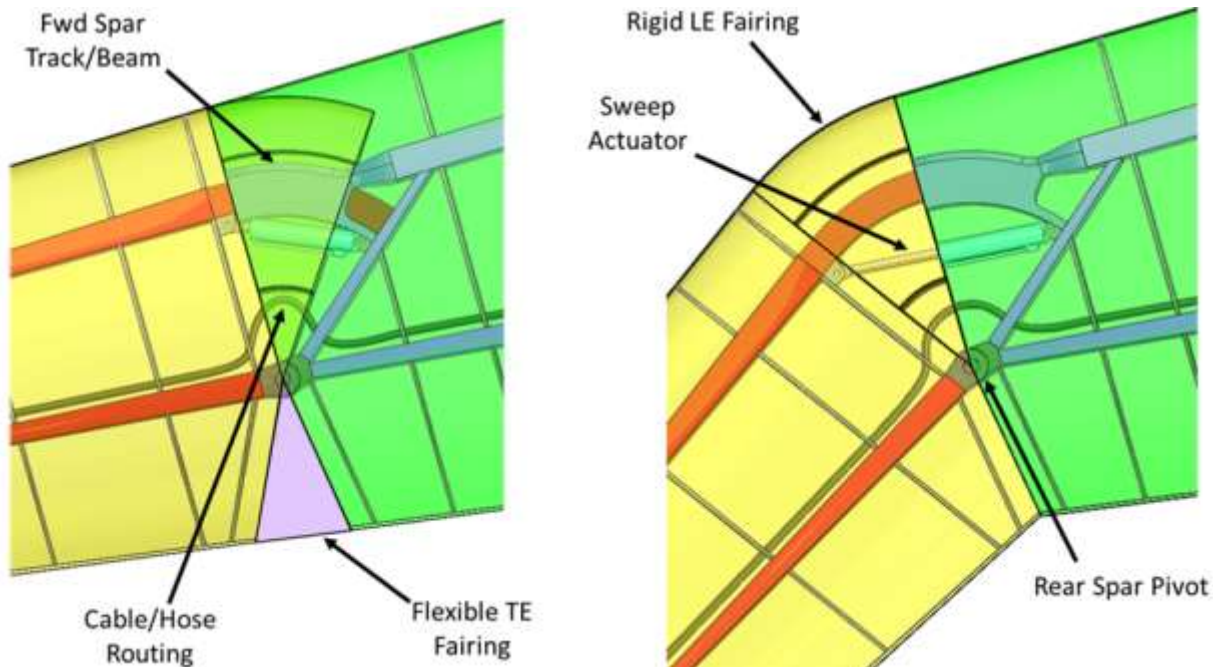


Figure 56. VGRWT Minimum (0 deg) and Maximum Sweep (35 deg)

Forward of the aft spar pivot is a rigid leading edge fairing which nests inside the wing skin when the tip is unswept and is exposed to the flow when the tip is swept. Aft of the pivot is a flexible trailing edge fairing. Provisions are also shown for cable and or hose routing to any systems in the tip requiring power or other subsystem support.

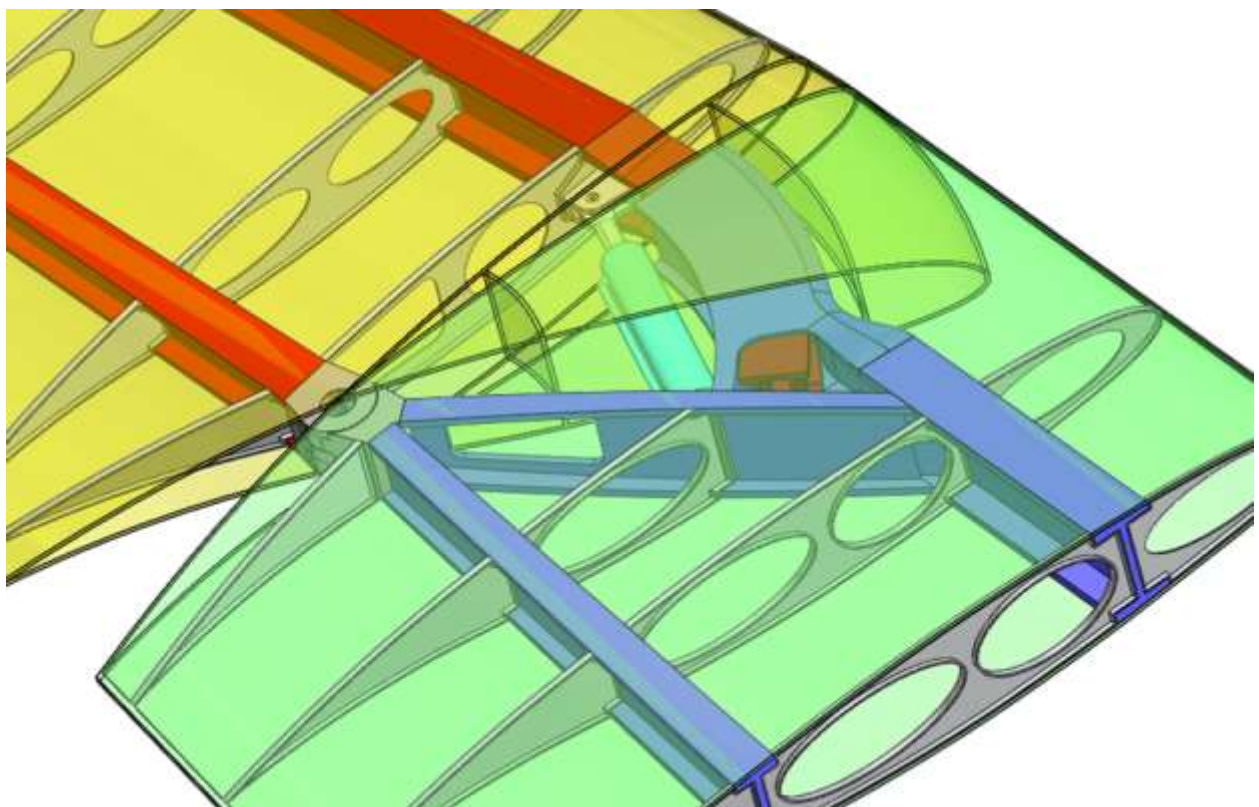


Figure 57. Mechanization Concept Details (aft fairing not shown)

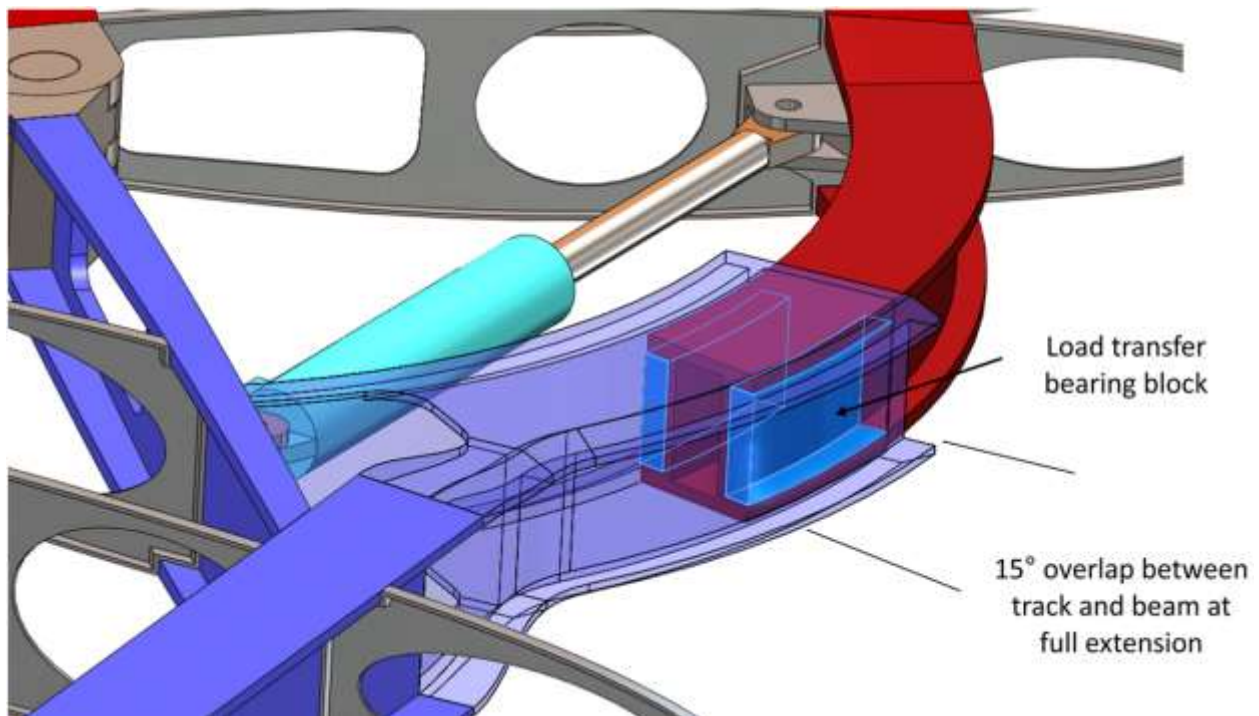


Figure 58. Forward Spar Track and Beam Mechanism (notional actuator shown)

## **6.2 SUBSYSTEM INTEGRATION**

Subsystem elements integrated into the VGRWT are basic. The primary subsystem elements are the actuators for the sweep actuation and for the aileron. Secondary subsystem elements have not been defined for the SUGAR aircraft but may include navigation lights, communications antennas and/or lightning strike protection equipment. The weight of these elements was not individually identified as part of the SUGAR program but has been accounted for by a non-structural distributed mass loading based on previous Boeing mass properties experience. The VGRWT incorporates the same nonstructural mass loading. The remaining subsystems integration issue is to ensure that cables, wire harnesses or other systems connections are not restricted by the design of the VGRWT. The selection of the fixed pivot at the aft spar easily facilitates the routing of power and control cables as shown in Figure 56. Routing of hydraulic lines is also possible however the SUGAR aircraft does not use hydraulically driven control surface actuators and no such actuators are required for the VGRWT.

## 7. AERODYNAMIC ANALYSIS

### 7.1 INTRODUCTION

The aerospace community is constantly investigating new and exciting concepts for the improved performance of transport aircraft. To this end, NASA commissioned a research project looking into the next generation of passenger aircraft, and Boeing developed several subsonic and supersonic concepts designed to meet NASA's goals. The subsonic ultra-green aircraft research (SUGAR) produced many concepts, from conventional low-wing configurations, to high-wing, truss-braced configurations, to blended-wing-body arrangements [22]. Of the conventional designs, the truss-braced wing (TBW) concept is particularly interesting for medium-range aircraft due to the fact that it is not entirely dependent on ambiguous "future technologies". The concept is also easily scalable to various aircraft sizes. Using current technology, tangible gains in fuel efficiency, range and payload, along with a reduction of aircraft weight, are possible simply by incorporating a strut and jury wing design [23]. With the baseline SUGAR research completed by Boeing, methods of further improving the designs are underway. A relatively straightforward way to improve aerodynamics and fuel efficiency is to include a wingtip treatment, such as a winglet or raked tip.

In the pursuit of fuel efficiency and drag reduction, the current crop of Boeing and Airbus airliners incorporates some type of wingtip treatment. One common type of treatment is vertically blended winglets, evident on the Boeing 737 and 747. The main benefits of blended winglets are to increase range and payload, while decreasing fuel usage. This is accomplished by decreasing the induced drag of the wing. The winglet decreases induced drag by increasing the velocity of the flow over the tip, which produces additional lift and improves the wing lift distribution. The end result of this procedure is a reduction in trailing vortex strength, which improves efficiency [24].

Another common type of treatment is the horizontally raked wingtip, found on the Boeing 767 and 787. Generally, a raked tip necessitates structural enhancements due to the increase in span and is, therefore, commonly only applied to new designs. The winglet however, does not suffer from this problem, thus it is more easily adapted to existing designs, as was carried out with the Boeing 737 and 747. Ideally, the wing span should be maximized during take-off and landing in order to produce the most lift during these critical flight regimes. However, in order to decrease drag during transonic cruise conditions, the wing should be swept and span reduced in order to avoid unnecessary drag caused by locally supersonic flow over the wing. The raked wingtip represents a compromise between these two extremes by having the tip swept at an angle such that improvements are made in all flight areas [25]. However, in order to gain the maximum performance increase over the entire flight envelope, the tip should swing in response to current flight conditions. A variable sweep wing is not a new concept, and has been incorporated on military aircraft in the past.

Messerschmitt first studied variable sweep wings during World War II, though the concept was unfinished before the war's conclusion. Experimental aircraft were built and flown in the United States in the post-war period, however results were mixed [26]. The first production swing wing aircraft was the F-111 Aardvark, however the most famous is arguably the F-14 Tomcat [27]. The F-14's mission represents all of the classic design conditions for a swing wing. The wing extends for carrier take-off and landing, when lift and maneuverability are paramount, and retracts during transonic cruise to decrease drag and allow a higher cruise Mach number [27]. The same performance gains are obtainable with a variable sweep raked wingtip, though to a lesser degree.

A study of the aerodynamics of a variable geometry raked wingtip (VGRWT) is of interest due to the possible improved aerodynamics of the wing system. Additionally, an important potential of a variable sweep wingtip is as a novel control effector (NCE), which utilizes the generation of torque on a flexible wing as a means of roll control, as well as gust and/or flutter alleviation. Thus, we will refer to this system as a VGRWT/NCE. Therefore, due to the possible aforementioned performance gains, a variable sweep raked wingtip was selected as the tip treatment for the Boeing SUGAR design employing a truss-braced wing to be studied by a team including Boeing, Virginia Tech, and NextGen Aeronautics.

Boeing designed the VGRWT/NCE to replace the conventional tip on the current SUGAR design. The tip is designed to be of the same area, however the span would be increased. This results in the unswept tip displaying nearly the same aerodynamic properties as the conventional tip. Furthermore, it was nominally decided to set the maximum sweep angle to  $50^\circ$ . Also the unswept state would have a sweep equal to the main wing structure, approximately  $15^\circ$ . Though it is possible to sweep the tip forward, this was not investigated due to the structural considerations required to resist divergence. Finally, since the tip is to be swept during cruise and the majority of flight time is spent at this stage, the fully-swept case was designed to be the default state of the tip.

The aerodynamic performance of the tip was analyzed using an inviscid vortex lattice method (VLM) Matlab code, as well as a computational fluid dynamics (CFD) program. The aim of this analysis is to produce the changes ("deltas") in force and moment on the tip compared to the baseline SUGAR wingtip over a range of tip sweep and aileron deflection angle. Using these tools, it will be shown that the VGRWT outperforms the unaffected tip, in terms of lift and moment produced.

## 7.2 METHODS AND MODELS

### 7.2.1 Vortex Lattice Method

The vortex lattice method was selected as the main tool for assessing aerodynamic performance changes on the wingtip, because it allows for comprehensive studies over a wide parameter space due to its speed and robustness [28]. Tornado is a VLM code written for Matlab, initially developed as a Master's thesis in Sweden [29]. It provides a way to examine many different aircraft shapes in a relatively short amount of time. With the excellent correlation with data provided by Cessna, Tornado provides a flexible and well-validated low fidelity aerodynamic analysis tool [29]. The code computes the vortical strength in the usual way, however a notable difference occurs in the handling of the freestream following the downwash. In Tornado, the wake vortex is realigned with the freestream at a point in the downwash where the aerodynamic influence of the vortex line is negligible. This method allows Tornado to incorporate wing twist and aileron deflections into the design. Therefore, given Tornado's large included airfoil database, as well as the ability to import custom airfoils, the range of wing profiles that can be created is very wide [29, 30]. This includes the ability to analyze more than one aerodynamic surface, which proved very useful considering that the baseline SUGAR configuration incorporates a strut and jury. Tornado also provides several options for panel distribution, and prior work has shown that the spanwise half-cosine method gives the least error in the prediction of the aerodynamic center [31]. Therefore, that was chosen for all models here. However, VLM codes do have some notable drawbacks.

Though Tornado is a useful tool for low-fidelity aerodynamic analysis, it lacks viscous modes. This is a shortcoming of all VLM codes and can be mitigated through the use of empirical corrections. Tornado also has no method to predict stall, leading to inaccuracy at high angles of attack. This is not a problem for this research, since all analysis is conducted at cruise conditions, which implies very small angles of attack. VLM codes also do not typically have compressibility corrections and indeed early versions of Tornado did not. However, current versions of Tornado do include the Prandtl-Glauert correction, and this has proven to be quite effective at modeling compressibility, with results comparing very well to experimental data [32]. Finally, a common complaint regarding VLM codes is perceived inaccuracy in the calculation of the pitching moment. However, careful placement of the moment reference point, in this case taken to be the quarter chord of the root, can somewhat lessen this inaccuracy.

### 7.2.2 Computational Fluid Dynamics

As computing power has increased, CFD has become a powerful tool for aerodynamic analysis. The program chosen here to do the analysis was ANSYS Fluent, due to previous research experience with the program and a largely automated configuration, especially regarding grid generation. Fluent proved relatively easy to use, once a reasonable amount of time had been spent learning its intricacies. Similar to Tornado, Fluent allows for nearly limitless model types, assuming they can be adequately reproduced with a CAD program, and proper mesh generation is performed. The CAD program used for this analysis was Fluent's built-in studio, DesignModeler. Similarly, the mesher used was Fluent's built-in mesh generator, which automatically generated the mesh based on a set of specifications, such as element size and shape, curvature angle, and grid type. This analysis was started with a relatively simple mesh, then adaptive gridding was conducted to demonstrate grid independence. Although Fluent ran quickly by CFD standards, this research required many iterations and geometries, therefore the time penalty became untenable. Consequently, this research uses Fluent as a collaborative tool with Tornado. The Fluent solutions were run inviscid and compressible, and they were used primarily to validate the Tornado results for a few interesting cases, but the bulk of the analysis was left to the considerably faster VLM code. This analysis strategy is deemed appropriate, since the goal is to determine the "deltas" between the tip of the baseline SUGAR wing and VGRWT/NCE wingtip.

### 7.2.3 Design of VGRWT/NCE Tip

In order to incorporate the VGRWT/NCE tip, the baseline SUGAR wing design was modified. After several concepts and iterations with Boeing engineers, it was decided that the location of the pivot point of the VGRWT/NCE tip should be at the rear spar of the wing, approximately 60% of the chord. This design necessitates tucking a portion of the leading edge into the main wing when the tip is unswept. When the VGRWT/NCE tip transitions to the fully swept position, this section will extend, while a portion of the trailing edge moves into the main wing. An early sketch of this design is shown as Figure 59. Note that although the pivot point is incorrect in this sketch, the concept for the pivot mechanism is the same.

The span of the VGRWT/NCE tip was designed to adhere to the "2/3 rule". This rule of thumb states that the span of the tip will only increase the span of the wing by 1/3 of the length of the span of the tip. The fully-swept span of the VGRWT/NCE tip was set to be 120 inches, which necessitates that the VGRWT/NCE tip will begin at the 939 inch span station of the SUGAR wing, for a net gain of 40 inches of span according to the 2/3 rule. However, this does not include the

span increase due to the deployment of the sweep mechanism. This deployment brings the total tip span to approximately 145 inches. A sketch of the fully-swept VGRWT/NCE tip geometry is shown as Figure 60. From this point, the geometry of the VGRWT/NCE tip determined that the unswept tip must have a span of 193 inches.

Planform data for the baseline SUGAR TBW main wing was provided by Boeing and is the result of their multidisciplinary design optimization (MDO) analysis. The wing twist per span and wing thickness per span is reproduced as Figure 61. Since the VGRWT/NCE tip increases the span, the thickness and twist profiles were adapted to reflect this increase. Also, the areas of constant twist and thickness, at approximately 0.9 span, reflect where the NCE tip joins the main SUGAR planform. Wing twist and thickness was kept constant in order to facilitate the implementation of the swing mechanism.

In order to accurately compare VGRWT/NCE tip performance with the baseline SUGAR tip, the boundary for the baseline SUGAR tip was extended inwards to the approximately 880 in span station. This allows the baseline SUGAR tip to be of comparable area to the VGRWT/NCE tip and to incorporate an equal size aileron, as will be discussed in Section 7.2.5. As will be seen in Section 7.3, this proves correct as the baseline SUGAR tip provides nearly identical performance to the unswept VGRWT/NCE tip, as desired.

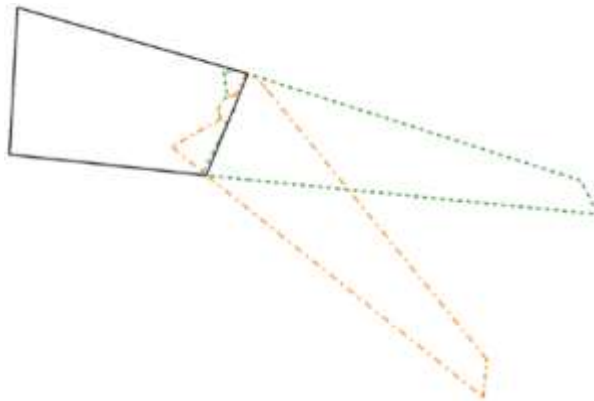


**Figure 59. Early Sketch of VGRWT/NCE Tip Pivot Concept**

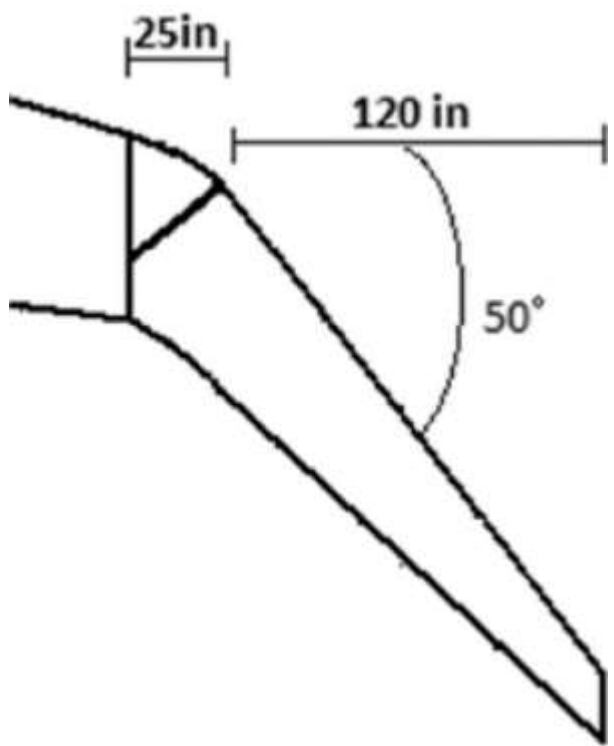


Figure 60. Geometry Sketch of Fully-Swept VGRWT/NCE Tip

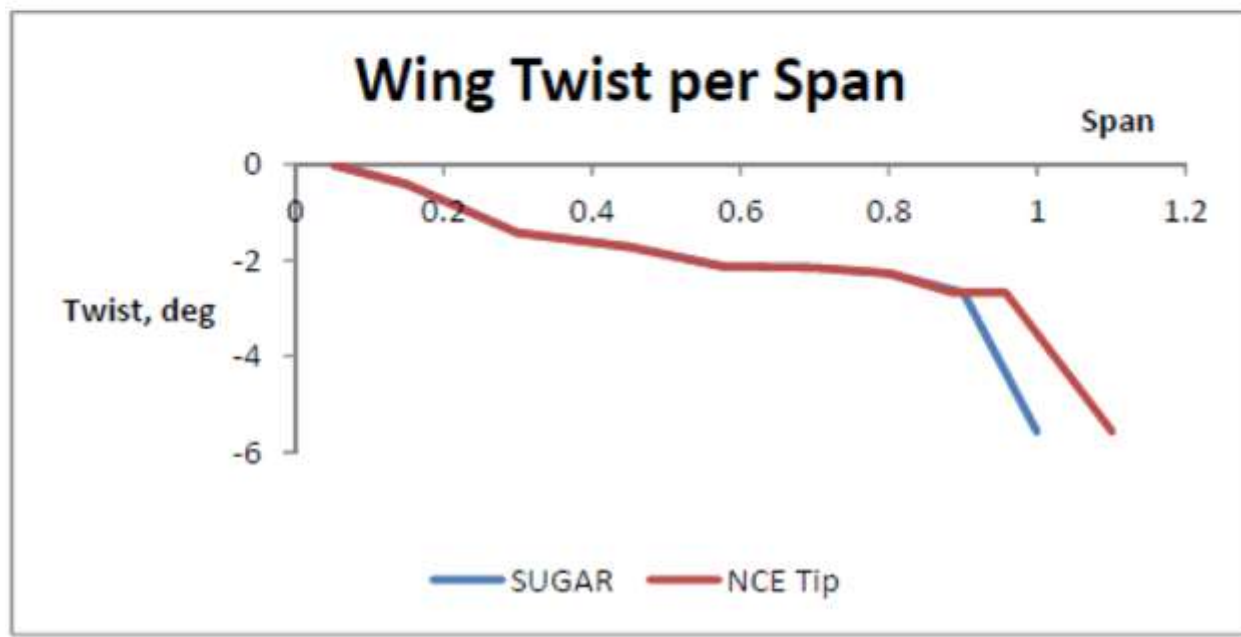
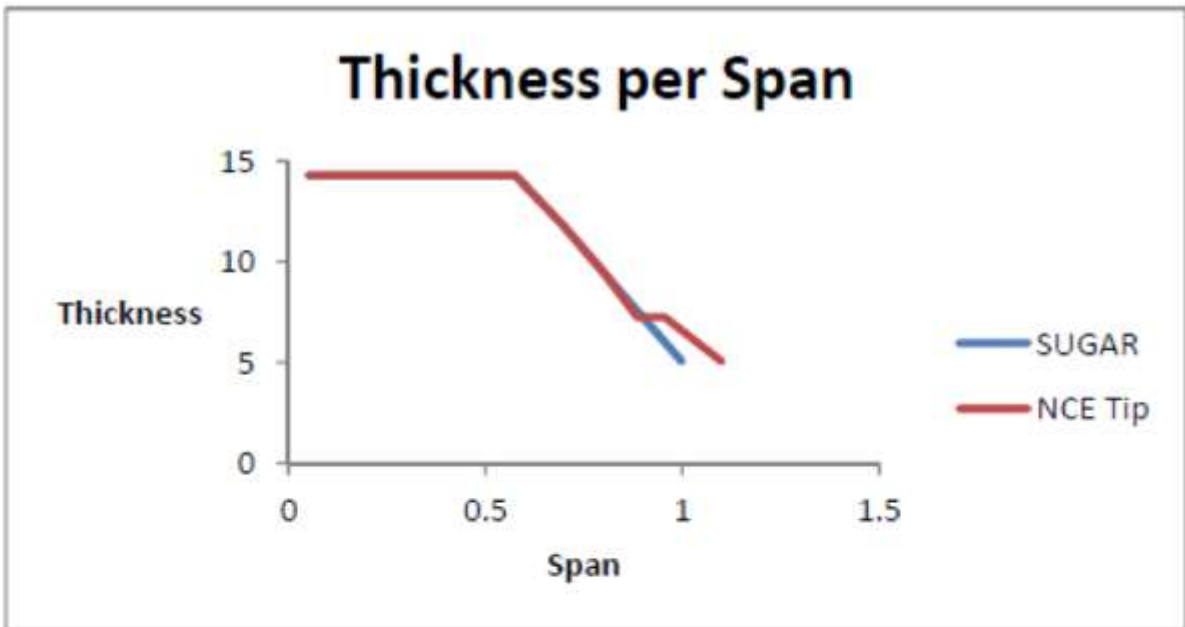


Figure 61. Wing Thickness and Twist per Span for SUGAR and VGRWT/NCE Tip

#### 7.2.4 Clean Wing Models

Preliminary analysis was first conducted using the baseline SUGAR TBW main wing, but without the strut, jury or ailerons. The publicly available Boeing Aircraft Company J (BACJ) airfoil was chosen as a suitable representative of the supercritical airfoils found on many current airliners, and Figure 62 depicts its shape [33]. All calculations were carried out at cruise conditions, specifically Mach 0.7 and 44,000 ft altitude.

Boeing Aircraft Company J Airfoil

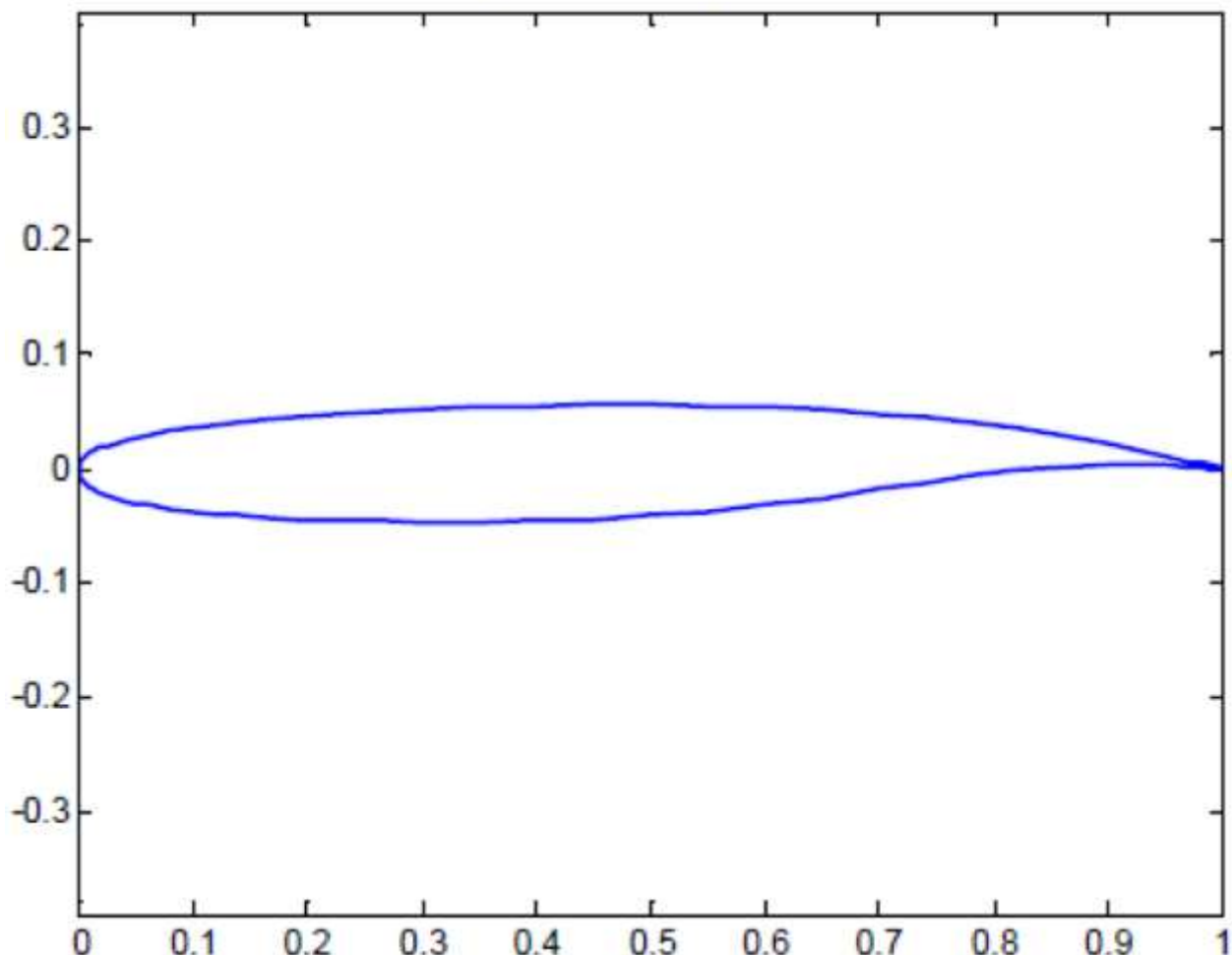


Figure 62. Boeing Aircraft Company J airfoil [33]

#### 7.2.4.1 Tornado Models

Models of the clean wing were constructed in Tornado for the baseline SUGAR main wing planform, unswept-tip case, and fully-swept VGRWT/NCE tip case. Tornado does not allow for geometry to be rotated to create a new model. Therefore, each model must be made independently of others. Further, the boundary of each wing section must be streamwise. In actuality, the boundary between the main wing and the NCE tip is normal to the leading edge, however, given the aforementioned limitation that section boundaries must be streamwise, this is impossible to model in Tornado. The resulting very slight reduction in tip area would not meaningfully influence the results. The baseline SUGAR model constructed in Tornado shows excellent convergence with the data provided by Boeing, as shown in Table 11. Table 12 compares all of the wing models constructed in Tornado, and shows good agreement between wing areas for the unswept and swept cases, as desired. Each model consists of approximately 300 panels, with panel density increasing towards the tip. Figure 63 shows the Tornado clean wing models used for preliminary analysis. Note that only the half span is shown for clarity.

Also, in a real application the design of the wingtip necessitates a small step at the joint of the main wing and the VGRWT/NCE tip. Due to the constraints of Tornado, this step was not incorporated into any Tornado models. A drag estimation method developed to deal with the influence of the step will be discussed in Section 7.3.3.

**Table 11. Comparison of SUGAR Main Wing Planforms**

	<b>Baseline SUGAR Planform</b>	<b>Tornado Model</b>
Area (ft <sup>2</sup> )	1477.11	1476.69
Span (in)	2039.3	2039.29
Aspect Ratio	19.55	19.56
Mean Aerodynamic Chord (in)	110.2S6	110.256

**Table 12. Comparison of Tornado Wing Models**

	<b>Baseline Main SUGAR Wing</b>	<b>SUGAR Main Wing with Unswept VGRWT/NCE Tip</b>	<b>SUGAR Main Wing with Fully-Swept VGRWT/NCE Tip</b>
Area (ft <sup>2</sup> )	1476.69	1512.39	1511.91
Span (in)	2039.29	2265.79	2172.87
Aspect Ratio	19.56	23.54	21.69
Mean Aerodynamic Chord (in)	110.26	108.15	108.73

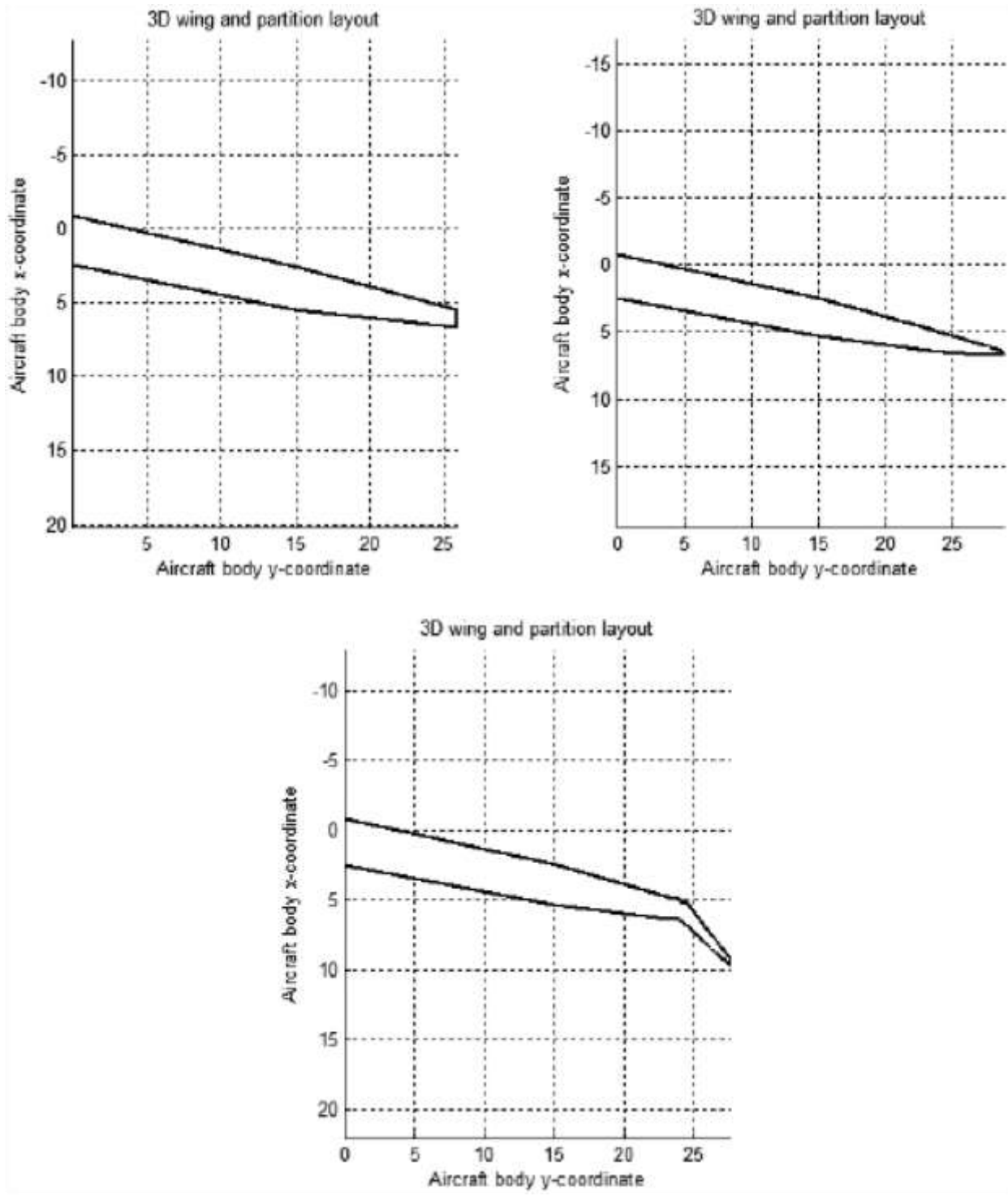


**Figure 63. Tornado Clean Wing Models (Half Span Only, Dimensions in Meters)**

#### 7.2.4.2 Fluent Models

Similar to Tornado, wing models were constructed in DesignModeler to match the data provided by Boeing. Due to the time constraint imposed by CFD analysis, only one half of the wing planform was modeled. The mesh consists of tetrahedral elements, with a minimum size of 1 mm.

Further, the curvature angle and proximity was set to the lowest possible setting to ensure a quality mesh. With these settings, all starting models contained approximately 6 million elements. After the completion of adaptive gridding, the models consisted of nearly 8 million elements. This process will be discussed further in Section 7.3. The wing models used are shown as Figure 64 with meshing overlaid before the adaptive gridding process commenced.

The fluid volume used to simulate the flow is a half circle, with one wall at the wing root and the other extending approximately 10 chord lengths past the wingtip. Similarly, the front and rear boundary also clear the leading and trailing edge by at least 10 chord lengths. The front face was set to be a pressure inlet, while the rear face is a pressure outlet. The left and right boundaries were set to be symmetry walls.

In order to obtain a fair comparison to the Tornado results, Fluent ran inviscid calculations with the energy equation enabled to simulate compressible flow. Using a six-core machine, each iteration took approximately 3 to 4 hours to complete. As with Tornado, the step between the main wing and the VGRWT/NCE tip was not modeled due to the complexity of the mechanism and the difficulty of obtaining a quality mesh over a very small step.

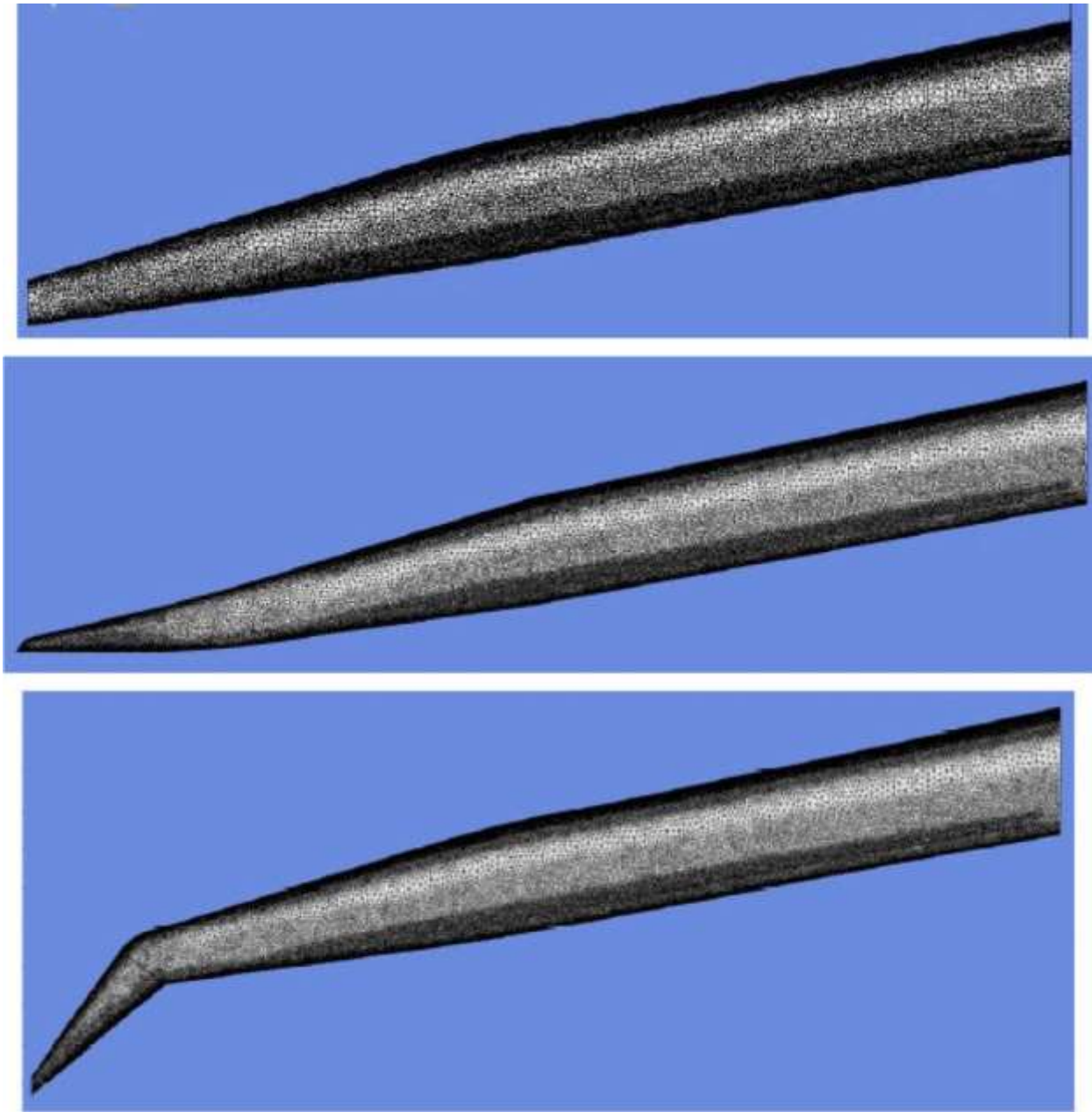


**Figure 64. Fluent Clean Wing Models before Adaptation**  
**Top: Baseline SUGAR Main Wing**  
**Middle: SUGAR Wing with Unswept VGRWT/NCE Tip**  
**Bottom: SUGAR Wing with Fully-Swept VGRWT/NCE Tip**

### 7.2.5 Wing Models with Strut and Jury

The baseline SUGAR wing incorporates a truss-braced system in its design, therefore a complete wing system was modeled to gain a true understanding of performance. The strut and jury were constructed from data provided by Boeing from previously completed SUGAR MDO analysis. Boeing specified that the strut and jury be non-lifting, therefore the airfoil shape was assumed to be a symmetric NACA 4-digit airfoil of thickness specified by the MDO analysis. Figure 65 provides a view of the modeled full SUGAR TBW wing configuration, while Table 13 summarizes

the geometry of the strut and jury. Figure 66 shows details of the strut and jury model. In order to evaluate the performance of the VGRWT/NCE tip against the baseline SUGAR tip, an aileron was added. Assumed to be 25% of chord, the aileron was allowed a typical maximum deflection of  $\pm 20^\circ$ . The length of the aileron was determined from existing passenger aircraft and set to be approximately 10 ft. In addition to the unswept and fully-swept cases, models of intermediate sweep were constructed to give a full picture of the VGRWT/NCE tip performance throughout the sweep range. These additional models reflect quarter-sweep, half-sweep, and three-quarter sweep positions. The area of the wing planform across the models was consistent, with a maximum deviation of approximately 0.45 ft<sup>2</sup>.

In order to truly isolate the performance of the tip, force data was extracted from Tornado for each VLM panel outboard of the 939 inch span station. Since the inboard profile did not change, Figure 67, 68, and 69 show the detail of the tip treatment for each sweep case and the baseline SUGAR case. The area considered in the tip calculations is shaded in each figure.

**Table 13. Geometry of Strut and Jury**

	Strut	Jury
Span, ft	49.08	4.76
Root Chord, ft	3.44	1.06
Tip Chord, ft	4.00	1.06
Sweep, deg	8.85	-7.29
Dihedral, deg	15.3	88.77

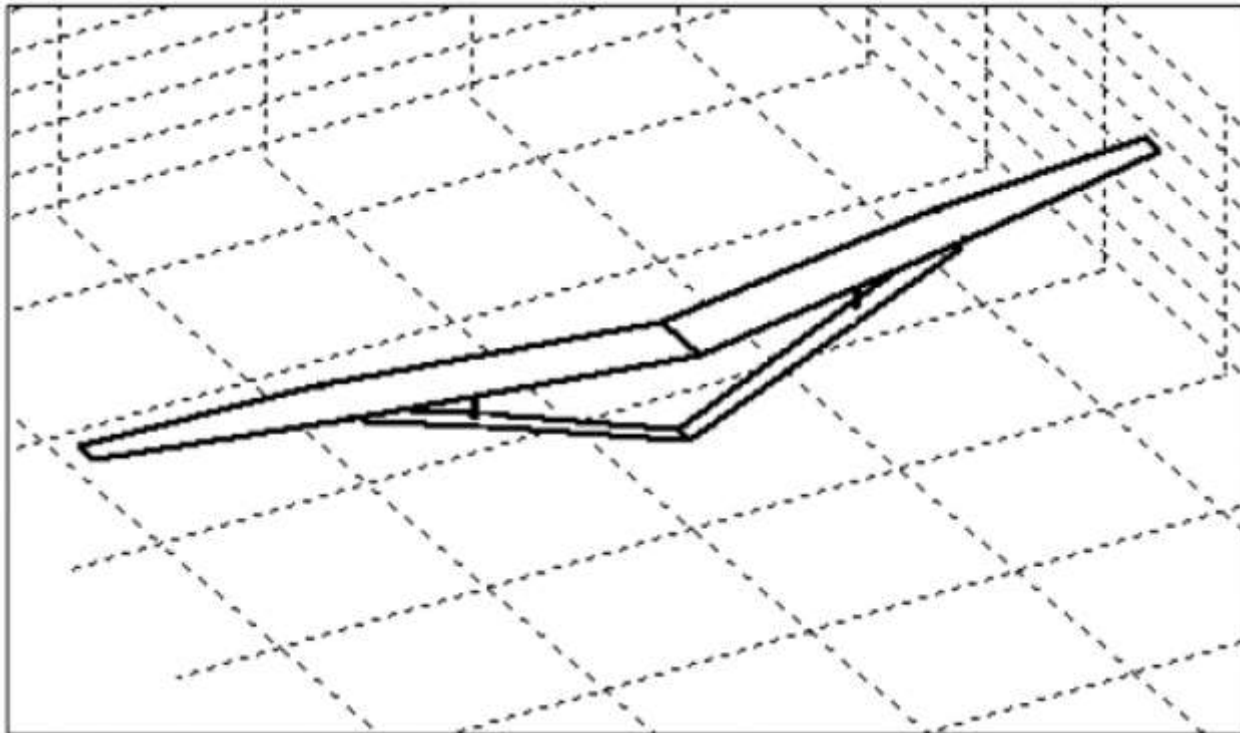


**Figure 65. Full Configuration with Strut and Jury**

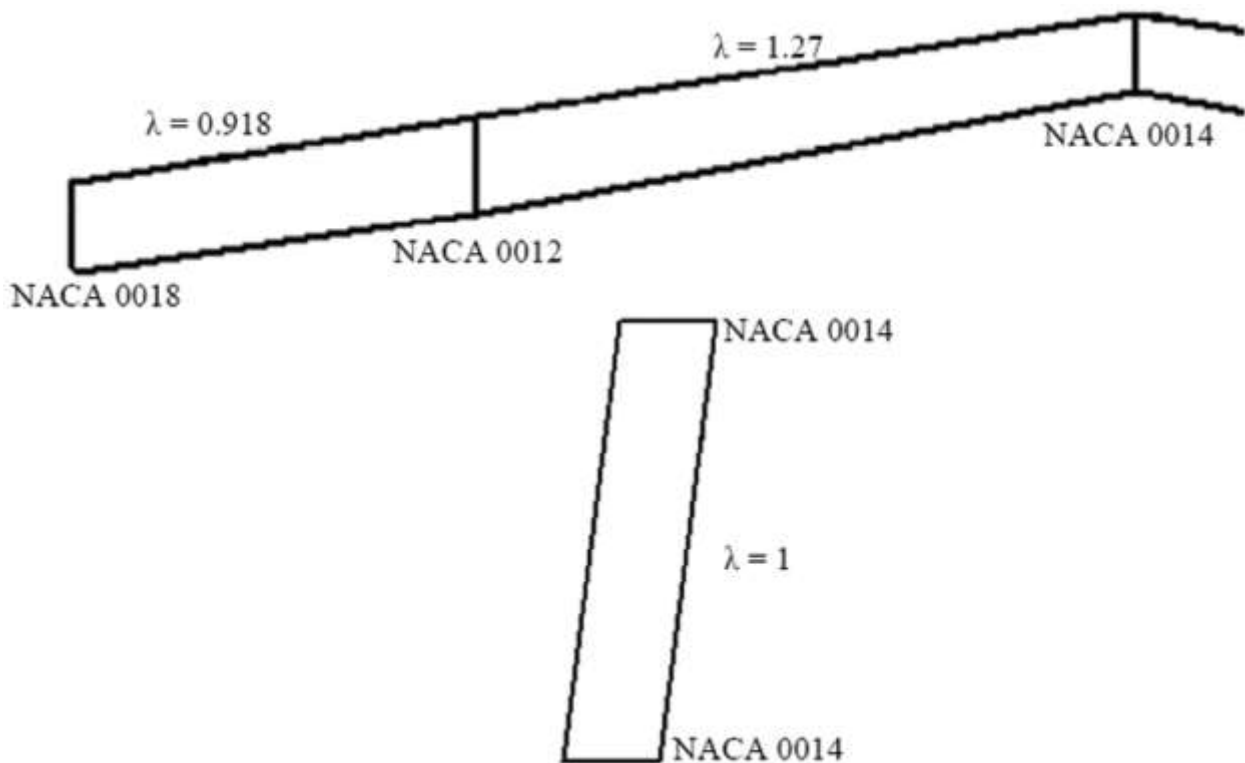


**Figure 66. Details of Strut (Top) and Jury (Bottom) Tornado Models (? = taper ratio)**

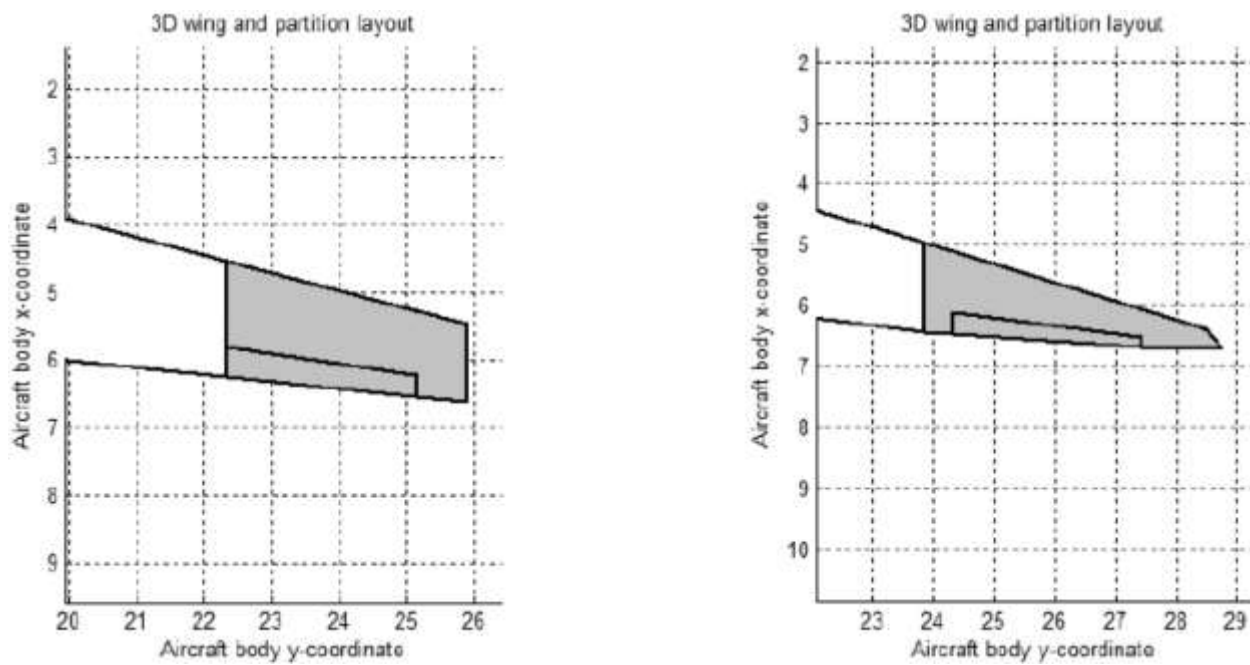


**Figure 67. Baseline SUGAR (Left) and Unswept (Right) VGRWT/NCE Tip Details, Dimensions in Meters, Tip Areas for Comparison are Shaded**

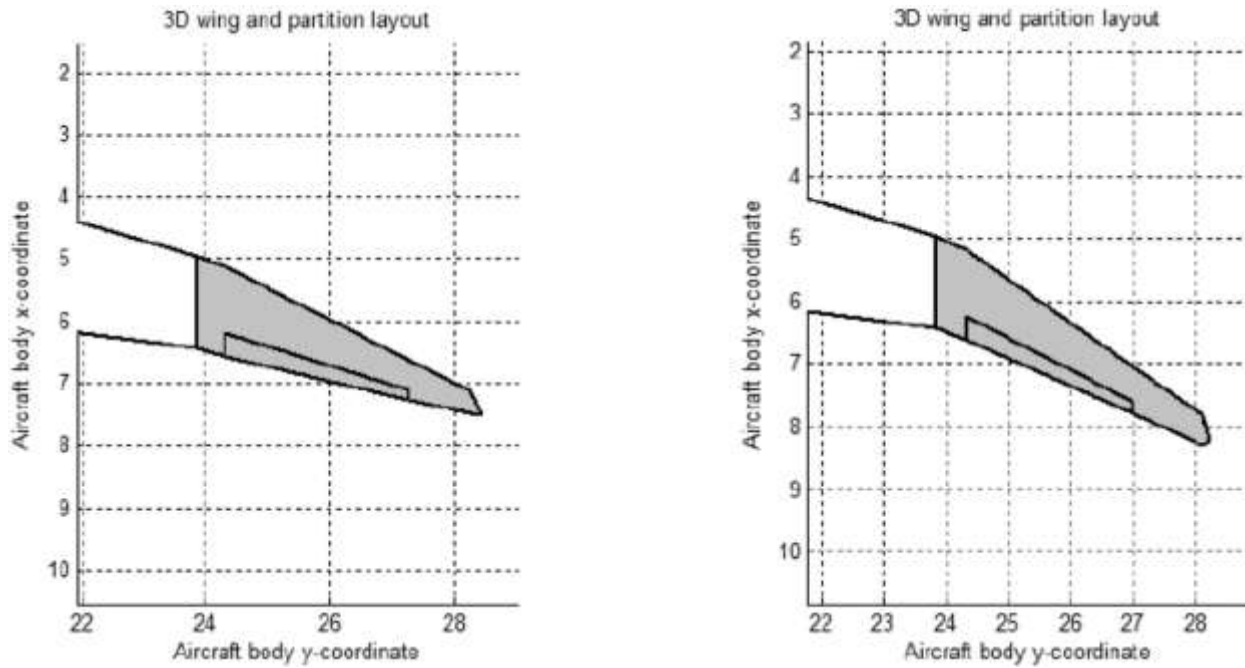


**Figure 68. Quarter-Sweep (Left) and Half-Sweep (Right) VGRWT/NCE Tip Details, Dimensions in Meters, Tip Areas for Comparison are Shaded**

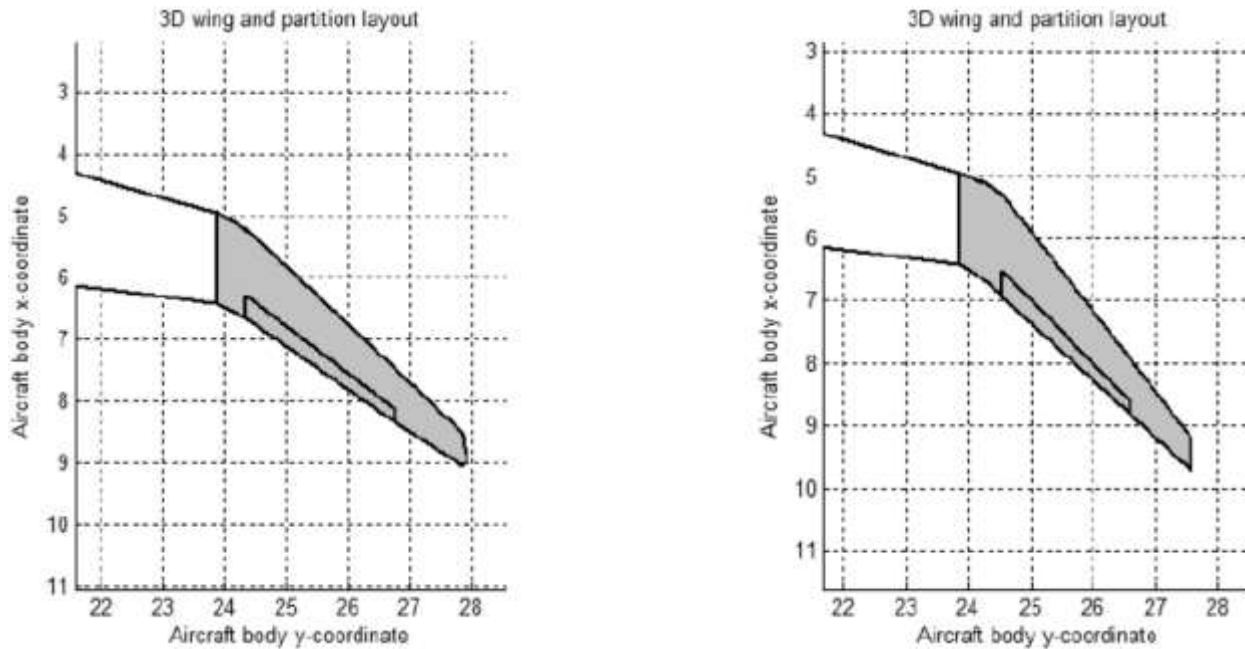


**Figure 69. Three-Quarter (Left) and Full-Sweep (Right) VGRWT/NCE Tip Details, Dimensions in Meters, Tip Areas for Comparison are Shaded**

## 7.3 RESULTS AND DISCUSSION

### 7.3.1 Clean Wing Results

The first stage of analysis centered on comparing the performance of the unmodified baseline SUGAR main wing with that of the SUGAR wing incorporating the VGRWT/NCE wingtip. The

full wing models described in Section 7.2.4.1 were used for this examination. The simulations were run at cruise conditions, Mach 0.7 and 44,000 ft altitude. Also, the design cruise lift coefficient of the baseline SUGAR wing is 0.7. Therefore, the incidence angle of the wing was adjusted for each case in order to maintain this value within a reasonable tolerance.

### 7.3.1.1 Tornado Results

The Tornado results for the clean wing (no strut or jury) configurations are summarized as Table 14. In order to maintain nearly the same CL for each configuration, the incidence angle only needed to decrease by approximately a quarter degree. For the same lift coefficient, the VGRWT/NCE configurations produce more total lift than the baseline SUGAR main wing. The difference for both the unswept and fully-swept case is approximately 2,800 lb. This is largely due to the increase in span and area that the wingtip provides. Furthermore, the unswept tip provides slightly more lift than the fully-swept configuration as intended, since the VGRWT/NCE will be unswept during take-off. The pitching moment coefficient also increases slightly after the VGRWT/NCE tip is added. This is expected as the increased area should increase the stability of the aircraft. No drag results were included in Table 4 due to the fact that Tornado is an inviscid code. A method for viscous drag estimation will be discussed in Section 7.3.1.4.

**Table 14. Tornado Results for Clean Wing Configurations**

Configuration	Baseline SUGAR Main Wing	SUGAR Wing with Unswept VGRWT/NCE Tip	SUGAR Wing with Fully-Swept VGRWT/NCE Tip
Incidence Angle ((deg))	2.95	2.7	2.75
Total Lift (lb)	114,950	117,800	117,775
Cl	0.702	0.702	0.703
$C_{M_{c=4}}$	-0.71	-0.75	-0.74

### 7.3.1.2 Fluent Results

In order to verify the results obtained by Tornado, CFD analysis was conducted using ANSYS Fluent. As described in Section 7.2.4.2, inviscid simulations were conducted and adaptive gridding was required to ensure converged results. After a run was completed and a lift coefficient had converged, the grid was adapted based on pressure gradients. Then, the simulation was run again, and the process was repeated until there was convergence between runs. Initial runs consisted of 1000 iterations, with subsequent runs consisting of 500 iterations. Figure 70 shows a plot of this process for the unswept VGRWT/NCE tip case. Plots were created for the baseline SUGAR and fully-swept cases but are not included due to redundancy. Figure 71 shows details of the grid at the wing root before and after the adaption occurred. Similar to Figure 70, this is also for the unswept case. Again, figures for the baseline SUGAR and fully swept tip cases are not included due to the similarity between all configurations.

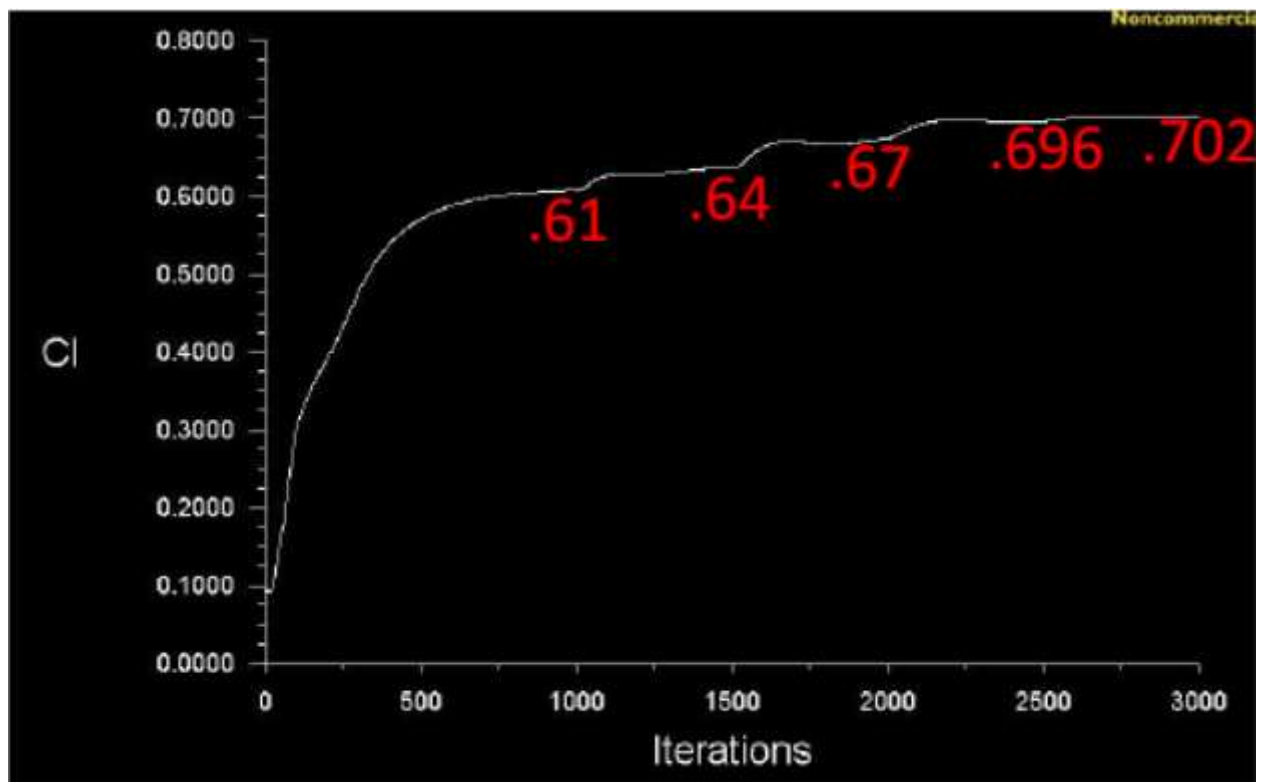
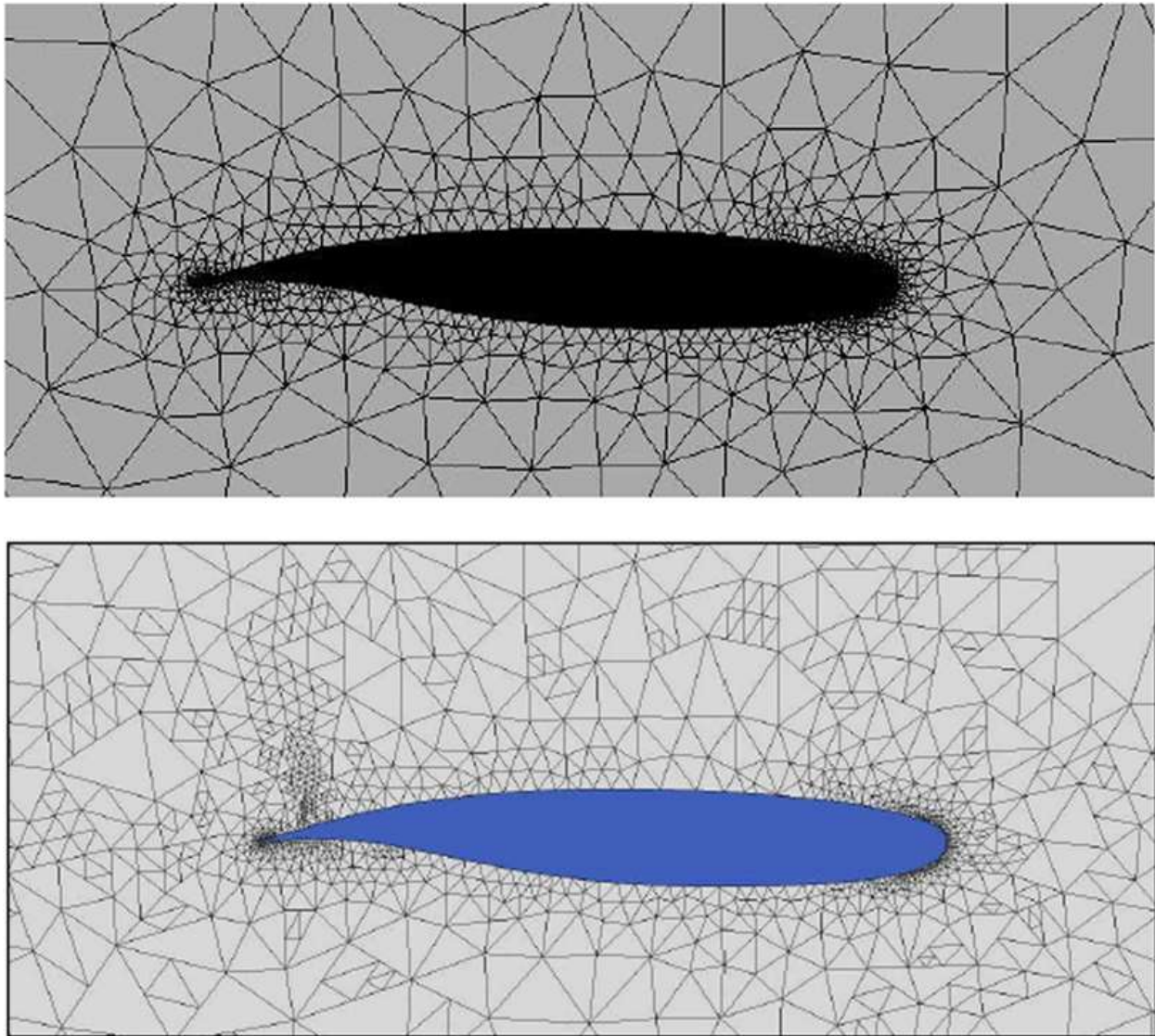


Figure 70. Adaptive Gridding Convergence for Unswept VGRWT/NCE Tip Case (CL in Red)



**Figure 71. Grids at the Wing Root for Unswept VGRWT/NCE Tip Case (Top – Original Grid; Bottom – Final Adapted Grid)**

Once the adaptive gridding was completed, suitable simulations were run, and final results are presented as Table 15. The VGRWT/NCE configurations again produce more lift than the unmodified SUGAR wing and also produce an increased moment coefficient. Figures 72 to 74 show pressure contour plots of the various configurations. A large region of low pressure is evident near the trailing edge, which suggests a region of supersonic flow over approximately 75% of the span. This is confirmed by velocity contours shown as Figure 75. The left picture shows a cut at the wing root, where a large supersonic region is evident, however at the 939 inch span station which corresponds to the main wing/VGRWT/NCE tip junction, there is no supersonic flow. This is consistent for all configurations and further facilitates the incorporation of the VGRWT/NCE tip, since locally supersonic flow will not be a concern. Finally, the streamlines over the wing are shown as Figure 76. The streamlines remain relatively straight over the entire span and suggest that the sweeping tip will not contribute large amounts of turbulent flow over the airfoil.

**Table 15. Fluent Results for Clean Wing Configurations**

Configuration	Baseline SUGAR Main Wing	SUGAR Wing with Unswept VGRWT/NCE Tip	SUGAR Wing with Fully-Swept VGRWT/NCE Tip
Incidence Angle (deg)	2.8	2.5	2.8
Total Lift (lb)	115,500	118,190	118,500
CL	0.700	0.702	0.704
$C_{M_{c=4}}$	-0.78	-0.795	-0.81

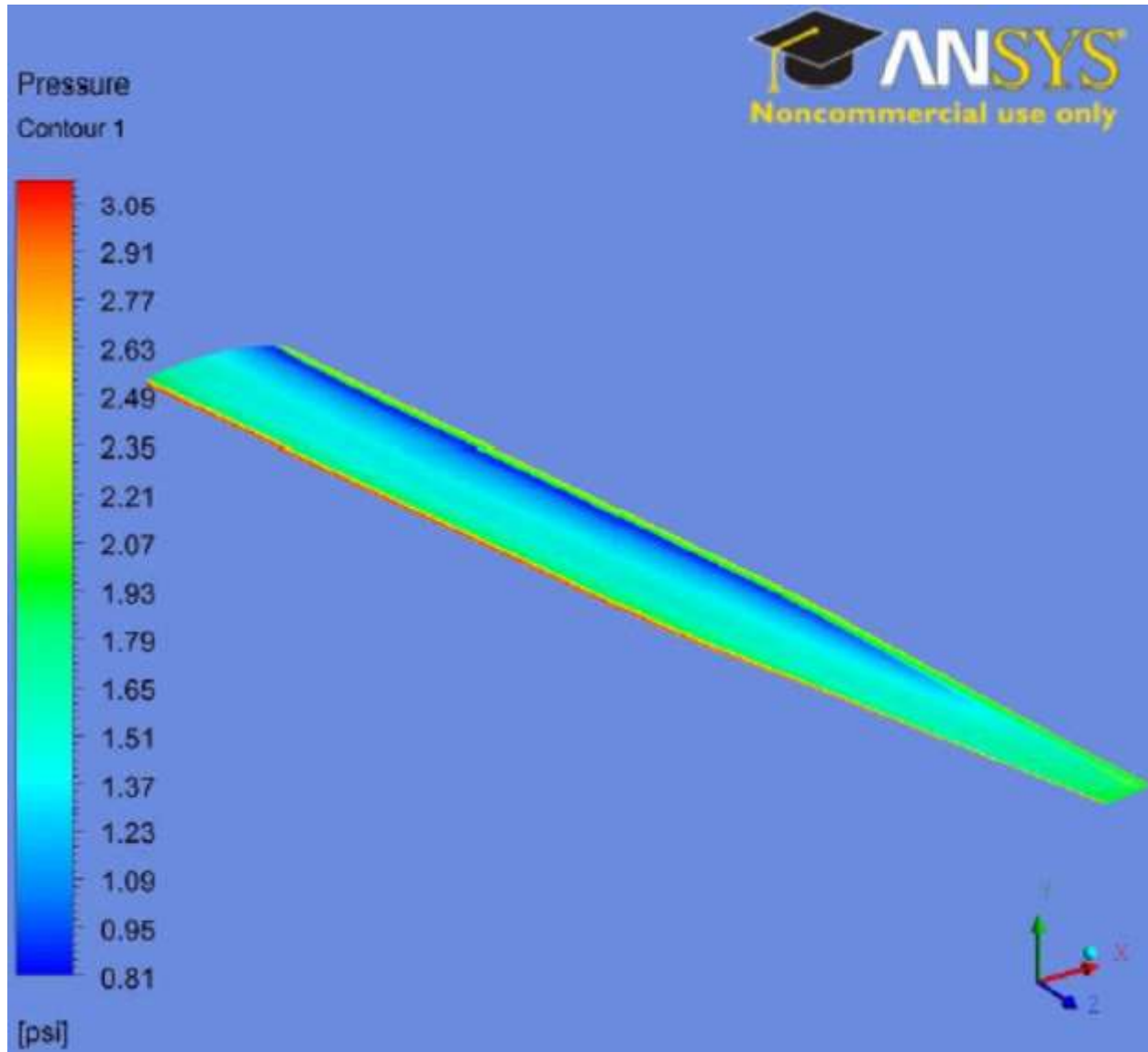


**Figure 72. Fluent Prediction of Top Surface Pressure Contours of Baseline SUGAR Main Wing**

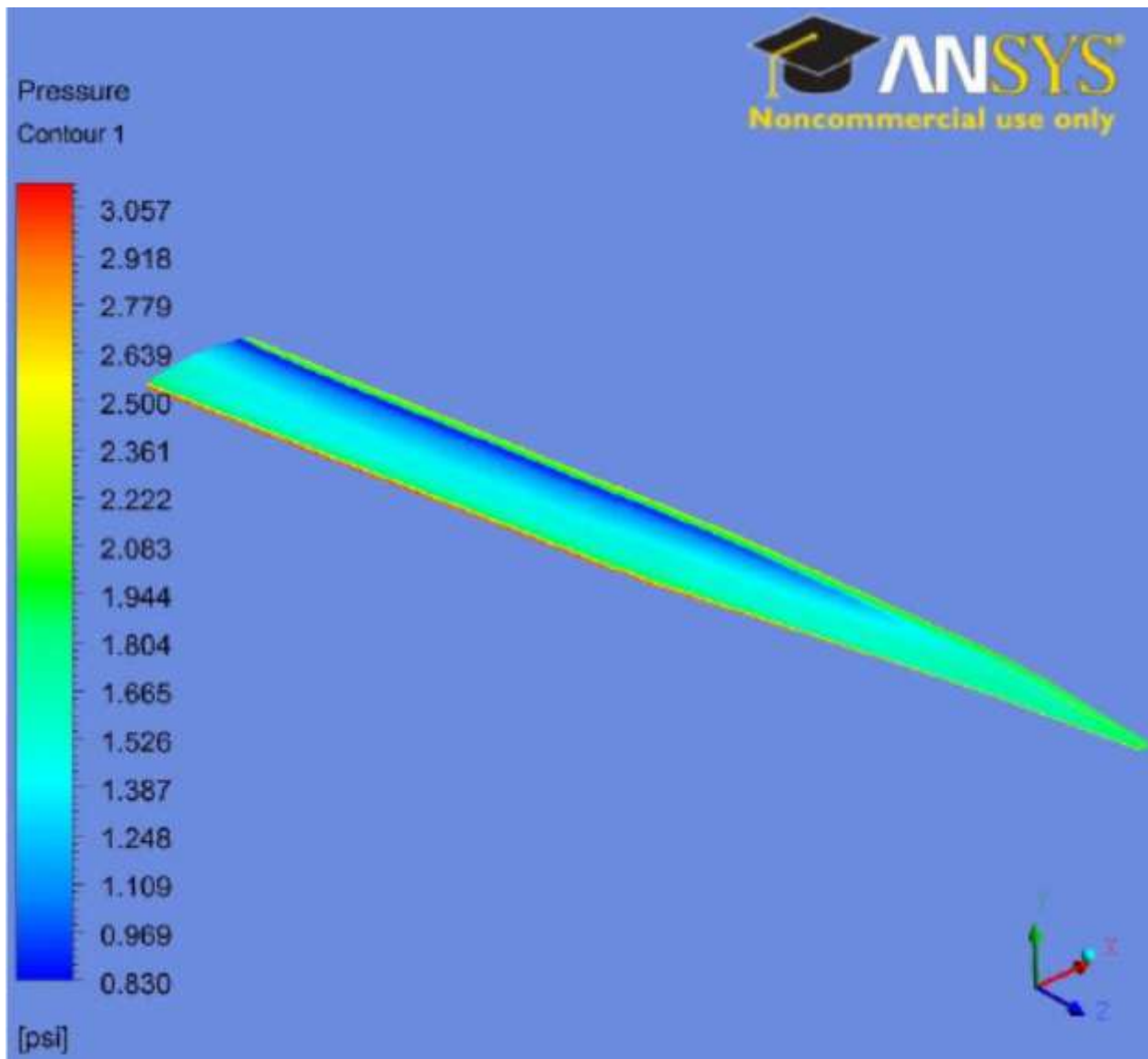


**Figure 73. Fluent Prediction of Top Surface Pressure Contours of SUGAR Wing with Unswept VGRWT/NCE Tip**

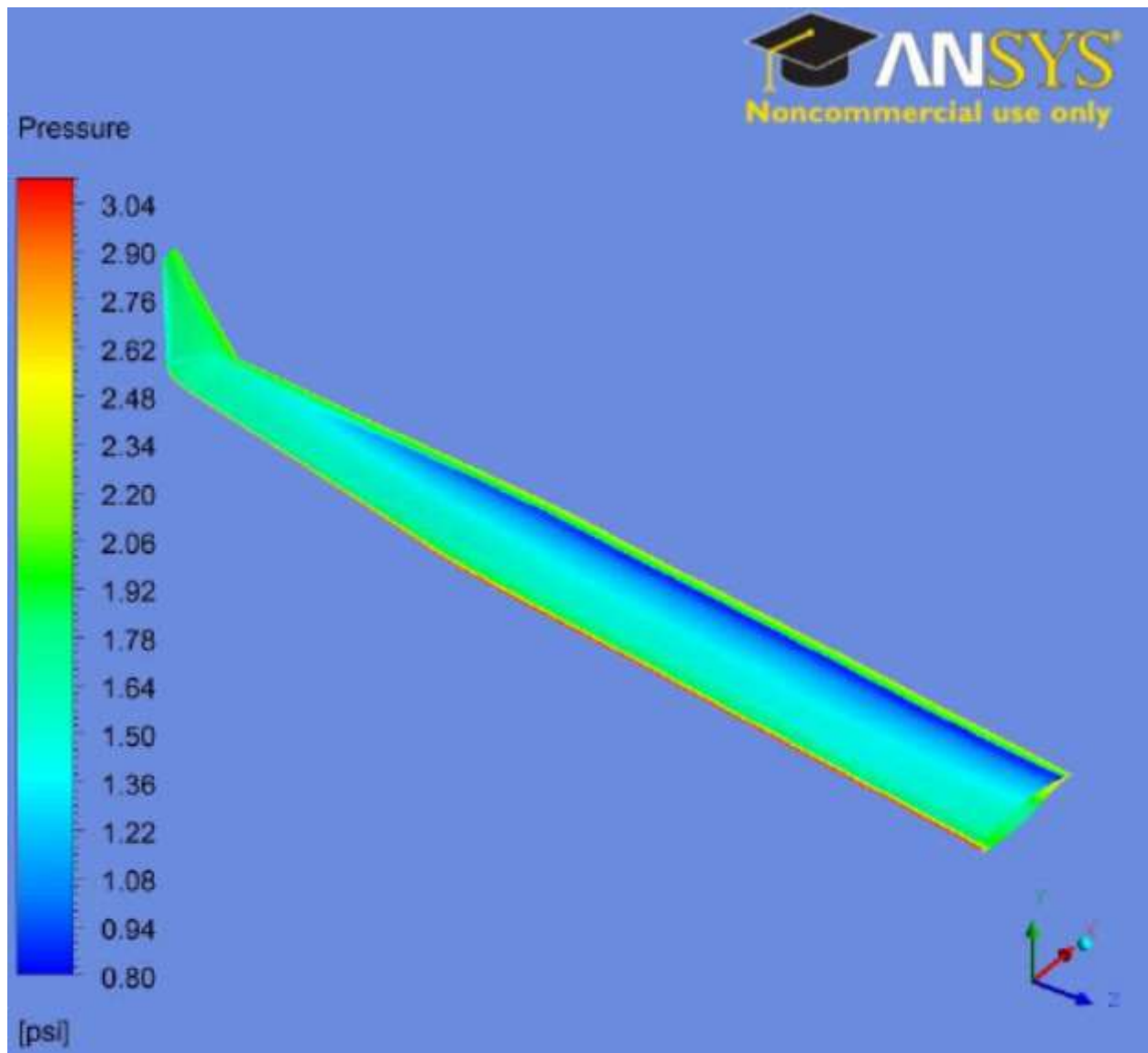
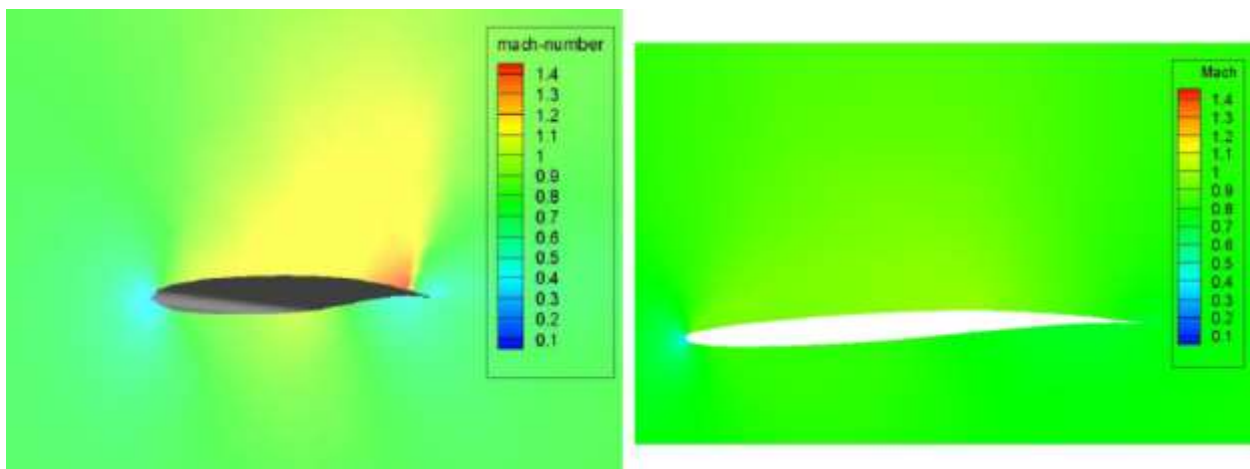
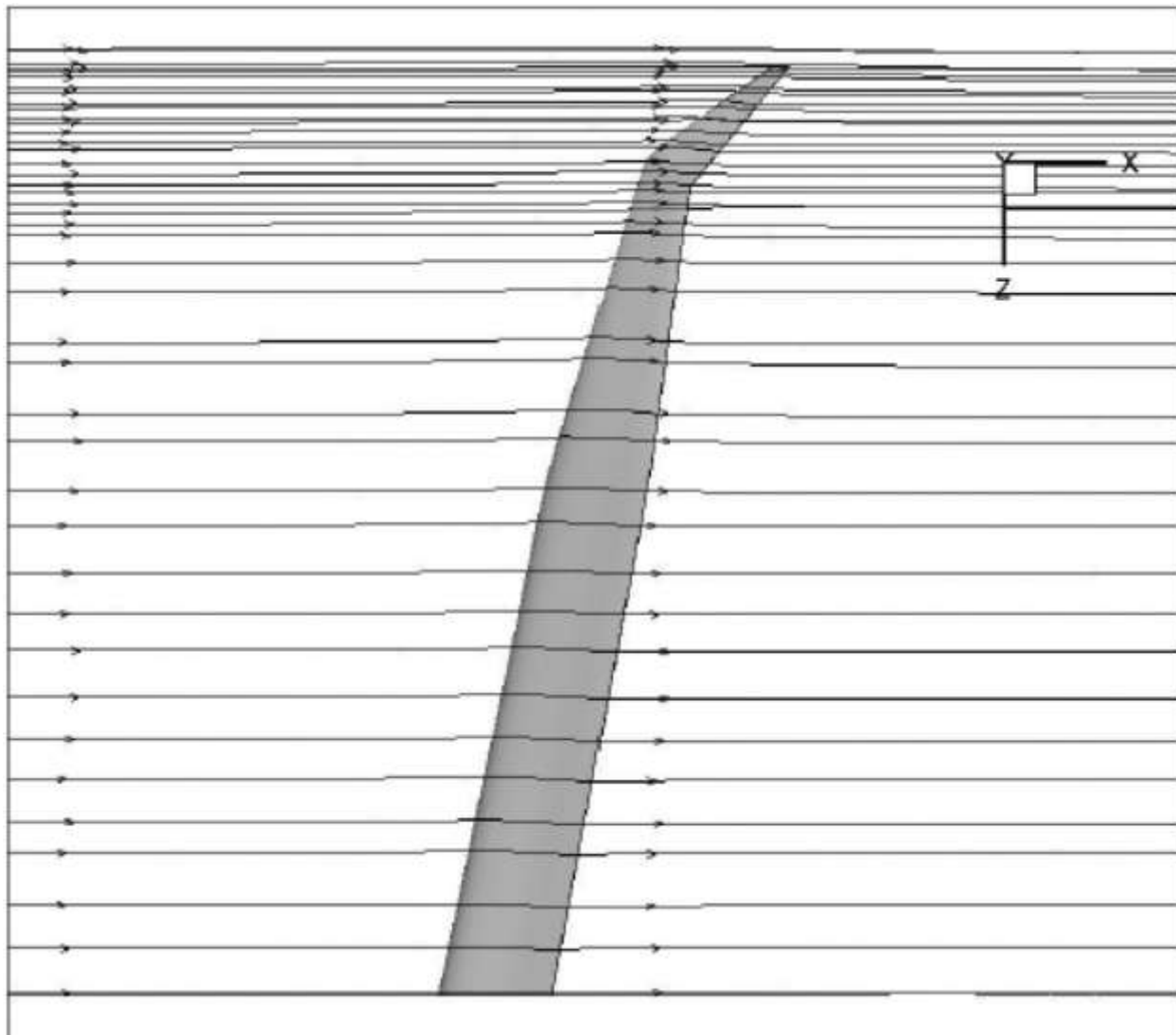


Figure 74. Fluent Prediction of Top Surface Pressure Contours of SUGAR Wing with Fully-Swept VGRWT/NCE Tip



**Figure 75. Fluent Prediction of Velocity Profile at Wing Root (Left) and Main Wing/VGRWT Junction (Right)**



**Figure 76. Fluent Prediction of Streamlines over SUGAR Wing with Fully-Swept VGRWT/NCE Tip**

### 7.3.1.3 Comparison of Results

Table 16 summarizes the data obtained by both the VLM (Tornado) and CFD (Fluent) methods of analysis. The results generally agree across all areas of comparison. Since the lift coefficient was forced to be close to 0.7, the lift forces generated by each method should be comparable. Indeed, both Fluent and Tornado show that the VGRWT/NCE configurations produce approximately 2,800 lb of additional lift compared to the unmodified configuration. Also, the Fluent results show approximately 500 lb of additional lift over the Tornado results for all cases. Fluent shows a more consistent incidence angle across configurations, but the difference between methods is approximately one-tenth of a degree, which again shows excellent agreement. Finally, the Fluent results give an approximate 9% higher pitching moment coefficient for each configuration. Since CFD calculations of moment coefficients are generally regarded as more accurate than those of VLM methods, this small difference is seen as a positive result and gives confidence in Tornado's moment predictions moving forward. With corroborating CFD results, it has been shown that VLM predictions are very useful in early design analysis and are capable of giving acceptably accurate results. One could use CFD results like these obtained here to develop a correction to the VLM results, but that was not deemed worthwhile. With this in mind, the analysis of the forces and moments produced solely by the wingtips was conducted with Tornado alone.

**Table 16. Comparison of Tornado and Fluent Results for Clean Wing Cases**

Configuration	Fluent	Tornado	Fluent	Tornado	Fluent	Tornado
	Baseline SUGAR Wing	Baseline SUGAR Wing	SUGAR Wing with Unswept VGRWT/NC E Tip	SUGAR Wing with Unswept VGRWT/NC E Tip	SUGAR Wing with Fully-Swept VGRWT/NC E Tip	SUGAR Wing with Fully-Swept VGRWT/NC E Tip
Incidence Angle (deg)	2.8	2.95	2.8	2.7	2.8	2.75
Total Lift (lb)	115,500	114,950	118,190	117,800	118,500	117,775
CL	0.700	0.702	0.702	0.702	0.704	0.703
$C_{M_{c-4}}$	-0.78	-0.71	-0.795	-0.75	-0.81	-0.74

### 7.3.1.4 Viscous Drag Estimation

In order to determine the effect that the VGRWT/NCE has on the baseline SUGAR planform, a viscous drag estimation was conducted. Equation 11 shows the drag coefficient in the usual way:

$$C_D = C_{D0} + \frac{C_L^2}{\pi A Re} \quad (11)$$

The Oswald efficiency factor,  $e$ , is given by Equation 12, and incorporates a high aspect ratio correction.

$$e = \frac{1}{\pi AR k + \frac{1}{us}} \quad (12)$$

The viscous drag due to lift factor,  $k$ , is a function of wing sweep and  $C_{D0}$ , and the induced drag due to the fuselage,  $s$ , is a function of span and fuselage diameter. Finally, the planform efficiency factor,  $u$ , is assumed to be 0.99 [34]. The zero-lift drag,  $C_{D0}$ , was computed by Tornado

which employs conventional low-order methods. Using this method, the total drag coefficient was determined for each configuration and is shown as Table 17. The VGRWT/NCE configurations show a reduced drag compared to the baseline SUGAR planform. This is largely due to the increased aspect ratio brought on by the addition of the VGRWT/NCE tip. Also, the highest lift to drag ratio is achieved by the unswept tip configuration, a feature which will be beneficial during take-off and landing. Finally, the zero lift-drag computed by Tornado is nearly identical across models due to the fact that approximately 90% of the planform is shared between configurations.

**Table 17. Viscous Drag Estimation for Each Configuration**

Configuration	Baseline SUGAR Wing	SUGAR Wing with Unswept VGRWT/NCE Tip	SUGAR Wing with Fully-Swept VGRWT/NCE Tip
$C_{D0}$	0.00889	0.00889	0.00882
Oswald Efficiency Factor	0.81	0.79	0.80
$C_D$	0.0187	0.0173	0.0178
L/D	37.4	40.4	39.2

### 7.3.2 Force and Moment Results on the Various Wingtips

The second stage of analysis focused on calculating the forces and moments generated by the respective wingtips themselves. In order to obtain a full understanding of the influence of the tips on the wing system, the strut and jury was added as described in Section 7.2.5. All tests were run at Mach 0.7, 44,000 ft. altitude, and the incidence angle was varied in order to maintain a lift coefficient of 0.7 within reasonable tolerances.

#### 7.3.2.1 Wingtip Results for All Configurations

Tornado calculates force data on each panel during every simulation. This data was extracted for panels existing on the wingtip and reduced to an equivalent point force on the wingtip. The force data presented is a resultant force of the lift, drag and side force. However, the drag and side force are consistently an order of magnitude less than the lift force. Therefore, the resultant force is overwhelming comprised of lift. The moment generated by each tip was calculated by multiplying this resultant force with its distance to the elastic axis of the main wing. The elastic axis was taken to be constant at 40% chord of the main wing, and it was assumed to be unaffected by the orientation of the VGRWT/NCE tip. Finally, the aileron was rotated through  $\pm 20^\circ$  to determine its effect on the moment. Figures 77, 78 and 79 show the location of the resultant force for each tip, along with the elastic axis. The location of the resultant point force did not vary appreciably with aileron deflection, therefore the locations, indicated as a red dot, are presented for the undeflected case. As in Section 7.2.5, the shaded grey area is the area considered for tip calculations. Figure 80 shows the force generated by each tip as a function of aileron deflection. Similarly, Figure 81 shows the moment generated as a function of aileron deflection.

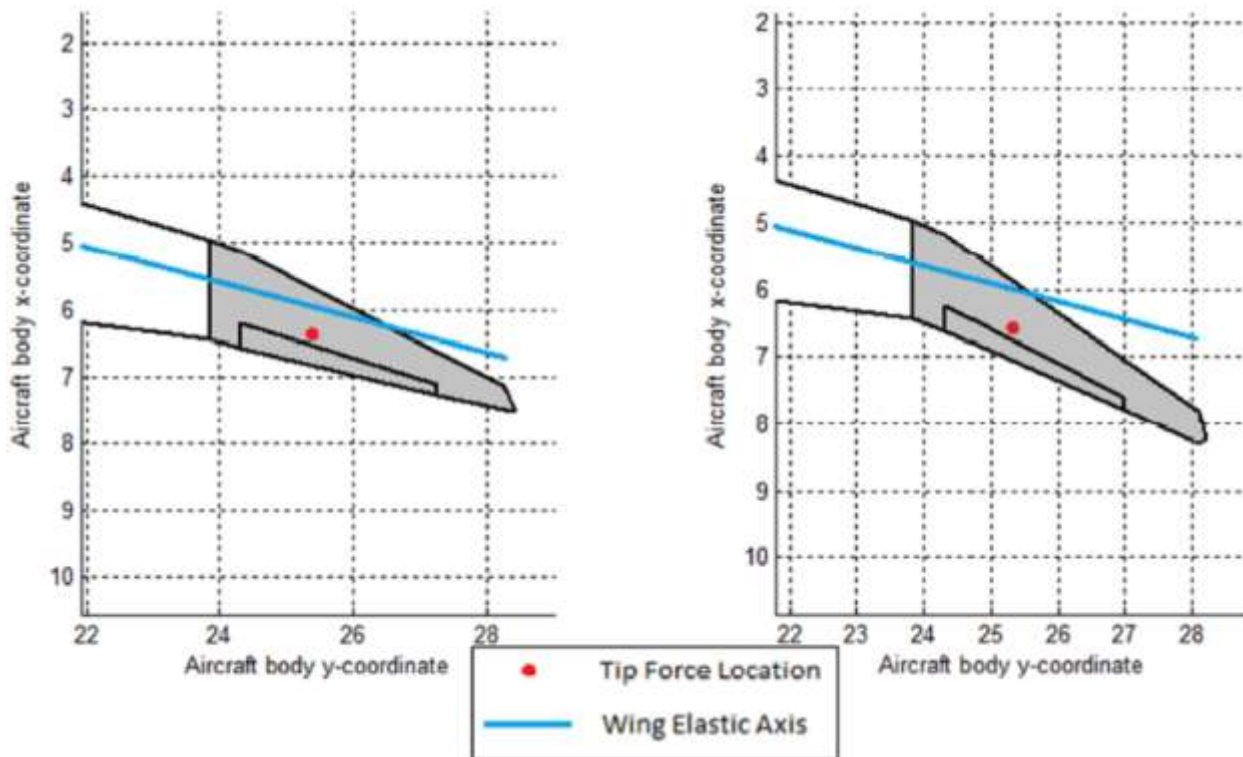


**Figure 77. Baseline SUGAR Tip (Left) and Unswept VGRWT/NCE Tip (Right) Force Location (Dimensions in Meters)**

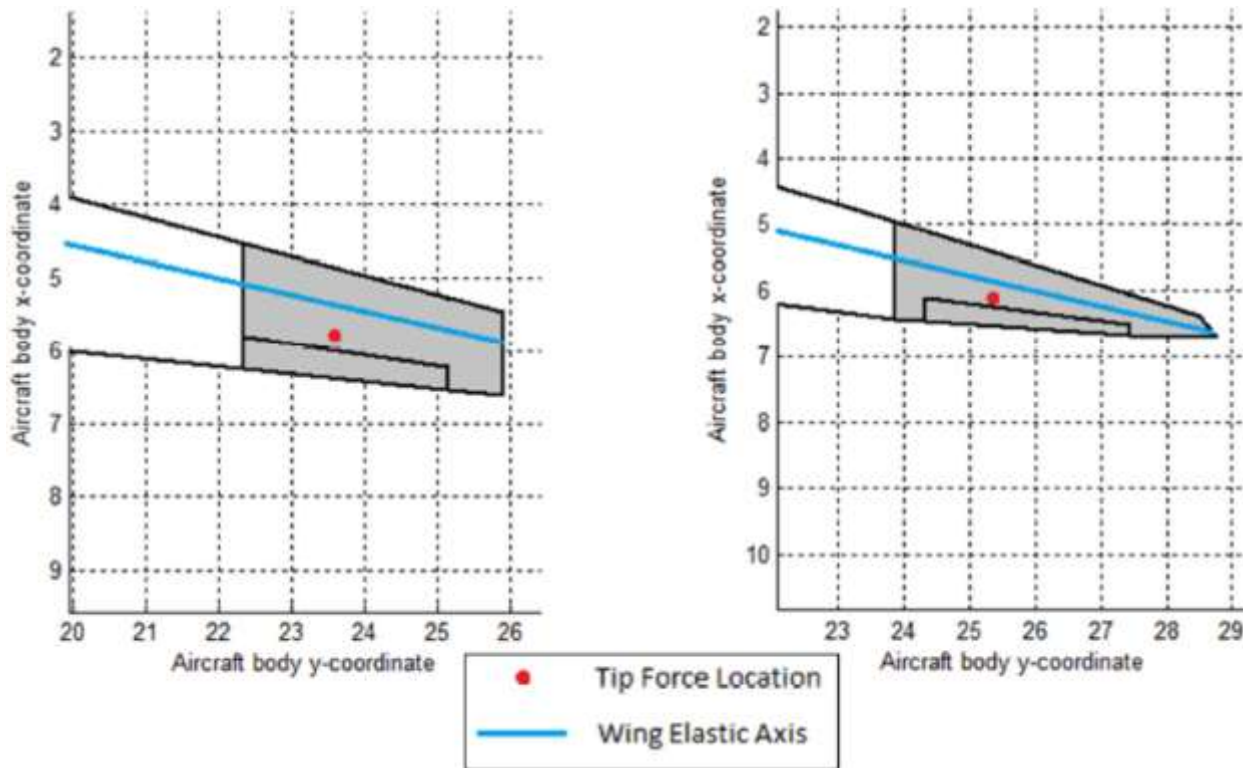


**Figure 78. Quarter-Sweep VGRWT/NCE Tip (Left) and Half-Sweep VGRWT/NCE Tip (Right) Force Location (Dimensions in Meters)**

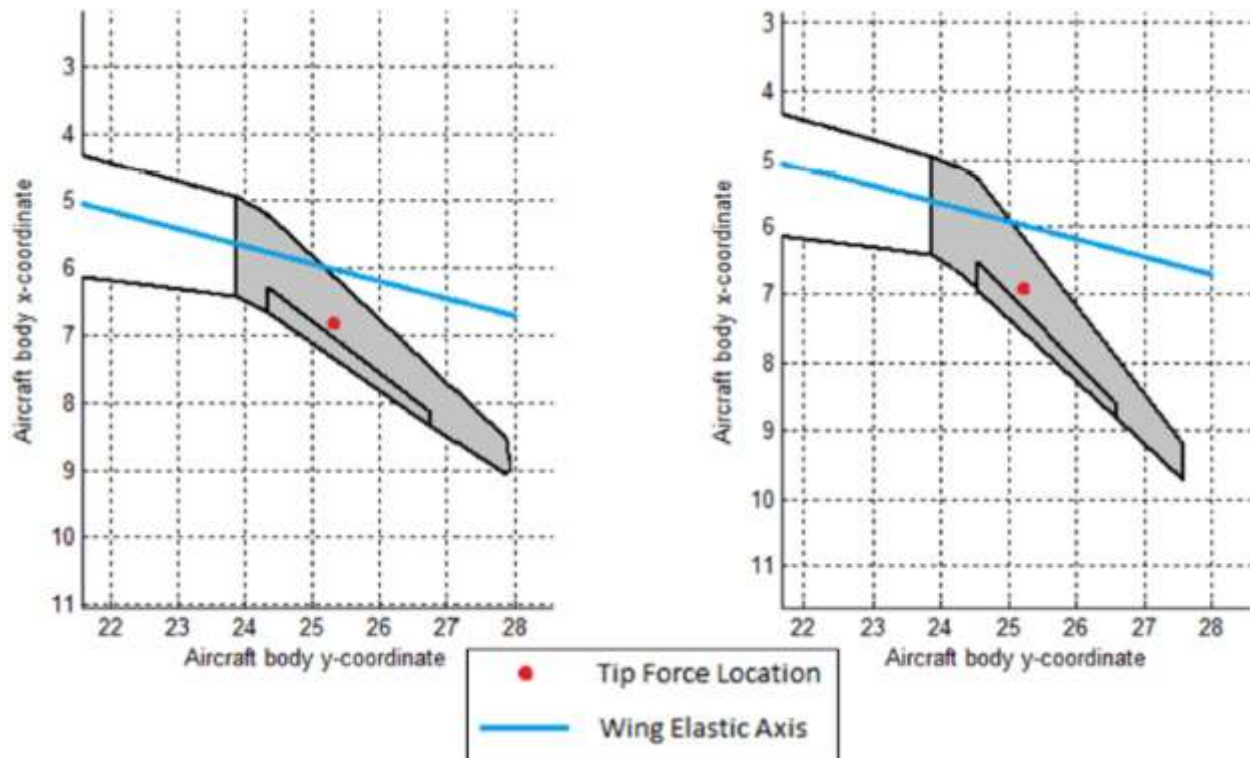


**Figure 79. Three-Quarter Sweep VGRWT/NCE Tip (Left) and Full-Sweep VGRWT/NCE Tip (Right) Force Location (Dimensions in Meters)**

## Wingtip Resultant Force vs Aileron Deflection

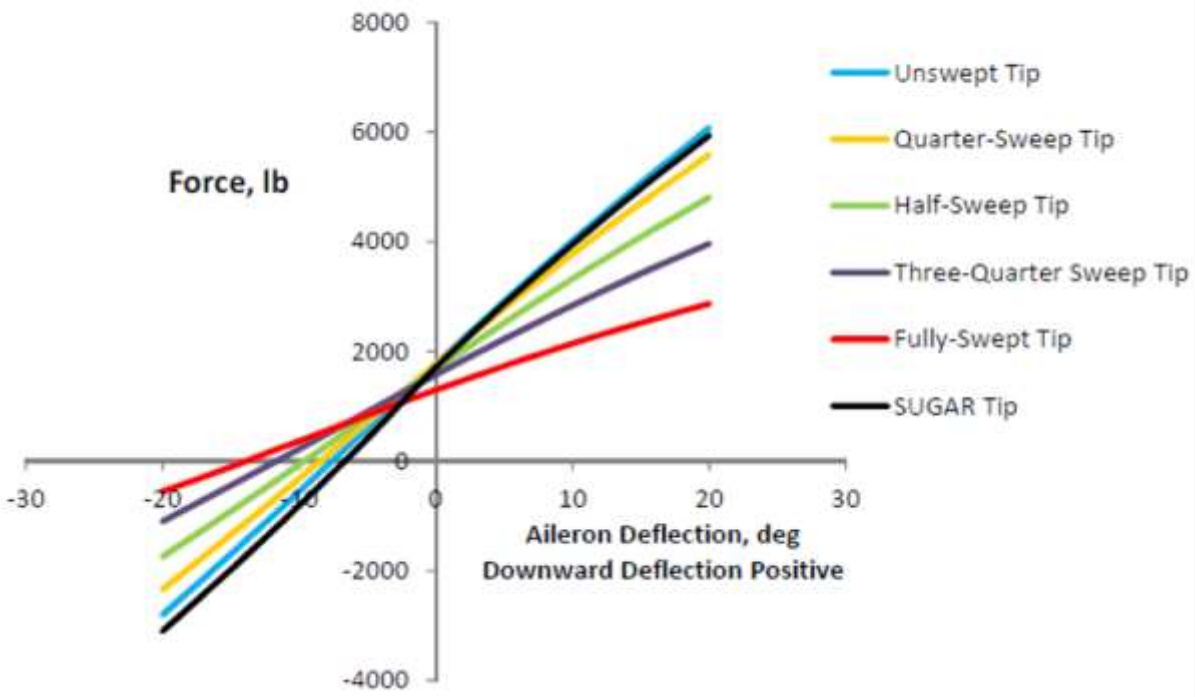
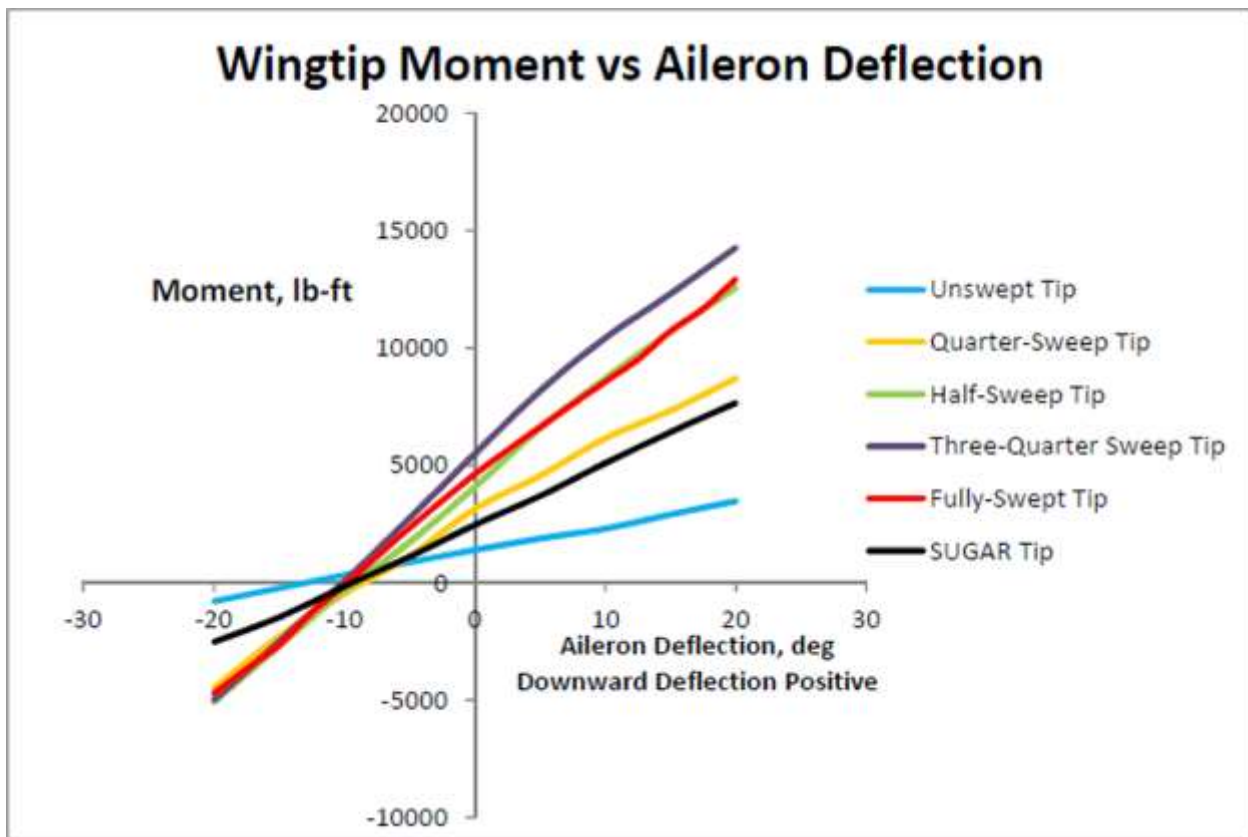


Figure 80. Wingtip Resultant Force as a Function of Sweep and Aileron Deflection



**Figure 81. Wingtip Moment as a Function of Sweep and Aileron Deflection**

From Figure 80, it can be seen that the performance of the unswept tip closely mirrors that of the SUGAR tip. This was the intention of the unswept tip design and successfully validates the modeling procedure outlined in Section 7.2.3. Also, the force generated by each wingtip decreases as the sweep angle increases. This was expected since highly-swept wings generate less lift than slightly-swept wings. While the difference in force produced between the unswept and swept tip cases is quite large at the extremes of aileron deflection, they are quite small at the neutral aileron position. The difference in the force generated for an undeflected aileron is approximately 450lb. per tip, which is a small variation considering each half of the wing produces nearly 60,000lb. of lift. Finally, the resultant forces generated for each VGRWT/NCE tip behave in a linear manner with respect to aileron deflection. This is to be expected, since the absolute value of the force produced by the aileron will be approximately equal for both positive and negative deflections.

The behavior of the moments with respect to aileron deflection, given as Figure 81, shows that the swept tip cases produce larger moments than the unswept tip case. The quarter-sweep configuration produces moments that are most comparable to the baseline SUGAR tip, with the unswept tip case producing substantially less moment. This is due to the close proximity of the force location to the elastic axis for the unswept tip case, as shown by Figure 77. An interesting result is that the three-quarter sweep tip case produces the largest moment. While the moment arm is indeed less than the fully-swept tip case, as shown in Figure 79, the force produced by the three-quarter sweep tip configuration is much larger than that of the fully-swept tip case, as evidenced by Figure 80. Therefore, this larger force overwhelms the small difference in moment arm and produces a larger tip moment overall. We also see that the half-sweep and fully-swept tip cases produce nearly

identical moment trends. As with the three-quarter sweep case, this is due to the balance achieved by having a larger moment arm for the fully-swept tip case, but with a smaller force, compared to that of the half-swept tip case, which has a larger force, but a smaller moment arm. Finally, all of the moments produced by the neutral aileron position are positive. With the convention that positive moments are clockwise, this means that the tip will be attempting to pitch down, which is the desired result to resist divergence as well as having the entire aircraft return to a neutral position should it suddenly pitch up as a result of wind turbulence, for example.

### 7.3.2.2 Wingtip Performance Deltas

To measure the performance of each sweep configuration with respect to the baseline SUGAR tip, a simple "delta" analysis was conducted. The deltas for each configuration are found according to the following equations, where  $q$  is the dynamic pressure and  $A$  is the planform area of the respective wingtip sections:

$$\Delta C_{Force} = \frac{F_{Sweep} - F_{Sugar}}{qA} \quad (13)$$

$$\Delta C_{Moment} = \frac{M_{Sweep} - M_{Sugar}}{qA} \quad (14)$$

The graphical results of this analysis are presented as Figure 82 and Figure 83, respectively. The trends of these plots are broadly similar to Figure 80 and Figure 81 presented above. Regarding the force delta plot, Figure 82, we can clearly see that the unswept tip provides very comparable performance to the baseline SUGAR tip, with a maximum delta coefficient of 0.048. The deltas for each configuration increase as the sweep angle increases, with the fully-swept tip providing the largest difference in force. For this configuration, the maximum delta coefficient occurs with the maximum aileron deflection angle and is approximately -0.49.

The moment delta plot, Figure 83, also shows similar behavior to Figure 80. We again see that the most comparable configuration to the baseline SUGAR tip is the quarter-sweep VGRWT/NCE tip case, for reasons outlined above. We also see that the maximum moment delta coefficient, approximately 1.05, is given by the three-quarter sweep VGRWT/NCE tip configuration, occurring again at maximum aileron deflection.

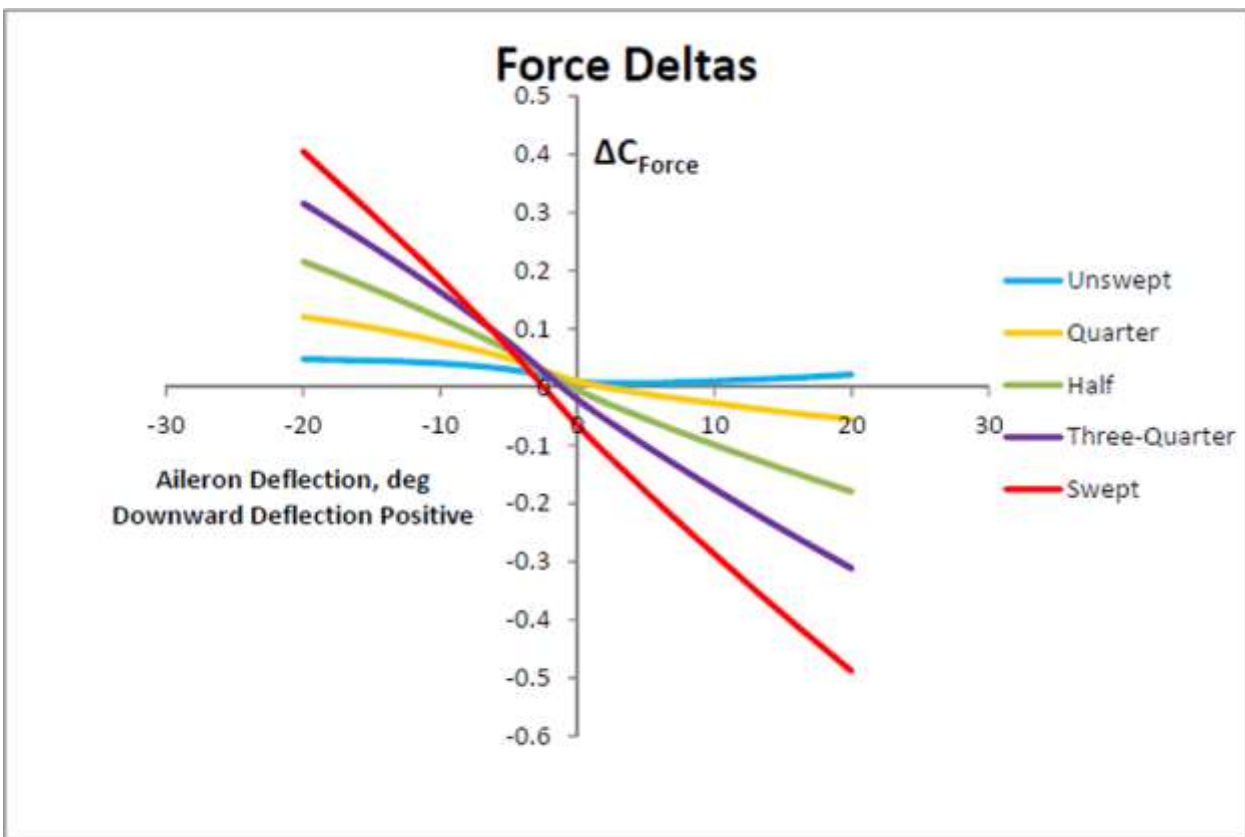
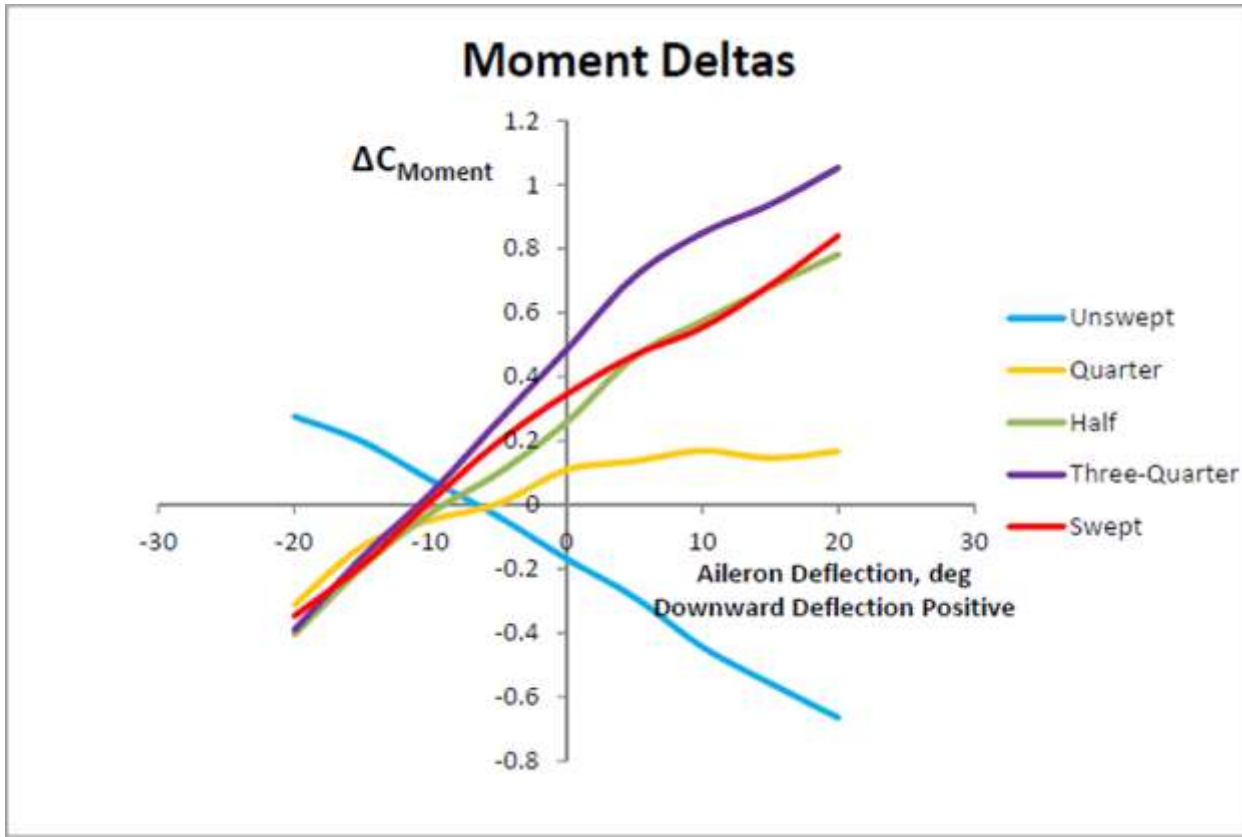


Figure 82. Wingtip Force Coefficient Deltas for VGRWT/NCE Tip as a Function of Sweep and Aileron Deflection



**Figure 83. Wingtip Moment Coefficient Deltas for VGRWT/NCE Tip as a Function of Sweep and Aileron Deflection**

### 7.3.2.3 Wingtip Viscous Drag Estimation

A viscous drag estimation study was conducted on the wingtips alone similar to the procedure described in Section 7.3.1.4. Equation 11 was again used to find the viscous drag coefficient, and the zero-lift drag was calculated by Tornado. However, since the aspect ratio of the wingtips is low compared to the total wing, the Oswald efficiency factor was calculated according to the methods outlined in Raymer [35]. For wing sweep below 30°,  $e$  is given by:

$$e = 1.78(1 - 0.045 * AR^{0.68}) - 0.64 \quad (15)$$

For wing sweeps larger than 30°, it is given as:

$$e = 4.61(1 - 0.045 * AR^{0.68})(\cos \Lambda_{LE})^{0.15} - 3.1 \quad (16)$$

Using these methods, the viscous drag was calculated for the SUGAR, unswept and fully-swept VGRWT/NCE tip configurations. The intermediate sweeps were not analyzed due to the small amount of time that will be spent in those transitional positions in flight. The results are presented in Table 18, and they show that the unswept VGRWT/NCE tip produces the lowest drag. Even though the tip area is the same, the unswept VGRWT/NCE tip has a larger span, which leads to a higher aspect ratio. This higher aspect ratio is largely the reason that the unswept tip produces the lowest drag, and consequently the highest L/D. As before, this would be helpful during take-off and landing, since lift is at a premium in those situations. The swept VGRWT/NCE tip also

has a lower drag coefficient than the baseline SUGAR tip, suggesting it will be more efficient at cruise conditions than the baseline SUGAR tip. Finally, the viscous drag force calculated from these results was of the same order of magnitude as predicted by the Tornado inviscid drag calculations. Therefore, the resultant forces presented in Section 7.3.2.1 were not amended to reflect the viscous correction, since the effect on the resultant force would be small.

**Table 18. Viscous Drag Estimation on Various Wingtip Configurations Configuration Baseline SUGAR Tip**

Configuration	Baseline SUGAR Tip	Unswept VGRWT/NCE Tip	Fully-Swept VGRWT/NCE Tip
$C_{D0}$	0.000549	0.000493	0.000426
Oswald Efficiency	0.99	0.86	0.74
$C_D$	0.0086	0.0063	0.0082
LD	29.0	47.2	31.8

### 7.3.3 Drag Estimation of Flow over Wing/VGRWT/NCE Tip Joint

As briefly mentioned in Section 7.2, the practical design of the VGRWT/NCE tip necessarily incorporates a small step between the main wing and the tip. As discussed in Section 7.2.3, portions of the tip must tuck into the main wing depending on the current orientation of the VGRWT/NCE tip. Therefore, the VGRWT/NCE tip is slightly thinner than the main wing, and drag issues due to the step must be addressed.

Figure 84 shows streamlines over the fully-swept VGRWT/NCE, with the approximate location of the step drawn in red. This shows that the streamlines over the step are generally straight. Considering the idealized case of an infinite swept wing, the components of the freestream can be decoupled according to Prandtl's independence principle. From this analysis, the normal component of flow is most important with regards to flow separation [36]. With the joint between the wing and VGRWT/NCE tip being nearly normal to the leading edge, taken to be  $16^\circ$  for this analysis, the normal component of the freestream flow over the step is  $M = 0.18$ . This is a low-speed flow, and compressibility effects would be negligible. Therefore, the results presented in Hoerner's classic drag reference, Fluid Dynamic Drag [37], are applicable to this case.

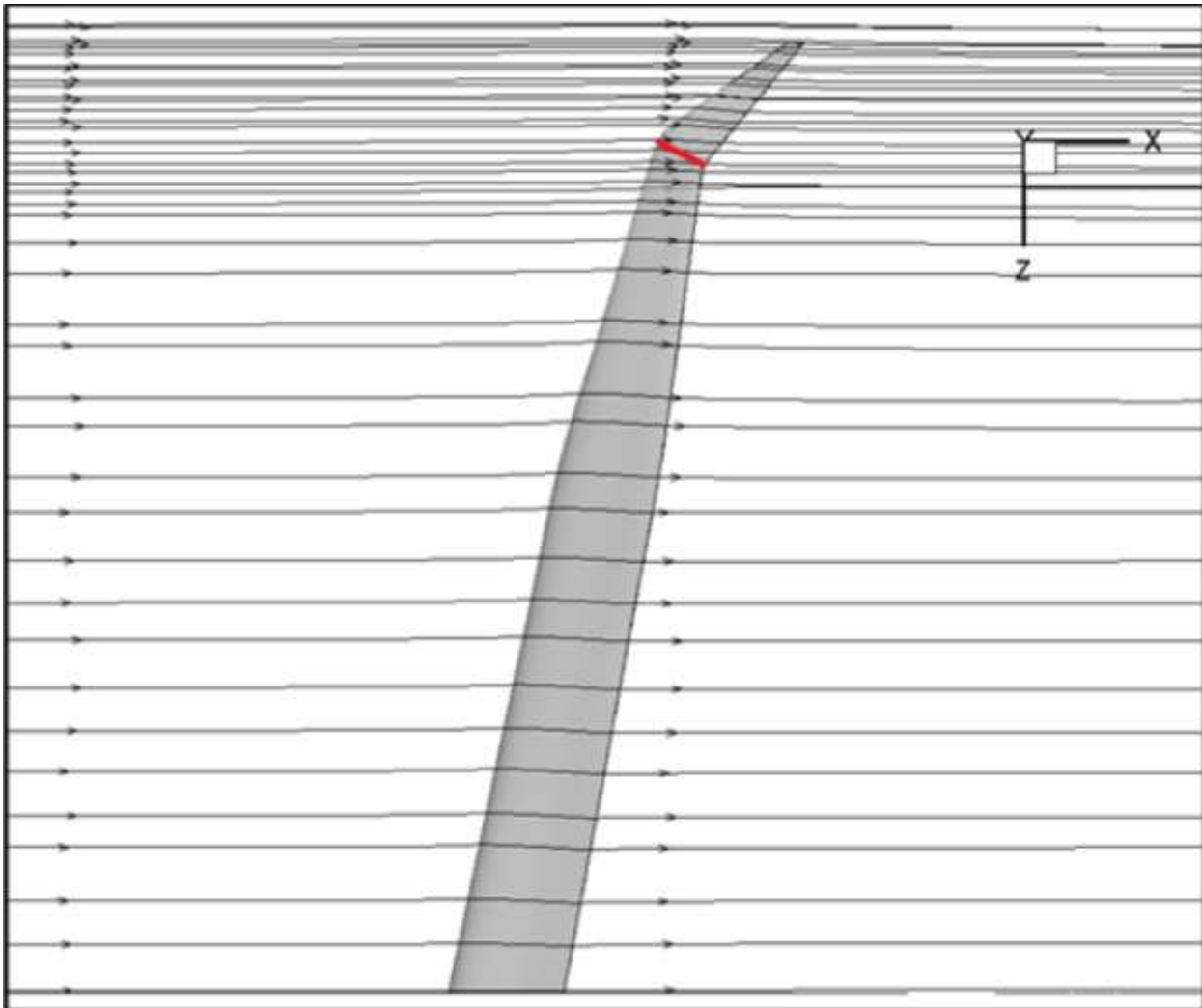


**Figure 84. Fluent Prediction of Streamlines over Step for Fully-Swept VGRWT/NCE Tip (Step Drawn in Red)**

Hoerner indicated that the drag coefficient over a surface imperfection can be given by:

$$C_D = 4 * C_D * \sqrt[3]{\frac{h}{x}} \quad (17)$$

In this instance,  $x$  is the distance from the leading edge to the imperfection,  $h$  is the height of the imperfection, and  $C_D$  is referred to as an independent coefficient that varies with the shape of the imperfection. For this study, the independent coefficient was taken to be  $C_D = 0.16$ , which corresponds to a rounded step [Ref. 37, Ch. 5, Fig. 10]. The height of the step was taken to be comparable to standard skin thickness, in this case between one and three tenths of an inch. Finally, the distance to the joint was taken to be mid-chord, approximately 30in. These results are presented assuming the joint is in crosswise flow. However, with the joint nearly normal to the wing leading edge, this is not true for the current case. Hoerner also presents a method to transition between crosswise and longitudinal flow with respect to a step, given by Equation 18:

$$C_D = \sin^2 \beta \quad (18)$$

where  $\beta$  is the angle of the joint,  $16^\circ$  in this case. Therefore, Equations 17 and 18 combine to form the final relation:

$$C_{D_{step}} = \left( 4 * C_D * \sqrt[3]{\frac{h}{x}} \right) * \sin^2 \beta \quad (19)$$

Using this result and the results of the viscous drag estimation from Section 7.3.2.3, we can estimate the influence of the step on the drag of the VGRWT/NCE tip in the following way:

$$\frac{D_{step}}{D_{tip}} = \frac{2 * h * c * C_{D_{step}}}{C_{D_{tip}} * S_{tip}} \quad (20)$$

For this analysis, the area of the tip,  $S_{tip}$ , was held constant at  $50 \text{ ft}^2$ , while the drag coefficient on the tip was also held constant at 0.0082, from the results presented in Table 18 for the fully swept VGRWT/NCE tip. The chord,  $c$ , was taken to be 60 inches, which is the approximate value of the chord at the VGRWT/NCE tip joint. The results are presented as Table 19. As expected, the drag coefficient is very dependent on the height of the step. Indeed, the maximum skin thickness contributes 0.5% more drag to the tip than the smallest step height. Though this seems small, any increase in drag will negatively impact fuel efficiency, therefore, with a common minimum skin thickness of 0.08 in, it is not unrealistic to design the height of the step as close to this minimum value as possible. It is also important to insure the step angle from Equation 18 is kept as small as possible. In the worst case scenario of a crosswise step, the drag would increase to nearly 15 times the values presented. Overall, the joint contributes a small, but not insignificant portion of the drag coefficient for the VGRWT/NCE tip.

**Table 19. Drag Due to Wing/VGRWT/NCE Joint**

Step Height $h$ , in	$C_{D_{step}}$	Percent of Drag on VGRWT/NCE Tip Due to Step
0.1	0.0073	0.14%
0.15	0.0083	0.25%
0.2	0.0092	0.37%
0.25	0.0098	0.50%
0.3	0.0105	0.64%

It should be noted that the above results assume a perfectly sealed joint. However, the results would change significantly if there is an open gap between the wing and tip. Hoerner demonstrates that for a perfect sharp-edged joint, the independent coefficient is 0.4. However, if there is a gap as little as 3 mm between layers, this coefficient increases to 0.6 when the gap faces the flow [37]. Though it is not anticipated that the joint will face the freestream, reverse flow into the joint would still contribute to an increase in drag, turbulence and noise. Therefore, care should be taken to ensure that the joint is as solid as possible. This will most likely involve sealing the joint with flexible skin or a rubber fairing.

Although reverse flow into an open joint is not anticipated, a large pressure difference could cause substantial airflow, as the pressure inside the airfoil attempts to equalize with the pressure outside the airfoil. Therefore, pressure contours were taken from the Fluent results for the unswept

VGRWT/NCE tip and the fully-swept VGRWT/NCE tip. The contours shown are at the main wing/VGRWT/NCE junction and are presented as Figure 85. At cruise altitude, the ambient pressure is approximately 2.25 psi. This is nearly identical to the pressure produced by the underside of the wing. However, the pressure above the wing is slightly lower, at approximately 1.45 psi. Therefore, some equalizing flow will be present. This leakage flow could also be minimized with the implementation of the aforementioned flexible skin or rubber strips.

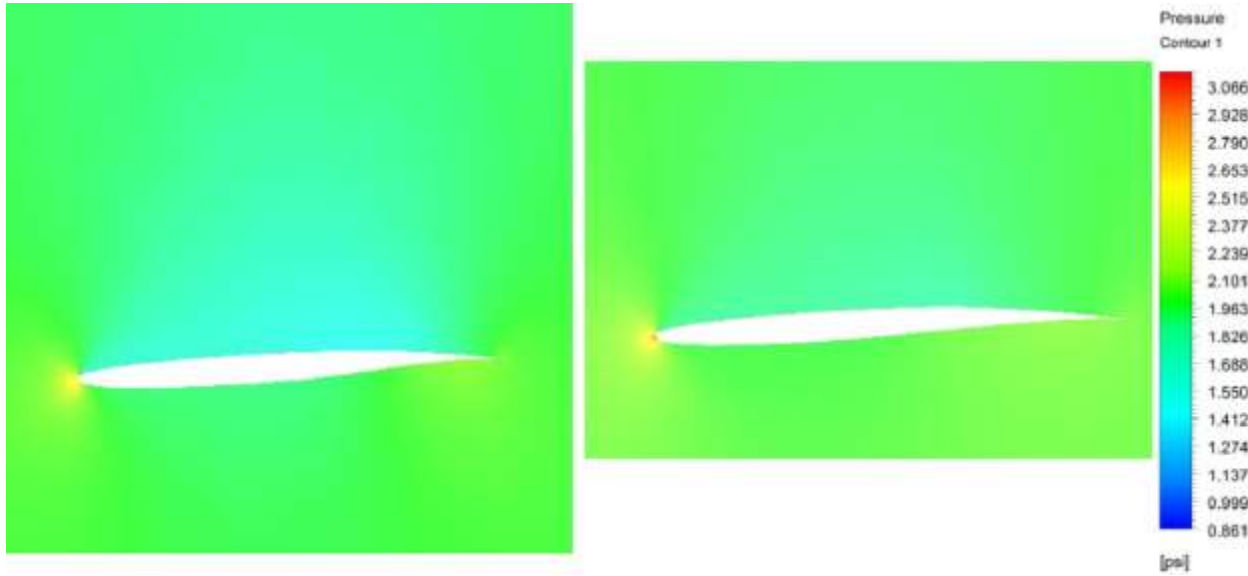


**Figure 85. Fluent Prediction of Pressure Contours of Unswept (Left) and Fully-Swept (Right) VGRWT/NCE Wingtip at Main Wing/Wingtip Junction**

#### 7.4 CONCLUSIONS

Previous applications of wingtip treatments have shown that tangible gains can be made with regard to drag reduction and fuel burn. However, these treatments, be they blended winglets or raked wingtips, are rarely optimized for all phases of flight. Generally a compromise is made to improve performance at cruise conditions, to the detriment of take-off and landing characteristics. With this in mind, a study was conducted analyzing the performance of a variable geometry raked wingtip applied to a baseline SUGAR TBW design. The VGRWT/NCE tip will be unswept for low-speed flight stages and swept for cruise conditions. We have shown that the VGRWT/NCE tip provides noticeable aerodynamic performance increases over an unmodified wingtip.

Preliminary analysis focused on the effect that the VGRWT/NCE has on the entire wing system. The VLM code, Tornado, analysis showed that the lift would increase, with a subsequent decrease in drag as a result of the new wingtip. Closer examination revealed that the unswept VGRWT/NCE tip provided more lift than the baseline wing tip and the swept VGRWT/NCE tip. This result justifies having the VGRWT/NCE tip unswept during take-off and landing, when lift is at a premium. Also, the swept configuration presented a lower drag coefficient than the baseline SUGAR wingtip, which validates the concept of a swept wingtip for cruise. The pitching moment of the wing would also increase, leading to a more stable platform. Inviscid CFD simulations run through ANSYS Fluent largely corroborated these results, with a difference in incidence angle of approximately one-tenth of a degree and a consistent 9% difference in pitching moment between

methods. The excellent agreement between methods confirms that VLM analysis, if conducted carefully, is a viable alternative to the often complicated and time consuming CFD simulations.

Thorough analysis was also conducted on the performance of the wingtips alone. This analysis showed that the lift performance of the unswept VGRWT/NCE tip and the baseline SUGAR tip was nearly identical, as designed. It also showed that the swept tip configurations produced increasingly smaller amounts of lift as the sweep angle increased. This was also expected as the sweep results in a smaller aspect ratio. The moments produced by the VGRWT/NCE tips provided unexpected results. It was found that the three-quarter sweep configuration produces the largest moment, while the one-quarter sweep model produces moments closest to the baseline SUGAR tip. Since the largest moment was produced with the three-quarter sweep tip, it could be argued that increasing the wingtip sweep beyond this configuration would result in only small gains in performance. Also, the large moments produced on the VGRWT/NCE tip can be used with a flexible wing for roll control or gust load alleviation. Due to the fact that the largest moments occur at the three-quarter sweep position, the actuator needed to move the VGRWT/NCE tip could be smaller than originally anticipated. Therefore, decreasing the maximum sweep may also result in the added benefit of reducing the cost, complexity, and weight of the swing mechanism itself.

Finally, a small study was performed on the effect of the step at the joint of the main wing and the VGRWT/NCE tip. This analysis revealed that the step would cause small additional drag, though careful design would minimize its impact.

The effect of the VGRWT/NCE tip on the SUGAR wing observed through this study is substantial. With these results in mind, the VGRWT/NCE tip is a viable option for the tip treatment of a next generation airliner. The VGRWT/NCE tip allows the wing to be optimized for all phases of flight and with fuel efficiency becoming an increasingly large design driver, even a small performance gain has the potential to be significant.

## 8. NOISE ASSESSMENT FOR BASELINE AND NOVEL CONTROL EFFECTORS

The technical memorandum documents the completion of Task 8, Noise Assessment for the Novel Control Effectors (NCE) Contract. The SOW for Task 8 is found in Section 3.1 "Requirements Development". The noise assessment is performed exclusively for the SUGAR single aisle aircraft with and without the VGRWT.

### 8.1 SUMMARY OF ACOUSTIC RESULTS

The total aircraft noise for the sized 765-095 airplane with gFan++ engines is given in Table 20 for the approach, cutback, and sideline certification conditions, in the metrics of Effective Perceived Noise Levels (EPNL dB). The certification regulatory limits of Stage 3 and the margins to the limits for all three conditions are also shown, including the cumulative margins to Stage 3 and Stage 4, the latter being the regulation currently in effect.

**Table 20. Noise Levels (EPNL dB) of the Baseline SUGAR Aircraft and their Margins to Regulatory Limits**

	SUGAR Baseline	Stage 3 Limits	Margin to Stage 3	Margin to Stage 4
Approach	88.9	100.0	11.1	
Cutback	80.7	90.5	9.8	
Sideline	84.4	96.1	11.7	
CUM	254.0	286.6	32.6	22.6

The noise levels for the baseline configuration are given here as a reference configuration, which is compared with the case with VGRWT implemented in Table 21, both for the three individual certification conditions and for the cumulative levels. The noise impact due to the implementation of VGRWT is shown in the last column of the table. As clearly shown by the data in this column, the overall conclusion of the noise assessment is that the implementation of VGRWT in the SUGAR aircraft has negligible noise impact.

**Table 21. Comparison of Noise Levels (EPNL dB) between the Baseline SUGAR Aircraft and that with VGRWT Implemented**

	SUGAR Baseline	SUGAR with VGRWT	Noise Impact
Approach	88.9	89.0	0.1
Cutback	80.7	80.7	0.0
Sideline	84.4	84.4	0.0
CUM	254.0	254.1	0.1

In deriving the noise levels shown in the above table, the implementation of VGRWT was assumed to align with the wing so that the VGRWT effectively consists of a smooth continuation of the wing with a small flap-like device. The VGRWT can also be deployed with a raking angle, in reference to the wing. The effects of raking on noise are shown in Table 22. It is clear that the impact is negligible.

**Table 22. Effects of VGRWT Raking on Noise Levels (EPNL dB)**

	Approach	Cutback	Sideline	CUM
Baseline	88.9	80.7	84.4	254.0
VGRWT	89.0	80.7	84.4	254.1

	<b>Approach</b>	<b>Cutback</b>	<b>Sideline</b>	<b>CUM</b>
+10°	89.0	80.7	84.4	254.1
+20°	89.0	80.7	84.4	254.1
+30°	89.1	80.7	84.4	254.2
+40°	89.1	80.7	84.4	254.2

In the following sections of this document, the technical details of the noise assessment will be given.

## 8.2 CONFIGURATION AND PERFORMANCE

The noise assessment was done for the SUGAR (765-095) sized configuration. The main geometric parameters of interest are the gear geometry (wheel diameter, strut diameter, etc.), and high-lift geometry (chord, span, deflection, etc.). Details for the specific values will be provided below in the detailed analysis discussion.

Noise analysis was determined for a prescribed FAR 36 flight performance profile/condition, depicted in Figure 86. The standard parameters are:

- environment temperature = 77 degrees F
- relative humidity = 77 percent
- minimum climb out speed = V2+10 knots
- distance to the microphone = 21,325 ft from brake release
- start of cutback = 3500 ft before the microphone
- end of cutback = 23,000 ft from brake release
- end of noise trajectory = 3000 ft altitude
- sideline noise measurement = 1000 ft altitude

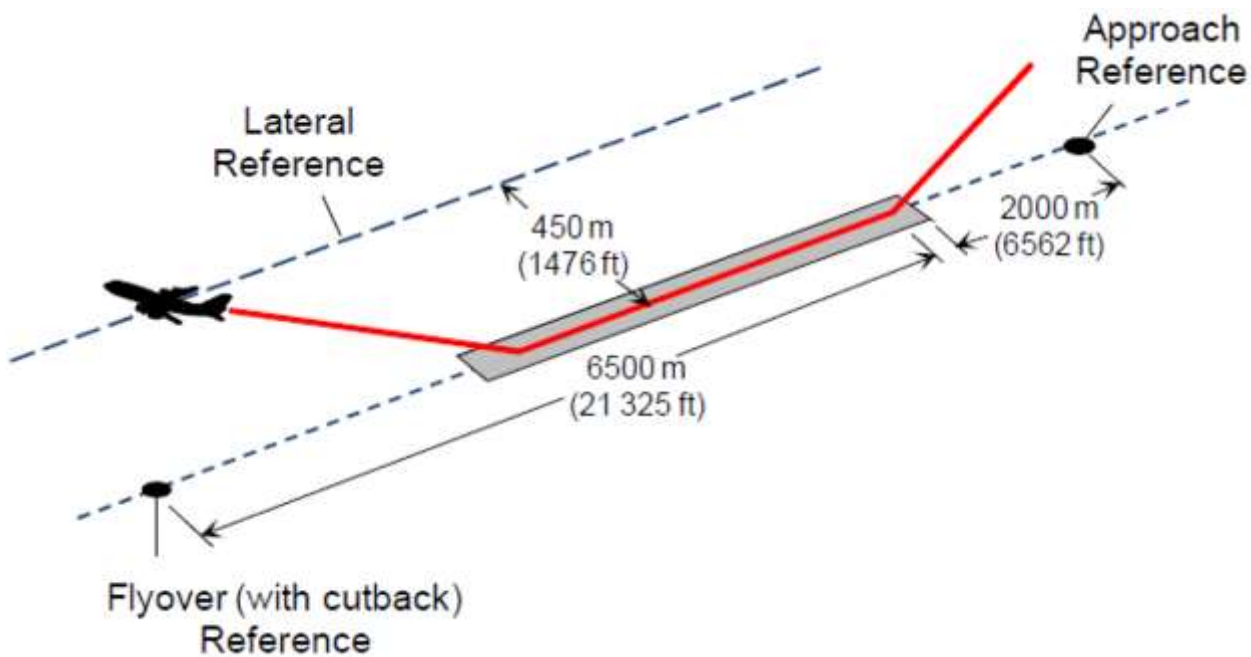


**Figure 86. FAR 36 Noise Profile**

The relevant flight performance parameters and values for the noise profiles for the noise analysis are provided in Table 23 below. Maximum Take-off Gross Weight = 140, 900 lbs was used for the noise analysis, and was used to derive the Stage 3 noise limits.

**Table 23. Flight Performance Parameters for Noise Analysis**

	Altitude (ft)	Velocity (kt)	Flight Path Angle (deg)	Engine Pitch Angle (deg)	AOA (deg)	Thrust per Engine (lb)
Approach	394	124.6	-300	3.86	6.86	1347
Cutback	1730	181.8	3.23	6.5	3.23	8537
Sideline	1000	179.9	8.37	11.5	3.13	15008

### 8.3 OVERALL METHOD OF ANALYSIS

The noise analysis was conducted in 3 major parts, namely, engine noise, airframe noise, and total aircraft (system noise). The overall noise analysis process is shown in Figure 87.

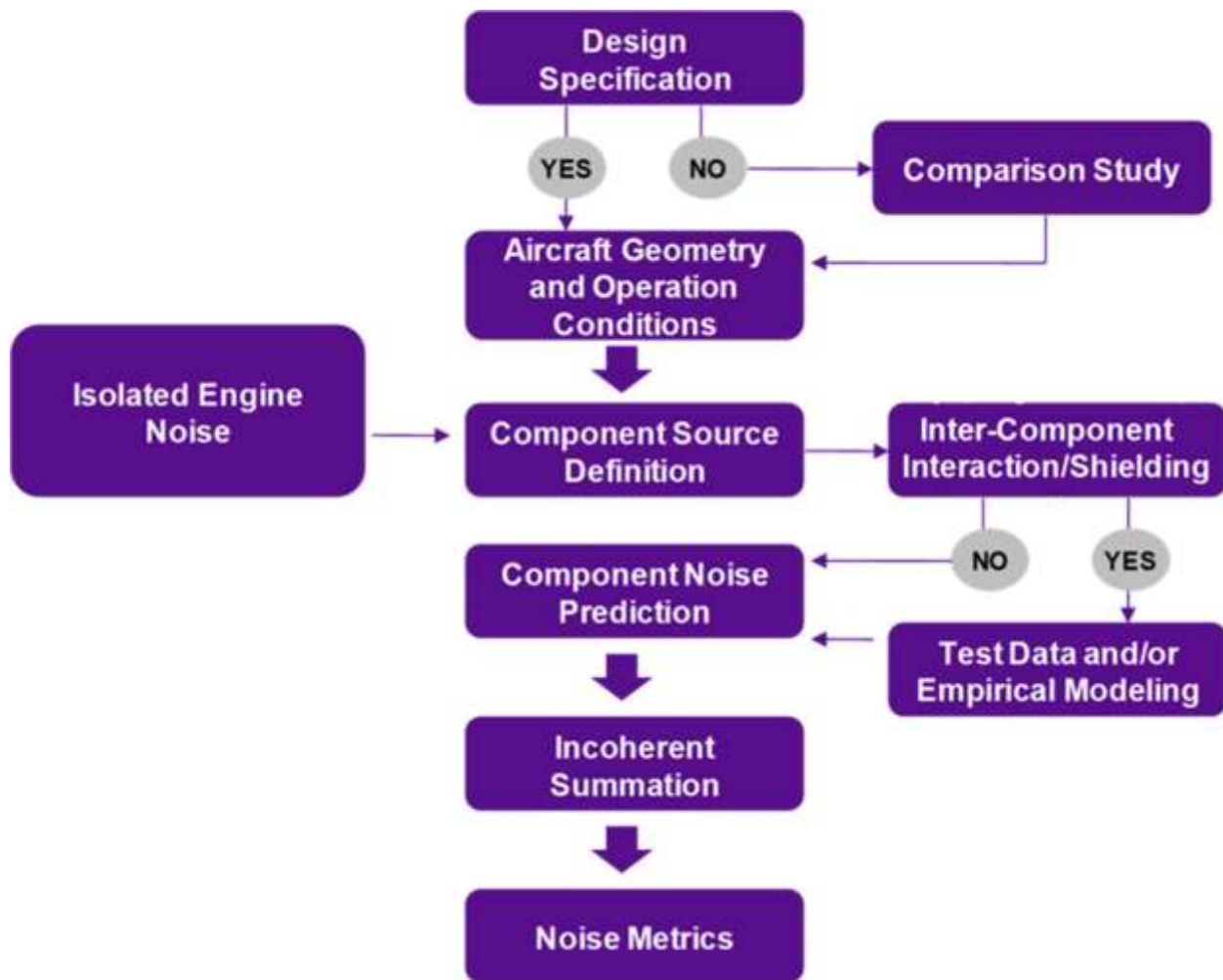


**Figure 87. Overall Noise Analysis Process**

The design specification inputs entail the airframe design, flight profiles, engine type, and engine power conditions. These parameters served as the inputs for the engine and airframe noise predictions. They provided the specific geometry values for the subcomponents, such as chords, spans, deflections, etc., and also the flight operating conditions for the specific noise certification points, such as altitude, velocity, etc.

The engine noise was developed and provided by GE, using their "GE Decomposition" in-house method. Non-treated (hardwall) in-flight Noise-Power-Distance (NPD) engine noise data was provided for the baseline (non-electric) engine and for all electric power settings. It included subcomponent 1/3rd octave spectral data for Fan-Inlet, Fan-Exhaust, Jet, and Combustor.

Airframe noise was derived by Boeing's component noise predictions which have been discussed and validated in References [38, 39, 40 and 41]. Airframe noise included 1/3rd octave spectral data for the nose gear, main gear, slat, and flap. Trailing edge noise was not analyzed in this preliminary analysis.

Engine and airframe noise data was extrapolated from flight to 150 foot polar-arc condition and then back to certification flight conditions. The data was then log summed to yield the total aircraft noise. System metrics of PNLT, PNL and EPNdB were derived. Extrapolation from flight

to 150ft polar-arc and back to flight was done so that all the predicted data would be processed through standard in-house extrapolation processes.

### 8.3.1 CFD Analysis for Noise

An unstructured grid CFD analysis was performed for the SUGAR configuration at the power-on, reference noise certification low-speed conditions using CFD++. The approach aircraft configuration geometry was modeled using CATIAv5 for approach with the landing gear (main and nose) down, the leading edge Krueger (Slat) set to  $40^\circ$ , and the trailing edge (TE) flaps deflected to  $35^\circ$ . The take-off (cutback) and sideline configuration had the landing gear retracted, the Slat set at  $40^\circ$ , and the TE flaps set at  $5^\circ$ . The surface grids were generated using CATIAv5 Advanced Mesh Generation workbench tools. Care was taken to resolve all the TE surfaces as well as the flap and slat surfaces. High grid density was enforced using background source functions near expected regions of large flow gradients. These regions included:

- Nacelle/pylon region to adequately resolve the powered flow field
- Around both the nose and main landing gears
- Around the wing and near LE Krueger, and TE flap

The AFLR hybrid volume grid size grew to  $\sim 125$  million cells. The power-on boundary conditions were applied at the fan inlet, fan exit, and core exit faces. Finally the CFD++ N-S analysis was performed at the appropriate flight conditions. The approach condition was at  $M=0.2$ , Altitude=394ft, and AOA = 6.859. The sideline and takeoff (cutback) condition were at,  $M=0.268$ , AOA = 6.000, and altitudes of 1000' and 1730', respectively. The power-on boundary condition engine parameters (mass flow and temperature) for the inlet primary and bypass exhaust flows, were interpolated from the engine cycle deck for these conditions.

The SUGAR unstructured grid geometry used for CFD, at approach, is shown in Figure 88.



**Figure 88. SUGAR Unstructured Geometry at Approach**

The unstructured grid geometry of the SUGAR configuration at take-off is shown in Figure 89. Areas of high density gridding are highlighted for the LE slat and TE flap. It is noted that the leading edge of the flap is tucked under the wing such that the integrated lift of the flap alone had to be approximated.

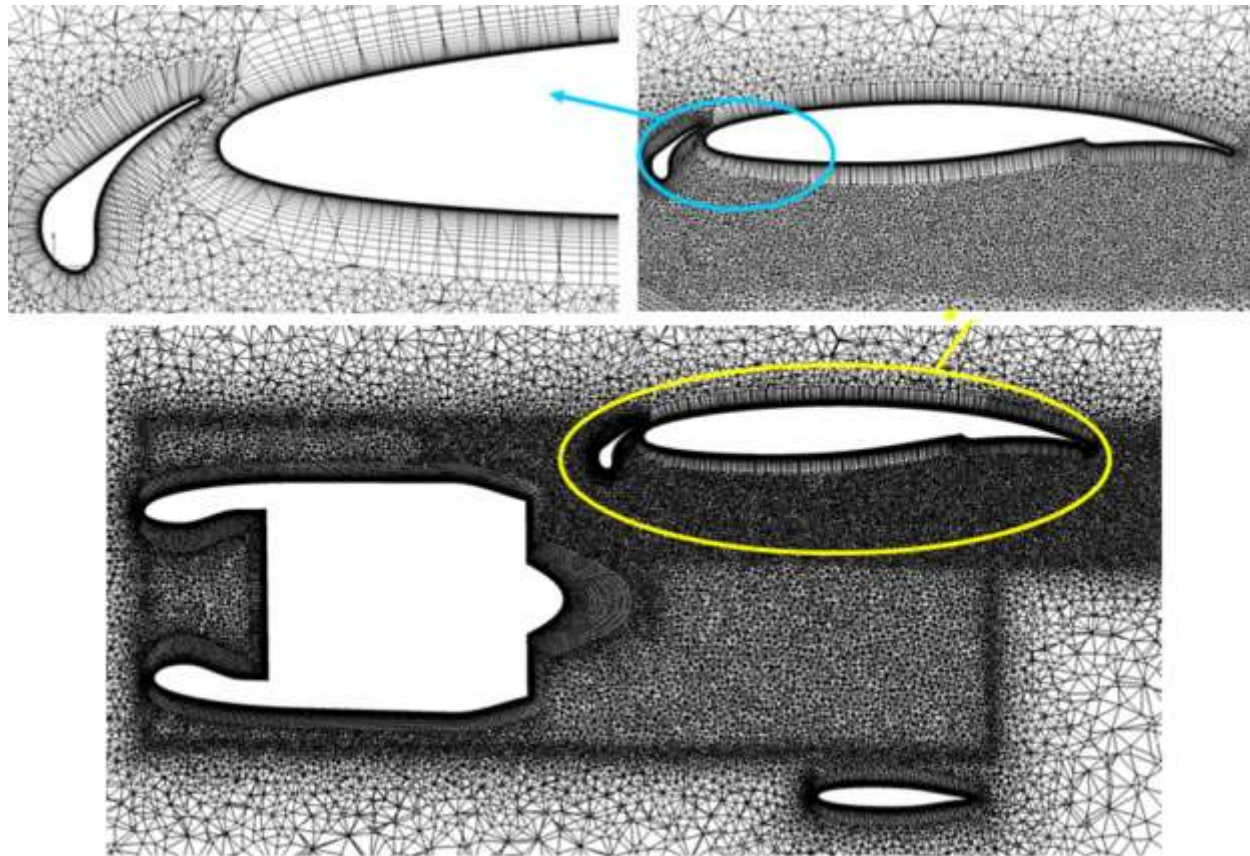


**Figure 89. SUGAR Unstructured Geometry at Takeoff**

The solution iteration history for CL, CM and CD parameters is shown in Figure 90. Note that the solution converged by ~600 iterations.

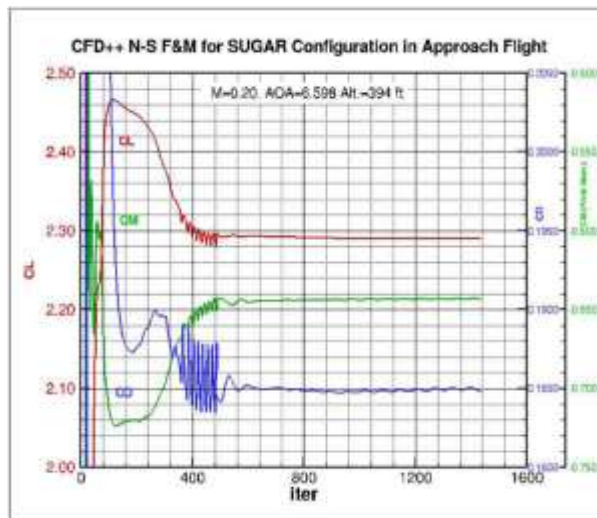


**Figure 90. CFD++ Solution Convergence**

Flow parameter data was extracted from the CFD Q files for the airframe noise component prediction codes. These included total  $C_l$ ,  $C_p$ , and Mach number. Figure 91 shows locations of streamwise and spanwise cuts used to calculate these parameters.

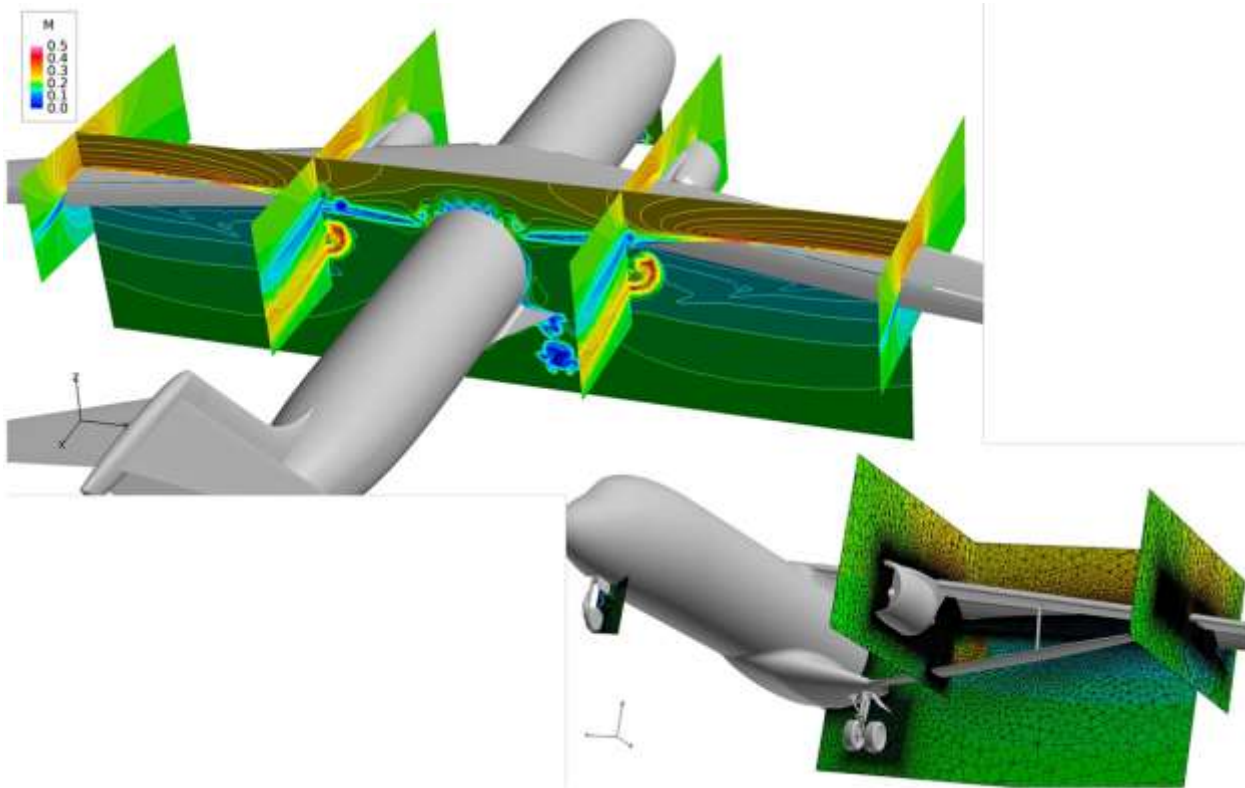


**Figure 91. CFD++ Computed Mach Cuts**

For gear noise, the flow field in front of the main and nose gears were used to calculate the local mach which was an important parameter for the gear noise prediction.

Since CFD++ uses unstructured grids, sectional  $C_l$  was not directly available from the results. Hence, two Matlab routines were written, one to sort, filter, and smooth the CFD data, and another to perform numerical integration and then sum  $C_p$  to get sectional  $C_l$ . This process is illustrated in Figure 92.

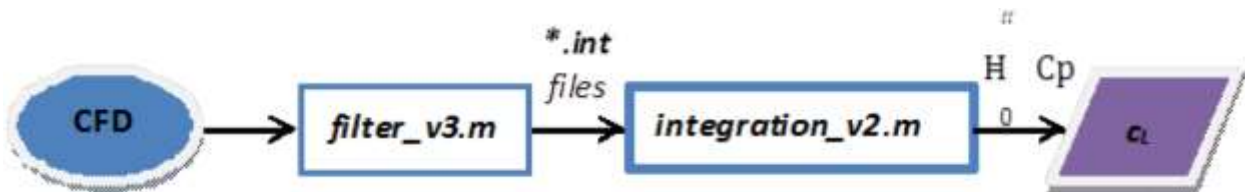


**Figure 92. Post-Processing of CFD++ Data for Computing Sectional Lift Coefficient**

In the first Matlab routine, **filter\_v3.m**, CFD results are filtered by  $C_p$  to separate wing upper surface and lower surface. The data points are then smoothed and **\*.int** files are generated. The second Matlab routine, **integration\_v2.m**, computes summations of  $C_p$  over the upper and lower

surfaces. The magnitudes of  $\sum C_p$  are added to obtain total  $C_l$ ; the sectional lift coefficient  $c_l$  is obtained by dividing  $C_l$  by chord length.

### 8.3.2 Airframe Noise

The preliminary noise analysis airframe noise included the nose gear, main gear, slat and flap components. The trailing edge noise was not included in this preliminary analysis but will be provided if appropriate in the final analysis. Furthermore, the Approach condition included all airframe components, but the Sideline and Cutback only included the slat and flap noise. It was assumed that the nose and main gear is stowed during cutback and sideline noise.

The SUGAR configuration is mostly a conventional "tube-and-wing" configuration other than the truss-braced wing aspect. Hence the methodologies developed for predicting the airframe components were relevant since they were validated for current generation aircraft. Moreover, the basis for the methods is aerodynamic sound generation theory, hence they are not limited to any particular aircraft type. Any effects specific to the SUGAR configuration will be captured by the input parameters.

The SUGAR configuration main and nose gear geometric input parameters are provide in Table 24. The flight performance for approach condition for the gear prediction is provided in Table 23.

**Table 24. Main Gear and Nose Gear Noise Prediction Input Parameters**

	Number of Wheels	Wheel Diameter (in)	Wheel Width (in)	Number of Main Strut	Strut Length (in)	Strut Diameter (in)
Main Gear	2	44	16	1	66	6
Nose Gear	2	27	7.75	1	41	4

Since the SUGAR (095,TBW) and SUGAR Free (tube and wing) configurations have very similar gear geometry hence some inputs were derived based on the SUGAR Free geometry. Aside from the geometry the most important input parameter for the gear noise prediction is the local mach in the proximity of the gear. As noted above, CFD++ was used to derive this value, in which it was found that the SUGAR local mach for both the nose gear and main gear was lower than for the SUGAR Free. Expectedly then the main gear and nose gear noise was lower for the SUGAR. A comparison is shown at 90 deg overhead for approach flight condition in Figure 93 below. The "S Free\_ref" is a prediction for the SUGAR Free with its own geometry and approach flight conditions. In comparison to the SUGAR noise it is higher. To normalize out the flight performance effects the SUGAR Free geometry was predicted at the SUGAR flight conditions (S Free\_SHE). In this comparison, the SUGAR gear noise is still lower but not as much.

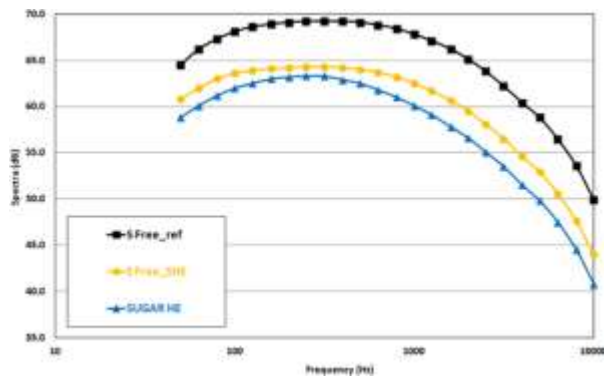


**Figure 93. SUGAR Free vs. SUGAR Total Gear Noise Comparison at Approach**

The SUGAR configuration slat system consists of an inboard leading edge Krueger flap and several outboard elements and all are Krueger flaps. The deflection for the slat is the same for approach, cutback, and sideline, and is depicted in Figure 94.

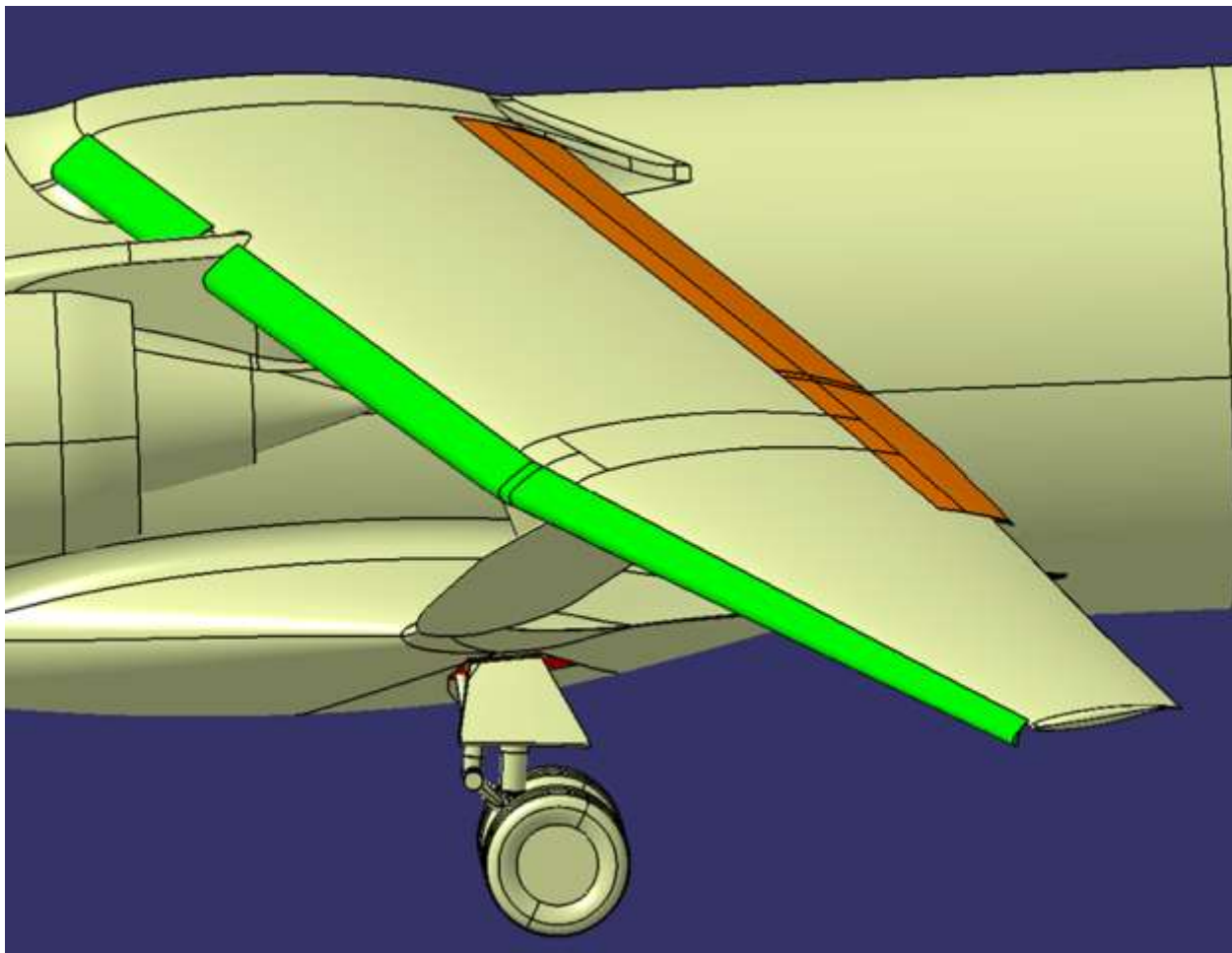


**Figure 94. SUGAR Slat System Deployment for Approach/Cutback/Sideline**

Note in Figure 94 that all the outboard elements deploy together, which implies effectively only two slat elements. However because there is a large change in sweep and chord length from

station 587.9305, hence the slat was treated as three elements, namely one from the wing centerline to the engine centerline, one between the engine and wing station 587 and one outboard to the tip, as illustrated in Figure 95.

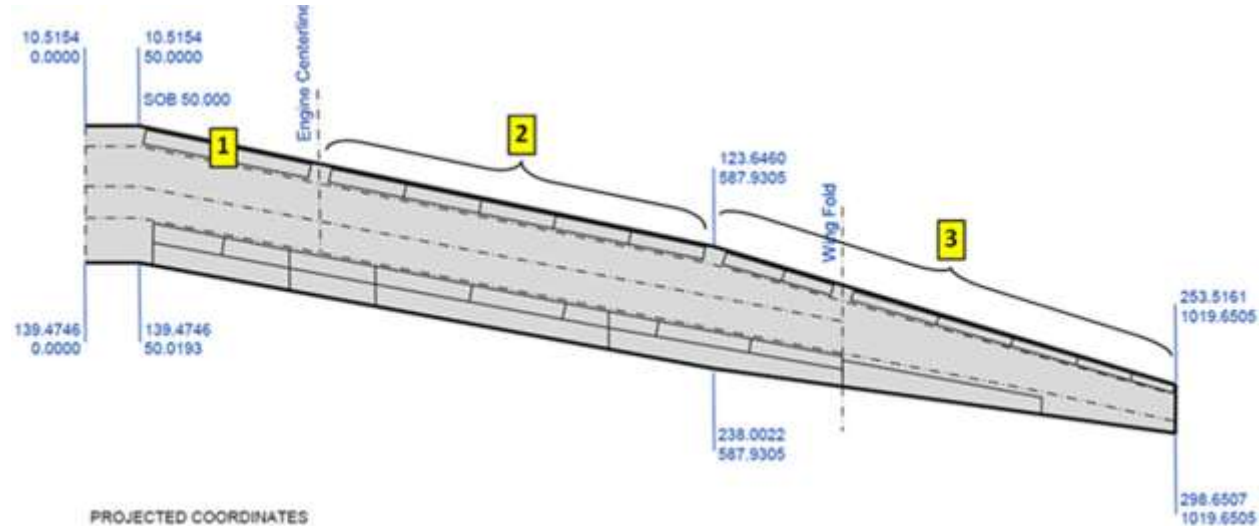


**Figure 95. SUGAR Slat System Definition for Noise Analysis**

The SUGAR configuration geometric input parameters for the slat are provided in Table 25. The flight performance for approach, cutback and sideline conditions for the gear noise prediction is provided in Table 23.

**Table 25. Slat Noise Prediction Input Parameters**

Slat Number	Chord (in)	Span (in)	Angle (deg)	Sweep (deg)	Gap (%)
1	17.11	145.9	49.5	11.84	1.97
2	16.14	350.1	51.3	11.91	2.25
3	17.98	431.7	49.4	16.78	1.89

The CFD++ analysis provided Slat lift coefficient data as well as total lift but at the time of the preliminary analysis only the geometry inputs option was active for the slat prediction. Similar to the gear analysis a comparison was made between the SUGAR slat noise and the SUGAR Free slat noise, which is depicted in Figure 96 for approach condition at 90 deg overhead. As shown, the SUGAR slat noise is indeed quieter than the SUGAR Free slat noise.

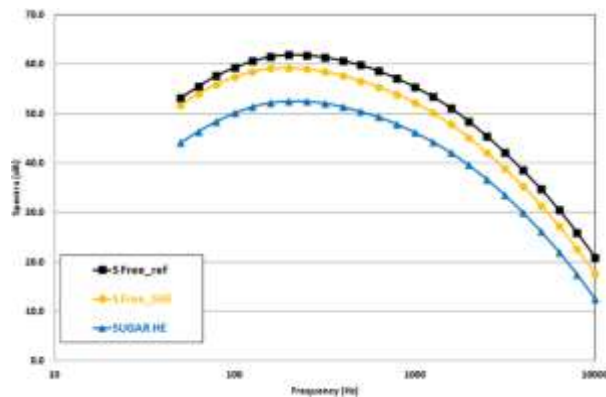


**Figure 96. SUGAR Free vs. SUGAR Slat Noise Comparison at Approach**

The SUGAR configuration flap system entails an inboard flap element, a flaperon, and two outboard flap elements. Both the inboard and outboard are single element fowler flaps. The flap system deflection for approach is illustrated in Figure 97. The deployment for cutback/sideline is depicted in Figure 98.

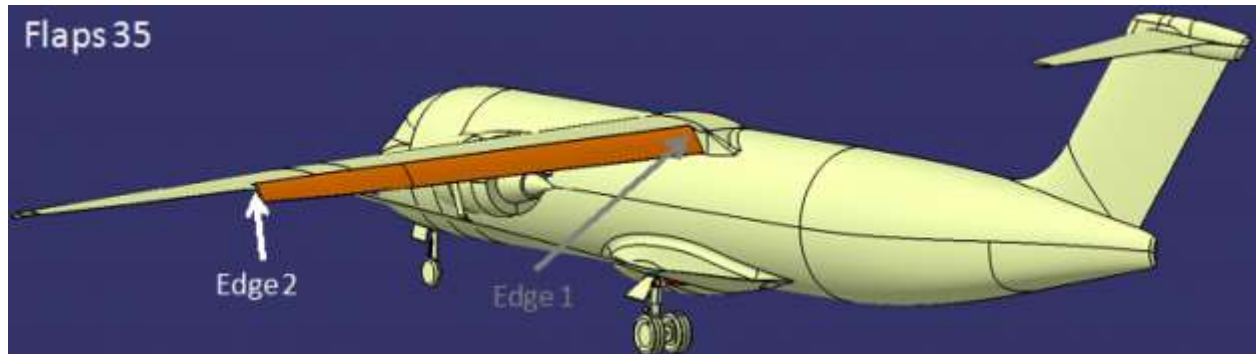


**Figure 97. SUGAR Flap System Deployment at Approach**

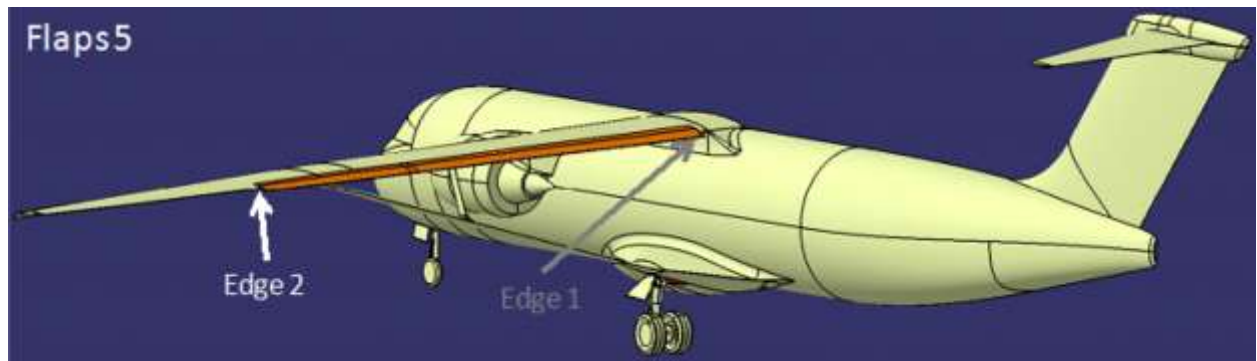


**Figure 98. SUGAR Flap System Deployment at Cutback/Sideline**

Note in Figure 97 and Figure 98 that all the flap elements deploy together, which implies that there are only two edges, one edge between the body and inboard side of the inboard flap and one edge between the outboard edge of the outboard flap and the aileron, as depicted in Figure 99 below.

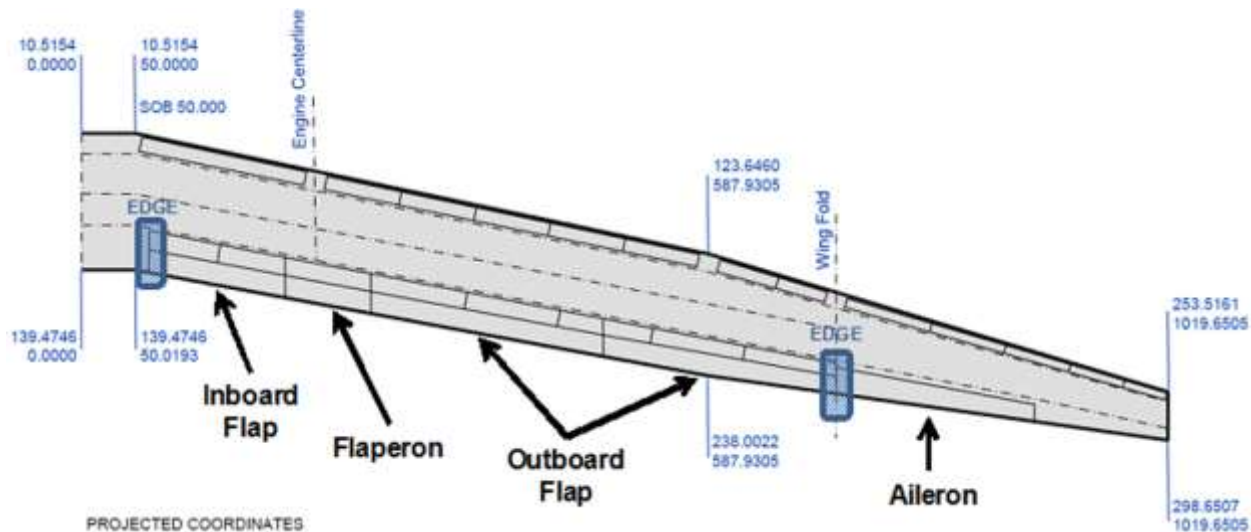


**Figure 99. SUGAR Flap System Definition for Noise Analysis**

The SUGAR configuration geometric input parameters for the flap at approach are provided in Table 26. The parameters for Cutback are provided in Table 27. Note that the only differences are in the deployment angle and CLs. The sideline parameters are provided in Table 28. Note that the cutback and sideline parameters are quite similar.

**Table 26. Flap Noise Prediction Input Parameters at Approach**

	Number of Flap Side Edges	Flap chord (in)	Flap Thickness (in)	Flap Span Length (in)	Flap Deployment Angle (Deg)	Flap Sweep Angle (Deg)	Flap Edge Type	Flap Lift Coefficient	Flap Sectional Lift
Flap – Approach	2	38.75	5.93	645.4	35	10.63	1	0.3539	1.63
		28.3	4.45	645.4	35	9.44	1	0.3539	1.23

**Table 27. Flap Noise Prediction Input Parameters at Cutback**

	Number of Flap Side Edges	Flap Chord (in)	Flap Thickness (in)	Flap Span Length (in)	Flap Deployment Angle (Deg)	Flap Sweep Angle (Deg)	Flap Edge Type	Flap Lift Coefficient	Flap Sectional Lift
Flap – Cutback	2	38.75	5.93	645.4	5	10.63	3	0.14X421	0.631
		28.3	4.45	645.4	5	9.44	3	0.141421	0.528

**Table 28. Flap Noise Prediction Input Parameters at Sideline**

	Number of Flap Side Edges	Flap Chord (in)	Flap Thickness (in)	Flap Span Length (in)	Flap Deployment Angle (Deg)	Flap Sweep Angle (Deg)	Flap Edge Type	Flap Lift Coefficient	Flap Sectional Lift
Flap – Sideline	2	38.75	5.93	645.4	5	10.63	3	0.141454	0.626
		28.3	4.45	645.4	5	9.44	3	0.141454	0.599

Similarly, a comparison was also made between the SUGAR flap noise and the SUGAR Free flap noise, which is depicted in Figure 100. Note that the SUGAR flap noise is quieter but the differences are not as pronounced as with the slat noise comparison.

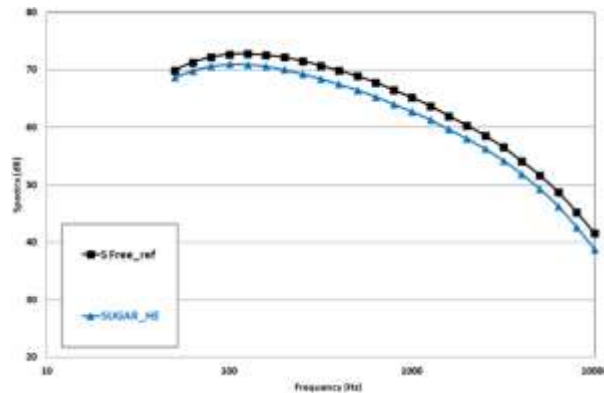


**Figure 100. SUGAR Free vs. SUGAR Flap Noise Comparison at Approach**

Overall then, the flap noise has been found to be the dominant airframe subcomponent noise aside from the very shallow angles in which the gear noise is dominant for approach. This outcome from the preliminary noise analysis means noise reduction technology should be focused on the flap in order to reduce the airframe noise.

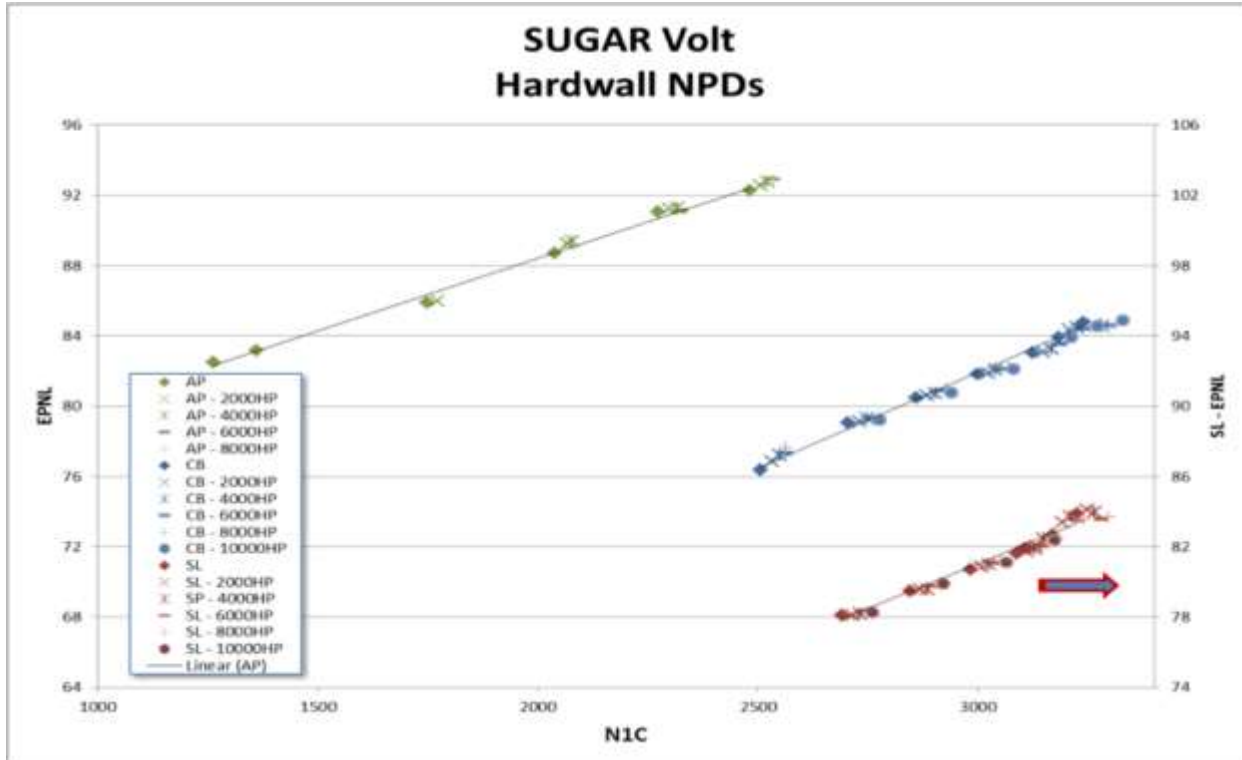
### 8.3.3 Engine Noise

A noise prediction analysis was provided by GE for this study. The data provided to Boeing from the GE noise analysis included spectral noise component predictions for hardwall engine noise-power-distance (NPD) levels at the reference SUGAR configuration noise certification conditions. The methodology and technology assumptions GE used for their predictions are shown in Table 29. The engine noise was derived from a "parent engine database" using the most advanced engine technology that was applicable to this design, namely the GE GEnx-1B engine. This acoustic database had to be scaled to the operating conditions of the SUGAR as well as account for any differences in the engine design.

**Table 29. GE Noise Modeling Assumptions for the SUGAR Volt Engine**

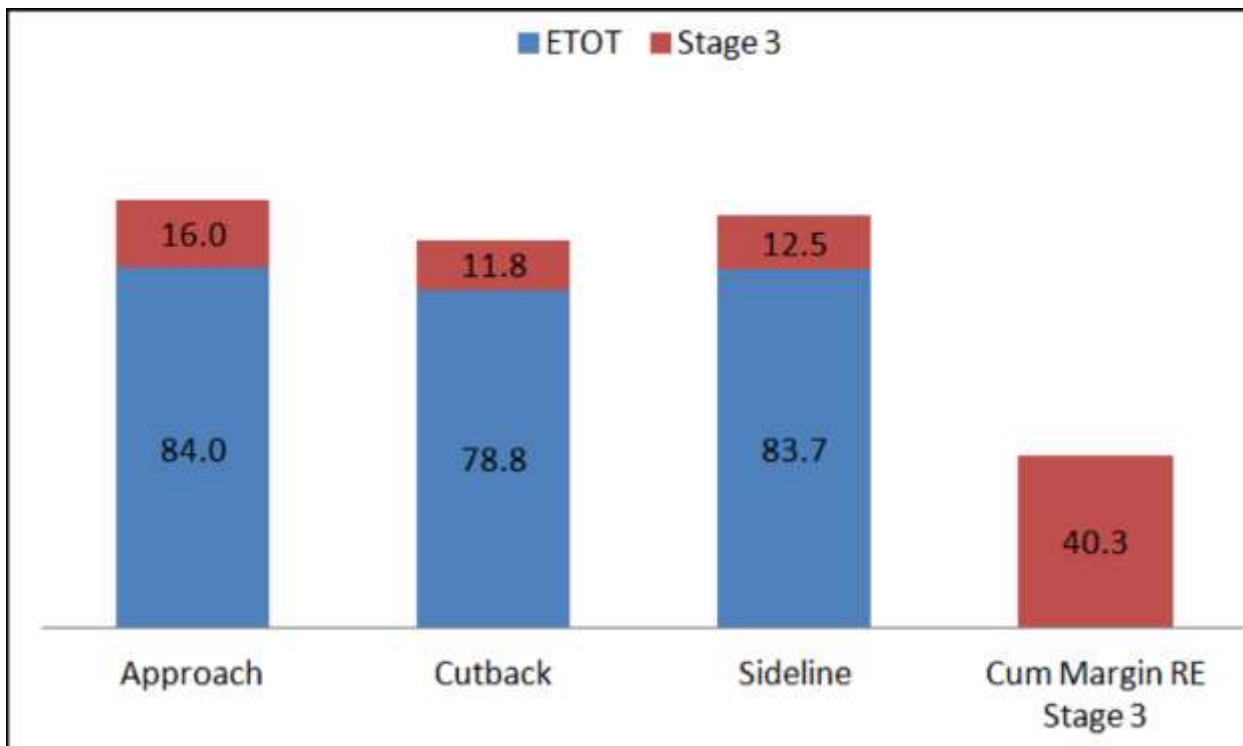
Source Category	Methodology
Parent Engine Model	GEnx-1 B Hardwall – GE Decomposition
Lining Model & Airframe Noise	N/A – Boeing is adding both
Rotor Stator Spacing	Assume same as Genx-1 B
Sweep and Lean OGV	Assume 30° sweep for benefit (-1.5 dB on Fan)
Shielding	1.5 dB on all components for SL due to fuselage
VFN	N/A
Electric Motor	Noise largely due to cooling fan – none assumed here
Core Chevron	Not included
Advanced Fan design	2dB benefit on Fan
Core & LPT	Core -3dB and no LPT shielding; Cutoff LPT
M-Factor	5 engine unified m-Factor
JIN	None assumed – built into m-Factor

Figure 101 below, gives the noise certification EPNL NPD levels at sideline, cutback and approach for the baseline (no electric motor) and for 2,000 – 10,000 Hp electric motor / engine designs. The noise curves shown here are for total system noise without the airframe noise and without engine noise treatment of the acoustic liners.



**Figure 101. GE Noise-Power-Distance (NPD) Predictions for Hardwall Engine**

At the reference MTOGW of 140,900 lbs, the Stage 3 noise limits are 100.0, 90.6, and 96.2 EPNdB for approach, cutback, and sideline, respectively. At this weight, the GE total engine noise only without airframe and without engine treatment yields levels of 84.0, 78.8, and 83.7 EPNdB, respectively for AP, CB, and SL, as noted in Figure 102. The associated Stage 3 noise margins at each condition as well as the cumulative noise margin, is also shown in Figure 102.



**Figure 102. GE Hardwall Engine System Noise Assessment (without Airframe and Acoustic Liners)**

Engine treatment was defined and analyzed by Boeing given that GE supplied hardwall engine data. Since detailed liner treatment analysis/design was out of scope for this study, hence a simpler approach was adopted, as illustrated in Figure 103 below.

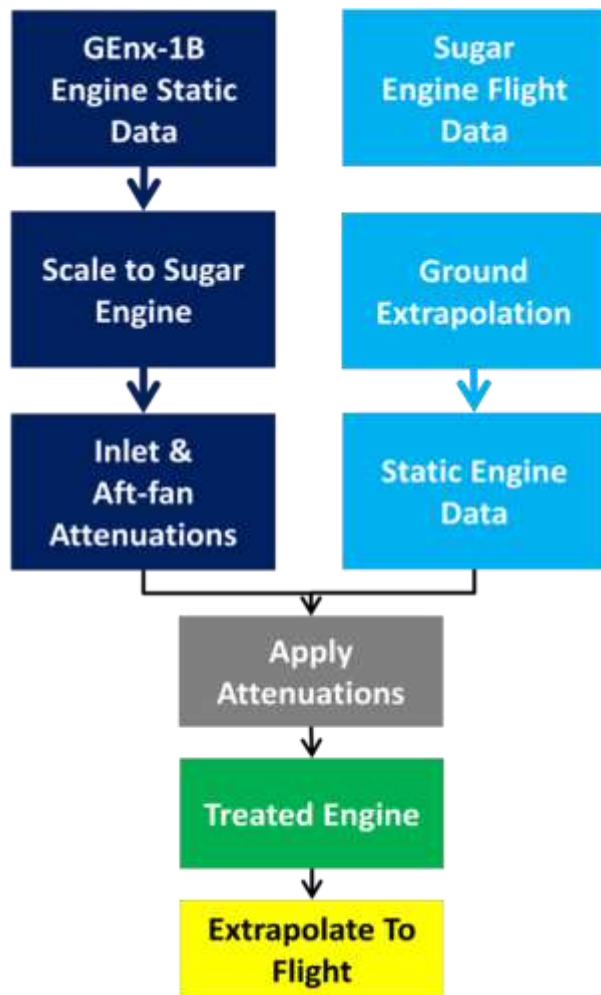


**Figure 103. Process for Derivation of SUGAR Treated Engine Noise**

Firstly, engine treatment developed for the GEnx-1B was used as the starting point since the GEnx-1B engine was also used as the starting point to define the SUGAR hardwall data. Secondly, similarity of treatment design was assumed, hence no actual engine treatment was designed. Instead the process started with GEnx-1B hardwall and treated static engine noise data. The treated and hardwall data was scaled using the gFan++ to GEnx-1B fan diameter ratio =  $71.2 / 111.1 = 0.64$ . A scaling routine designated to handle tones rather than just broadband scaling was utilized. Once the data was scaled the hardwall and treated data were subtracted from each other to derive the scaled treatment spectral attenuations. This was done for both the inlet and aft-fan on a spectral basis. The GE supplied in-flight engine data was extrapolated to 150 foot polar-arc static conditions. The fan-inlet and fan-exhaust partitions at the specific AP/CB/SL conditions were then adjusted by the attenuations to derive the treated fan-inlet and fan-exhaust data. Care was taken to align the correct power setting conditions between the scaled GEnx-1B data and the SUGAR data so that tones aligned. In this preliminary noise analysis treated engine analysis was not completed and only hardwall analysis results are provided.

### 8.3.4 Total Aircraft (System Noise)

The total aircraft noise was derived by projecting to flight the 150 foot polar-arc airframe data and also the 150 foot polar-arc engine data, and then log summing. A comparison of component noise sources is shown in Figure 104, Figure 105, and Figure 106, for the SUGAR configuration with VGRWT, respectively at the sideline, cutback, and approach certification conditions. It is noted that at the sideline condition when the engine is at full thrust, engine noise is the dominant component. At cutback conditions, engine noise is reduced by the reduced engine power so that the airframe and the engine noise component are comparable. At approach conditions, the engine power is further reduced and the airframe component is the major contribution to the total. In all three cases, the contributions due to VGRWT are seen to be very small, only making negligible impact on the total aircraft noise.

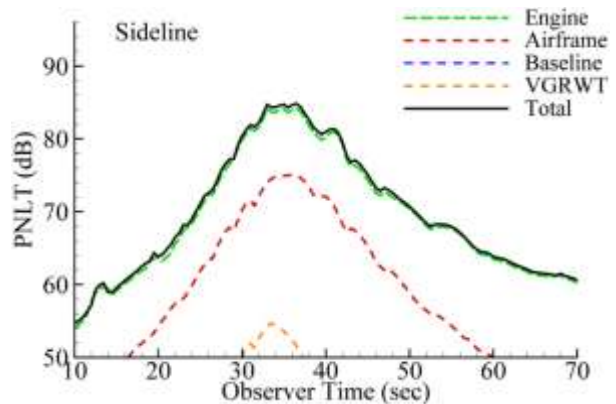


**Figure 104. SUGAR/RGWRT Sideline Aircraft Noise**

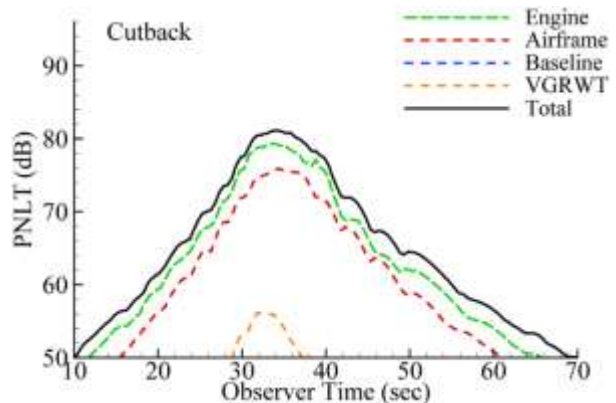


**Figure 105. SUGAR/RGWRT Cutback Aircraft Noise**

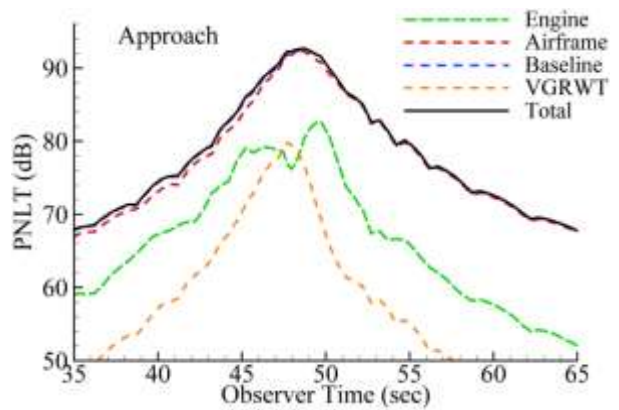


**Figure 106. SUGAR/RGWRT Approach Aircraft Noise**

## 9. NOVEL CONTROL EFFECTOR AEROELASTIC FINITE ELEMENT MODEL

This report documents the transmission of the complete SUGAR/VGRWT finite element model. The finite element model was developed using PATRAN/NASTRAN and provided both in PATRAN database (.db) as well as bulk data file (.bdf) formats.

### 9.1 DEVELOP SUGAR VGRWT FINITE ELEMENT MODEL

#### 9.1.1 Integration with Baseline SUGAR Model

Boeing provided the current PATRAN model of the SUGAR truss braced wing design used as a baseline for this effort. The initial NCE wingtip kinematic model developed for Task 3.0 (Figure 107) utilized a simplified version of the twist distribution developed in Task 5.1 low fidelity aerodynamic calculations and only nominally extended beyond the area of the track and beam mechanism. Proper integration with the baseline SUGAR FEM required that the NCE geometry exactly match at the junction between the two models. A revised CAD model aligned the NCE geometry with the SUGAR outer mold line (OML) at span station 894 inches, measured from the aircraft centerline. The wing twist distribution was set to match that provided by Virginia Tech (VT). Additionally, the wingtip load-bearing structures were extended in the CAD model to complete the remainder of the wingtip OML, as the simplified kinematic model developed in Task 3.0 only extended 60 inches beyond the variable sweep mechanisms. Elements in the baseline SUGAR FEM outboard of span station 894 were removed.

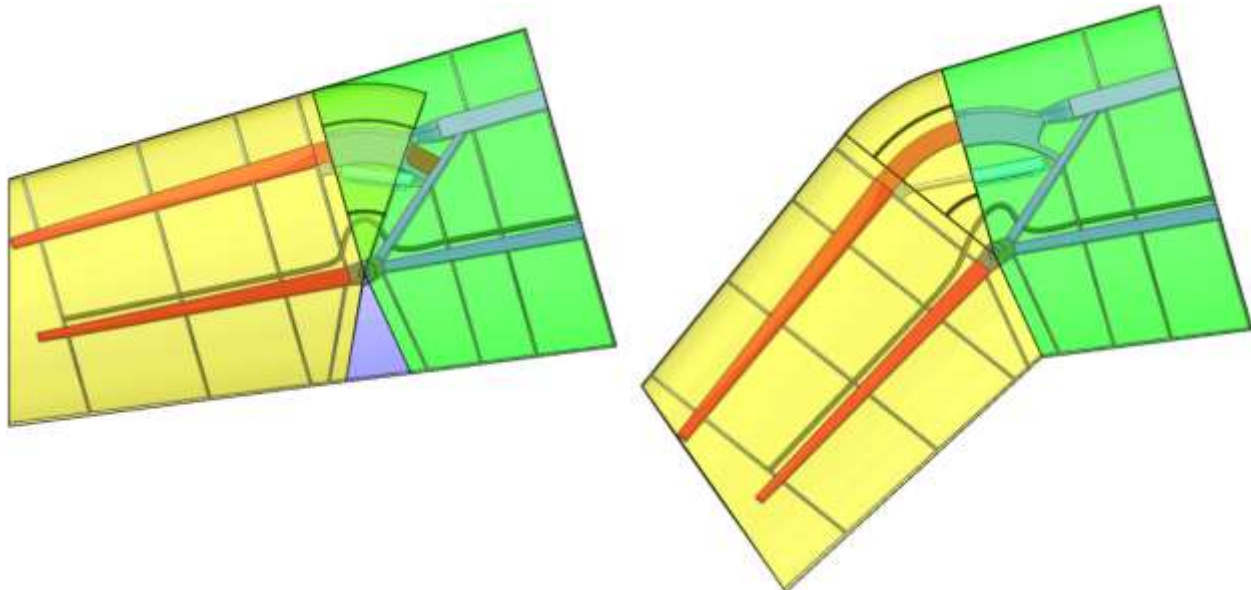


**Figure 107. Simplified kinematic model of the variable geometry raked wingtip kinematic developed in Task 3.0 in fully unswept 0° (left) and fully swept 35° (right) sweep positions.**

The baseline SUGAR FEM near the cut-line consisted of a low fidelity mesh for the skin and internal structures. To reconcile the simple load paths of the SUGAR wing with the more complex load paths of the NCE joint geometry, element density was transitioned between the two sections. Mesh control points added to the NCE geometry ensured that the element size and node locations matched the existing SUGAR mesh. Element density near the variable geometry load path was set using control points and the mesh in between automatically generated. Front and rear spar shear

webs on the SUGAR FEM were meshed with single elements connecting the upper and lower spar caps. The VGRWT spar shear webs were meshed using two elements between the spar caps. At the junction between the two areas, midpoint nodes were added to the coarser mesh and element corners on the finer mesh were connected to them.

### 9.1.2 Overall NCE FEM Design

The NCE FEM was created using the SUGAR FEM design as a basis. Similar modeling techniques were implemented and materials found in the SUGAR model were used wherever possible. Grouping within the FEM was arranged to allow for easy selection and visualization of model components (Table 30). The baseline SUGAR FEM was separated into a group by itself, while the NCE root, tip, and aileron geometry and mesh sections were grouped individually. Master FEM groups were used to generate meshes on the components of a single wingtip at a single sweep angle. Individual mesh properties were linked to their parent construction geometry to allow changes to be made if necessary following completion. These meshes were then mirrored and rotated in order to create the opposing wingtip and the additional sweep angles. This ensures that all cases have identical element geometry and consistent behavior. These elements were placed into separate groups with group names identifying the contents according to their location and sweep angle. Additionally, normally covered internal structures, such as the track and beam system, front and rear spars, and ribs, were included in separate groups to provide easier visualization and selection.

Groups containing variable wingtip components were rotated at the wingtip pivot axis and separated into unswept 0 degree, three quarter sweep 26 degree, and fully swept 35 degree sets (Figure 108). Additional wingtip angles can be analyzed by copying and rotating the wingtip groups to the desired angle and creating separate groups for the new case. Top-level groups containing all the SUGAR, NCE root, and NCE tip elements required for each case allow for easy selection of each wingtip angle for analysis.

The mesh element and node numbering was organized according to the mesh location and sweep angle. SUGAR baseline element and node numbering were not changed, however all new elements and nodes were numbered in the 90 millions range, with left side starting at 90,000,000 and the right indexed up by 500,000. New elements associated with the fixed side of the VGRWT were assigned numbers starting with 90,000,000 on the left wing and 90,500,000 on the right wing. Elements and nodes contained in the left and right 0 degree wingtips were numbered from 91,000,000 and 91,500,000 respectively. The 26 degree and 35 degree sweep cases were numbered similarly, starting from 92 and 93 millions ranges.

**Table 30. NCE FEM Groups**

Group Name	Variants	Description
Sugar Baseline	None	Complete SUGAR FEM inboard of BL894
Geo L Root	L/R	Geometry for skin and internal structure from BL894 to cut-line
Geo L Root Beam	L/R	Geometry for track and beam structure on fixed side of VGRWT
Geo L Root Inner	L/R	Geometry for internal structure from BL894 to cut-line
Geo # L Ail	L/R 0°/26°/35°	Geometry for aileron on VGRWT
Geo # L Tip	L/R 0°/26°/35°	Geometry for skin and internal structure from cut-line to end of wingtip
Geo # L Tip Beam	L/R 0°/26°/35°	Geometry for track and beam structure on moving side of VGRWT
Geo # L Tip Inner	L/R 0°/26°/35°	Geometry for internal structure from cut-line to end of wingtip
FEM L Root	L/R	Finite element mesh for skin and internal structure from BL894 to cut-line

<b>Group Name</b>	<b>Variants</b>	<b>Description</b>
FEM L Root Beam	L/R	Finite element mesh for track and beam structure on fixed side of VGRWT
FEM L Root Inner	L/R	Finite element mesh for internal structure from BL894 to cut-line
FEM # Degrees	0°/26°/35°	Finite element mesh for full SUGAR/VGRTW vehicle
FEM # L Tip	L/R 0°/26°/35°	Finite element mesh for skin and internal structure on moving side of VGRWT
FEM # L Tip Beam	L/R 0°/26°/35°	Finite element mesh for track and beam structure on moving side of VGRWT
FEM # L Tip Inner	L/R 0°/26°/35°	Finite element mesh for internal structure on moving side of VGRWT
FEM # L Tip w Ail	L/R 0°/26°/35°	Finite element mesh for skin, internal structure, and aileron on moving side of VGRWT

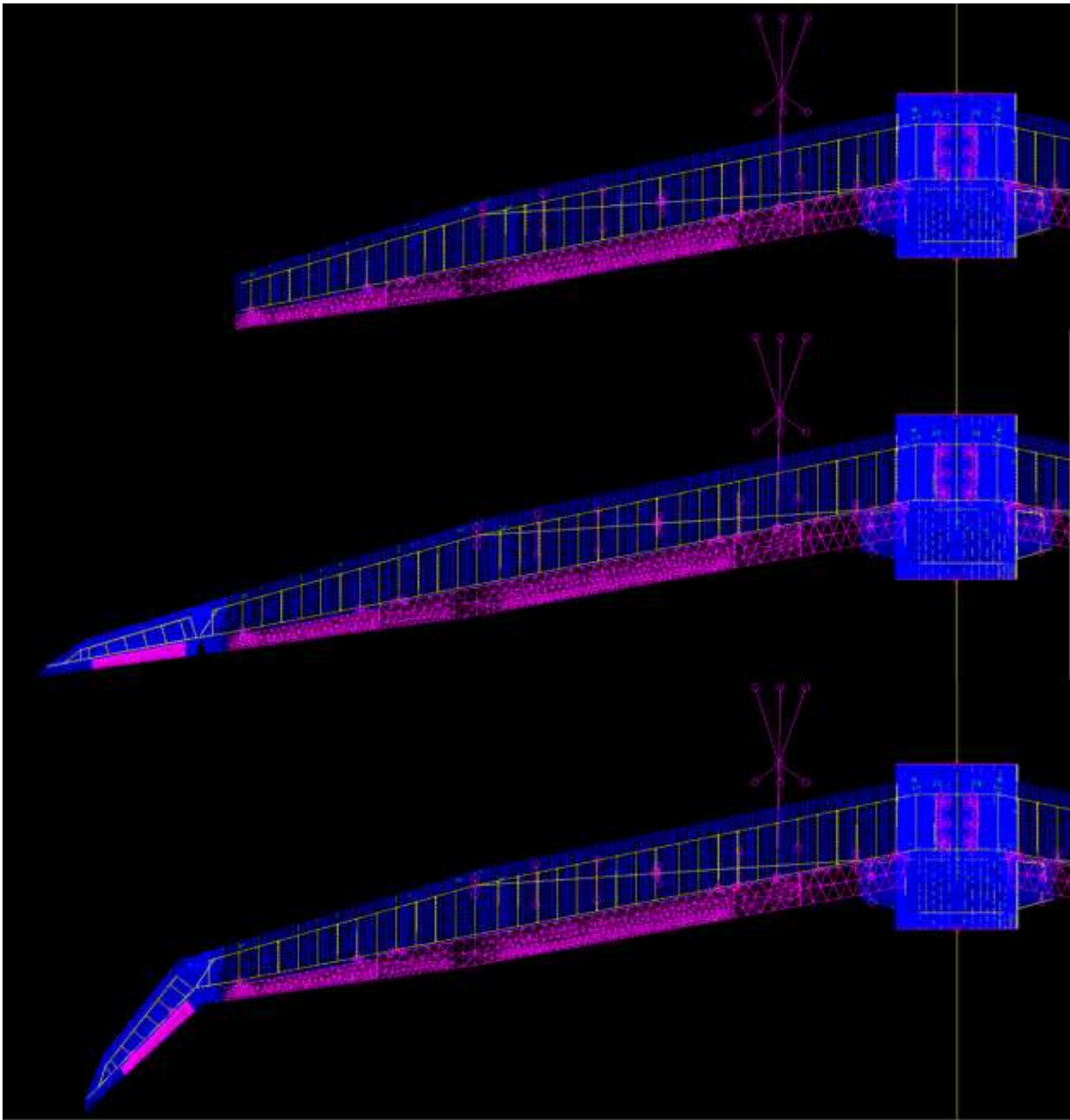


**Figure 108. Top-level view of the baseline SUGAR PATRAN model (top) and integrated VGRWT/SUGAR model in the unswept 0 degree (middle) and fully swept 35 degree (bottom) positions.**

### 9.1.3 Material and Element Selection

The baseline SUGAR model utilizes an optimized distribution of multi-layer oriented composite laminate materials for wing skin and rib web panels. These structures also incorporate smeared stringer reinforcement layers based upon the local load requirements. At the time it was developed, the NCE wingtip structure and loading were not mature enough to require or benefit from this added complexity and detail. Therefore, a single thickness of quasi-isotropic carbon fiber woven composite material found in the SUGAR model was selected for the NCE wingtip skins and spars

and a duplicate material was created (NCE\_mat1.5). The material properties were duplicated so that they might be modified during Task 7.0 without affecting the material properties inboard of the VGRWT. Shell element thickness and spar cap dimensions were initially set based upon prior structural sizing analysis. Quad4 shell elements were used on all skin panels, spar webs, and rib faces. Additionally, 2-D beam elements serve as caps on all spars, as well as on inter-spar rib sections (Figure 109). The wingtip ailerons were modeled as solid features and meshed using Tet4 solid elements, similar to control surfaces in the SUGAR FEM.

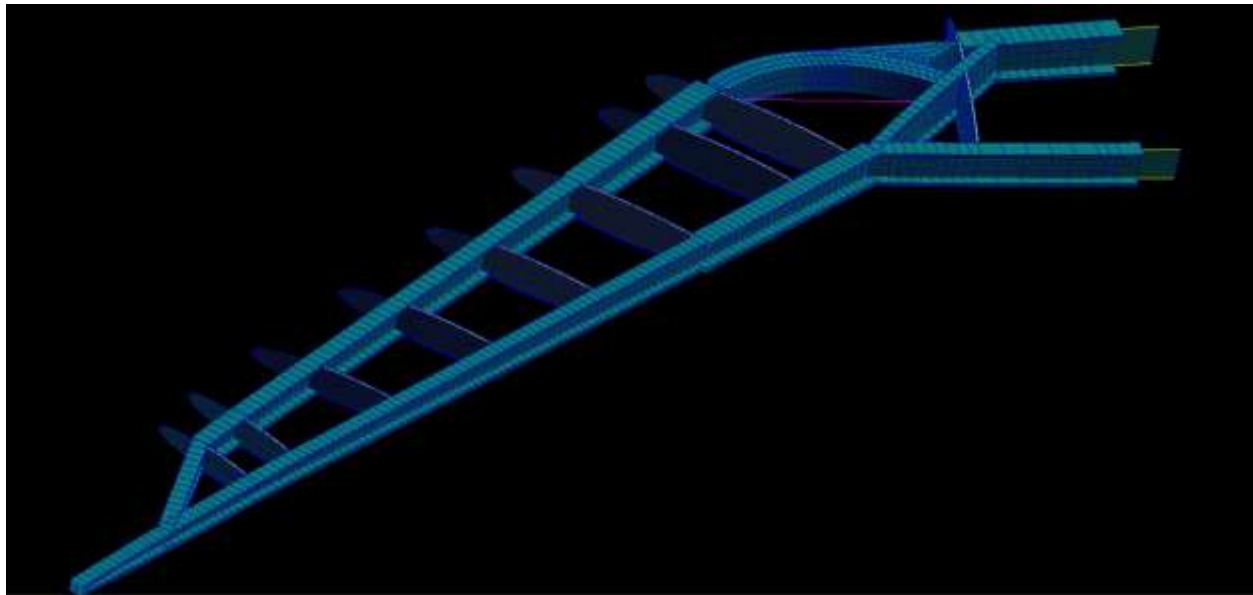


**Figure 109. NCE wingtip internal structural mesh showing element basic layout with 2-D beam element dimensions displayed.**

#### 9.1.4 Component Interfaces

The mechanical interfaces between the variable sweep wingtip and the supporting structures found on the non-moving side of the wing are complex, highly stressed structures (Figure 110). The rear pivot joint in the kinematic model consists of a pinned hinge block with overlapping joint segments. The forward spar load transfer mechanism uses a curved track with a nested beam of equal radius. Both structures have box beam/I-beam hybrid cross sections. Wingtip loads are transferred through contact of the outermost beam surfaces with those that they nest with inside the box portion of the track. Additionally, bearing blocks inside the box portion of the track fill the areas between the beam's outer flange areas for the last 15 degrees of the arc, which always overlap. Within the scope of the aeroelastic analysis, detailed modeling of these load paths was not feasible, requiring that the mechanisms be simplified.

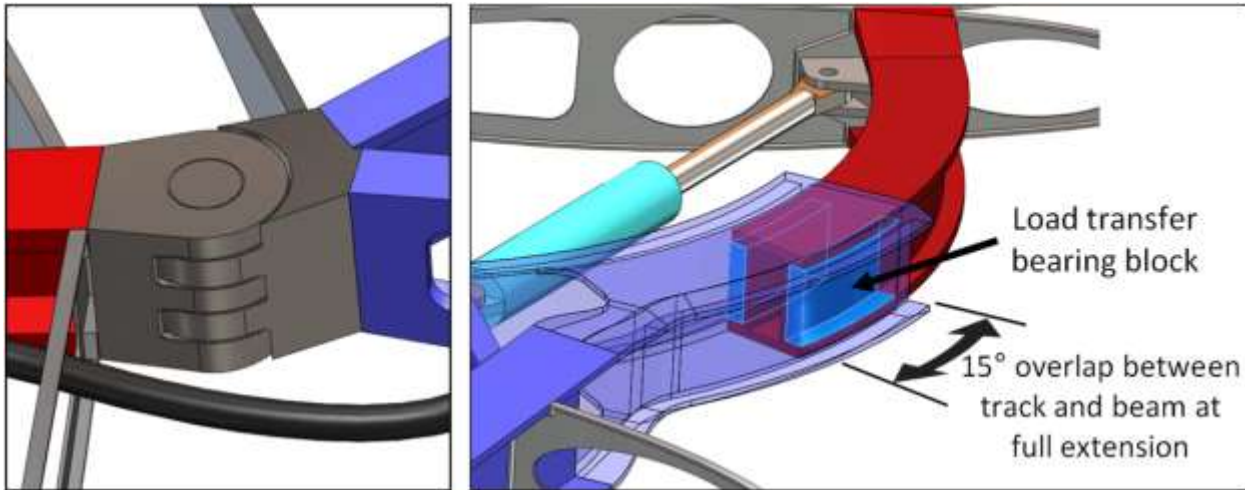


**Figure 110. Kinematic model of variable sweep mechanisms showing rear spar pinned hinge pivot joint (left) and forward track and beam (right) with bearing blocks highlighted (light blue) and track structure set to be transparent (clear blue).**

The rear pivot joint was modeled using RJOINT multi-point constraint (MPC) elements to join the upper and lower spar caps with their counterparts on the variable sweep wingtip (Figure 111). A local coordinate system was created with the Z axis along the pivot axis. The RJOINT elements were constrained in all degrees of freedom except for rotation about the Z axis. This allows for free rotational motion about the wingtip sweep axis while allowing the joint to resist bending and torsional loads from the wingtip.

Initially, the track and beam interface was developed using contact analyses to transfer loads from the wingtip to the root wing spar. Due to requirements for aeroelastic analysis, the non-linear solution required for contact analysis could not be used. As such, the track and beam interface was modeled with a pair of rigid body element 2 (RBE2) MPC's connecting the upper and lower ends of the beam to the nearest surface nodes on the track and vice versa (Figures 111, 112). These MPC's were constrained against translation along the pivot joint coordinate system's Z axis and against rotation about the X and Y axes as defined by the pivot joint local coordinate system. This kept the upper and lower track and beam contact surfaces in the same plane at the MPC attachment points, transferring bending and torsional loads, while keeping the beam free to slide in and out of the track. The fixed ends of the track and beam were attached to their respective spar caps using RBE2's with all degrees of freedom constrained.

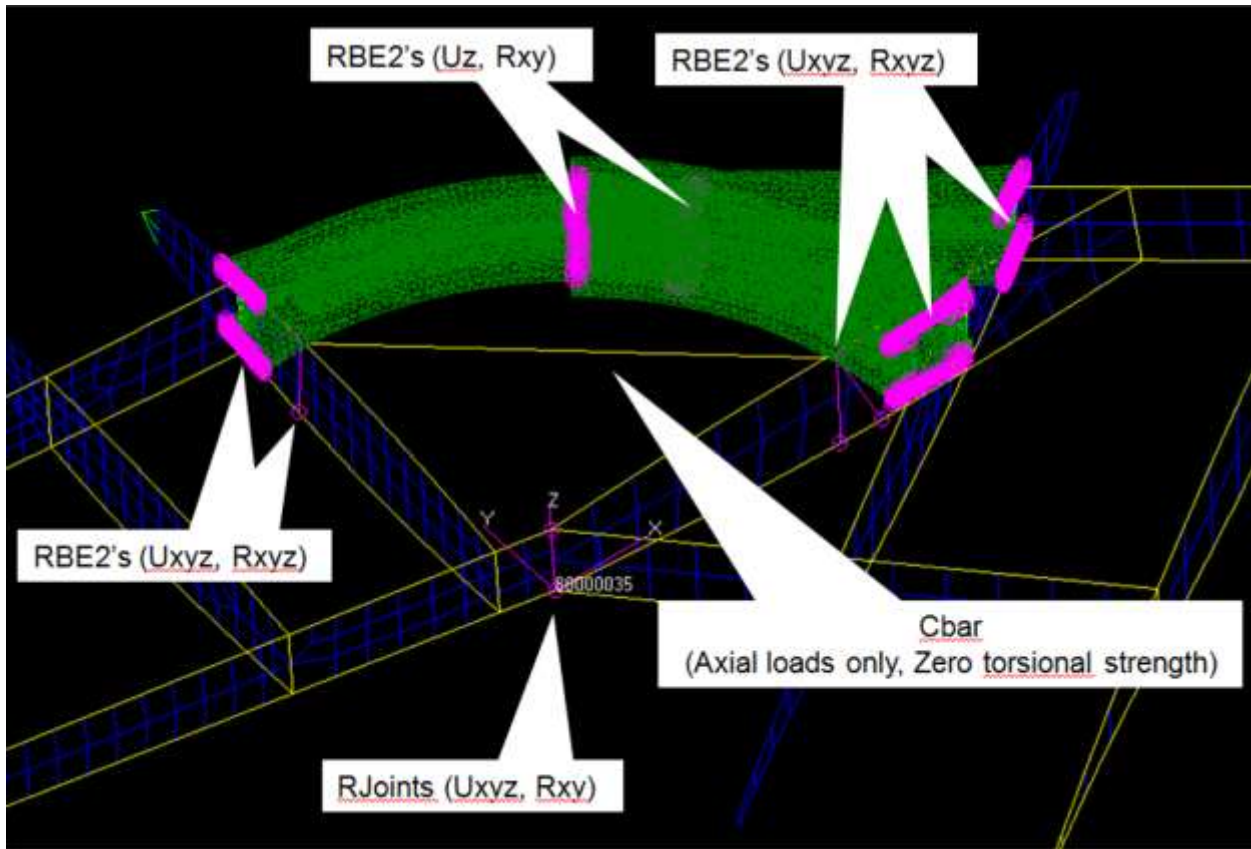
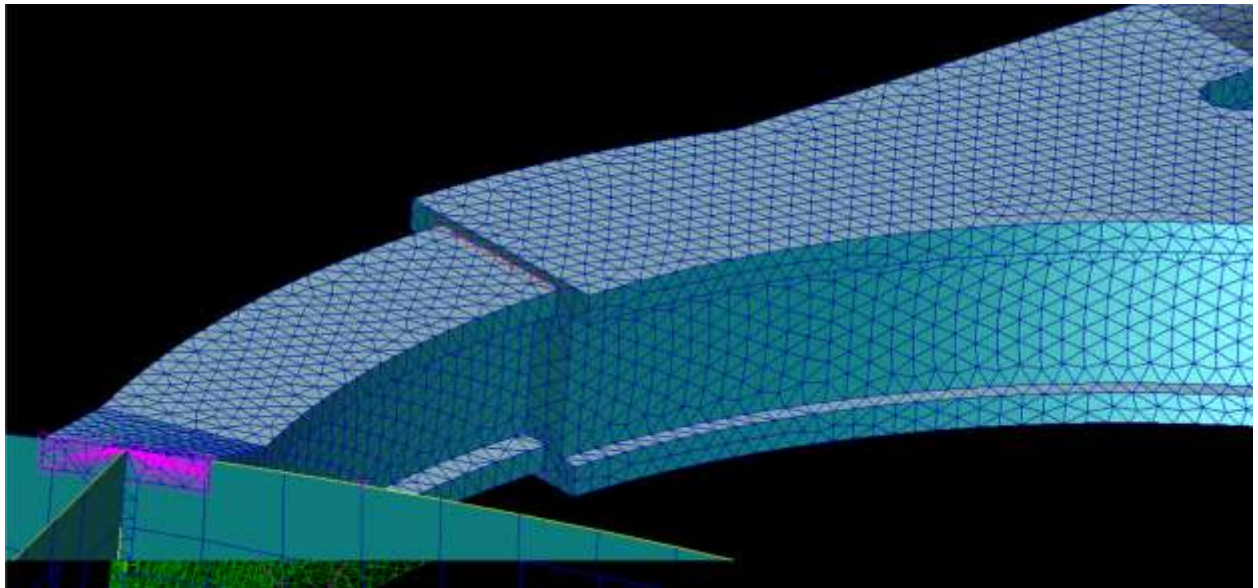


Figure 111. MPC elements used to model the track and beam interface, track and beam attachment points, rear pivot joint, and wingtip sweep actuator attachment points. Constrained degrees of freedom are listed for each element group and are referenced to the local coordinate system defining the wing sweep pivot axis.



**Figure 112.** Track and beam interface for 26 degree sweep case. MPC elements (pink) are located at the upper and lower ends of the track and the upper and lower ends of the beam which nests inside the track. Solid elements show on top for clarity. Skeleton view on bottom shows the internal connection between the end of the beam and inside of the track. Note that the MPC on far left is used to rigidly attach the upper beam cap to the wingtip upper spar cap.

At the time the FEM was being developed, no wing sweep or aileron actuator parameters or requirements had been specifically identified. As such, the wing sweep actuator was assumed to effectively lock the wingtip sweep angle and was modeled using a CBAR element with a representative cross sectional area connecting two RBE2's which represented actuator attachment points. Once an actual actuator is selected and its performance is described, the CBAR element can be replaced with a spring element incorporating appropriate axial stiffness and deflection limits.

The aileron hinges were modeled in the same manner as the control surfaces found in the baseline SUGAR model. Aileron attachment points were created using sets of RBE2 MPCs at the ribs nearest the aileron root and tip similar to the SUGAR FEM (Figure 113). One RBE2 rigidly connects the aileron to the hinge axis while a second rigidly connects the hinge axis to the base of the local rib. A third RBE2 connects the other two RBE2's to each other at their hinge axis ends and constrains motion about the axis. A local coordinate system was created to define the aileron hinge axis for each wingtip sweep angle case.

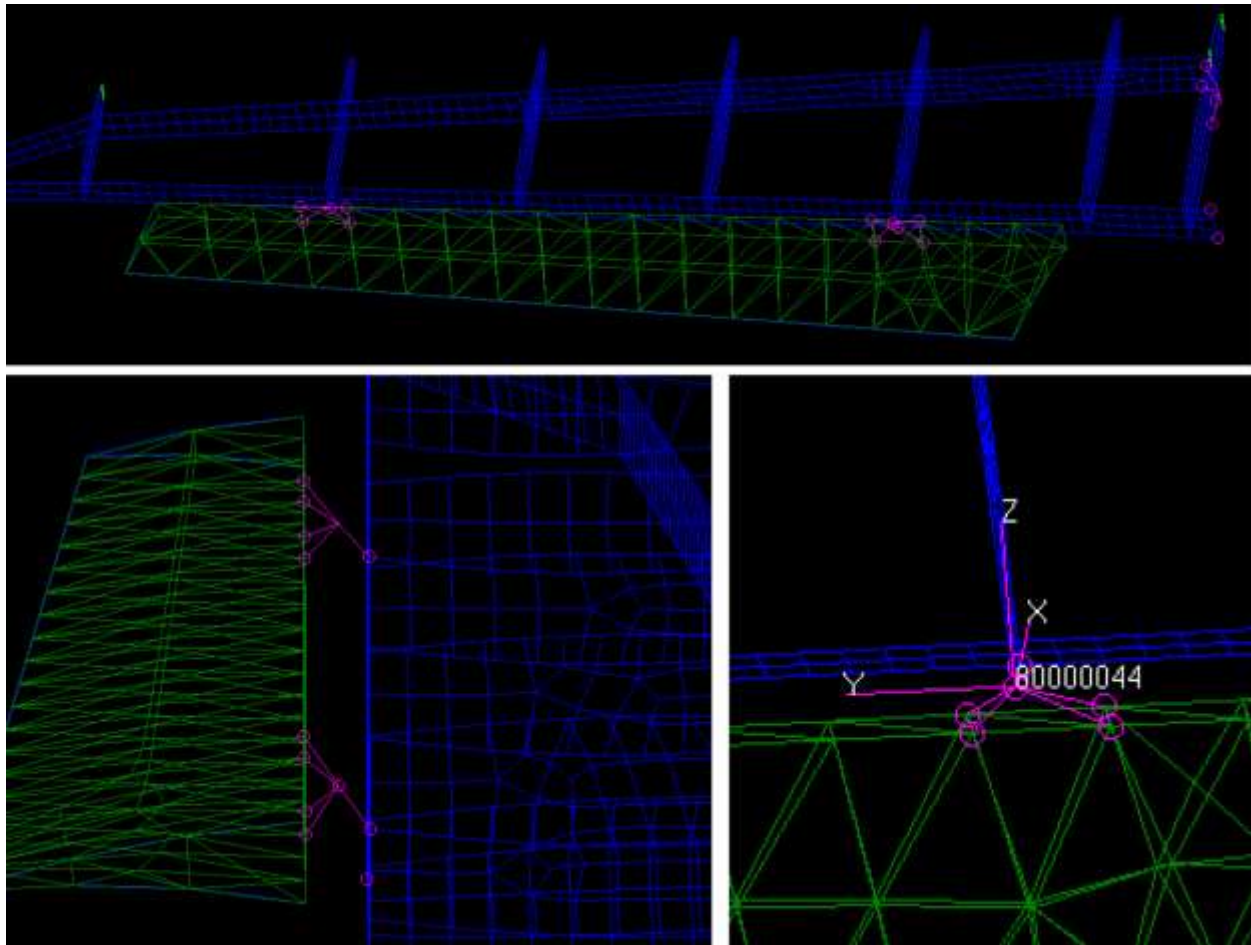


**Figure 113. RBE2 Elements (pink) Modeling the Aileron Hinges (top, bottom left) and the Local Coordinate System Defining the Hinge Axis and MPC Constraints**

The leading edge wingtip fairing was modeled similarly to the wing skin. The fairing is attached on the wingtip side only and does not currently interact or transfer load to the root side skin, forcing aerodynamic loading on the fairing to be transferred through the track and beam and rear pivot structures. The trailing edge fairing was not included as it was not yet defined when the FEM was being developed, however the aerodynamic loads that it would normally carry will be applied to the nearest internal structural hardpoint for the Task 7.0 aeroelastic analysis. Also, non-structural mass was added at that time to account for the estimated mass of the rear fairing.

### 9.1.5 FEM Analysis

Development of the initial VGRWT FEM was completed and the model was delivered to Virginia Tech for use in Task 7.0. Completing a clean analysis run with the model proved difficult due to errors resulting from single point constraint (SPC)/multi-point constraints generating unsolvable load paths. The model would not run without incorporating a bailout parameter, however the results from running with the bailout included appeared to be appropriate. Initially, it was thought that these errors were due to the MPC's used to model the rear pivot point and track/beam connections (Figure 111). Simplified test models were created to allow testing variations of these connection designs in order to resolve the analysis error. These tests did not indicate that the design of the wingtip mechanism connections were the source of the error. After much investigation, it

was determined that the error was due to solid Tet10 elements used to model the ailerons. An error in the PATRAN software included rotational degrees of freedom for midpoint nodes on these elements, which are not allowed for solid elements. Changing these elements to Tet4 solid elements resolved the error messages, allowing the model to be run without a bailout parameter.

Nonstructural masses were added to the VGRWT FEM by VT during Task 7.0 according to information provided by Boeing. These masses represented wiring, electromagnetic protection, lighting, paint, actuators for wing sweep and ailerons, and the flexible trailing edge fairing. Additional nonstructural masses were added to represent various fuel load cases.

## 10. AIRPLANE AEROELASTIC/CONTROLLABILITY VALIDATION

### 10.1 SUGAR VGRWT AEROELASTIC ANALYSIS

The goal of Task 7 was to assess aeroelastic performance of the SUGAR aircraft when equipped with the Variable Geometry Raked WingTip (VGRWT). The VGRWT is also referred to as the Novel Control Effector (NCE) due to its functionality in providing active aeroelastic tuning of the vehicle roll control capability. Specific items for this task were: 1) to predict flutter speeds of the new aircraft for different values of the NCE sweep, and 2) to predict lateral stability derivatives and Elastic-to-Rigid Ratios (E/R) for the various sweep configurations. These calculations were performed using NASTRAN Flightloads software. For purposes of comparison, results for the baseline SUGAR aircraft without VGRWT are also provided when useful. This baseline SUGAR aircraft FEM was provided by Boeing on Sept 22<sup>nd</sup> 2012 and was titled "sugar\_tbw\_config1\_1.1Vd\_r120917".

#### 10.1.1 Finite Element Model

Virginia Tech (VT) was provided a structural FEM from NextGen Aeronautics which included the NCE actuation mechanism and NCE wingtip additions to the SUGAR aircraft. This structural FEM is shown in Figure 114 for the case of  $\frac{3}{4}$  sweep (26 degree) configuration. VT then worked with NextGen and Boeing team members to develop the appropriate mass allocation for the NCE wingtip. The final mass allocation, including the structural and nonstructural mass, resulted in an NCE wingtip with a planform weight of approximately 10 psf, which was similar to that of the baseline SUGAR wingtip. The NCE wingtip with the included nonstructural mass items is shown in Figure 115. Once the structural FEM of the NCE aircraft was complete, VT performed a normal modes analysis and compared results to the baseline SUGAR aircraft. This comparison of the flexible modes for the 0-degree NCE is provided in Appendix C (Figure C-1 through Figure C-18) for the case of full-fuel.

Once the structural FEM was complete VT developed the NASTRAN FlightLoads aero-mesh, aero-to-structure splines, and associated aeroelastic analyses for Task 7. During the previously completed Task 5, VT calculated the forces and moments generated by the NCE aileron about the wing elastic axis. It was determined that the maximum moment occurred at the  $\frac{3}{4}$  sweep, or 26-degree position. For this reason the 26-degree configuration was selected for analysis during Task 7 in addition to the 0-degree configuration. The vortex lattice aero-mesh for the 0-degree and 26-degree configurations is shown in Figure 116 and Figure 117, respectively. A detailed view of the corresponding NCE structural FEM is also shown in these figures. These models provided the basis for the flutter and lateral trim analyses presented in the sections below.

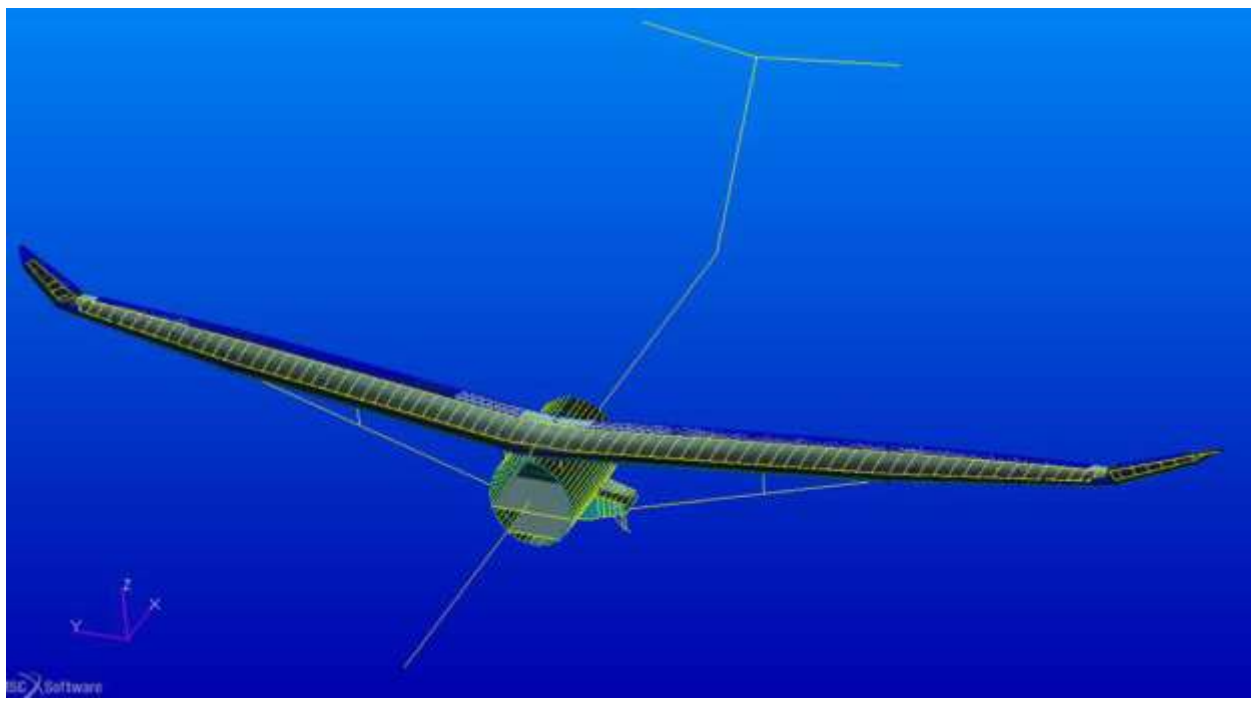


Figure 114. The structural FEM of the NCE equipped aircraft was developed by NextGen and provided to VT. The 26-degree, or  $\frac{3}{4}$  sweep configuration is shown here.

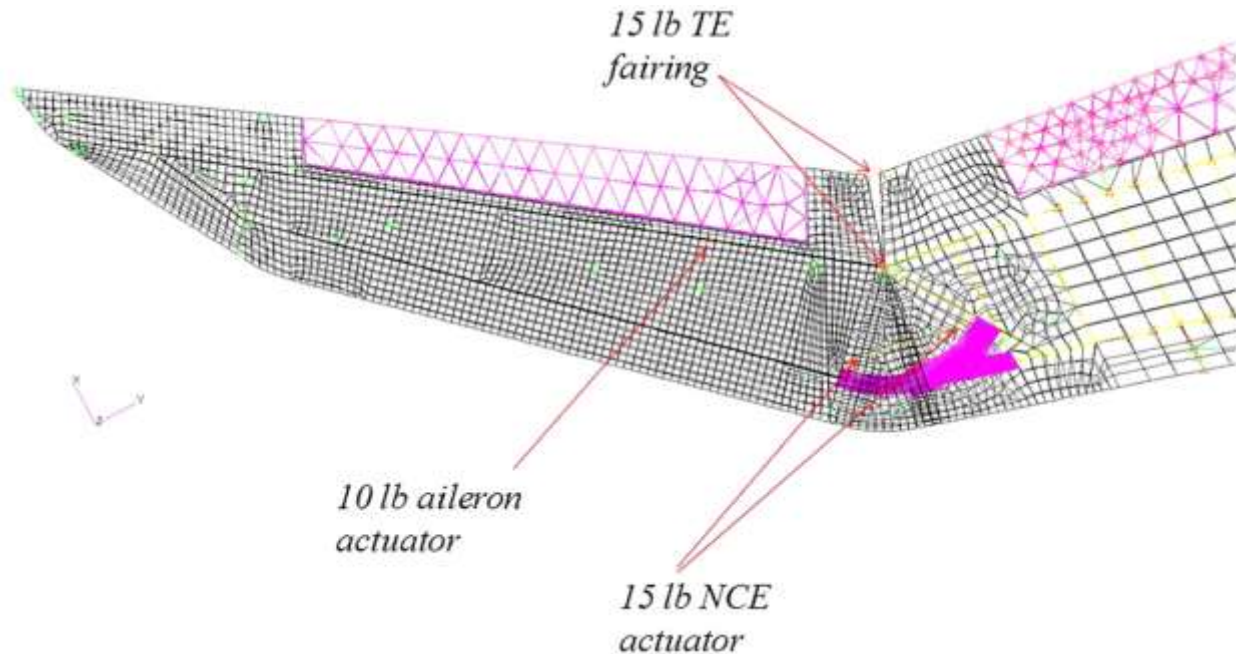


Figure 115. The important nonstructural masses were added to the FEM. The total planform weight of the NCE wingtip (structural + non-structural) was similar to the baseline sugar (10 psf).

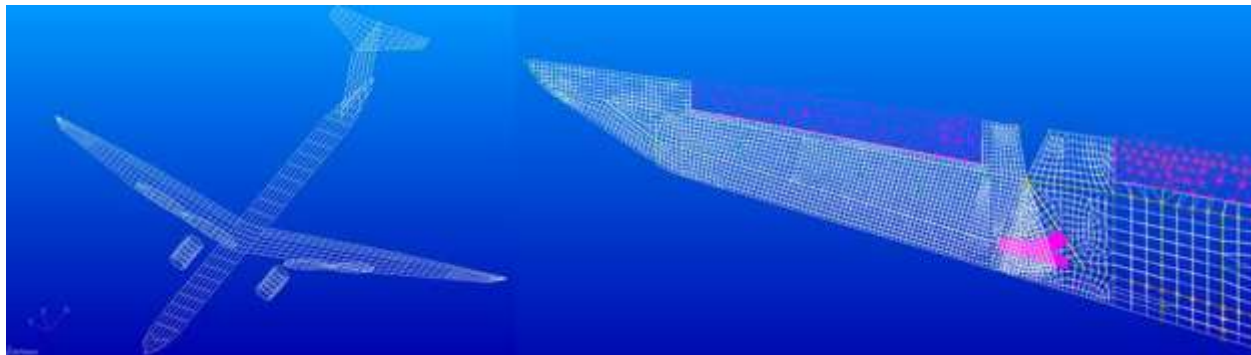


Figure 116. A new aero-mesh (left) was developed for the 0-degree NCE FEM (right).

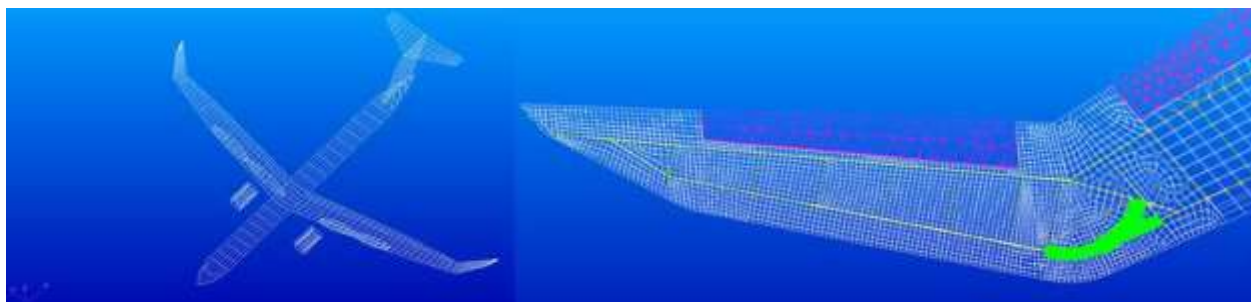


Figure 117. A new aero-mesh (left) was developed for the 26-degree NCE FEM (right).

### 10.1.2 Flutter Analysis

The doublet lattice aerodynamic model of the NCE aircraft included aerodynamic correction factors used to improve estimates of the lift slope (WTFAC). The aerodynamic corrections applied to the NCE aerodynamic model were based on Boeing Overflow CFD analyses performed for the baseline SUGAR aircraft during the NASA Contract NNL08AA16B - NNL11AA00T - Subsonic Ultra Green Aircraft Research. Since the NCE aero-mesh inboard of the NCE wingtip remained unchanged, the existing SUGAR aerodynamic correction factors could be applied directly. However, for the NCE wingtip, the aerodynamic corrections were extrapolated from the values just inboard of the NCE cut-line and applied to the new aero-mesh elements that comprised the NCE wingtip. Figure 118 illustrates the baseline SUGAR wingtip overlaid with the NCE wingtip and the extrapolated WTFAC values that were applied to new portions of the NCE aero-mesh.

Previous work by Boeing on the baseline SUGAR aircraft determined that the critical Mach for flutter instabilities occurred at Mach 0.82 for the two mass cases considered. The first mass case has full-fuel and payload to reach maximum takeoff weight. The second mass case has reserve-fuel and maximum payload. Flutter analysis of the NCE equipped SUGAR aircraft were also run at Mach 0.82 and for the full-fuel and reserve-fuel mass cases and included all modes up to 20 Hz. In addition to the two mass cases, the NCE model was also analyzed at 2 different sweep settings (0-degree and 26-degree). Finally, a wing-tip mass sensitivity study was performed to determine the impact on flutter velocity when mass was added to the aft portion of the wing. Details of the Full Fuel, Reserve Fuel, and Mass Sensitivity analyses are provided in Sections 10.1.2.1, 10.1.2.2, and 10.1.2.3, respectively. A summary of the flutter results is provided in Table 31.

**Table 31. Summary of flutter speeds for the baseline SUGAR aircraft and the NCE equipped aircraft.**

Configuration	Flutter Speed (keas)	
	Full Fuel	Reserve Fuel
Baseline SUGAR	401	401
0-degree NCE	320	296
26-degree NCE	363	327

#### 10.1.2.1 Full-Fuel Results

Appendix C provides illustrations of the structural modes contributing to flutter for the 0-degree and 26-degree full fuel case. Figure 119 shows the velocity vs. damping ( $v-g$ ) plot for the critical flutter modes of the 0-degree and 26-degree NCE configurations when loaded with full-fuel and max-payload. The baseline SUGAR critical flutter mode is also shown for comparison. Critical flutter speeds were taken as the point where the curve crosses the 2% damping line in order to allow for some amount of inherent structural damping. It can be seen that the baseline SUGAR flutter speed was 401 KEAS while the 26-degree NCE flutter speed was reduced to 363 KEAS and the 0-degree NCE reduced even further to 320 KEAS.

The flutter mode for the full-fuel 0-degree NCE is shown in Figure 120 while plots of velocity vs. frequency ( $v-f$ ) and  $v-g$  for all modes are provided in Figure 121 and Figure 122. It can be seen in Figure 121 that symmetric structural modes 11(bending) and 16 (torsion) are converging along with the anti-symmetric mode 15 to initiate the flutter mode evident in Figure 120. The flutter mode is primarily symmetric but close inspection of the wingtip contours reveals some asymmetric contribution from mode 15.

The flutter mode for the full-fuel 26-degree NCE is shown in Figure 123 while plots of velocity vs. frequency ( $v-f$ ) and  $v-g$  for all modes are provided in Figure 124 and Figure 125. Similar to the 0-degree results, it can be seen in Figure 123 that symmetric structural modes 11 (bending) and 16 (torsion) are converging along with the anti-symmetric mode 15 to initiate the flutter mode evident in Figure 123. The flutter mode is primarily symmetric but close inspection of the wingtip contours reveals some asymmetric contribution from mode 15.

#### 10.1.2.2 Reserve-Fuel Results

Appendix C provides illustrations of the structural modes contributing to flutter for the 0-degree and 26-degree reserve fuel case. Figure 126 shows the velocity vs. damping ( $v-g$ ) plot for the critical flutter modes of the 0-degree and 26-degree NCE configurations when loaded with reserve fuel and max-payload. The baseline SUGAR critical flutter mode is also shown for comparison. Critical flutter speeds were taken as the point where the curve crosses the 2% damping line in order to allow for some amount of inherent structural damping. It can be seen that the baseline SUGAR flutter speed was 401 KEAS while the 26-degree NCE flutter speed was reduced to 327 KEAS and the 0-degree NCE reduced even further to 296 KEAS.

The flutter mode for the reserve-fuel 0-degree NCE is shown in Figure 127 while plots of velocity vs. frequency ( $v-f$ ) and  $v-g$  for all modes are provided in Figure 128 and Figure 129. It can be seen in Figure 128 that symmetric structural modes 11 (bending) and 16 (torsion) are converging along with the anti-symmetric modes 10 and 15 to initiate the flutter mode evident in Figure 120. The flutter mode is primarily symmetric but close inspection of the wingtip contours reveals some asymmetric contribution from modes 10 and 15.

The flutter mode for the reserve-fuel 26-degree NCE is shown in Figure 130 while plots of velocity vs. frequency (v-f) and v-g for all modes are provided in Figure 131 and Figure 132. Similar to the 0-degree results, it can be seen in Figure 130 that symmetric structural modes 11 (bending) and 16 (torsion) are converging along with the anti-symmetric modes 10 and 15 to initiate the flutter mode evident in Figure 130. The flutter mode is primarily symmetric but close inspection of the wingtip contours reveals some asymmetric contribution from mode 15.

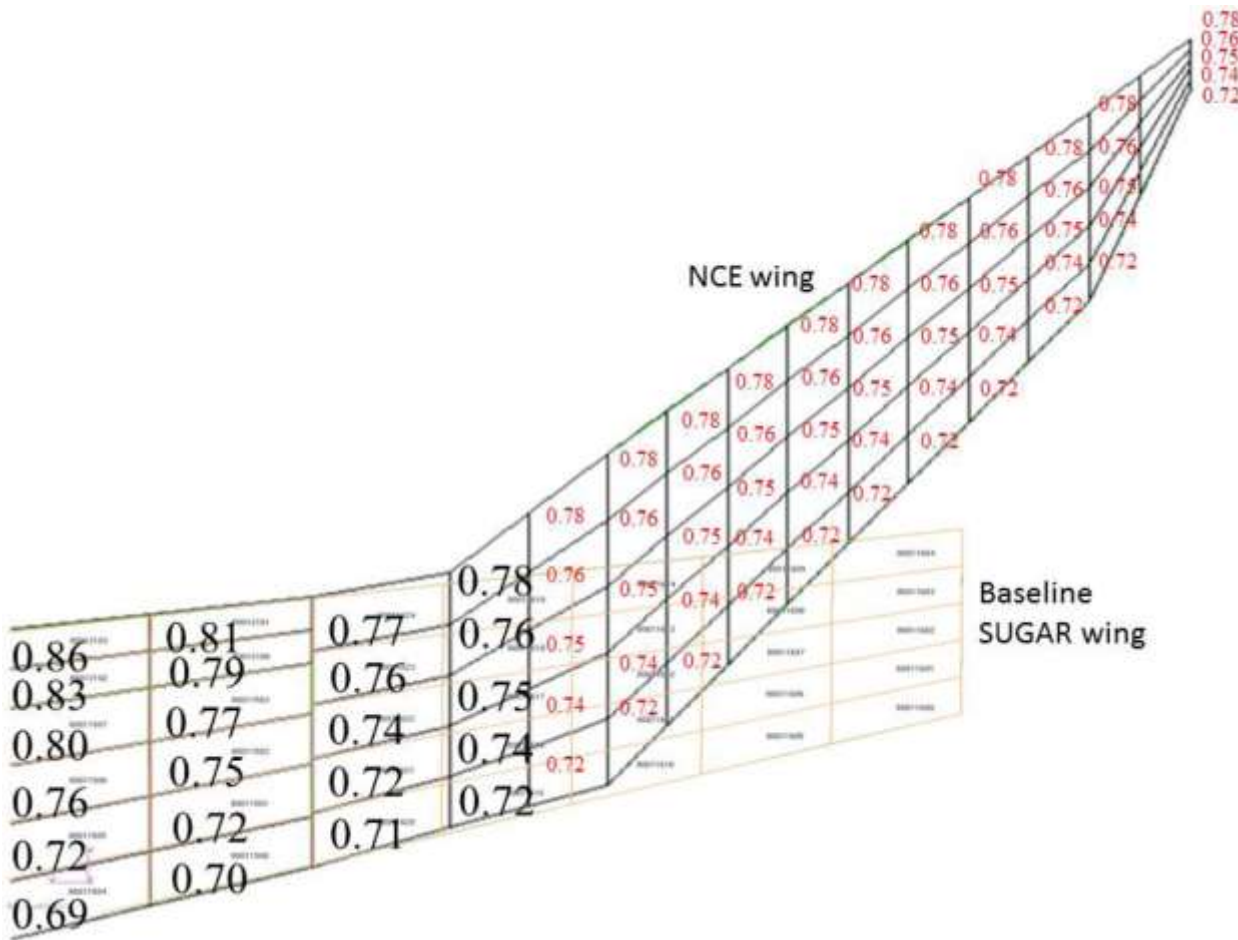


**Figure 118.** Box-by-box aerodynamic weight factors (NASTRAN WTFAC) were applied to the NCE. These values were approximated from the baseline SUGAR aircraft (Boeing Overflow #'s @ Mach 0.82).

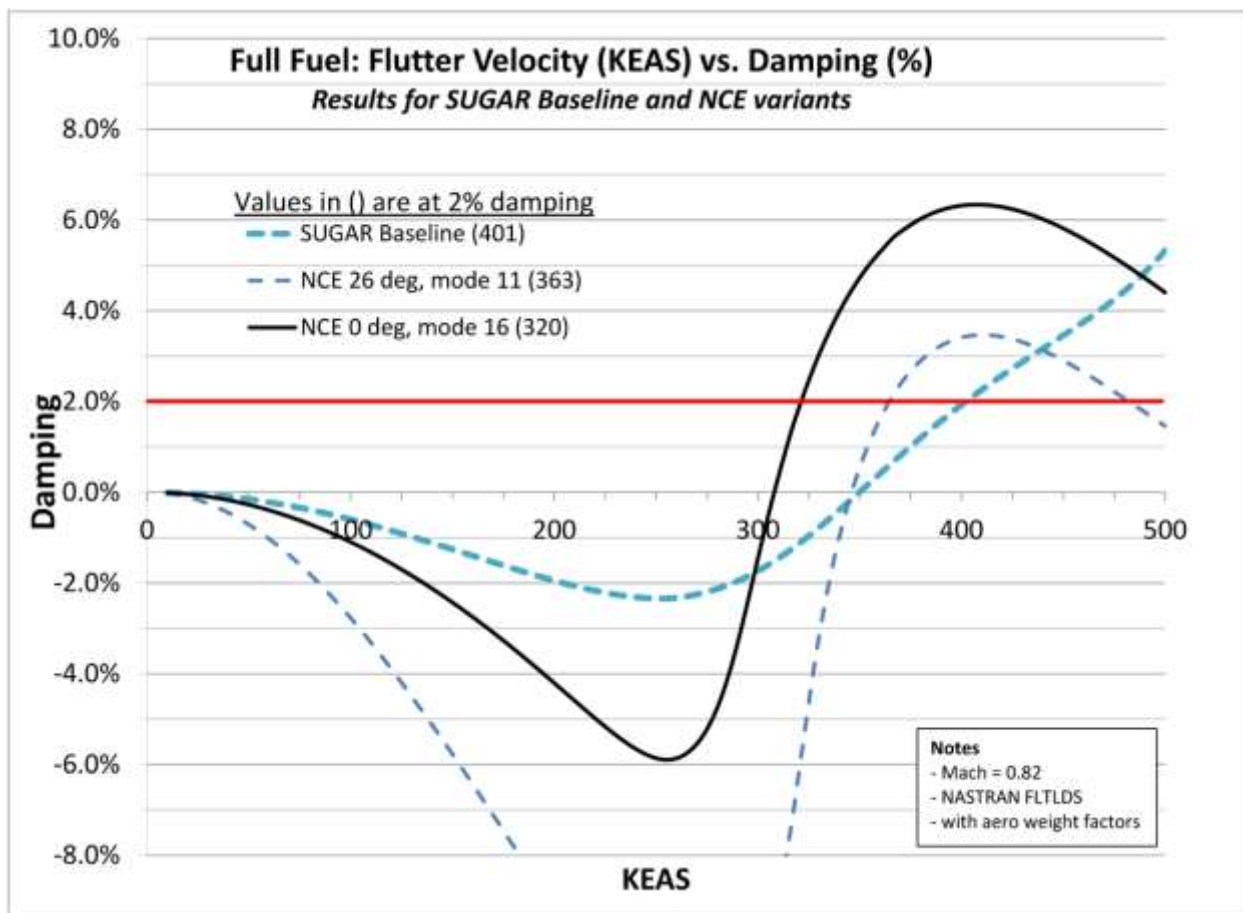


Figure 119. The V-G plot of the critical flutter mode for the full fuel case. Results are shown for the 0-degree and 26-degree NCE configurations as well as the baseline SUGAR aircraft.

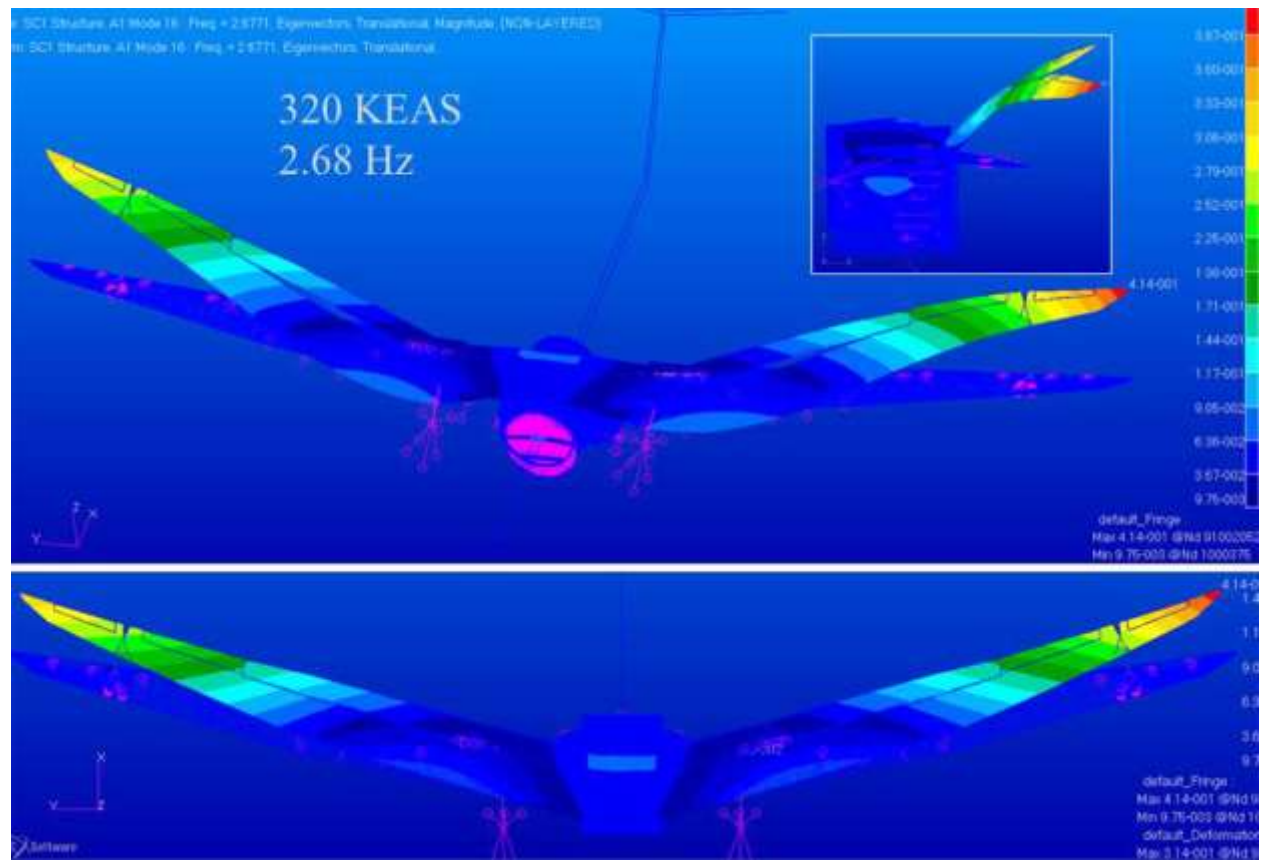


Figure 120. Critical flutter mode for 0-degree NCE full fuel case. 320 KEAS and 2.68 Hz.

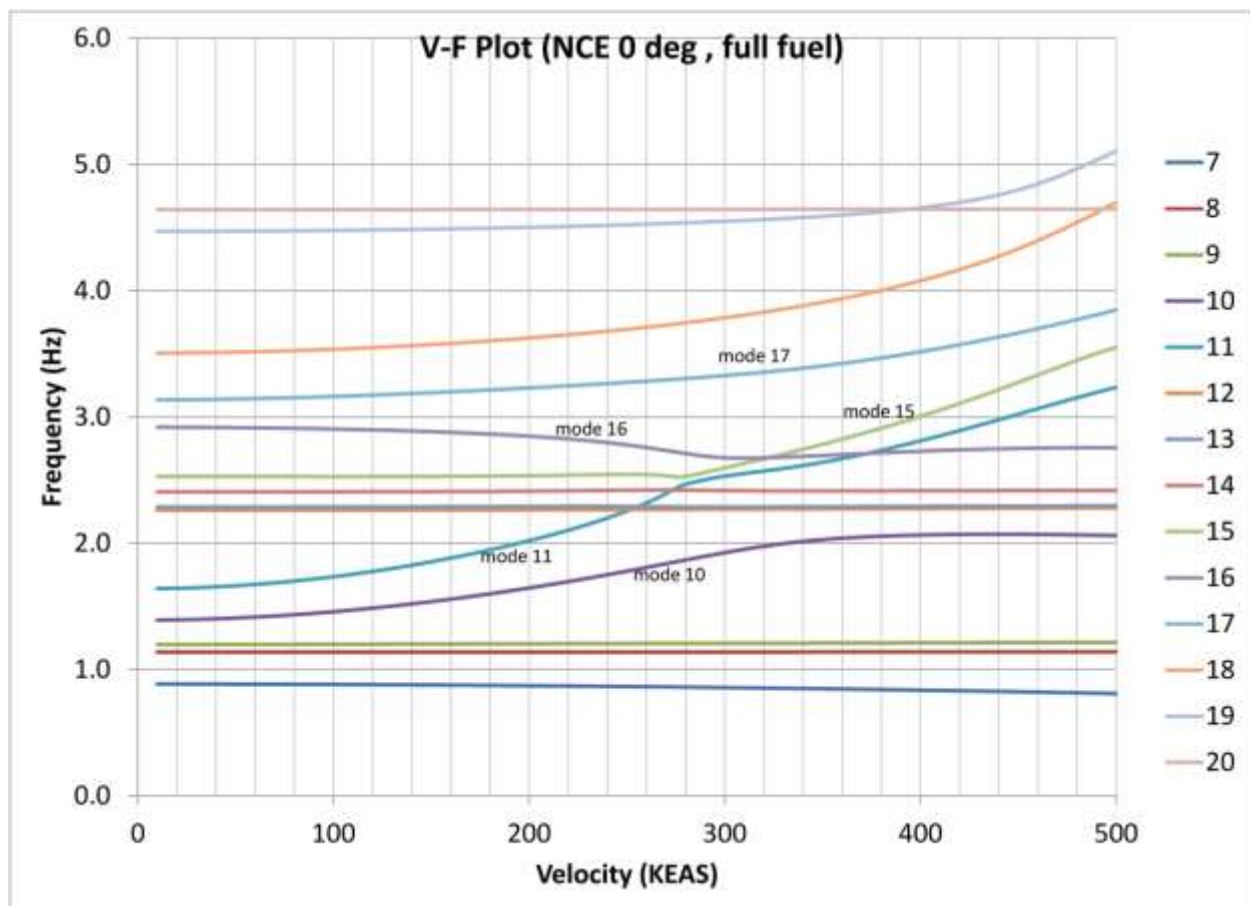


Figure 121. V-F plot for NCE 0-degree full fuel case.

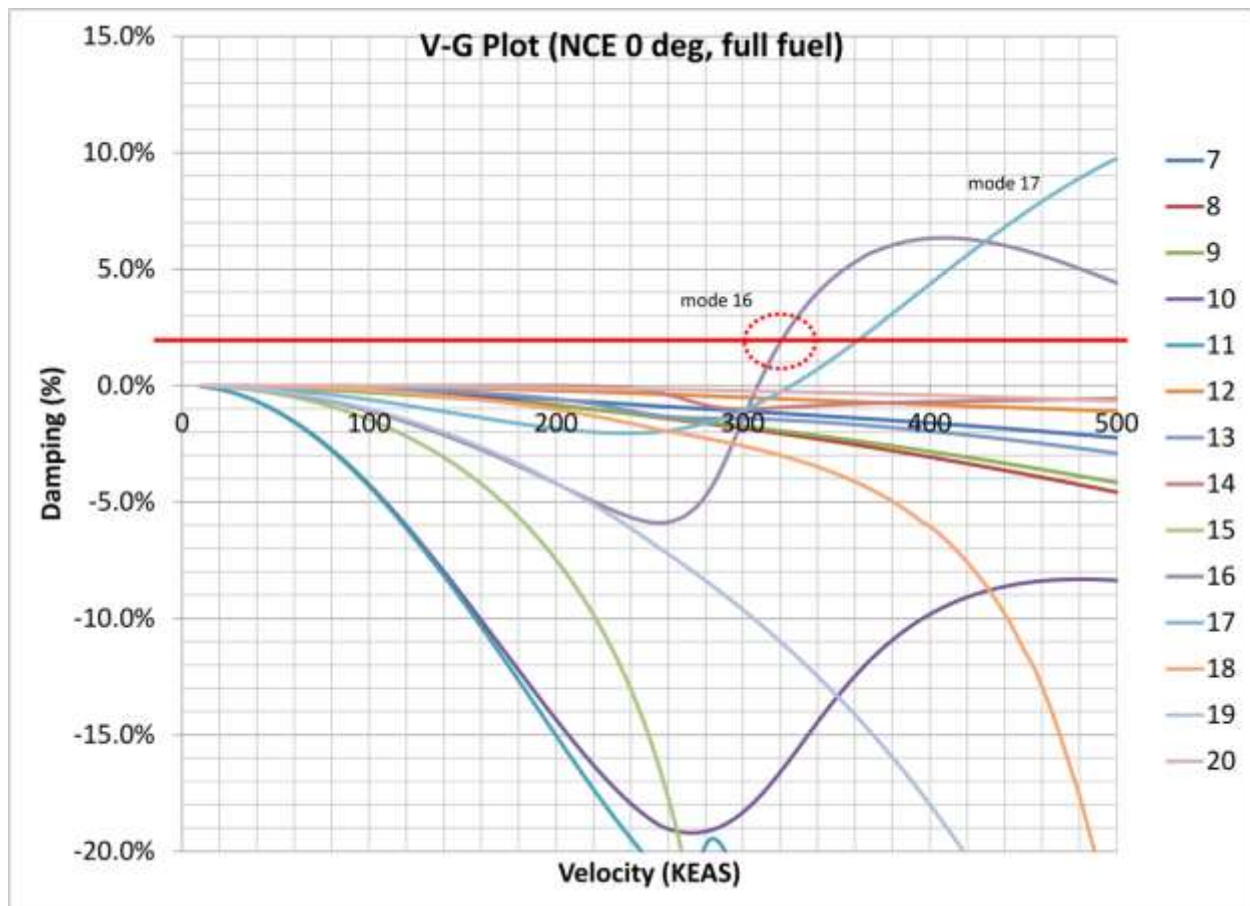
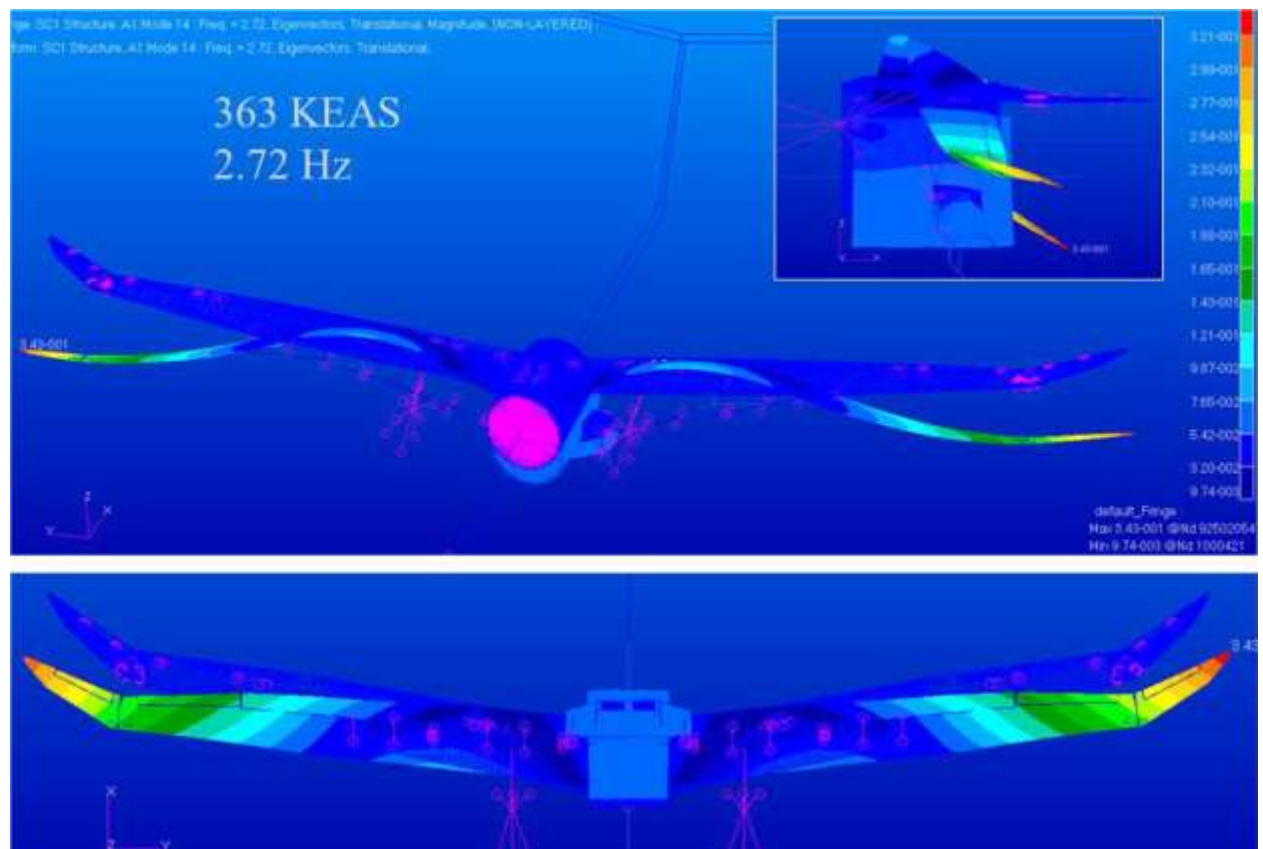


Figure 122. V-G plot for NCE 0-degree full fuel case.



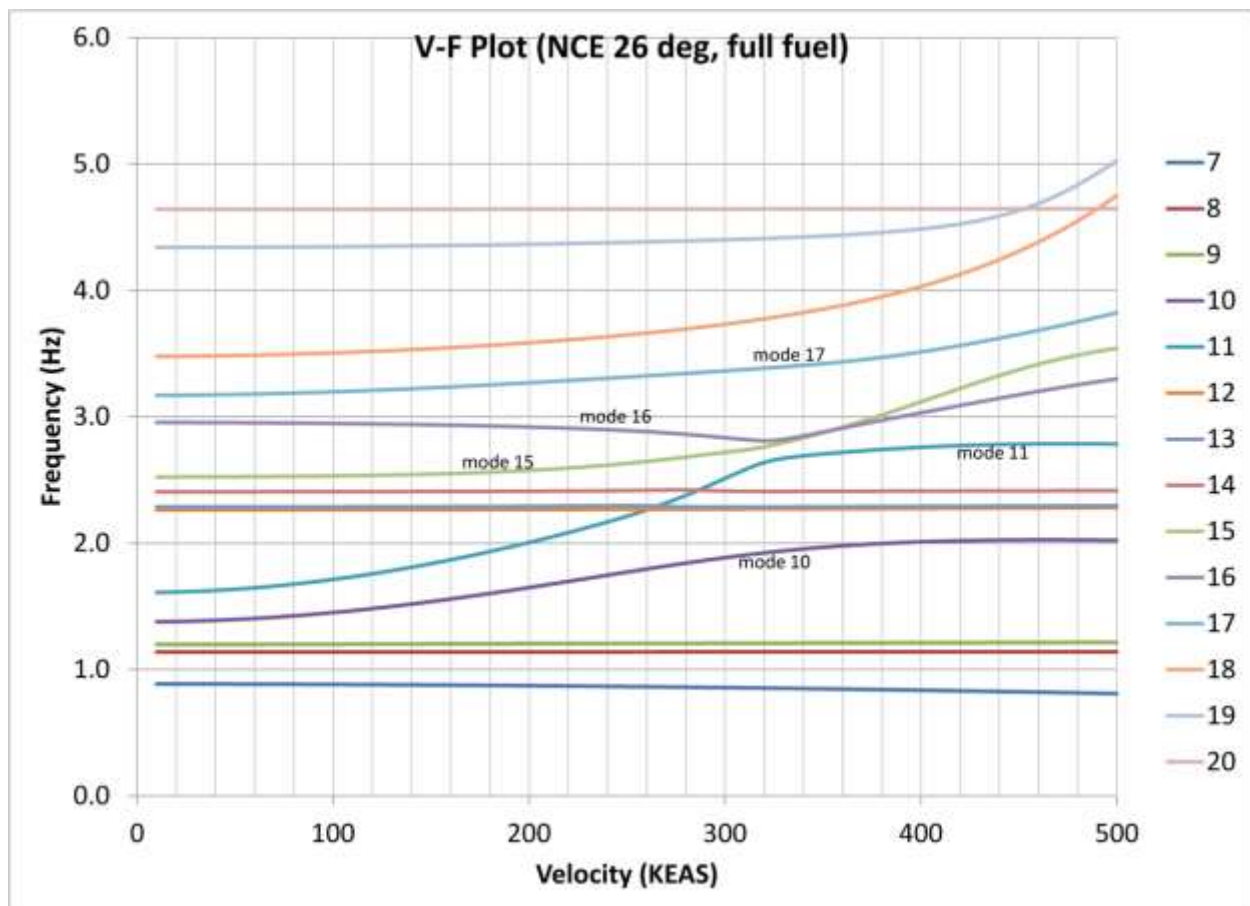


Figure 124. V-F plot for NCE 26-degree full fuel case.

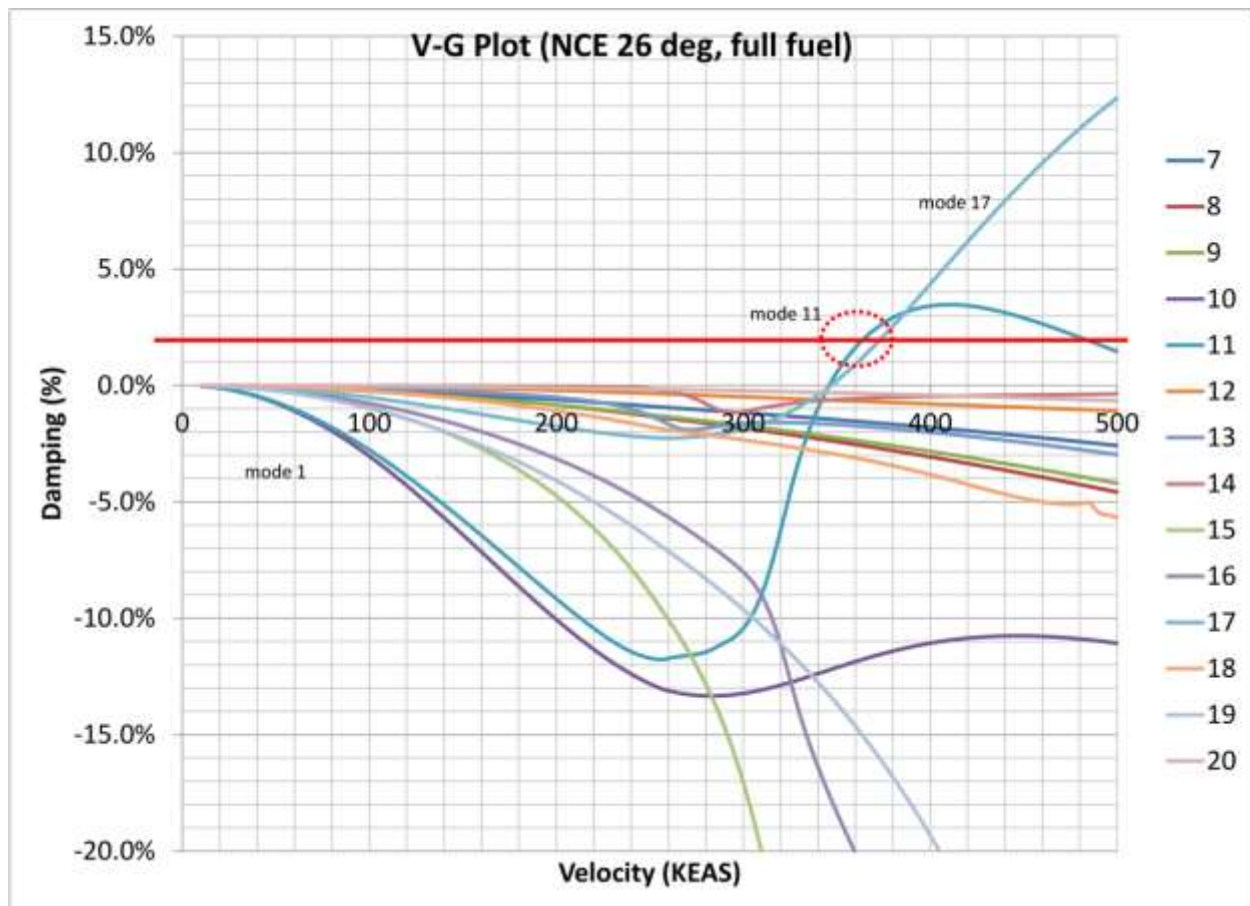


Figure 125. V-G plot for NCE 26-degree full fuel case.

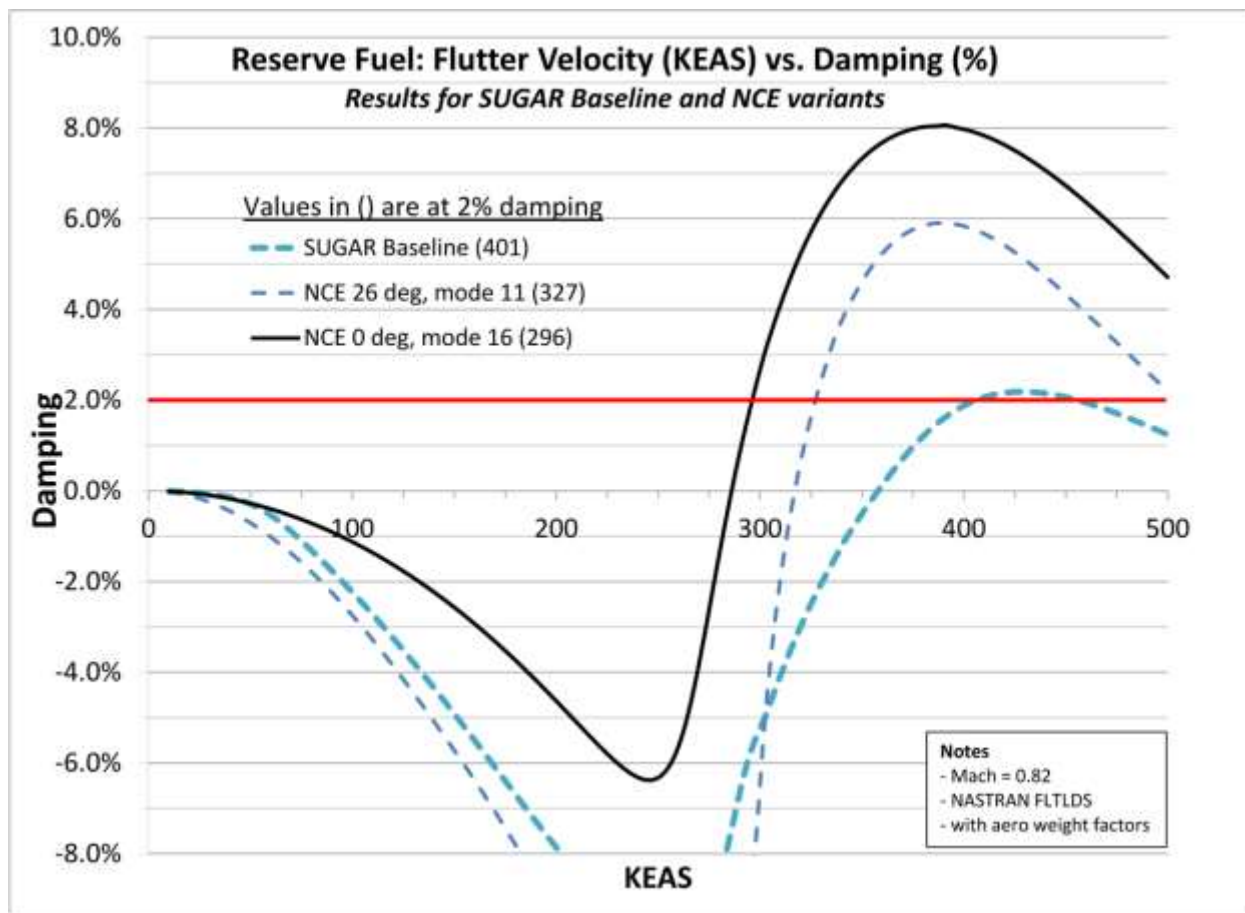


Figure 126. The V-G plot of the critical flutter mode for the reserve fuel case. Results are shown for the 0-degree and 26-degree NCE configurations as well as the baseline SUGAR aircraft.

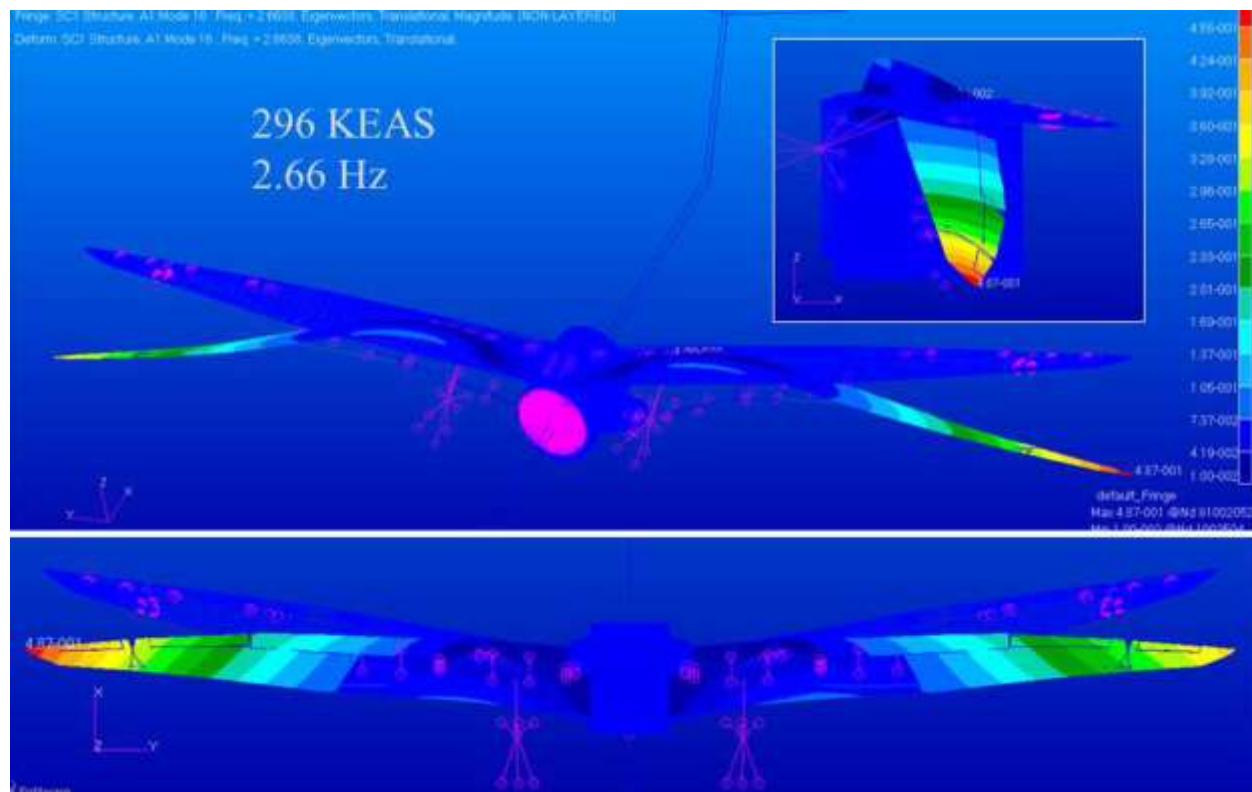


Figure 127. Critical flutter mode for 0-degree NCE reserve fuel case. 296 KEAS and 2.66 Hz.

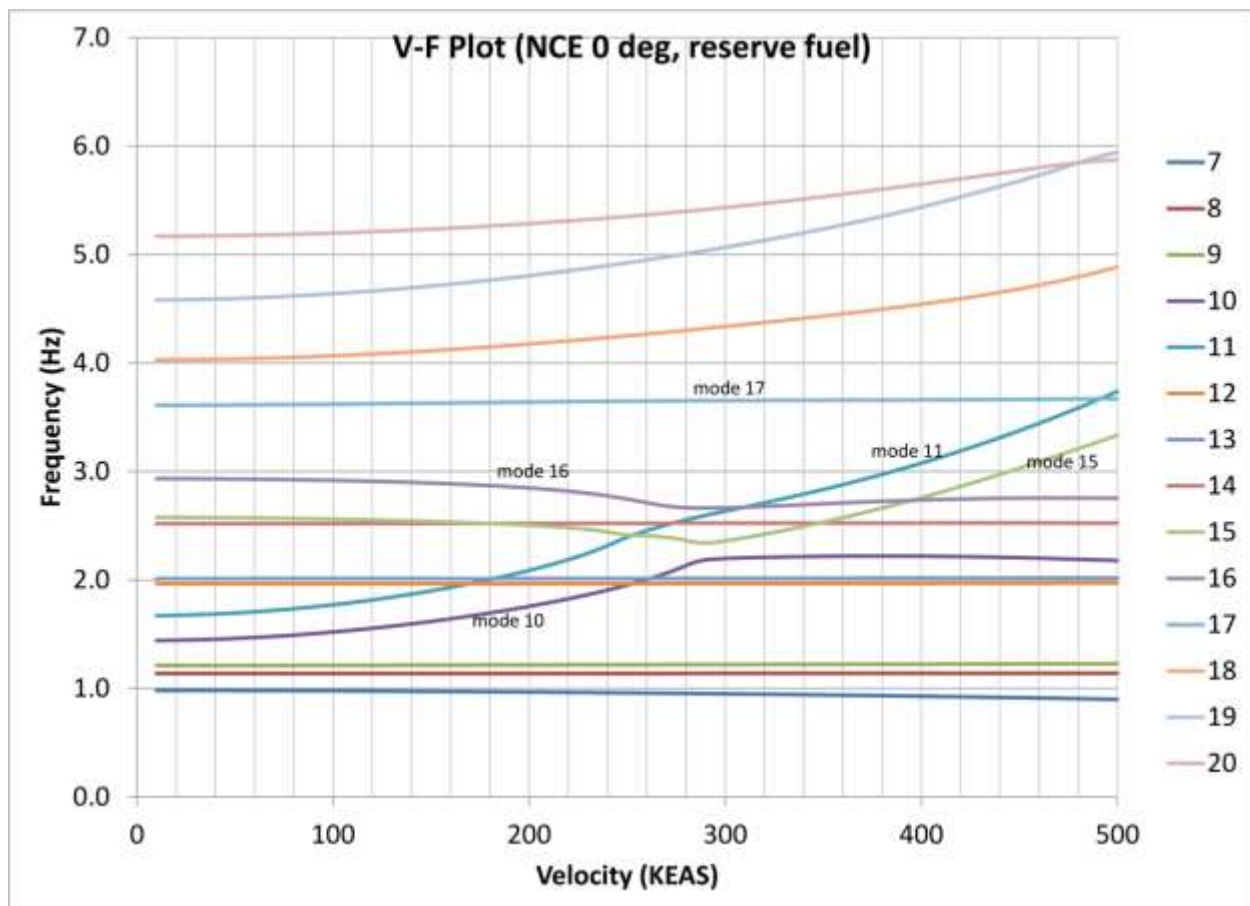
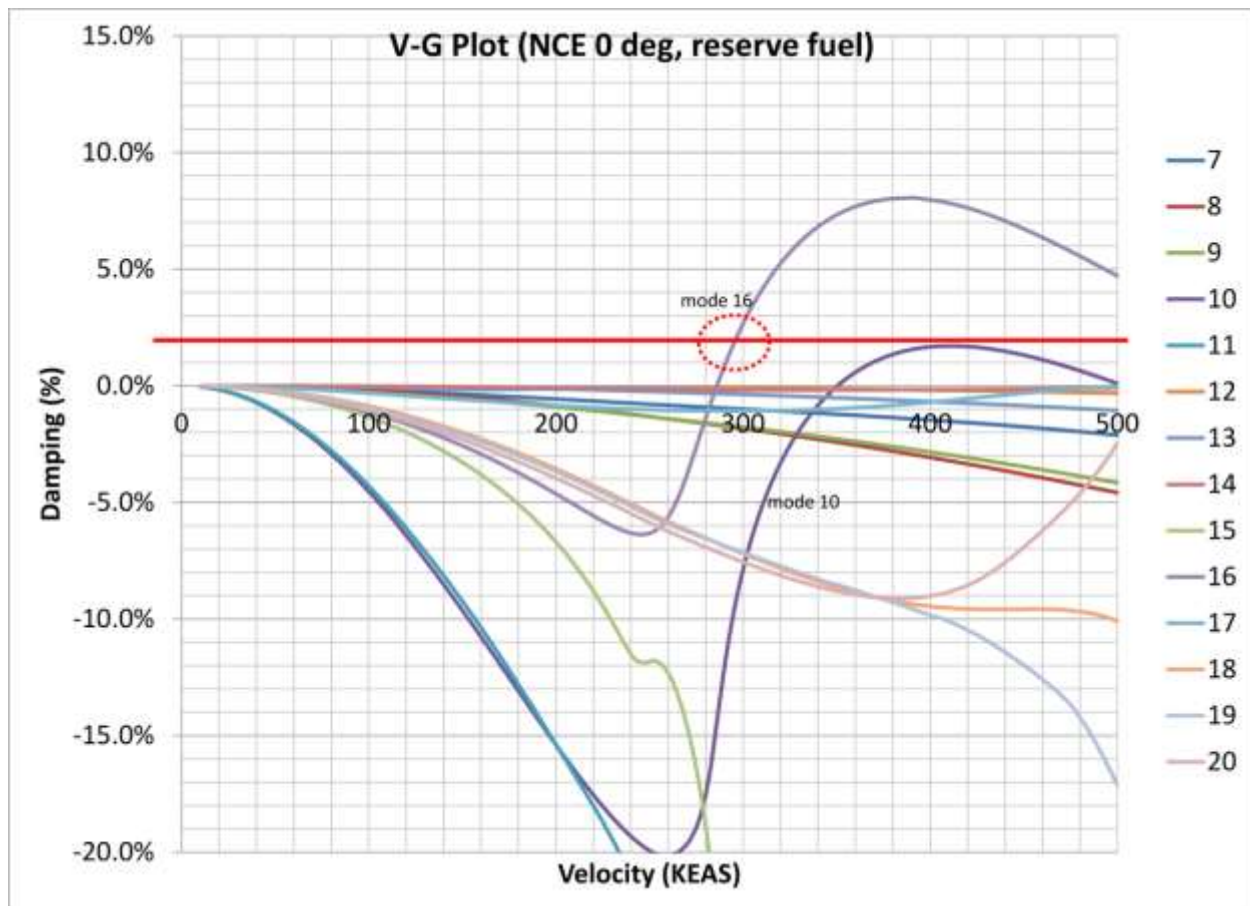
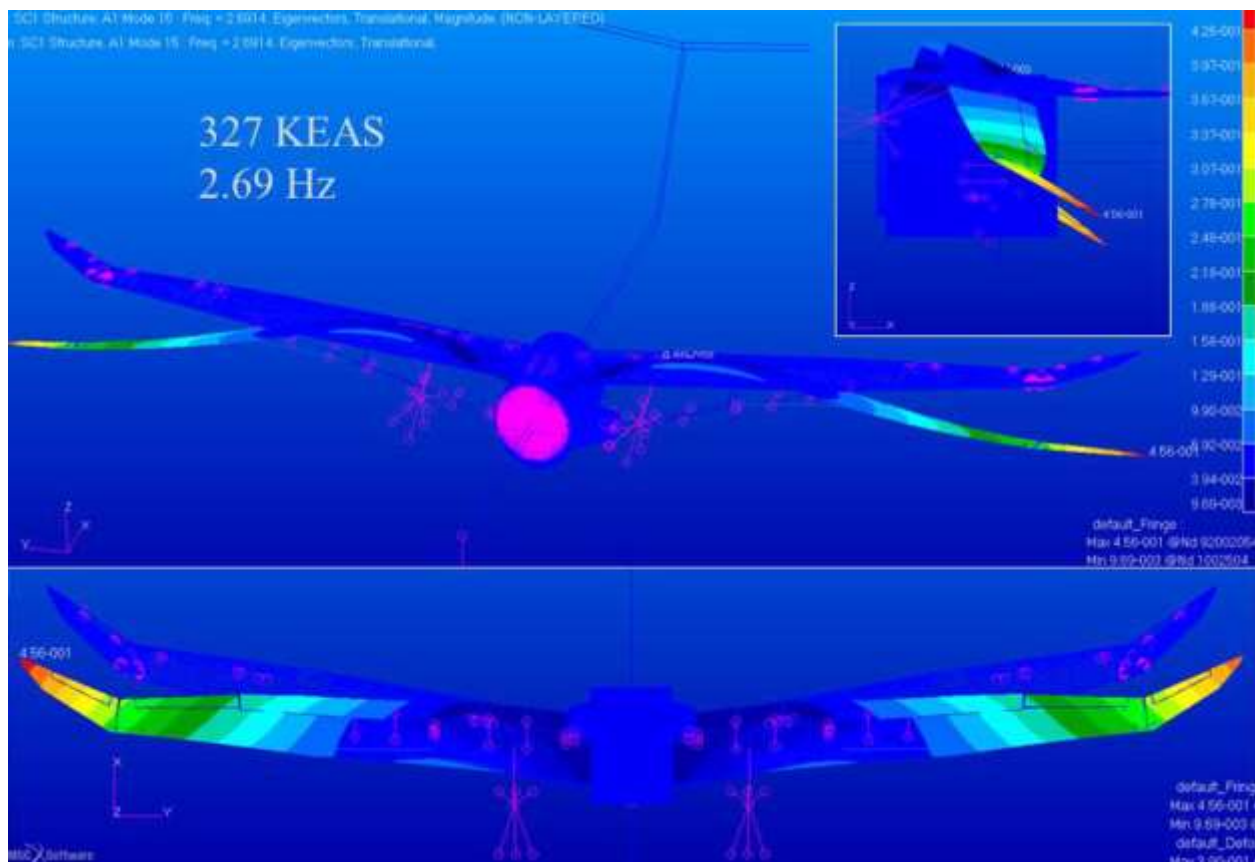


Figure 128. V-F plot for NCE 0-degree reserve fuel case.



**Figure 129.** V-G plot for NCE 0-degree reserve fuel case.



**Figure 130.** Critical flutter mode for 26-degree NCE full fuel case. 327 KEAS and 2.69 Hz.

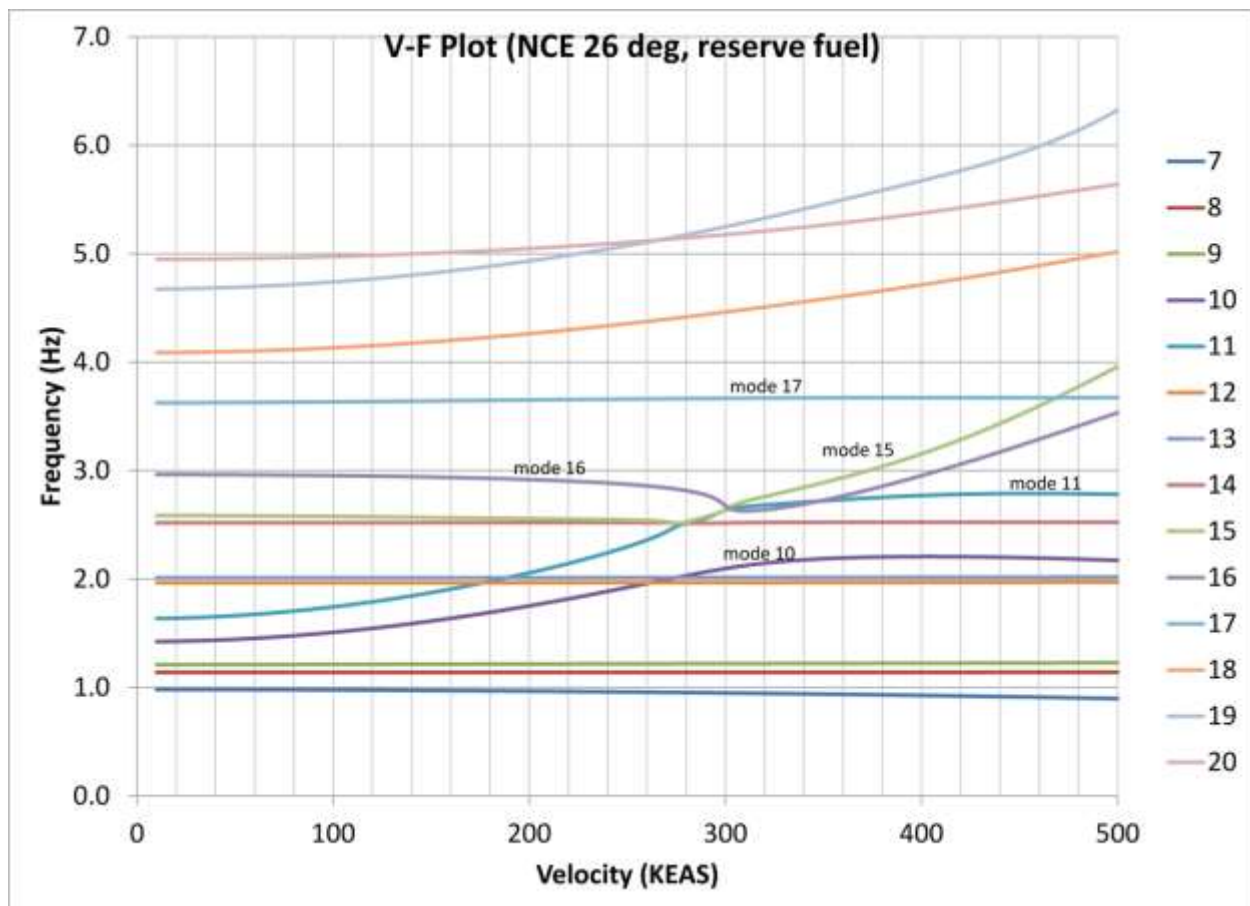
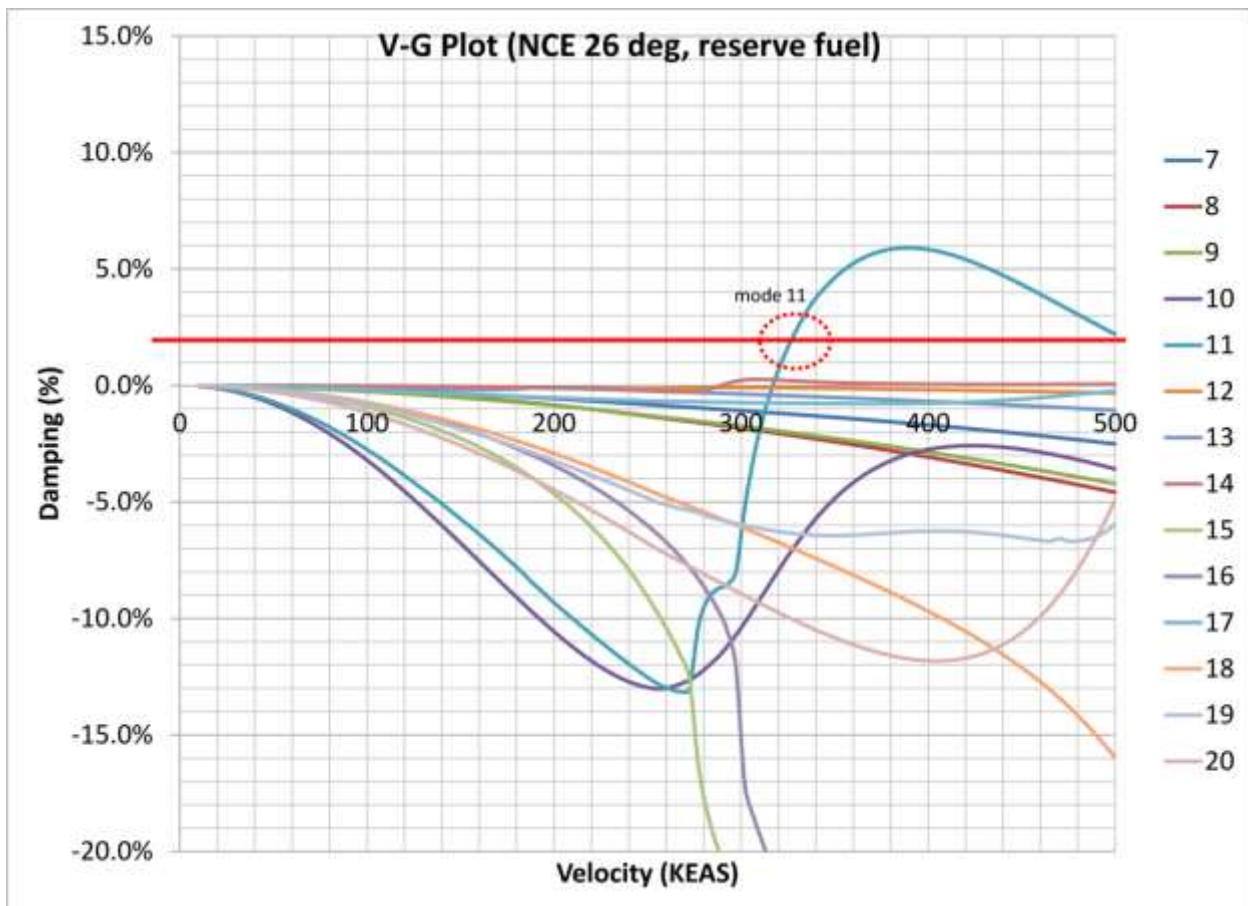


Figure 131. V-F plot for NCE 26-degree reserve fuel case.



**Figure 132.** V-G plot for NCE 26-degree reserve fuel case.

#### 10.1.2.3 Mass Sensitivity Study

During efforts to size the NCE wing structure, it was noticed that the flutter velocity had a counter-intuitive relationship to the location of the wing fore/aft center of gravity. For this reason a brief mass sensitivity study was performed on both the baseline SUGAR aircraft and two variants of the NCE equipped aircraft. Consultation with Boeing engineers with regard to use of flutter ballast on traditional cantilever wings revealed that typically flutter speeds decrease when weight is added to the wing trailing edge. In order to investigate the behavior on the TBW based aircraft, ballast weights were added to the trailing edge and the flutter speed was calculated. A schematic of the ballast weight applied to the baseline SUGAR aircraft is shown in Figure 133. Ballast was applied to the NCE FEM in a similar manner. The flutter speed dependence on ballast weight is shown in Figure 134. The trend shown for these TBW based aircraft is for the flutter speed to increase with the addition of ballast; which is counter to the behavior typically seen for a cantilever wing.

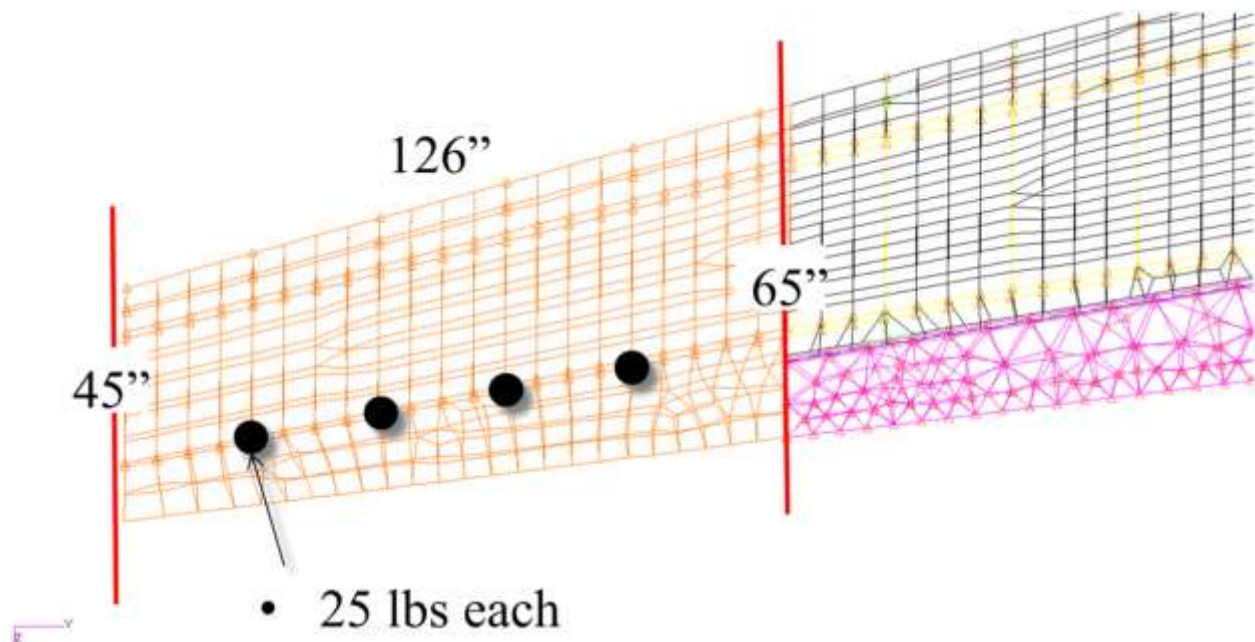
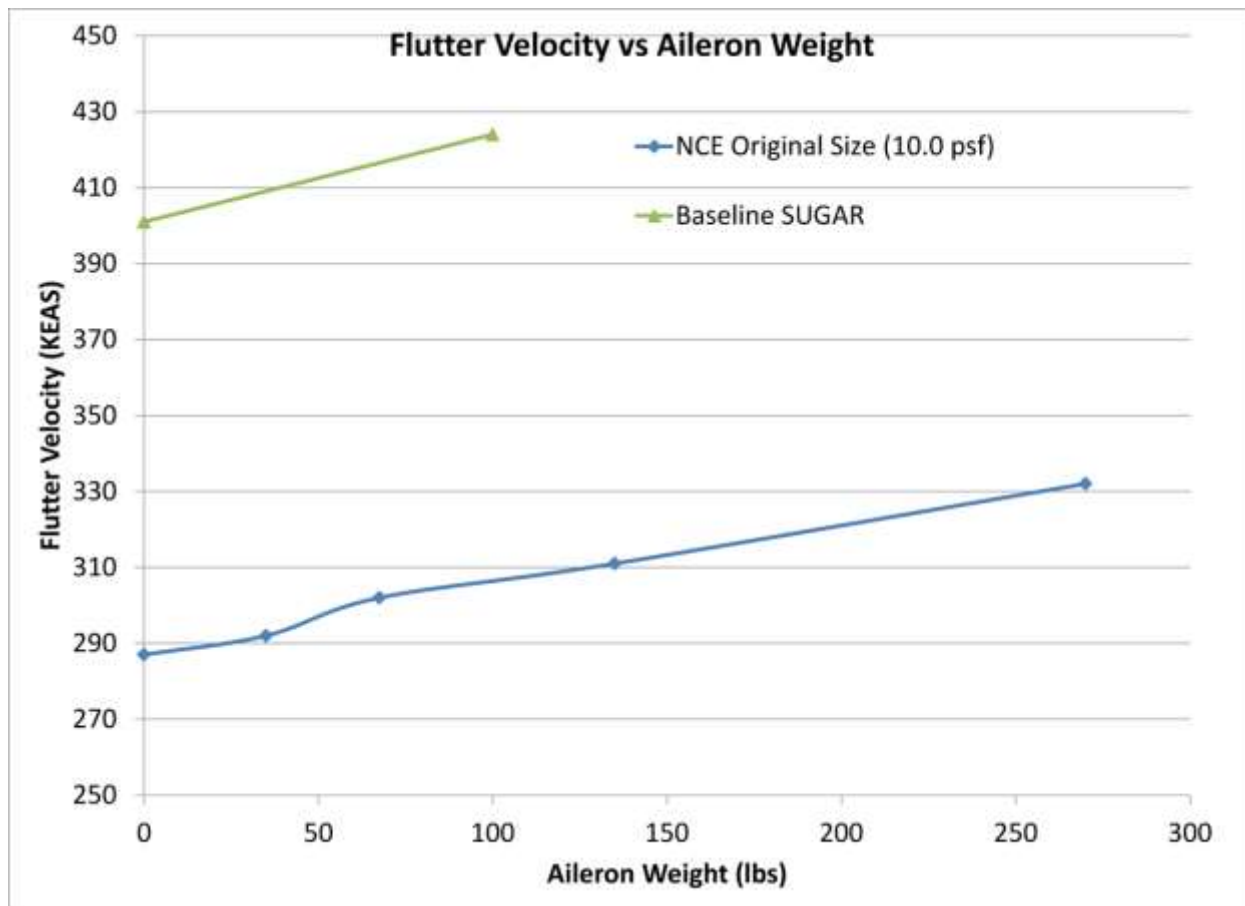


Figure 133. A study was conducted to evaluate the effect of an aft shift in the wing center of gravity on flutter speed. Ballast weight was added along the aileron hingeline.



**Figure 134.** The effect on flutter velocity by adding weight to the aft portion of the wing. Results are shown for the baseline SUGAR wing, the baseline NCE wing, and a minimum gauge structure NCE wing. The trend seen is that flutter speed increases with the addition of aft weights. This result is contrary to typical behavior seen in a traditional cantilever wing (i.e., not a TBW).

### 10.1.3 Lateral Trim Analysis

Lateral trim analysis was performed in order to provide lateral stability derivatives and Elastic-to-Rigid (E/R) ratios as input to the Boeing Stability and Control (S&C) analysis in Task 10. The needed stability derivatives were roll control ( $C_{L\delta}$ ) and roll damping ( $C_{Lp}$ ) which are used by S&C to calculate the aircraft roll-rate. The roll requirement was specified by Boeing S&C to be 13 degrees/sec. Consistent with the goals of the NCE project it was desired that this roll rate be achieved in aileron reversal.

The E/R ratios are used to determine the effect of flexibility on the aircraft controls and to determine the aileron reversal characteristics. Nomenclature for the various control surfaces on the NCE aircraft is provided in Figure 135. Stability derivatives and E/R ratios were calculated for the NCE aileron and the SUGAR aileron. These analyses assumed only one (or the other) control surface was actuated for any given analysis. Analyses for both control surfaces actuated simultaneously were not performed since in the doublet lattice aerodynamic model these effects are independent, linear, and can therefore be superimposed. As desired by Boeing S&C, the analyses utilized a small, 1 degree, downward aileron deflection of the right wingtip only. By specifying the required roll-rate of 13 degrees/sec, a maximum aileron deflection of 40 degrees, and that both

ailers can be utilized; the required roll-rate due to a single aileron deflection of 1 degree can be calculated to be 0.163 degrees/sec.

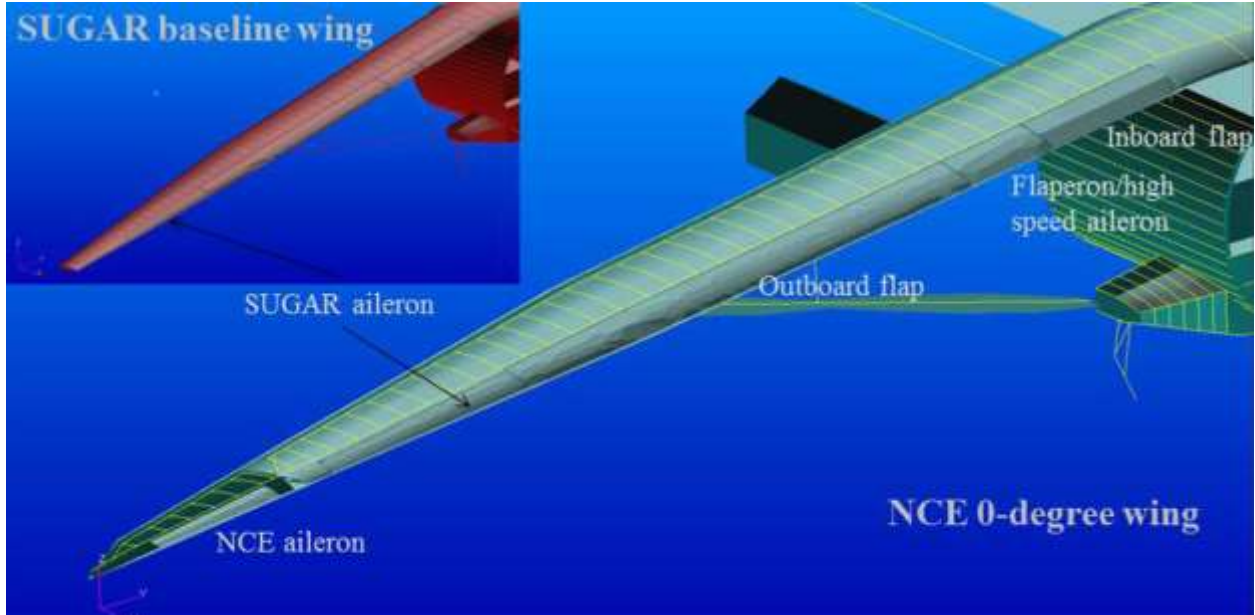


**Figure 135. Locations and names of the various control surfaces on the NCE equipped aircraft. For comparison the original SUGAR wing is shown in the inset picture upper left.**

The trim analyses described here were conducted for the two sweep configurations (0-degree and 26-degree) and for two flight conditions (cruise and approach). The cruise condition was Mach 0.7 at 40,000 ft and with full-fuel. Standard atmosphere tables for this condition provide an air density equal to 0.000585 slug/ft<sup>3</sup> and a speed of sound equal to 968.08 ft/s. Based on these numbers the aircraft velocity is calculated to be 677.66 ft/s and the dynamic pressure is 134.32 lb/ft<sup>2</sup>. The approach condition was Mach 0.15 at sea level with reserve-fuel and full span flaps deflected to 30 degrees. Standard atmosphere tables for this condition provide an air density equal to 0.002377 slug/ft<sup>3</sup> and a speed of sound equal to 1116.5 ft/s. Based on these numbers the aircraft velocity is calculated to be 167.48 ft/s and the dynamic pressure is 33.33 lb/ft<sup>2</sup>.

Table 32 provides the stability derivative information for the 0-degree NCE aircraft as well as the baseline SUGAR aircraft while Table 33 provided information for the 26-degree NCE configuration. The first column of the table indicates the sweep angle (0-degree or 26-degree) and the aileron (NCE or SUGAR) used in the analysis (The rows highlighted yellow in Table 32 indicate analysis of the baseline SUGAR aircraft and therefore sweep angle is not applicable for these entries and inherently only the SUGAR aileron is considered). The second column indicates the flight condition considered, cruise or approach. The third column indicates whether the stability derivative provided is the rigid or elastic value. The fourth and fifth columns provide the stability derivatives for roll control ( $C_{L\delta}$ ) and roll damping ( $C_{Lp}$ ), respectively. The sixth column indicates the roll rate "p" in deg/s and is calculated as

$$p = \left( \frac{C_{L\delta}}{C_{Lp}} \right) \left( 2 \frac{v}{b} \right) \left( \frac{180}{\pi} \right) \quad (21)$$

Where aileron deflection  $\delta = 0.01744$  rad, span  $b = 146.4$  ft, and the velocity "v" is either 677.66 ft/s (cruise) or 167.48 ft/s (approach), depending on the flight condition provided in column 2.

The final column provides the E/R ratio of  $C_{L\delta}$ , which is a positive value when the aileron is providing traditional control, and would be a negative value if acting in aileron reversal. The dynamic pressure associated with a zero value of E/R  $C_{L\delta}$  is deemed the reversal point and is illustrated in Figure 136. It can be seen that the NCE equipped aircraft when using NCE aileron for roll control, has a lower reversal speed than the SUGAR aircraft using the SUGAR aileron. It can also be seen that the 26-degree swept NCE further reduces the aileron reversal speed below that of the 0-degree sweep configuration. However, none of the configurations have a negative E/R indicating that aileron reversal is not achieved. It can be calculated that a E/R  $C_{L\delta}$  of approximately -0.6 would be needed in order to satisfy the goal of achieving the required roll-rate acting in aileron reversal; this point is also illustrated in Figure 136.

**Table 32. Dynamic derivatives for the lateral trim analysis of the 0-degree NCE configuration. Results for the baseline SUGAR are also provided in the highlighted rows.**

Sweep/Aileron	Condition	Rigid/Elastic	$C_{L\delta}$	$C_{LP}$	Roll-rate (deg/s) 1° defl Rt aileron only	E/R $C_{L\delta}$
0-deg NCE aileron	Cruise	Rigid	-0.062	-1.58	-0.36	0.45
		Elastic	-0.028	-1.27	-0.20	
0-deg SUGAR aileron	Cruise	Rigid	-0.14	-1.58	-0.80	0.57
		Elastic	-0.08	-1.27	-0.59	
Baseline SUGAR	Cruise	Rigid	-0.13	-1.35	-0.88	0.62
		Elastic	-0.08	-1.17	-0.63	
0-deg NCE aileron	Approach	Rigid	-0.049	-1.25	-0.089	0.86
		Elastic	-0.042	-1.19	-0.080	
0-deg SUGAR aileron	Approach	Rigid	-0.11	-1.25	-0.195	0.88
		Elastic	-0.097	-1.19	-0.185	
Baseline SUGAR	Approach	Rigid	-0.10	-1.09	-0.21	0.93
		Elastic	-0.093	-1.05	-0.20	

**Table 33. Dynamic derivatives for the lateral trim analysis of the 26-degree NCE configuration.**

Configuration/	Condition	Rigid/Elastic	$C_{L\delta}$	$C_{LP}$	Roll-rate (deg/s) 1° defl Rt aileron only	E/R $C_{L\delta}$
26-deg NCE aileron	Cruise	Rigid	-0.033	-1.47	-0.21	0.28
		Elastic	-0.0094	-1.18	-0.07	
26-deg SUGAR aileron	Cruise	Rigid	-0.14	-1.47	-0.85	0.57
		Elastic	-0.08	-1.18	-0.63	
26-deg NCE aileron	Approach	Rigid	-0.029	-1.19	-0.056	0.79
		Elastic	-0.023	-1.12	-0.047	
26-deg SUGAR aileron	Approach	Rigid	-0.11	-1.19	-0.20	0.86
		Elastic	-0.095	-1.12	-0.19	

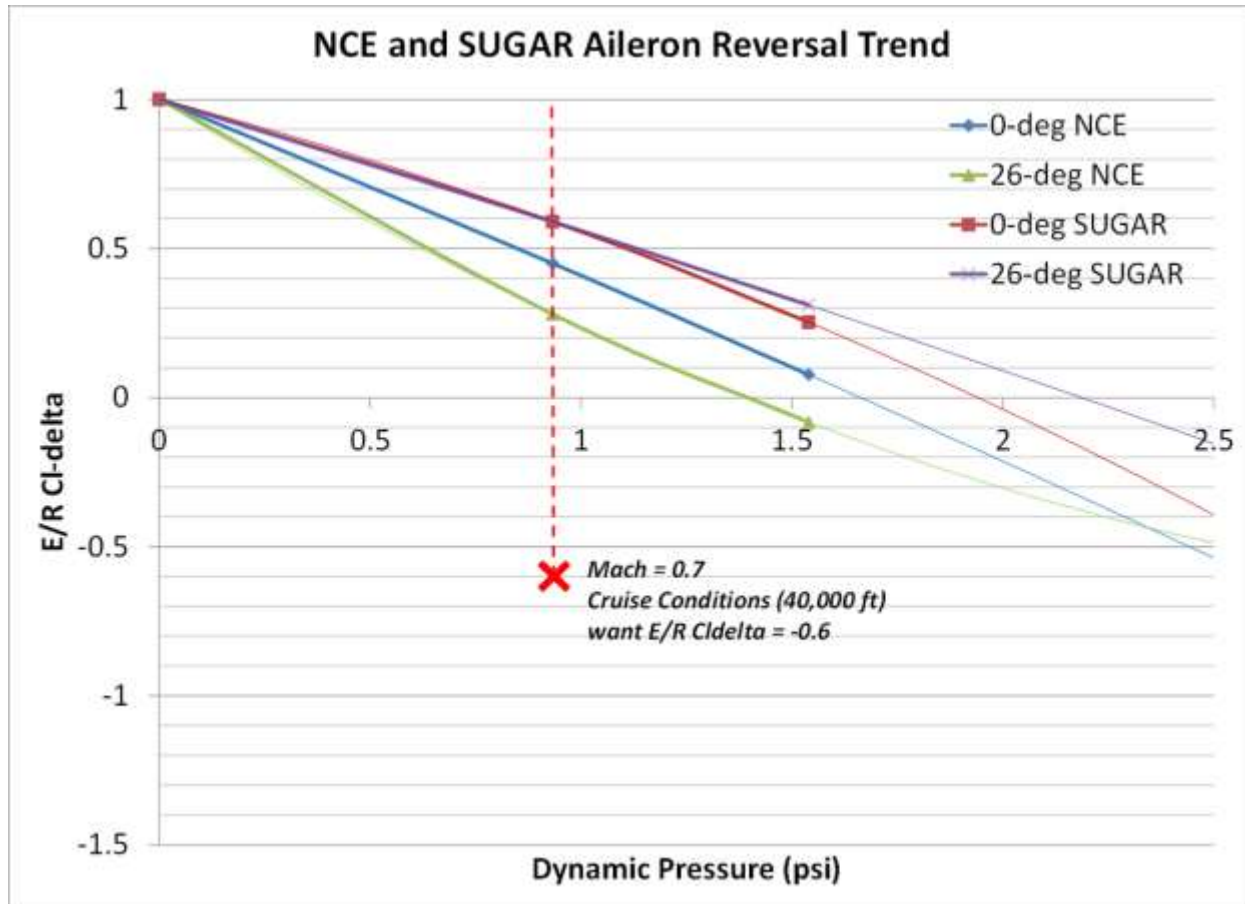


**Figure 136.** E/R  $C_{L\delta}$  vs. dynamic pressure for 0-degree and 26-degree NCE aircraft. Results are provided for control configurations using NCE aileron only, or SUGAR aileron only. Zero crossings indicate the dynamic pressure at which aileron reversal occurs. The desired value to achieve sufficient roll control at cruise condition, acting in aileron reversal, is -0.6.

In order to investigate potential improvements to the original NCE configuration, several modifications were developed and analyzed to determine their ability to achieve the desired E/R value of -0.6. These variations included ailerons of different sizes, full-flying aileron wingtips with fore (or aft) hinge points, and a point force controller located at the very distal end of the wing. These modifications are illustrated in Figure 137.

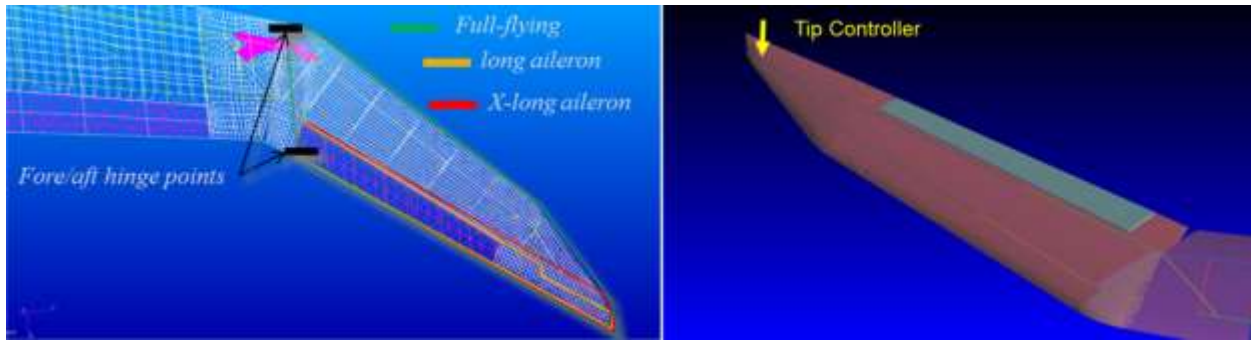


**Figure 137.** Various control surface arrangements were considered for their ability to achieve the desired aileron reversal control. These variations included ailerons of different sizes, full-flying aileron wingtips with fore (or aft) hinge points, and a point force controller located at the very distal end of the wing.

In addition to the control surface variations, a modification to the baseline NCE structural stiffness was also examined for its impact on the E/R value. The structural modification was to take the NCE wingtip to the Boeing recommended minimum gage structural values for the skin and spars, resulting in an overall NCE plan-form weight of 3.5 psf. Recall the baseline NCE structure was sized to have a plan-form weight similar to the SUGAR wingtip (10 psf). A summary of results showing the E/R value for these various configurations is shown in Figure 138.

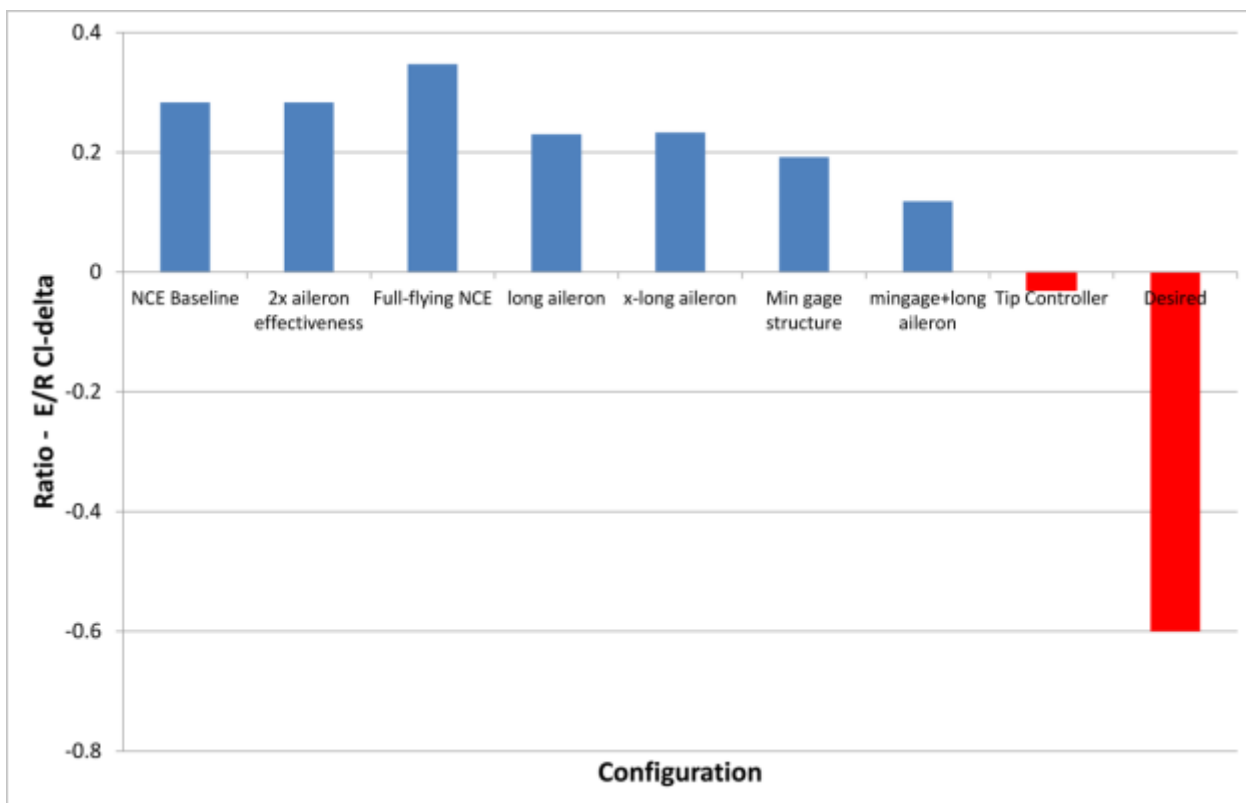


**Figure 138.** Several variations on the original NCE FEM were evaluated with the goal to achieve the desired role-rate acting in roll reversal.

#### 10.1.4 Conclusions

The NCE FEM developed in Task 6 was analyzed for flutter and lateral roll control performance. Flutter analyses were performed for full-fuel and reserve fuel mass cases, as well as for the 0 degree and 26 degree sweep cases. The addition of the NCE wingtip caused a reduction in flutter speed when compared to the baseline SUGAR wing. The baseline SUGAR aircraft was optimized to have a flutter speed of 401 KEAS. The worst case NCE flutter analysis was for the 0-degree sweep NCE reserve fuel mass case and showed a flutter speed of 296 KEAS. The flutter speed dependence on ballast weight was examined in Section 10.1.2.3. The trend shown for this TBW based aircraft is for the flutter speed to increase with the addition of ballast; which is counter to the behavior typically seen for a cantilever wing.

The lateral control analysis indicated that sufficient roll-control authority was achieved for 0-degree sweep configuration at cruise, but that the wing was not acting in control reversal. Sweeping the NCE to 26 degrees moved operation closer to the reversal point but did not achieve reversal and also lacked sufficient roll authority. Several alternative aileron and structural designs were considered for their ability to achieve the goal of adequate roll-control acting in aileron reversal (see Figure 137 and Figure 138). The results indicated that designs which used a more flexible wing ("minimum gauge structure") increased the aileron reversal effect. Similarly, aileron designs whose Center of Pressure (CP) moved aft of the baseline, such as the "long aileron" and "extra-long aileron" also improved the aileron reversal effect. Designs which did not change the aileron CP ("2x effectiveness") had no effect on the reversal effect while designs that moved the CP forward ("Full flying NCE") were actually detrimental to achieving aileron reversal. These results indicate that the magnitude of the aileron force does not influence the E/R but rather it is the location of the force that is important. This behavior is best illustrated by the "tip controller" variation which demonstrates an E/R value which is closest to the desired goal of -0.6.

## 10.2 DUAL AISLE AIRCRAFT MDO CONFIGURATION AEROELASTIC ANALYSIS

Boeing team used the process described in Figure 139 to convert vehicle configuration data from Virginia Tech MDO to a buildup FEM for flutter and static aeroelasticity analysis. This process assumes the following properties for the FEM:

- Wing leading edge and trailing edge only carry aero loads. Because of this assumption, the leading and trailing edge wing skins are not modeled. Leading and trailing edge ribs in the Boeing FEM are used only to transfer loads from doublet lattice aero panel into the wing box. These leading and trailing edge ribs are given high stiffness and zero density so it can carry aero load without affecting the dynamic behavior of the wing.
- The NCE mechanism will carry all loads through both front and rear spars. Wing skins and stringers at the joint will be discontinuous due to the NCE mechanism, so they will not be able to carry loads. This assumption will need to be updated once details of the mechanism and structural layout are developed.
- Fuel mass is divided into three tanks. One main tank and two wing tanks. Each tank is modeled with Nastran lump mass element (CONM2) placed at center of the fuel tank. The mass is evenly distributed throughout the wingbox by connecting the CONM2 elements to hardpoints in the wing using Nastran RBE3 elements. Note: Hardpoints are nodes that have supports, such as nodes at intersection of skin and rib, or skin and spar.

- The wing deformation is assumed to be linear. Future study will include large displacement effect when running flutter with pre-stiffened model.
- All connections amongst wing, jury, and strut are assumed to have all 6 degree-of-freedom connected.
- Aerodynamic data will be supplied by doublet-lattice model without additional corrections.
- Fuselage is assumed to be rigid in this round of analysis, since the main goal is to determine the effectiveness of the novel control effector.

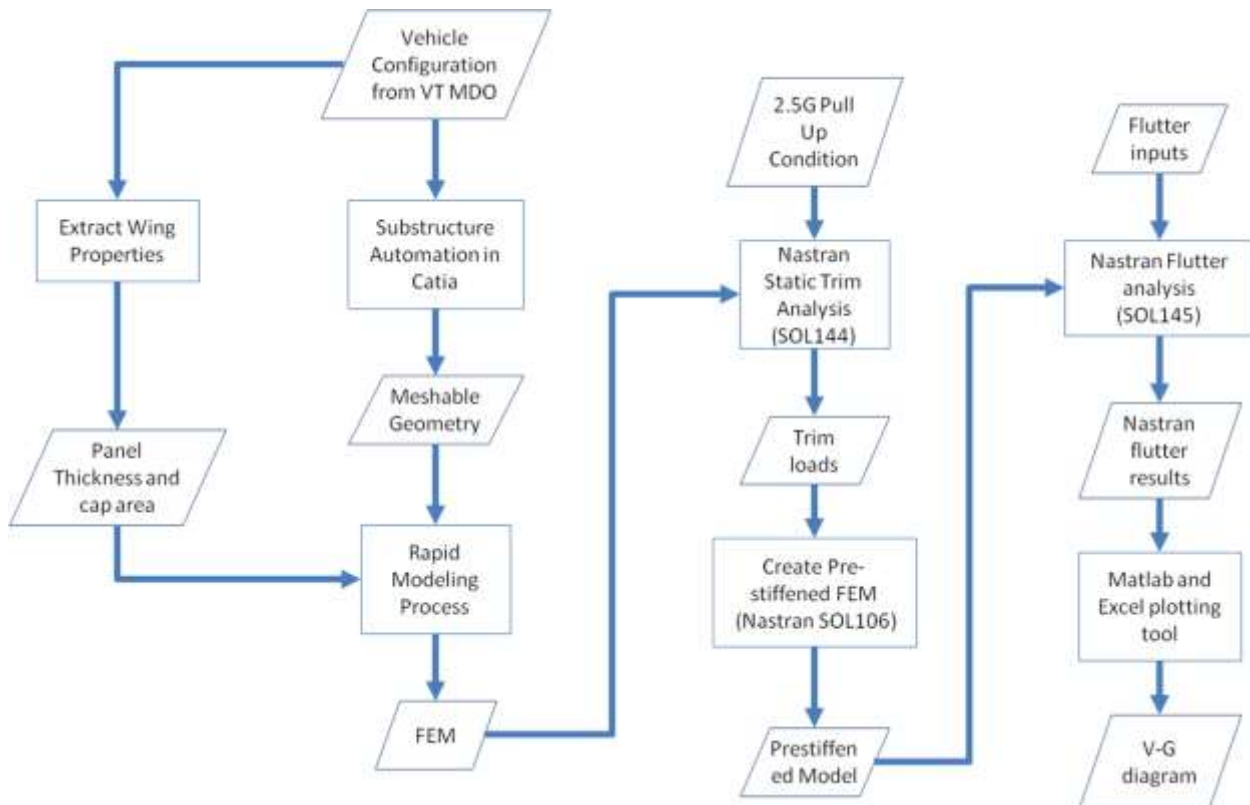


**Figure 139. Boeing Process for Modeling and Analyzing Virginia Tech MDO Vehicle**

### 10.2.1 Half Span Model

There were two finite element models constructed by the Boeing team. The first model is a half span model used to validate Virginia Tech's flutter data. Shown in Figure 140, the wing is a build-up FEM consists of Nastran shell elements for skin and beam elements for caps and stringers. The strut and jury are modeled using beam elements, and are connected to the wing using Nastran RBE2 rigid elements. The root of wing and strut are connected together using a mix of RBE2 and RBE3, and are constrained in all six degrees of freedom. The structural mass of the model is provided by the density of the material, with the fuel mass added to the wing using lumped mass elements that distributed evenly using RBE3 connected to the. Additionally, a separate lumped mass element is used to represents mass of the remainder of the vehicle and to ensure center of gravity is in the correct location. The aerodynamic model is modeled using the doublet lattice

method, and is shown in Figure 141. The structural FEM was connected to the aero model using the Nastran SPLINE4 (infinite plate) method.

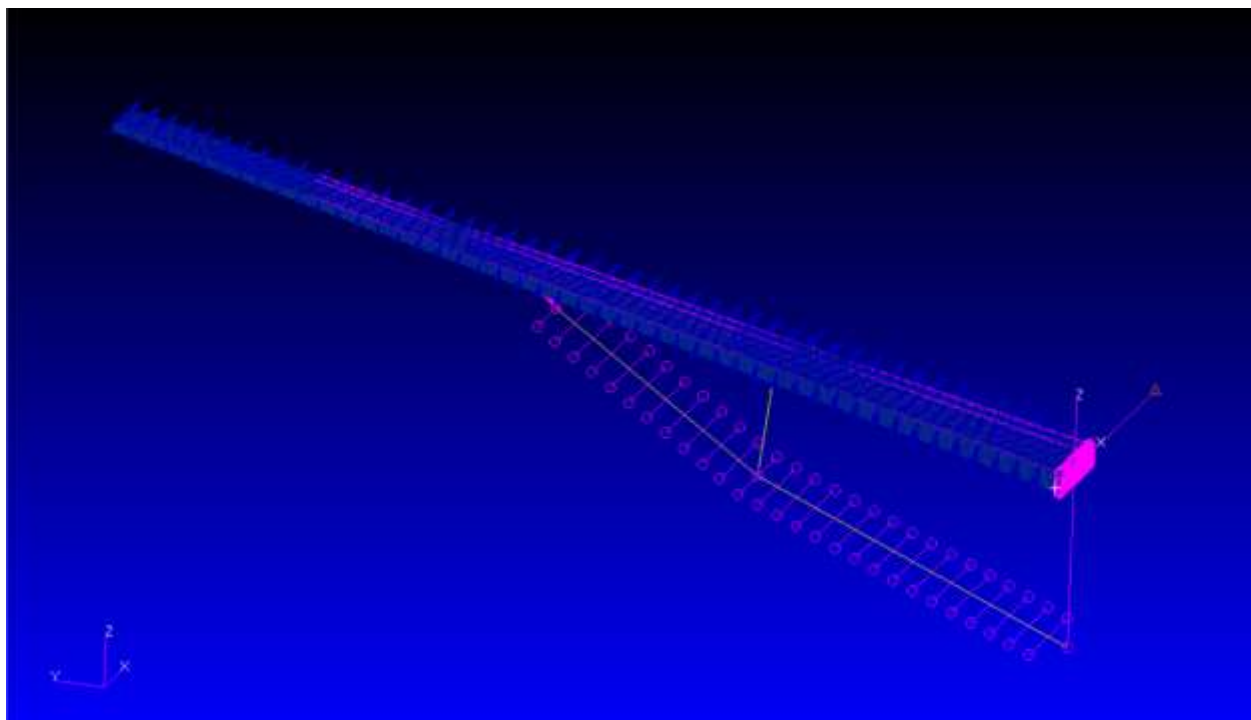


Figure 140. Half Span Structural Model

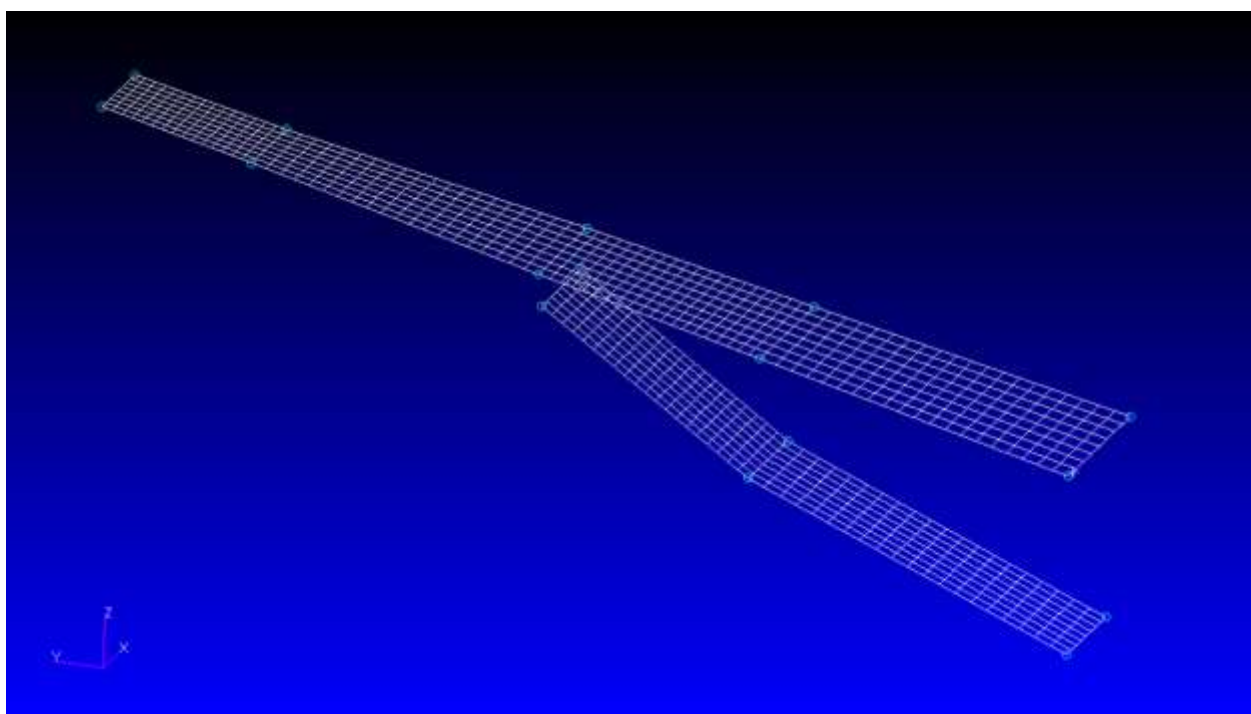


Figure 141. Half Span Doublet Lattice Aero Model

### 10.2.2 Flutter Analysis with strut pre-load for Half Span Model

The flutter analysis on this model is performed with a pre-stiffened truss-braced structure. The first step in pre-loading the model is to perform an aeroelastic analysis to obtain the forces needed to create the deform shape. This is done using Nastran static aeroelasticity solver with a condition of 2.5G of vertical load at Mach 0.8 and 35,000 ft. Nastran would produce a set of nodal loads at the completion of the static aeroelasticity analysis, and this set of loads is then used in Nastran SOL106 to generate a deformed structural model. This pre-stiffened model is then used in Nastran Sol145 flutter. The resulting velocity versus damping diagram is shown in the plot below, Figure 142. For this half span model, the flutter speed was determined to be 351KEAS.

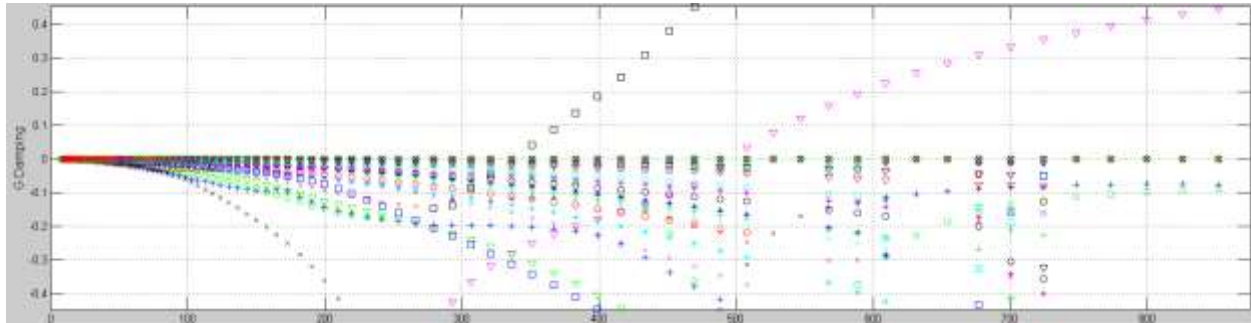
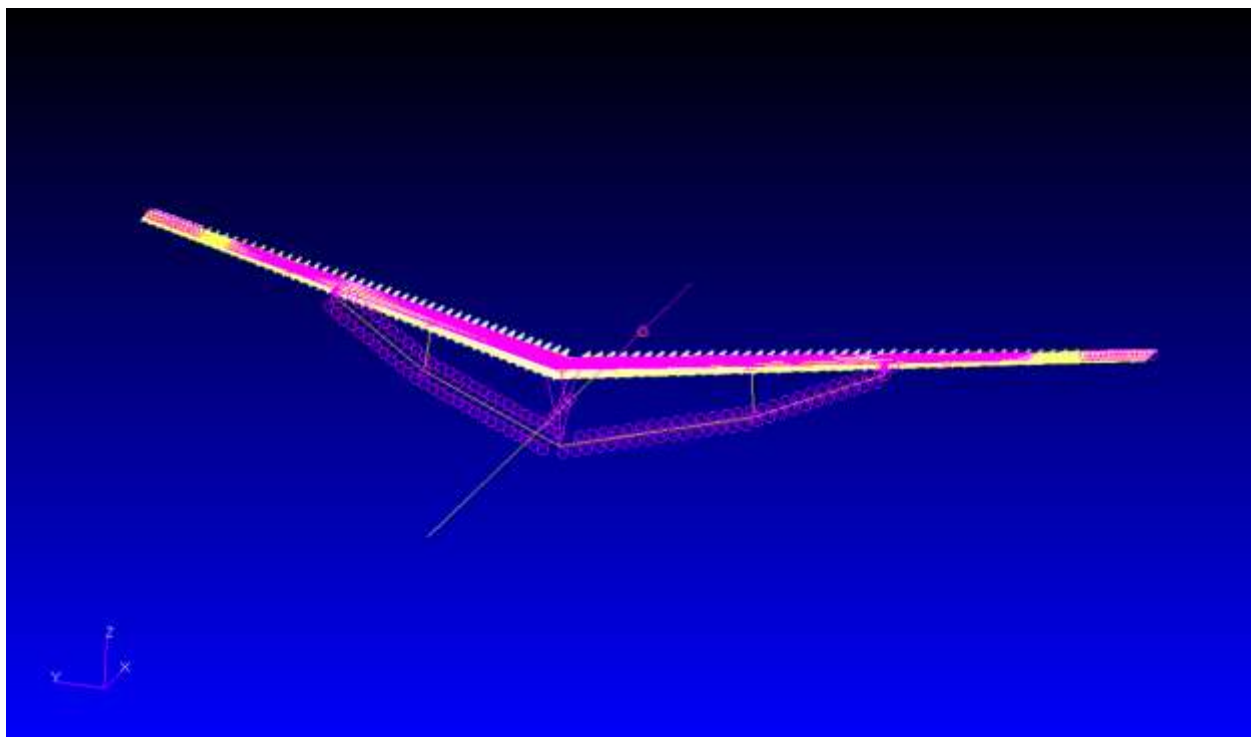


Figure 142. V-G Diagram of Half Span Model

### 10.2.3 Full Span Model

A full span model was created to perform roll analysis and compute effectiveness of novel control effector in performing roll maneuvers. It was also used to compare flutter performance of the forward swept and aft swept NCE configurations. Figure 143 shows the full span model with a beam fuselage. This beam fuselage was modeled with higher stiffness material to avoid affecting the dynamic response of the wing. The mass distribution and wing/strut/jury connectivity utilize the same modeling technique and assumptions as the half span model.



**Figure 143. Full Span Structural Model**

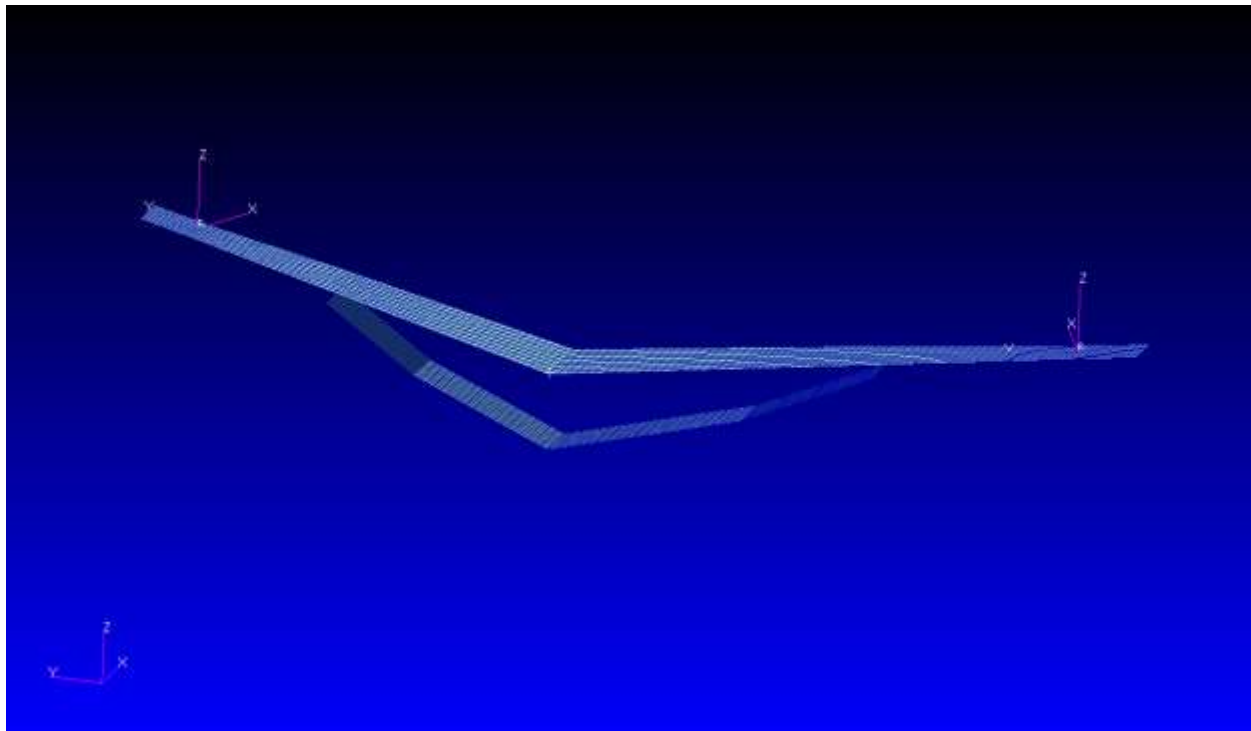


**Figure 144. Full Span Doublet Lattice Aero Model**

Figure 145 is the mass table in Nastran. This shows that the full span model matches the mass and CG of the TOGW configuration provided by Virginia Tech.

DIRECTION		MASS	X-C.G.	Y-C.G.	Z-C.G.
MASS	AXIS SYSTEM (S)				
X		4.749999E+05	-2.773131E-17	-6.185791E-03	-4.188490E+00
Y		4.749999E+05	4.140183E+02	4.376364E-17	-4.188490E+00
Z		4.749999E+05	4.140183E+02	-6.185791E-03	-1.603233E-17

Figure 145. Mass Property Table in Nastran

#### 10.2.4 Modeling NCE Configurations

The FEM of NCE was modeled with the same technique and assumptions used to construct the wing FEM. Because NCE is designed to rotate in flight to achieve optimized (Figure 146), the connectivity of the NCE to wing was modeled such that loads can only be transferred through the front and rear spar. Figure 147 shows the RBE2 elements used to connect the front and rear spars of the NCE to the wing, with the pivoting point located at the intersection of NCE and wing rear spars. RBE2 is also used to connect front spar of NCE to the front spar of wing, as the NCE mechanism design has yet to be matured enough to be incorporated into the FEM. The team does anticipate different front spar connectivity modeling once the mechanism design has matured. In addition to the modeling of NCE connectivity to the wing, the NCE also has a control surface that would act as control tab to enable the entire NCE to act as a roll controller. Figure 148 shows the control surface model on the NCE, which is a simple rigid flat plate. The control surface is assumed to be rigid because its structural layout has yet to be design and is needed to transfer aero loads into the NCE. This control surface is connected to the NCE using RBE2 and RBE3 elements to represent hinges, and a Nastran CBUSH (6-DOF spring) to represent the stiffness of the actuator.

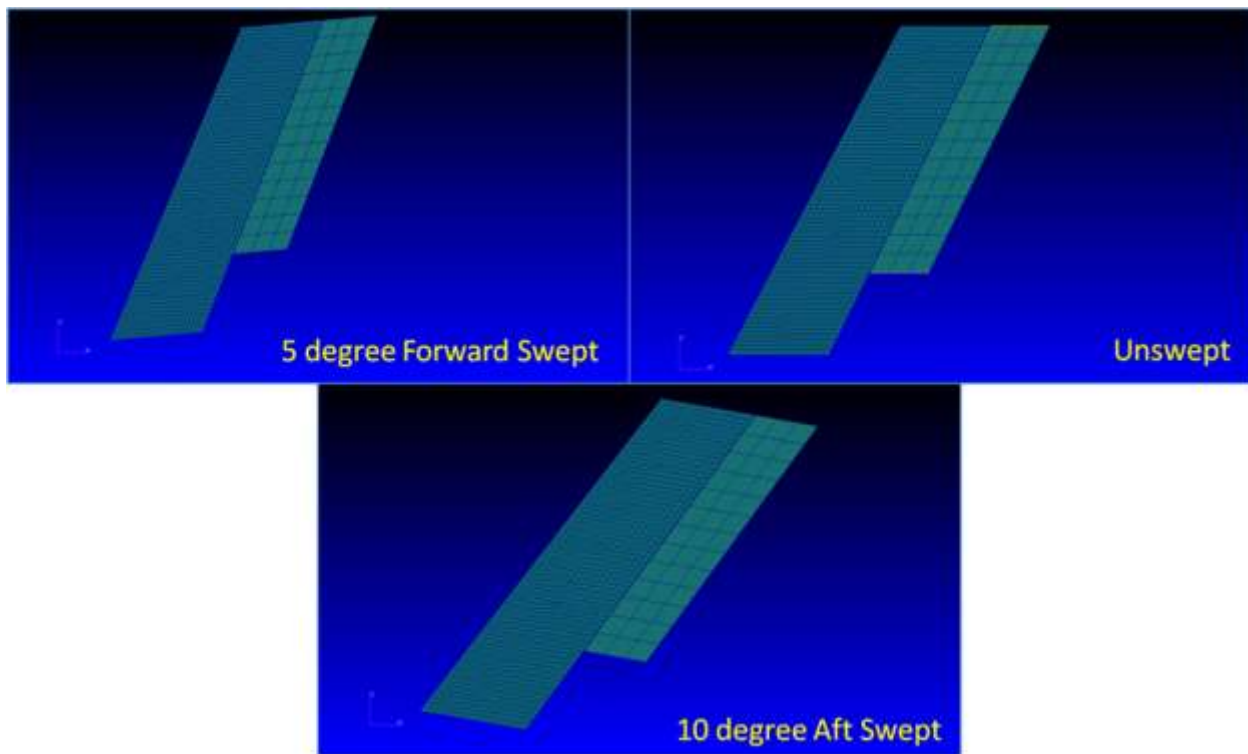
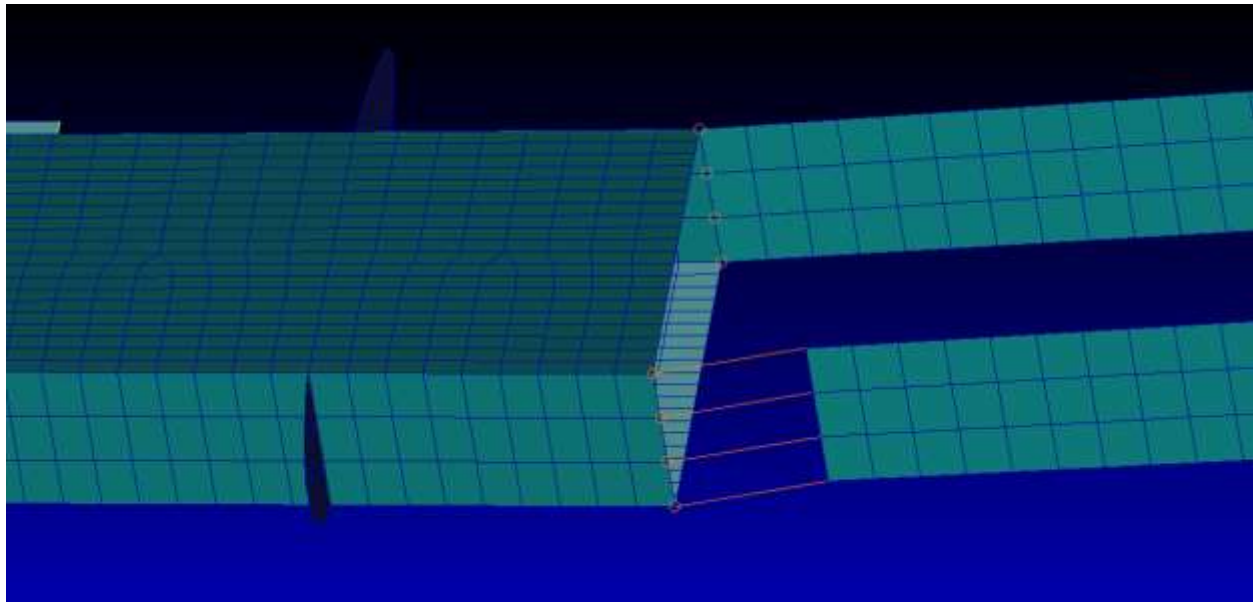
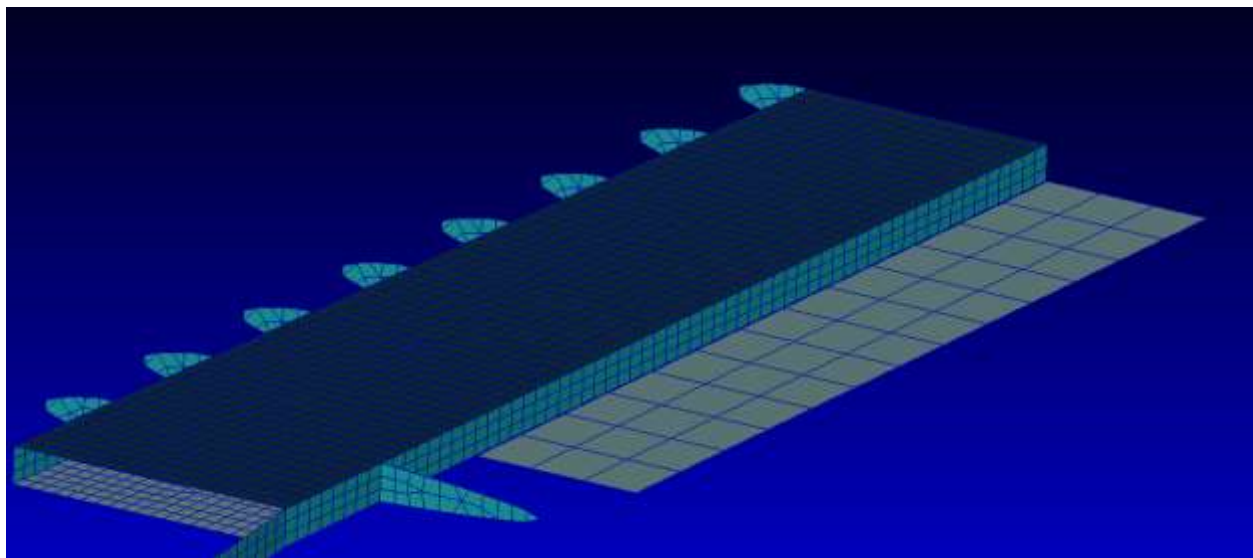


Figure 146. Model of NCE in 3 Different Configurations



**Figure 147. NCE to Wing Connectivity**



**Figure 148. NCE Control Surface**

#### 10.2.5 Flutter Analysis

Below are the v-g diagram from the flutter analysis on the three different NCE configuration.

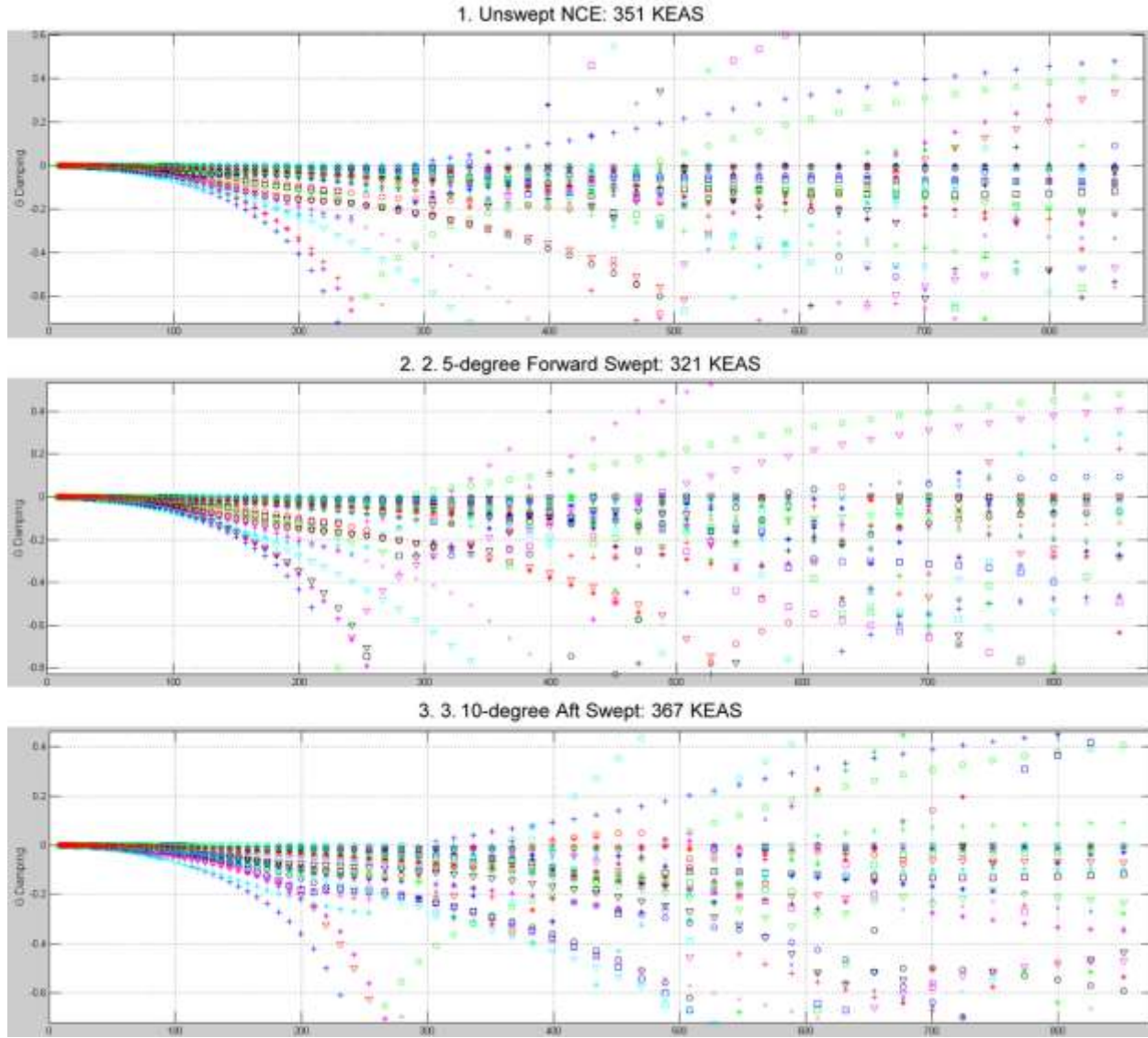
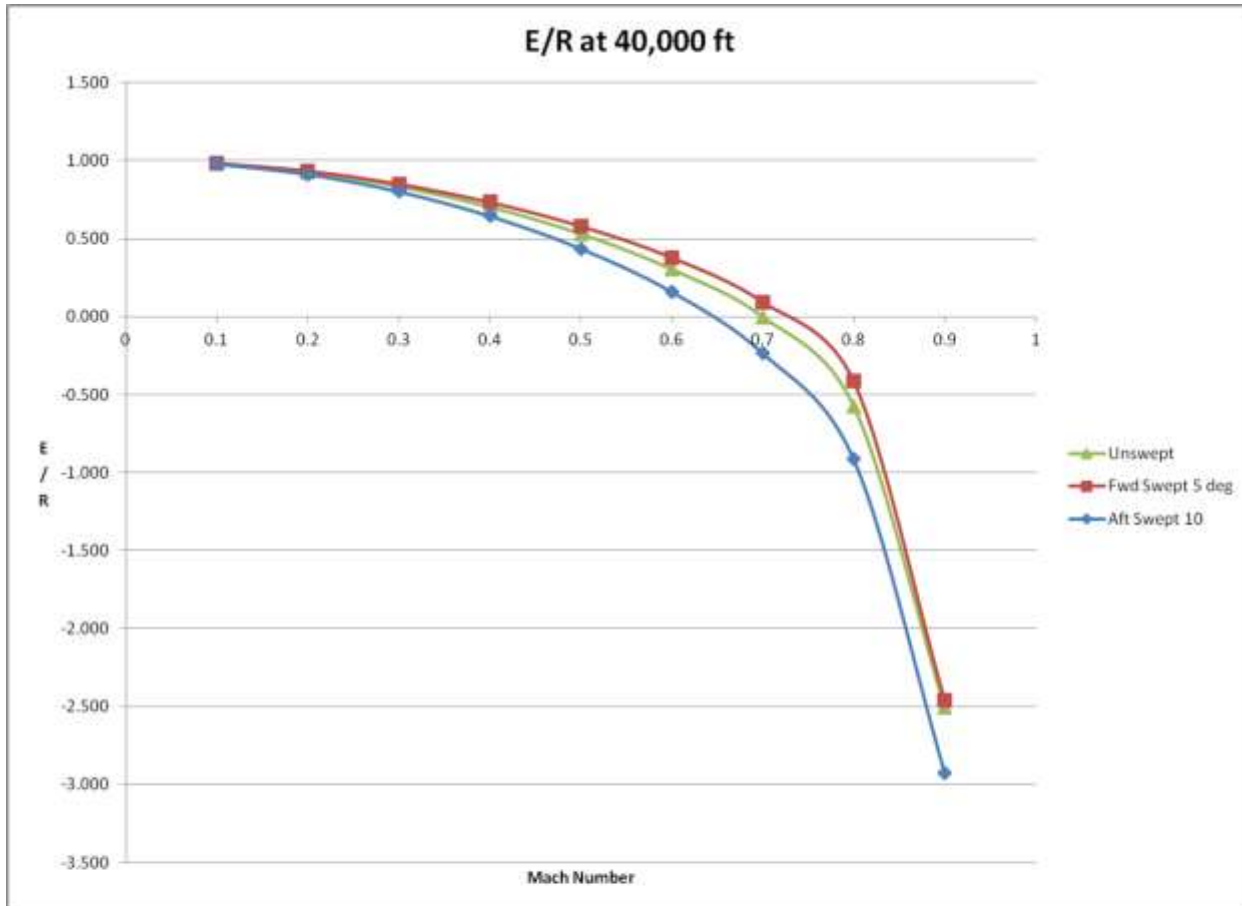


**Figure 149. V-G Diagram for Dual Aisle Aircraft with Unswept, 5° Forward Swept, and 10° Aft Swept Novel Control Effector Wing Tip**

#### 10.2.6 Novel Control Effector Effectiveness Analysis

The design goal of novel control effector is to use it to perform roll performance, which mean its control surface would have negative elastic-to-rigid ratio. To demonstrate that the vehicle actually did satisfy this goal, Nastran SOL144 and the full span FEM were used to compute the E/R ratio and the effectiveness of roll rate. The analysis was done by trimming the airplane for roll at 35,000 ft and Mach 0.8. The roll maneuver of the vehicle is assumed to be controlled only by the controller on the NCE. Data from the completed Nastran analysis showed that E/R ratio to be -0.65, which indicated reversal of the NCE controller would indeed occur during a roll maneuver. To validate this data, a roll case with a roll rate of 15 degrees per sec was performed in Nastran SOL144. The resulting data shown below shows that the controller on the right was deflected up and the left NCE controller was deflected down. This typically would cause the vehicle to roll to the right. However, the vehicle actually was rolling to the left at 15 degree per sec, which indicated

the desired reversal behavior did indeed occur. This table also showed that the 15 degrees per second roll rate can be achieved using a NCE controller angle of 54.6 degrees.



#### AEROELASTIC TRIM VARIABLES

ID	LABEL	TYPE	TRIM STATUS	VALUE OF UX	
101	INTERCEPT	RIGID BODY	FIXED	1.000000E+00	
101	ANGLEA	RIGID BODY	FREE	1.213576E-01	RADIANS
102	PITCH	RIGID BODY	FREE	1.418455E-02	NONDIMEN. RATE
103	URDD3	RIGID BODY	FIXED	2.500000E+00	LOAD FACTOR
104	ROLL	RIGID BODY	FIXED	4.400000E-02	NONDIMEN. RATE
105	URDD4	RIGID BODY	FIXED	0.000000E+00	RAD/S/S PER G
301	NCECS_L	CONTROL SURFACE	LINKED	9.544452E-01	RADIANS
302	NCECS_R	CONTROL SURFACE	FREE	-9.544452E-01	RADIANS

Figure 150. Aeroelastic Trim Results from Nastran

#### 10.2.7 Sizing Analysis

Another objective of the Boeing team was to perform a sizing analysis to ensure the buildup FEM was indeed globally optimized. Typically, this is done using Nastran SOL200, but SOL200 is limited to one structural FEM. In the case of NCE, there were three configurations of the wing FEM: Forward swept, aft swept, and unswept. To properly size this vehicle, all three NCE configurations would need to be involved simultaneously. This was done using the Nastran MultiOpt

feature, which ran three SOL200 jobs (one for each configuration) simultaneously with an additional algorithm to link and perform optimization with all 3 models to determine a solution that would be global optimal for all three configurations.

### 10.3 AIRPLANE CONTROLLABILITY ANALYSIS

Stability and Control analysis was conducted on several VGRW/wing configurations as the concept matured. Requirements were defined using MIL-STD-1797A and are presented with discussion in Section 3.1. Roll capability in the form of rolling moment coefficients and/or maximum attainable roll rate and roll acceleration were provided by VT as part of Task 10, Subtask Revision 4. Roll control power and roll damping were used to estimate aeroelastic coefficient ratios ('flex-to-rigid ratios') based on a time-domain 1st order lateral equation of motion approximation and a small angle approximation such that stability axis parameters  $\equiv$  body axis values:

$$\dot{P} = \frac{L}{I_{xx}} = \frac{\bar{q}Sb}{I_{xx}} \sum Cl \quad (22)$$

Limiting terms to roll control power and roll damping,

$$\dot{P} \approx \frac{\bar{q}Sb}{I_{xx}} \left( Cl_{\delta} \delta + Cl_p \frac{Pb}{2V_T} \right) \quad (23)$$

When roll rate reaches steady-state, roll acceleration will be zero, or:

$$P_{ss} \approx -\frac{2V_T}{b} \frac{Cl_{\delta}}{Cl_p} \delta_{max} \quad (24)$$

Flex-to-rigid ratios for control power and damping are given by:

$$K_{flex,\delta} = K_{e/r,\delta} = \frac{Cl_{\delta,flex}}{Cl_{\delta,rigid}} \quad (25)$$

and

$$K_{flex,p} = K_{e/r,p} = \frac{Cl_{p,flex}}{Cl_{p,rigid}} \quad (26)$$

Roll performance will exceed requirements if sufficient control power is available such that:

$$P_{ss} \geq P_{ss,required} \quad (27)$$

Combining (24) - (26) and rearranging terms yields the relationship in terms of flex-to-rigid ratios:

$$Cl_{\delta} K_{flex,\delta} \delta_{max} \geq Cl_P K_{flex,P} \frac{P_{ss,required} b}{2V_t} \quad (28)$$

For a rough estimate it can be assumed that aeroelasticity does not significantly increase roll damping. In this case, assuming the rigid body roll control power meets roll requirements (sufficient for an order-of-magnitude estimate) then the aeroelastic control must be equal but opposite the rigid body term ( $K_{flex,\delta} = -1.0$ ) representing a 100% effective control reversal. In that it is likely that rigid body requirements may be exceeded at speeds where aeroelasticity dominates roll control power, it is assumed that aeroelastic coefficients approximately 1 order of magnitude less than rigid body ( $K_{flex,\delta} = -0.1$ ) would be sufficient to meet requirements.

As presented in the Section 10.1.3, flex to rigid ratios in cruise with the VGRWT unswept were on the order of ~0.45 and swept were on the order of ~0.28 and resulting performance was significantly less than required. This indicates a reduction in aeroelastic control power with the VGRWT swept. In that the goal of the VGRWT program was to demonstrate an improvement in control power with the VGRWT swept using aeroelasticity as an effector, the required flex to rigid ratio must be negative in sign, indicating a control reversal. Because of this characteristic and the inability to achieve it using the pre-optimized SUGAR wing configuration, swept wings with higher cruise speeds were added to the evaluation matrix.

Swept-wing results for several configurations were evaluated using a screening criteria of 30 deg bank angle change in 2.5 sec through role reversal. Downselection based on this criteria yielded the configuration described in Section 4.4.2.1 and referred to as TBW Design 2 (or Configuration 5). Roll performance results for TBW Design 2 were evaluated using 30 degrees of primary effector (conventional TE effector on VGRWT) deflection. Roll performance results from configuration downselect were provided in terms of maximum roll rate and roll acceleration attainable as a function of VGRWT sweep, Mach no., and altitude.

Roll rate and roll acceleration capability were used to estimate time to bank and roll mode time constant (RMTC) based on a time-domain 1st order lateral equation of motion approximation and a small angle approximation such that stability axis parameters  $\equiv$  body axis values:

$$P(t) = P_{ss} \left( 1 - e^{-t/\tau} \right) \quad (29)$$

Integrating (21):

$$\phi(\Delta t) = \int_0^{\Delta t} P(t) dt = \int_0^{\Delta t} P_{ss} \left( 1 - e^{-t/\tau} \right) dt \quad (30)$$

Yields the time to bank relationship:

$$\phi(\Delta t) = P_{ss} \tau \left( \frac{\Delta t}{\tau} + e^{-\Delta t/\tau} - 1 \right) \quad (31)$$

To obtain RMTC as a function of fundamental (measured) terms from the lateral 1st order differential equation approximation:

$$\dot{P}(t) = \frac{P_{ss} - P(t)}{\tau} \quad (32)$$

and assuming at roll initiation roll rate = 0 and roll acceleration is at a maximum:

$$\tau = \frac{P_{ss}}{\dot{P}_{\max}} \quad (33)$$

Using (30) and (32) roll performance metrics for specification compliance can be estimated based on maximum attainable roll rate and roll acceleration. Results for TBW Design 2 at conditions representative of climb and cruise are presented in Figures 151 through 154.

Contours of constant bank angle change in 2.3 sec for TBW Design 2 (Configuration 5) are presented in Figure 151. From these curves a simplified saturate linear VGRWT sweep schedule (black line) and an improved multi-point schedule (blue line) were developed. Bank angle change sweep schedule breakpoints is shown along each schedule curve.

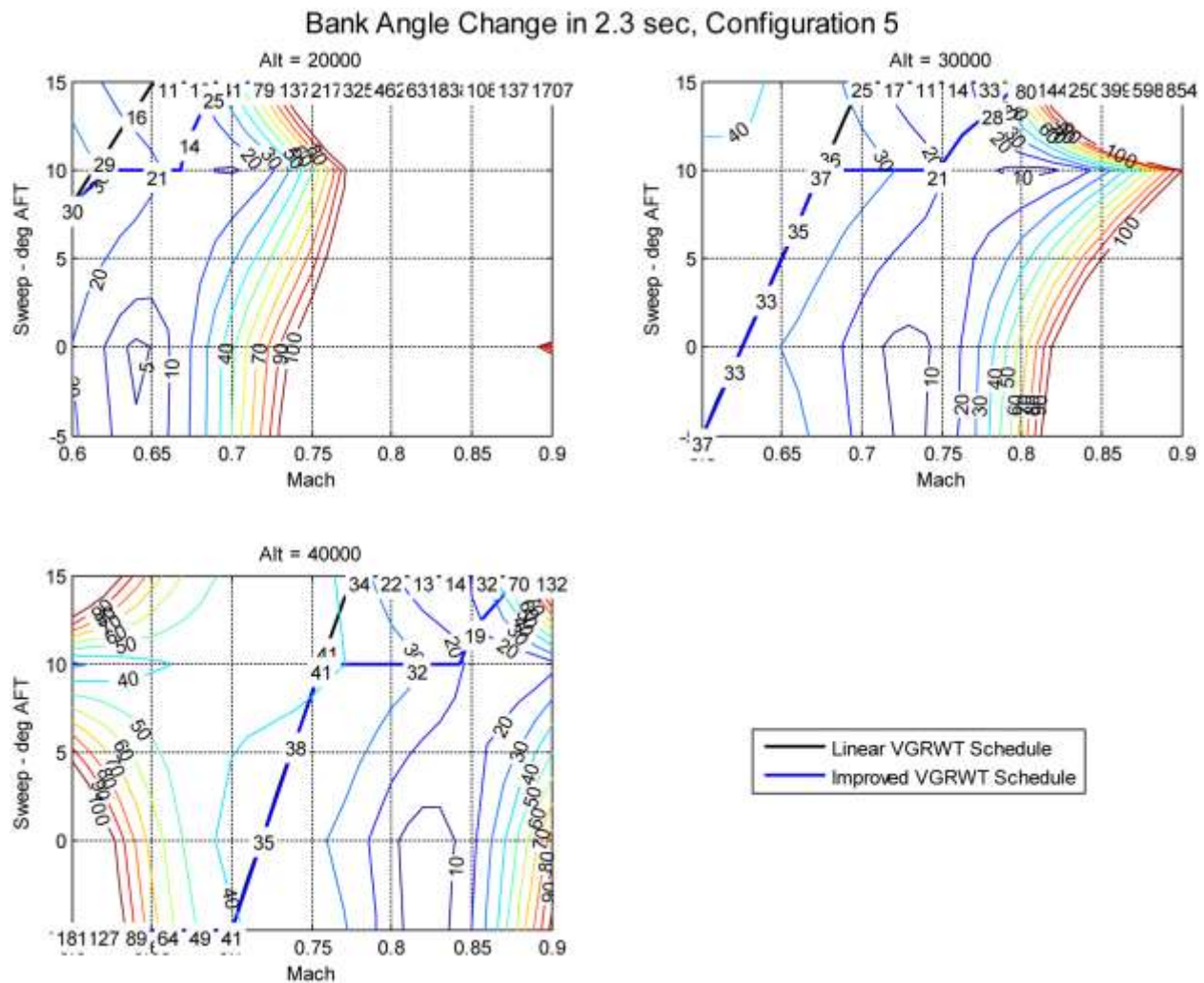


**Figure 151. TBW Design 2 Bank Angle Change in 2.3 sec.**

Contours of constant time to achieve 30 deg bank angle change for TBW Design 2 (Configuration 5) are presented in Figure 152. The linear and improved VGRWT schedules are also shown on these plots.

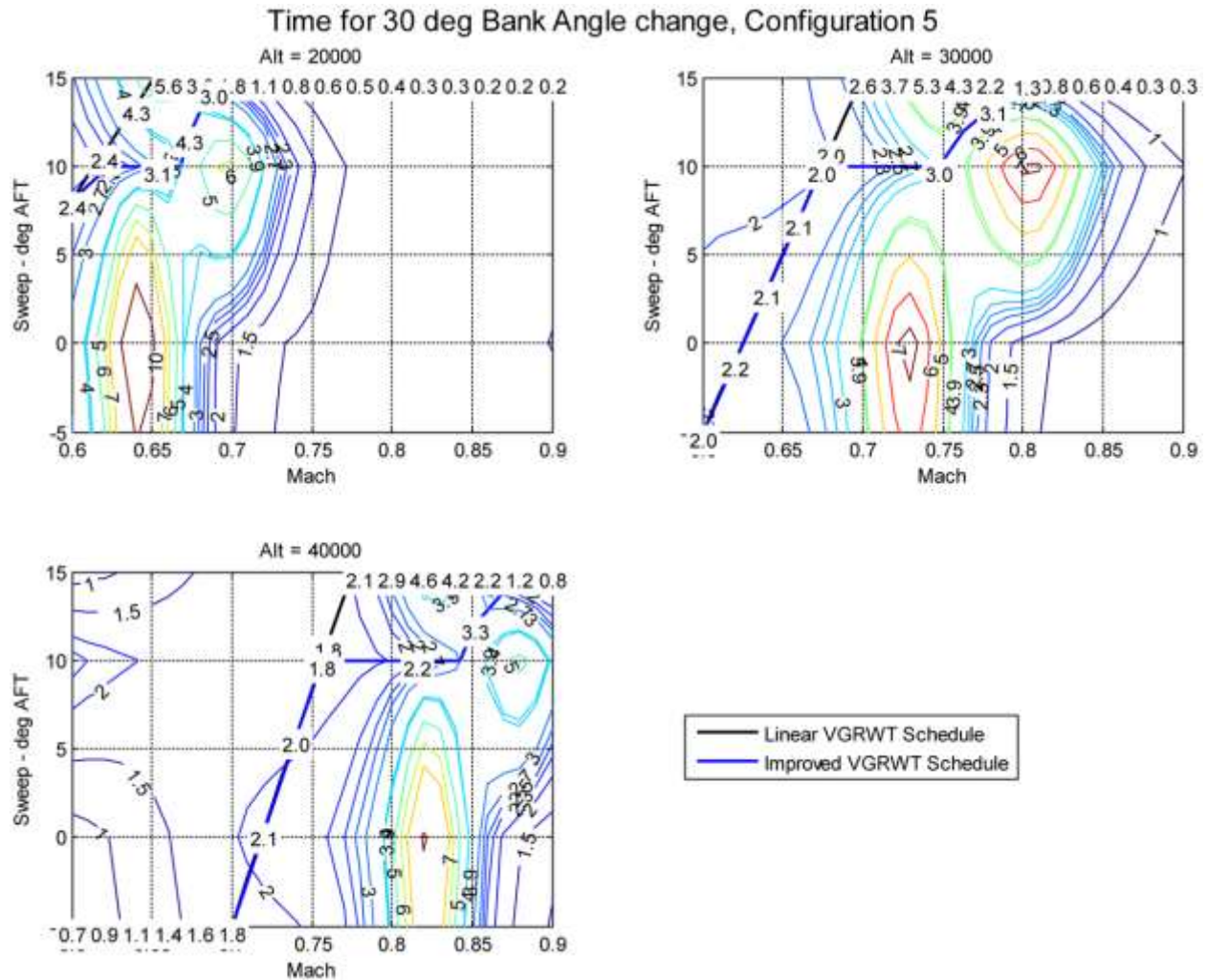


**Figure 152. TBW Design 2 Time for 30 deg Bank Angle Change.**

These results can be compared directly to the requirements of MIL-STD-1797A as summarized in Table I. Throughout the envelope evaluated roll performance, defined as time to bang 30 deg at or below Level 1 requirements was generally adequate, with values as low as <1 sec at high altitude, low speed, with the VGRWT unswept (conventional effector as aileron) and <<1 sec at low altitude, low speed, with the VGRWT swept (conventional effector as servo tab). There are also somewhat large areas of reduced roll performance in areas where the flex to rigid ratio approaches zero for a given sweep and Mach no. These areas appear as 'bullseyes' on the Time to Bank plots. With careful scheduling it is possible to minimize exposure to these areas; however, it was not possible to develop a schedule that avoided the reduced performance entirely. It may be possible to augment roll performance using other existing conventional deflectors in these regions, or to develop other mitigation strategies to take advantage of the weight reduction afforded by the VGRWT. Also notable is the region of improving performance at 10 deg sweep and increasing Mach that appears as a contour 'spike' pointing to the right on the plots. It is possible to take advantage of this area by maintaining 10 deg sweep to transition ranges of reduced performance more rapidly and then resume an aft sweep schedule to further improve performance, as enabled by the

improved VGRWT schedule. It is also expected that additional refinement could yield an additional roll performance improvement.

Contours of constant roll mode time constant for TBW Design 2 (Configuration 5) are presented in Figure 153. The linear and improved VGRWT schedules are also shown on these plots.

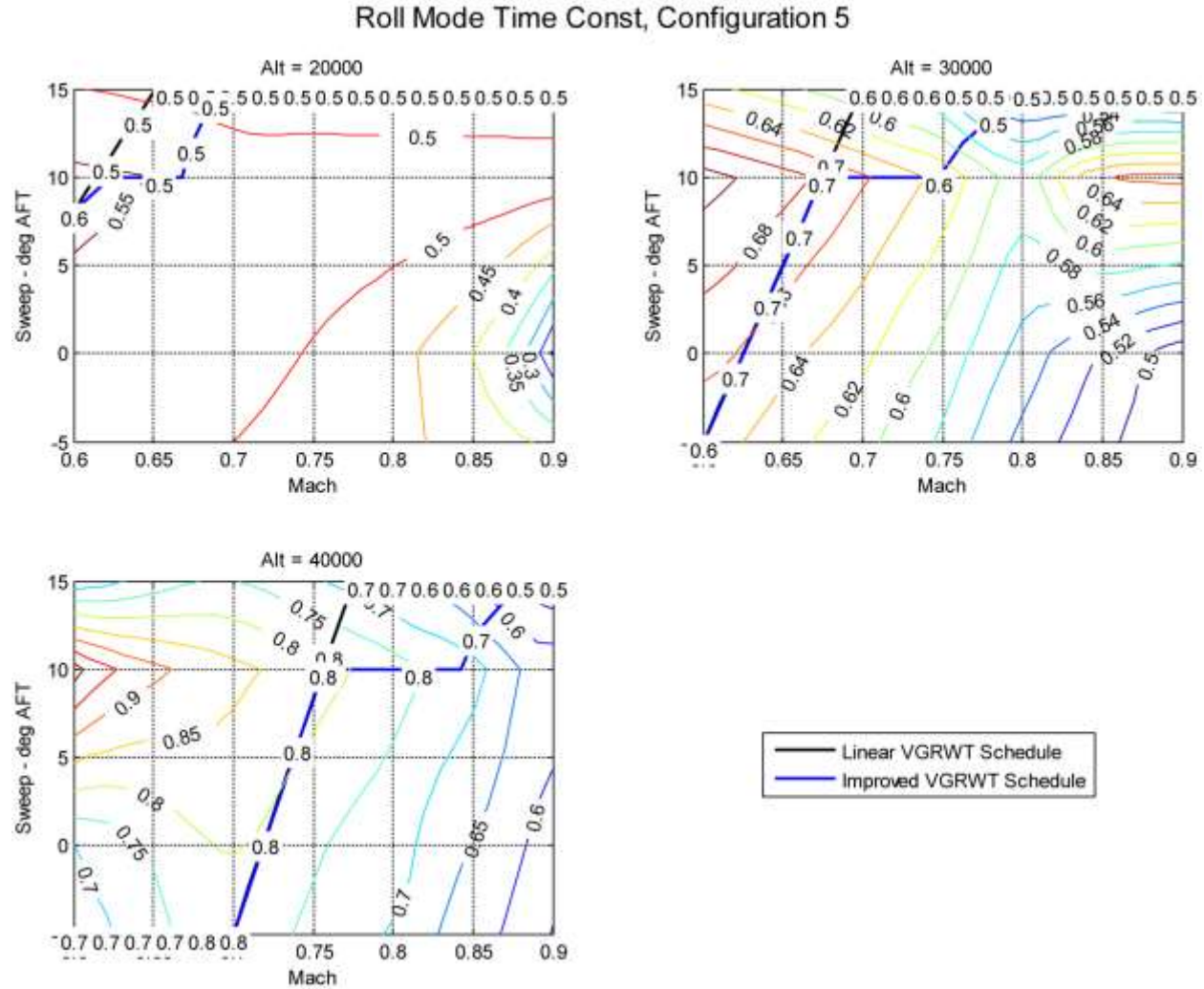


**Figure 153. TBW Design 2 Roll Mode Time Constant.**

RMTCA at most conditions readily met the 1797A requirement of RMTCA <1.4 sec and is not considered a risk for the VGRWT concept.

A notional mid- to high-altitude climb/cruise envelope is presented in Figure 154 with representative schedules for Limit Speed/Mach, Normal Operating Speed/Mach, and Turbulence Penetration Speed/Mach.

### Time for 30 deg Bank Angle change, Configuration 5, Improved Sweep Schedules

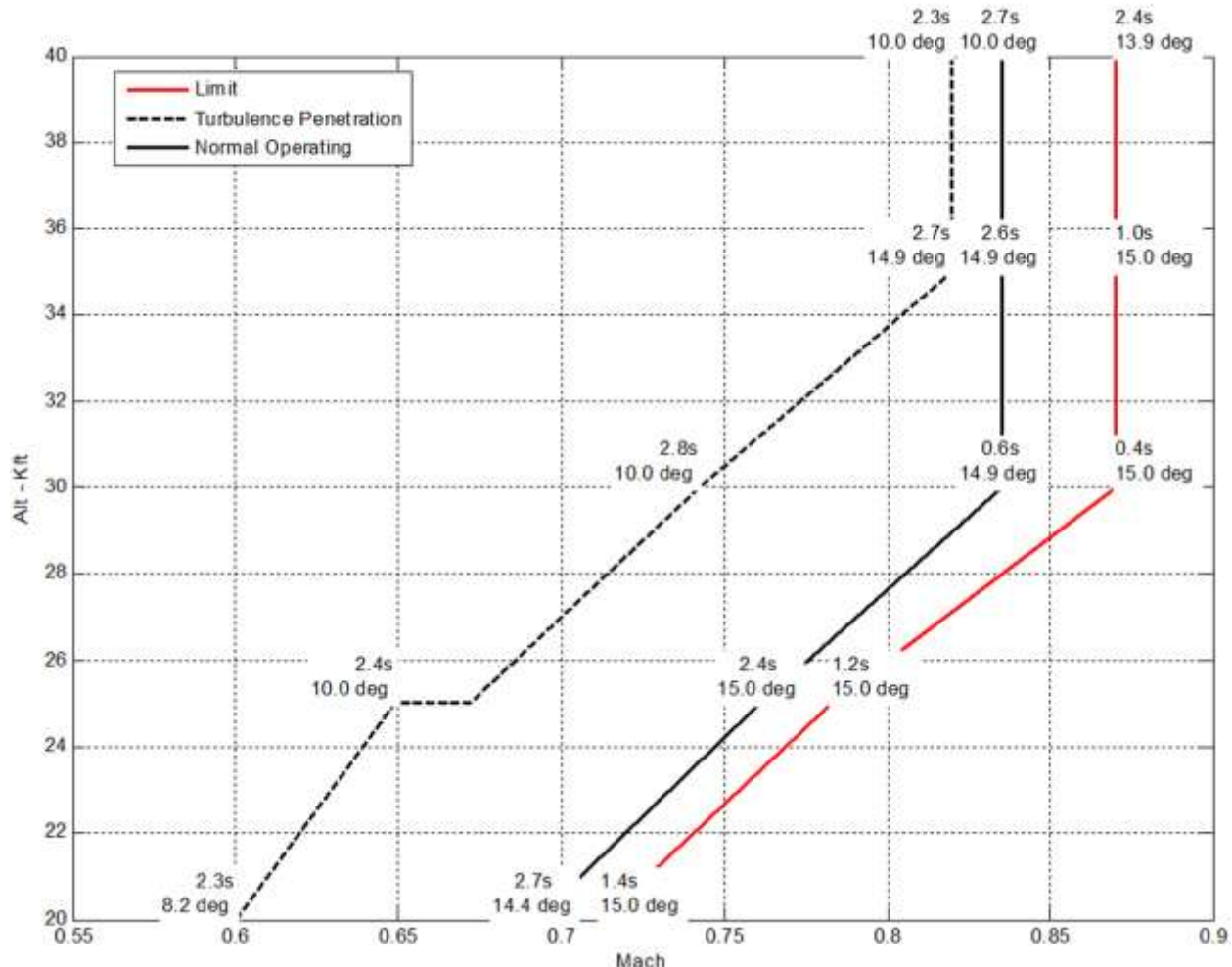


**Figure 154. TBW Design 2 Representative Climb and Cruise Roll Performance.**

Both limit and normal operating ranges correspond to the high speed range of 1797A, with the time to 30 deg requirement of 2.3 sec for Level 1 handling qualities and 3.9 sec for Level 2. The turbulence penetration speed corresponds to the 1797A mid-speed range, with the time to bank requirement of 2.0 and 3.3 sec for Level 1 and 2 handling respectively. Time to bank 30 deg at 20K, 30K and 40K altitudes and Mach on schedule is shown in Figure 154 along with the VGRWT sweep at these conditions from the improved schedule of Figures 151-153. This clearly shows the change from unswept at low speed/low altitude to swept at high Mach, high altitude, and the resulting roll performance benefit.

Initial results indicate that the VGRWT incorporated on TBW Design 2 is capable of roll performance approaching or exceeding the guidelines of MIL-STD-1797B. This performance is realized by using the surface as a conventional roll control effector (i.e. aileron) at lower climb/cruise speeds and as a servo tab at higher climb/cruise speeds and/or dynamic pressure. It is expected that additional performance benefits could be gained through further design optimization; however, in its current state the performance exceeded the Class III Category B Level 3 requirements by a large margin, indicating that adequate performance with moderate pilot workload should be achievable.

using the current configuration. The VGRWT on a swept wing with typical cruise Mach nos. shows excellent potential as a weight reduction technology for future aircraft.

## 11. QUANTITATIVE ANALYSIS SYSTEM OF TECHNICAL PERFORMANCE

The primary technical performance measures identified at the start of the program were evaluated. The TPM's were: impact of the NCE on weight, drag, noise, and power consumption. The primary TPM was fuel burn, expressed as fuel weight required for the baseline reference mission. After the initial study on the SUGAR 059 configuration indicated that it was not suitable for evaluation, a different and more challenging reference mission was selected. This included a payload and long-range mission similar to a Boeing 777-200 LR with a range of 7730 NM at a cruise Mach of 0.85. Because the SUGAR could no longer be used as a baseline, a baseline vehicle was developed using the same analysis techniques as the NCE equipped aircraft.

Some of the TPM's, specifically drag increment, noise and power were evaluated for the SUGAR configuration and found to have a very small impact. Details of the drag estimate can be found in section 7.3.1.4. The fact that there are no protuberances required for the NCE mechanism that would increase excrescence drag leaves the only remaining drag increase due to the sliding joints of the skin. The height of these joints is similar to existing joints such as leading edge slats coupled with their close to streamwise orientation indicates these will provide only a small increase in drag. Noise for the tips was evaluated and again due to the absence of any protuberances is estimated to provide a very small increase in noise. The power estimate was evaluated and shown to be small due to the very slow actuation speed of the NCE variable sweep combined with an aileron that is similar in size and configuration to current technology ailerons. These quantitative estimates were not updated for the new configuration since the design features of the NCE would be very similar and not expected to change the initial assessment for the SUGAR configuration NCE.

The primary finding for the more challenging reference mission was that a configuration was identified that achieved a 12% reduction in fuel burn. The details of the TPM calculations are found in the various preceding report sections and are summarized in Table 34.

**Table 34. Summary of Quantitative Technical Performance Measures**

TPM	Design 2 TBW without NCE	Design 2 TBW with NCE
Fuel Weight – Lbs Section 4.4.2.1	157,000	138,000 (-12:1%)
Weight – Lbs Section 4.4.2.1	482,000	476,700
Drag – CD Section 7.3.1.4	Baseline	Negligible Increase
Noise – EPNL dB Section 8.1	Baseline	+0.1 to +0.2 dB
Power	Baseline	Negligible Increase

## 12. CONCLUSIONS

The novel control effectors for truss braced wing research concluded the following points with respect to the four primary objectives:

- Design of a Variable-Geometry Raked Wingtip (VGRWT) for a truss-braced wing was completed. A wingtip with high-rate control effectors can be raked in flight to modify the location of the surface's aerodynamic center as a function of flight condition. The wingtip's high-rate control effectors have sufficient bandwidth for stabilization and control of aeroelastic wing dynamics and load alleviation.
- A subsystem layout and kinematic model study for the VGRWT found load paths, geometry, and integration of electrical, hydraulic, and other lines acceptable. The track and beam design with its pivot point along the aft beam minimized weight and facilitated subsystem integration.
- A vehicle-level analysis was performed to quantify the impact of the VGRWT on vehicle lift, drag, noise, and weight as compared against a baseline truss-braced wing. The VLM code, Tornado, analysis showed that the lift would increase, with a subsequent decrease in drag as a result of the new wingtip. The unswept VGRWT/NCE tip provided more lift than the baseline wing tip and the swept VGRWT/NCE tip. This result justifies having the VGRWT/NCE tip unswept during take-off and landing, when lift is at a premium. Also, the swept configuration presented a lower drag coefficient than the baseline SUGAR wingtip, which validates the concept of a swept wingtip for cruise. The pitching moment of the wing would also increase, leading to a more stable platform. Inviscid CFD simulations run through ANSYS Fluent largely corroborated these results. The contributions due to VGRWT are seen to be very small, only making negligible impact on the total aircraft noise. Minimum additional subsystem weight for the VGRWT compared to the baseline SUGAR configuration coupled with reduced drag and fuel burn leads to potential TOGW weight reductions.
- A dynamics model of a dual-aisle, truss braced wing aircraft with a VGRWT was developed and used to assess vehicle aeroelastic and controllability characteristics. VGRWT on a swept wing with typical cruise Mach numbers showed excellent potential as a weight reduction (i.e. reduced fuel burn) technology for future aircraft. For a dual-aisle truss braced wing aircraft, a VGRWT was needed to provide roll control across the flight envelope and had a level of negative flutter margin within the capabilities expected for active flutter suppression.

Many of the key project findings are illustrated by Figure 155 which summarizes the results of the MDO for the TBW dual-aisle configuration. The abscissa is flutter margin with negative margin indicating flutter occurs at a speed less than would be required for conventional designs. This is essentially an indicator of wing torsional stiffness. The ordinate is fuel burn for the reference mission (similar to 777-200 capability). Minimizing fuel burn was the primary objective function of the MDO. The dots represent individual configurations identified by the genetic algorithm optimizer.

The MDO results fall into three distinct regions. Region 1 has adequate flutter margin to meet current design requirements. The best fuel burn achieved in this region (designated Configuration 3) was  $1.51 \times 10^5$  lbs. The torsional stiffness of the wings for the designs in Region 1 is sufficiently

high that the VGRWT does not function as intended because aileron reversal sufficient to control the airplane is not achieved. On the left-hand side designs in Region 3 are torsionally compliant but have a very attractive fuel burn up to 10% better than the best Region 1 design. The torsional compliance of the Region 3 designs results in negative flutter margins, although still within a range that could be controlled with active flutter suppression. But more importantly, an outboard aileron operates predominately in aileron reversal such that the variable geometry of the VGRWT is of little use and the aircraft would likely need additional roll control effectors to function across the flight envelope. A last observation on Region 3 is that there is little or no fuel burn improvement to be gained with increasing torsional compliance (as indicated by increasing negative flutter margin). In general, Region 1 cannot benefit from VGRWT because the wings are too stiff. Region 3 gets little benefit from VGRWT because the wings are too soft.

In Region 2 the wing stiffness is in a range where the VGWRT can provide unassisted roll control authority across the flight envelope. At the left end of Region 2 is a configuration (designated Design 2 or Configuration 5) that has the 10% improved fuel burn equal to the lower pareto front of the Region 3 designs and possesses a modest negative flutter margin that can be easily controlled by active flutter suppression. Design 2 (Configuration 5) was selected for further verification modeling and analyses conducted by Boeing and NextGen Aeronautics. This verification analyses independent of the MDO methods showed that Design 2 (Configuration 5) is in fact a valid design and fully confirmed the results of the VT MDO.

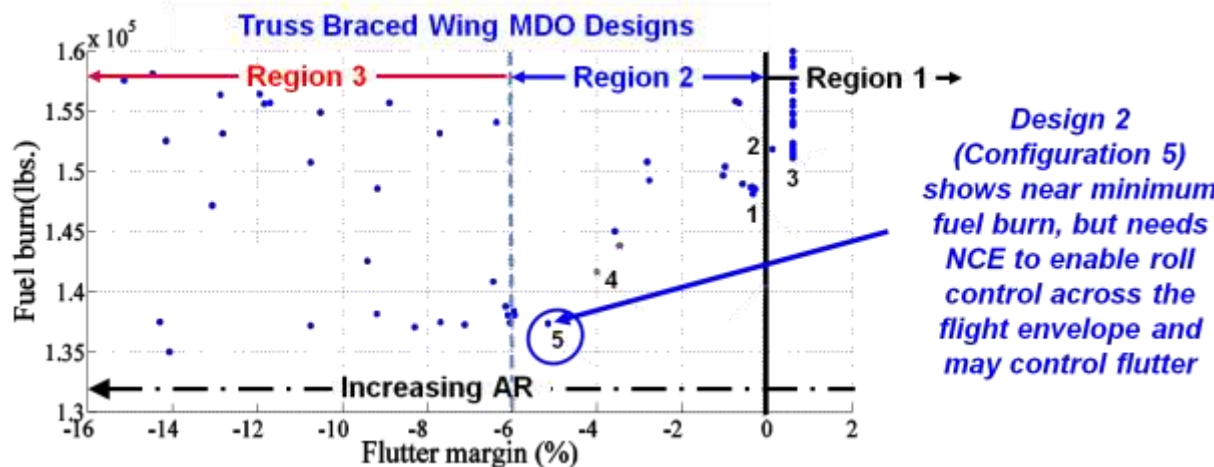


**Figure 155. Key VT MDO Summarized Results for Dual-Aisle TBW Configuration**

A key conclusion of this effort extends well beyond the novel control effector studied herein. The NCE is characteristic of a class of advanced technology that current MDO tools are not set up to handle. The initial conclusion of this study was that the NCE did not function and could not provide benefit to the original N+3 SUGAR 765-059 configuration. Frequently advanced technology ideas are evaluated on existing aircraft configurations and then discarded if benefits are found to be insufficient even though it is realized that the benefits may be highly configuration dependent. The question is not asked, "is there a high performance configuration that could significantly benefit from the technology?" Without the ability to answer this question, many valuable advanced technology concepts are abandoned based on the false underlying assumption that if the technology does not benefit the selected aircraft, it cannot adequately benefit any aircraft. The second half of this study directly addressed this difficult question. To the author's knowledge, this is the first

attempt to use MDO to find an aircraft configuration that can benefit from a given technology. This was successful but involved both significant upgrades to an MDO system as well as a significant amount of external analysis of results followed by user intervention to explore parts of a design space that the MDO optimizer may not explore due to inherent simplifications in the MDO objective function.

### 13. RECOMMENDATIONS

This report documents detailed and extensive studies of many aspects of the application of an NCE wingtip to transonic, transport aircraft with very flexible wings. Two major findings are first that an NCE tip can provide sufficient control authority to meet government/industry requirements with the outboard aileron on the main wing in aeroelastic reversal while achieving reduced fuel consumption for some aircraft missions. Second, we have found an added, unexpected simultaneous benefit in the form of flutter alleviation. While extensive studies have been performed, the mission and geometry design space is very large, and the results obtained to date show that the utility of an NCE wingtip depends critically upon the location of the study in the mission and geometry design space. Taken together with the favorable potential demonstrated, this strongly indicates that much broader explorations of the mission and geometry design space are very likely to lead to large improvements in NCE wingtip performance. We strongly recommend that such studies be undertaken following the successful model of a collaborative team of industry and academic partners employing integration of Multidisciplinary Design Optimization (MDO) and detailed simulations, especially in the transonic range, developed and proven in the current effort. In addition, experimental verification of the aeroelastic and aerodynamic predictions, especially in the TDT, at the end of the next phase of this research is clearly warranted. Finally, we recommend that the efficacy of using NCE for gust alleviation be investigated, first analytically and then experimentally.

While the MDO output was successfully used to generate a solid model of the NCE/wing interface, there is plenty of room for the process to be streamlined to produce time and cost savings in the design effort. An update and expansion of the MDO manual would provide a large step in the right direction. Specific additions to the manual should include a full explanation of the output, as well as details about the use of different coordinate systems in use and how properties are transferred between them in the MDO. Additional improvements to the whole system, some simple some more complex, could make the resulting output more realistic to a final design, enhancing the value of the system.

In developing the solid model of the vehicle we identified some items that could use further study to improve the design, and reduce complexity of the required structure at the joint between the NCE and wing. The most important is determining the load path through the joint, to obtain the load carried by the NCE hinge and how much must be carried through a sliding mechanism for the other spar. Another area of interest is the impact of small OML changes at the joint, such as a small bulge in the planform to accommodate the sweeping OML of the NCE. These recommendations, and others, are explained in more detail above in Section 5.7.

It is recommended that additional optimization studies be conducted to further refine the performance of the VGRWT/swept-wing configuration at climb and cruise conditions. Low-speed roll performance should also be evaluated. Dynamic models should also be developed to assess the potential for the device as a maneuver load alleviation and flutter-suppression effector. Finally, a dynamic model of a wing fitted with VGRWT should be incorporated in a closed-loop simulation and offline and piloted evaluations conducted directly assess the handling qualities achievable with the VGRWT concept.

To further mature the novel control effector design, the fidelity of finite element analysis will need to be increased to reduce uncertainty of NCE design. The current structural analysis assumed that loads from NCE to wing are carried by both front and rear spars. However, this is likely not

the case once the mechanism design matures, because the front spar will be moving to support the NCE movement. This is an area where the modeling fidelity will need to be increased, so correct load path can be modeled to obtain proper structural sizing in that region. Additionally, all connections between wing and body, wing and strut, strut and jury, and strut and body will need to be revised. The FEM used in this report assumed all six degrees of freedom are connected between all the components, but often in reality there are less degrees of freedom connected in these connections. Also, current FEM has fuel mass as the only non-structural mass on the wing. Typically, there are also non-structural masses representing actuators, fuel plumbing, and other systems in the wing. These mass will need to be added and distributed properly on the wing so their effect on the dynamic of the structure are captured. Lastly, aerodynamic corrections should be added to the aero model of the wing to increase accuracy of aero load on the wing, and to reduce uncertainty when it comes to flutter margin and roll performance.

## 14. REFERENCES

- [1] Joshi, S., "Wind Tunnel Test and Results of NextGen Morphing Wind-Tunnel Model," 48th AIAA/ASME/ASCE/AHS/ASC Structures, Structural Dynamics, and Materials Conference, Sheraton Waikiki - Honolulu, HI, April 25, 2007, Oral Presentation.
- [2] "NASA Subsonic Fixed Wing Project Overview," [http://www.aeronautics.nasa.gov/fap/2012-PRESENTATIONS/SFW\\_2012\\_508.pdf](http://www.aeronautics.nasa.gov/fap/2012-PRESENTATIONS/SFW_2012_508.pdf).
- [3] Gur, O., Bhatia, M., Mason, W., Schetz, J., Kapania, R., and Nam, T. "Development of a framework for truss-braced wing conceptual MDO," Structural and Multidisciplinary Optimization Vol. 44, No. 2, 2011, pp. 277-298.
- [4] Gur, O., Schetz, J. A., and Mason, W. H. "Aerodynamic Considerations in the Design of Truss-Braced-Wing Aircraft," Journal of Aircraft Vol. 48, No. 3, 2011, pp. 919-939.
- [5] Gur, O., Bhatia, M., Schetz, J. A., Mason, W. H., Kapania, R. K., and Mavris, D. N. "Design optimization of a truss-braced-wing transonic transport aircraft," Journal of Aircraft Vol. 47, No. 6, 2010, pp. 1907-1917.
- [6] Mallik, W., Kapania, R. K., and Schetz, J. A. "Multidisciplinary Design Optimization of Medium-Range Transonic Truss-Braced Wing Aircraft with Flutter Constraint," 54th AIAA/ASME/ASCE/AHS/ASC Structures, Structural Dynamics, and Materials Conference. American Institute of Aeronautics and Astronautics, 2013.
- [7] Miller, G. D., "Active Flexible Wing (AFW) Technology," Tech. rep., DTIC Document, 1988.
- [8] Griffin, K. E. and Hopkins, M. A., "Smart stiffness for improved roll control," Journal of aircraft, Vol. 34, No. 3, 1997, pp. 445-447.
- [9] Pendleton, E. W., Bessette, D., Field, P. B., Miller, G. D., and Griffin, K. E., "Active aeroelastic wing flight research program: technical program and model analytical development," Journal of Aircraft, Vol. 37, No. 4, 2000, pp. 554-561.
- [10] Dowell, E. H., Bliss, D. B., and Clark, R. L., "Aeroelastic wing with leading-and trailing-edge control surfaces," Journal of Aircraft, Vol. 40, No. 3, 2003, pp. 559-565.
- [11] Platanitis, G. and Strganac, T. W., "Suppression of control reversal using leading-and trailing-edge control surfaces," Journal of guidance, control, and dynamics, Vol. 28, No. 3, 2005, pp. 452-460.
- [12] Meadows, N. A., Schetz, J. A., Kapania, R. K., Bhatia, M., and Seber, G. "Multidisciplinary Design Optimization of Medium-Range Transonic Truss-Braced Wing Transport Aircraft," Journal of Aircraft Vol. 49, No. 6, 2012, pp. 1844-1856.
- [13] Gupta, R., Mallik, W., Kapania, R. K., and Schetz, J. A. "Multidisciplinary Design Optimization of Subsonic Strut-Braced Wing Aircraft," 52nd Aerospace Sciences Meeting. American Institute of Aeronautics and Astronautics, 2014.
- [14] Megson, T. H. G. Aircraft structures for engineering students: Elsevier, 2012.
- [15] Timoshenko, S. P., and Gere, J. M. Theory of elastic stability: Courier Dover Publications, 2012.
- [16] Hoerner, S. F., and Borst, H. V. Fluid-dynamic lift: Practical information on aerodynamic and hydrodynamic lift, 1975.
- [17] Hyde, D., Private Communication, Boeing Research and Technology, September, 2014.

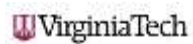
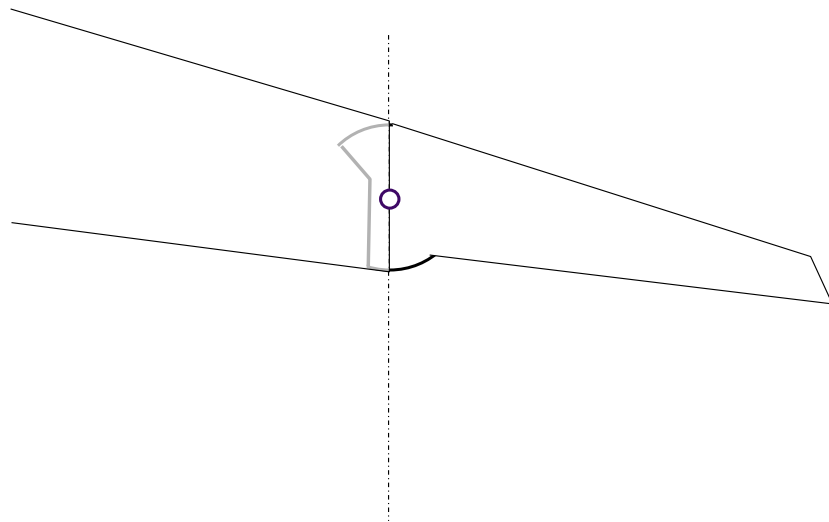
- [18] "<http://www.phoenix-int.com/software/phx-modelcenter.php>." 10.0 ed., Phoenix Integration, p. ModelCenter.
- [19] Rodden, W. P. Theoretical and Computational Aeroelasticity: Crest Pub., 2011.
- [20] Bisplinghoff, R. L., Ashley, H., and Halfman, R. L., Aeroelasticity, Courier Dover Publications, 2013.
- [21] Seber, G., Gur, O., Bhatia, M., Schetz, J. A., Mason, W. H., Kapania, R. K., Nam, T., Ran, H., Perullo, C., Mavris, D. N., "Truss-Braced Wing MDO in ModelCenter Framework, Revision 3" MAD Center Report 2011-01, September, 20011.
- [22] Stephenson, D. "Envisioning Tomorrow's Aircraft." The Boeing Company, 16 August 2010. Web. <[http://www.boeing.com/Features/2010/06/corp\\_envision\\_06\\_14\\_10.html](http://www.boeing.com/Features/2010/06/corp_envision_06_14_10.html)>.
- [23] Gur, O., Schetz, J.A., Mason, W.H. "Aerodynamic Considerations in the Design of Truss-Braced Wing Aircraft," AIAA Paper 2010-4813, 28th AIAA Applied Aerodynamics Conference, June 28 - July 1, 2010, Chicago, Illinois.
- [24] de Mattos, B., Macedo, A., da Silva Filho, D. "Considerations about Winglet Design," AIA Paper 2003-3502, 21st Applied Aerodynamics Conference, June 23-26, 2003, Orlando, Florida.
- [25] Halpert, J., Prescott, D., Yechout, T., Arndt, M. "Aerodynamic Optimization and Evaluation of KC-135R Winglets, Raked Wingtips, and a Wingspan Extension," AIAA Paper 2010-57, 48th AIAA Aerospace Sciences Meeting Including the New Horizons Forum and Aerospace Exposition, January 4-7, 2010, Orlando, Florida.
- [26] Spearman, M. L. "Aerodynamic Research at NACA/NASA Langley Related to the Use of Variable-Sweep Wings," AIAA Paper 2012-0956, 50th AIAA Aerospace Sciences Meeting including the New Horizons Forum and Aerospace Exposition, January 9-12, 2012, Nashville, Tennessee.
- [27] Kress, R. "Variable Sweep Wing Design," AIAA Paper 83-1051, Archive Set 237: Generic Session, January 1, 1963.
- [28] Bertin, J. Aerodynamics for Engineers. 4th ed. Upper Saddle River, NJ: Prentice Hall, 2002. pp. 260-78.
- [29] Melin, T. A Vortex Lattice MATLAB Implementation for Linear Aerodynamic Wing Applications. MS Thesis. Royal Institute of Technology, Stockholm, 2000. Web. <<http://www.redhammer.se/Tornado/thesis.pdf>>.
- [30] Melin, T. User's Manual, Reference Guide Tornado 1.0. Royal Institute of Technology, Stockholm, 2000. Web. <<http://www.redhammer.se/Tornado/manual.pdf>>.
- [31] Welsted, J., Reitz, B., Crouse, G. "Modeling Fuselage Aerodynamic Effects in Aircraft Design Optimization," AIAA Paper 2012-0394, 50th AIAA Aerospace Sciences Meeting including the New Horizons Forum and Aerospace Exposition, January 9-12, 2012, Nashville, Tennessee.
- [32] Melin, T., Isikveren, A. Friswell, M., "Induced-Drag Compressibility Correction for Three-Dimensional Vortex-Lattice Methods," Journal of Aircraft, Vol. 47, No. 4, 2010, pp. 1458 - 1460.
- [33] "UIUC Airfoil Coordinates Database." UIUC Airfoil Data Site. University of Illinois at Urbana-Champaign, Web. <[http://www.ae.illinois.edu/m-selig/ads/coord\\_database.html](http://www.ae.illinois.edu/m-selig/ads/coord_database.html)>

- [34] Hays, A. "12.6 Drag Due to Lift (Induced Drag)." ADAC, 28 March 2009. Web. <[http://www.adac.aero/linked/12.6\\_drag\\_due\\_to\\_lift.pdf](http://www.adac.aero/linked/12.6_drag_due_to_lift.pdf)>.
- [35] Raymer, D. Aircraft Design: A Conceptual Approach. 4th ed. Reston, VA: American Institute of Aeronautics and Astronautics, 2006. pp. 347-348.
- [36] White, F. Viscous Fluid Flow. 3rd ed. New York, NY: McGraw-Hill Higher Education, 2006. pp. 314-315.
- [37] Hoerner, S. Fluid-dynamic Drag: Practical Information on Aerodynamic Drag and Hydrodynamic Resistance. Midland Park, N.J: Dr.-Ing. S.F. Hoerner, 1958. pp. 5-6 - 5-9.
- [38] Thomas, R.H. and Burley, C.L., "Progress Toward the N+2 Noise Goal: HWB Propulsion Airframe Aeroacoustics Boeing/NASA Low Speed Aeroacoustics Facility Experiment and System Noise Assessment," presentation to the NASA Fundamental Aeronautics Program Third Annual Meeting, Atlanta, Georgia, September 29-October 1, 2009.
- [39] Y. P. Guo, Aircraft Slat Noise Modeling and Prediction, AIAA Paper 2010-3837 (2010)
- [40] Y. P. Guo, Aircraft Flap Side Edge Noise Modeling and Prediction, AIAA Paper (2011).
- [41] Guo, Y., "An Improved Landing Gear Noise Prediction Scheme," NASA/CR NAS1-NNL04AA11B Task NNL06AB63T, The Boeing Company, Huntington Beach, CA, November 2006.

## **APPENDIX A. VGRWT MECHANIZATION CONCEPTS SUMMARY**

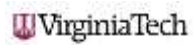
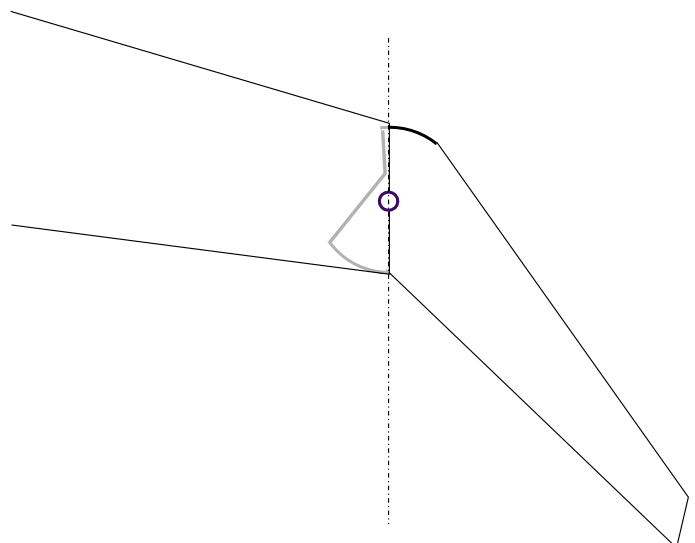
## Simple Pivot - Unswept

Engineering, Operations & Technology



## Simple Pivot - Swept

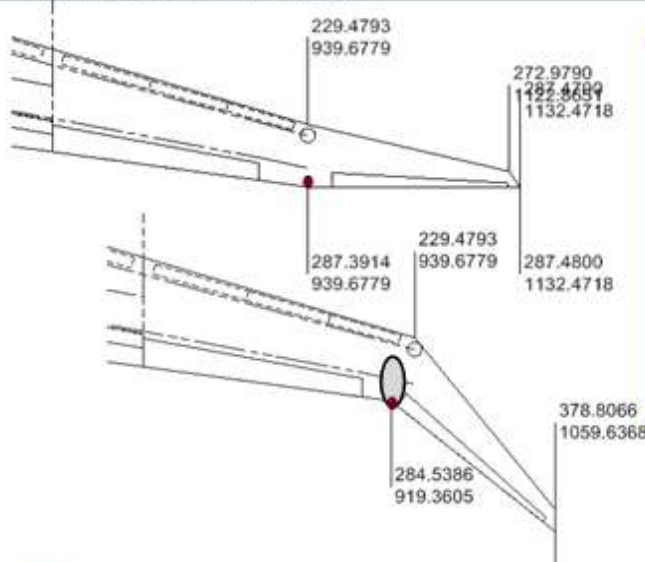
Engineering, Operations & Technology



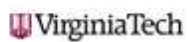
Copyright © 2011 Boeing. All rights reserved.

## Pivot about Trailing Edge

Engineering, Operations & Technology

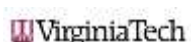
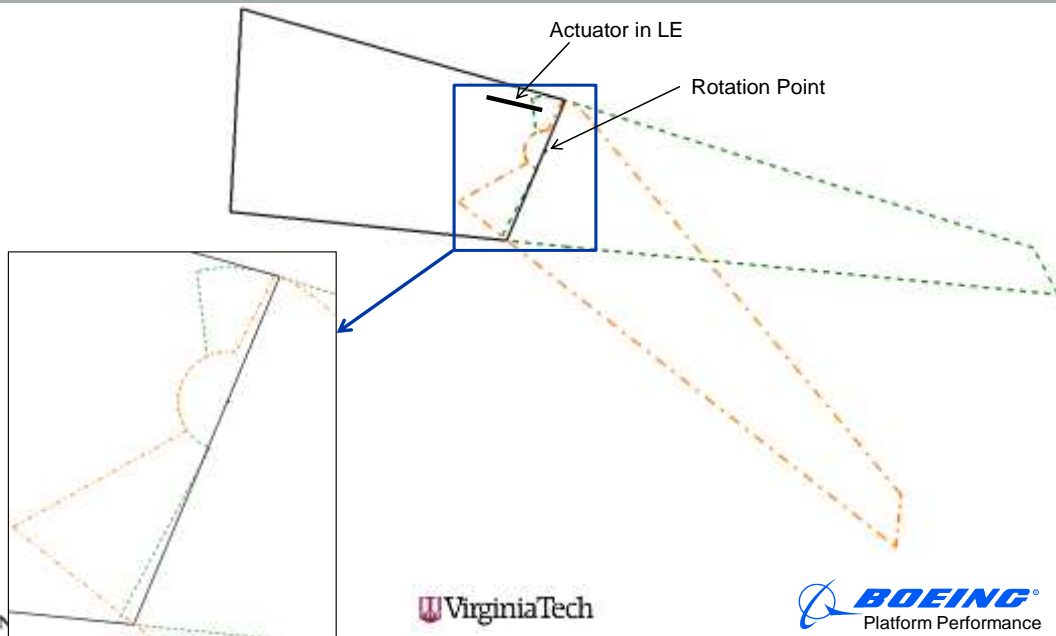


Rotate about trailing edge point. Trailing edge is thinnest portion of airfoil and may need to bump geometry like canoe fairing on F/A-18 aileron hinge fittings. This keeps trailing edge constant. Leading edge which is thicker can have sliding covers.



## Concept 1

Engineering, Operations & Technology

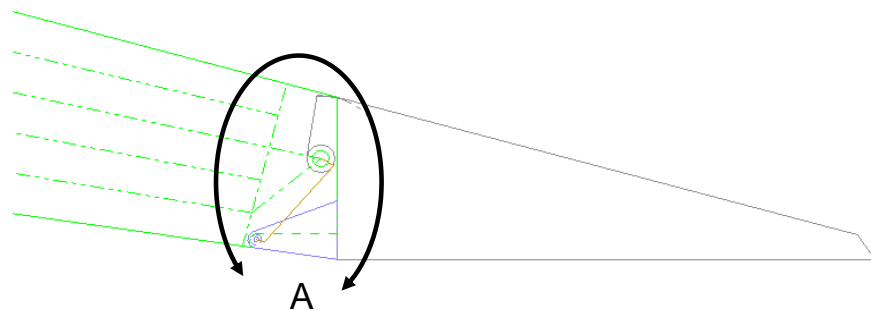


Copyright © 2011 Boeing. All rights reserved.

## Concept 1

### Un-rotated Wingtip

Engineering, Operations & Technology



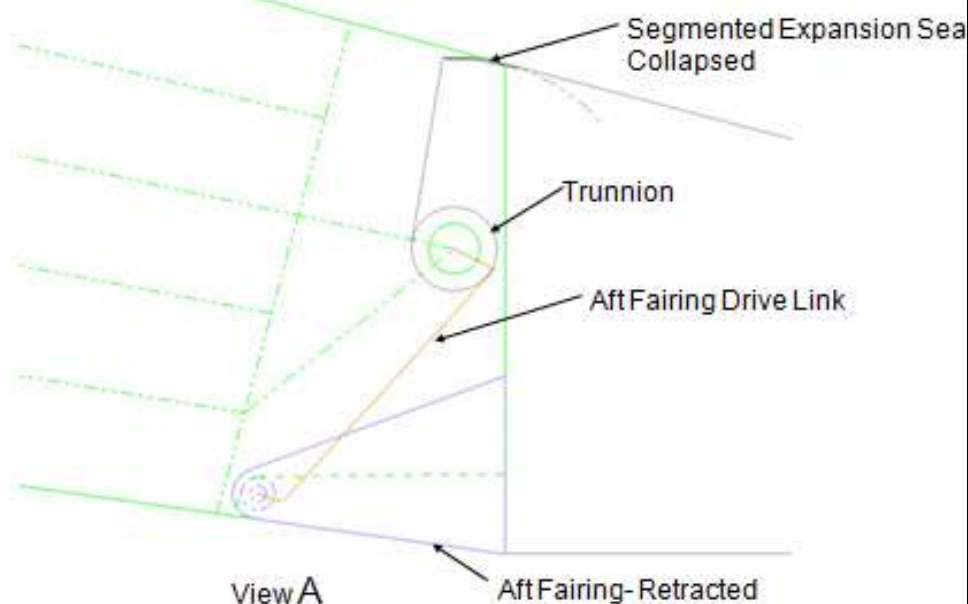
Copyright © 2011 Boeing. All rights reserved.

11

## Concept 1

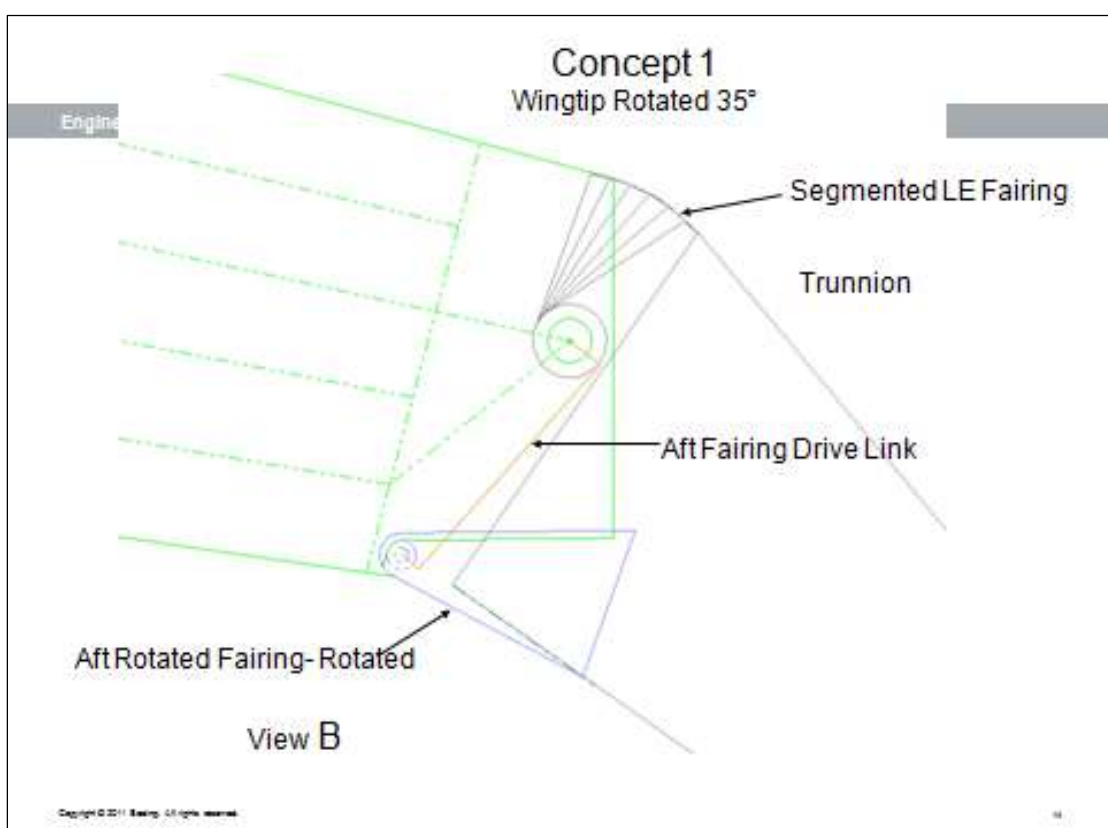
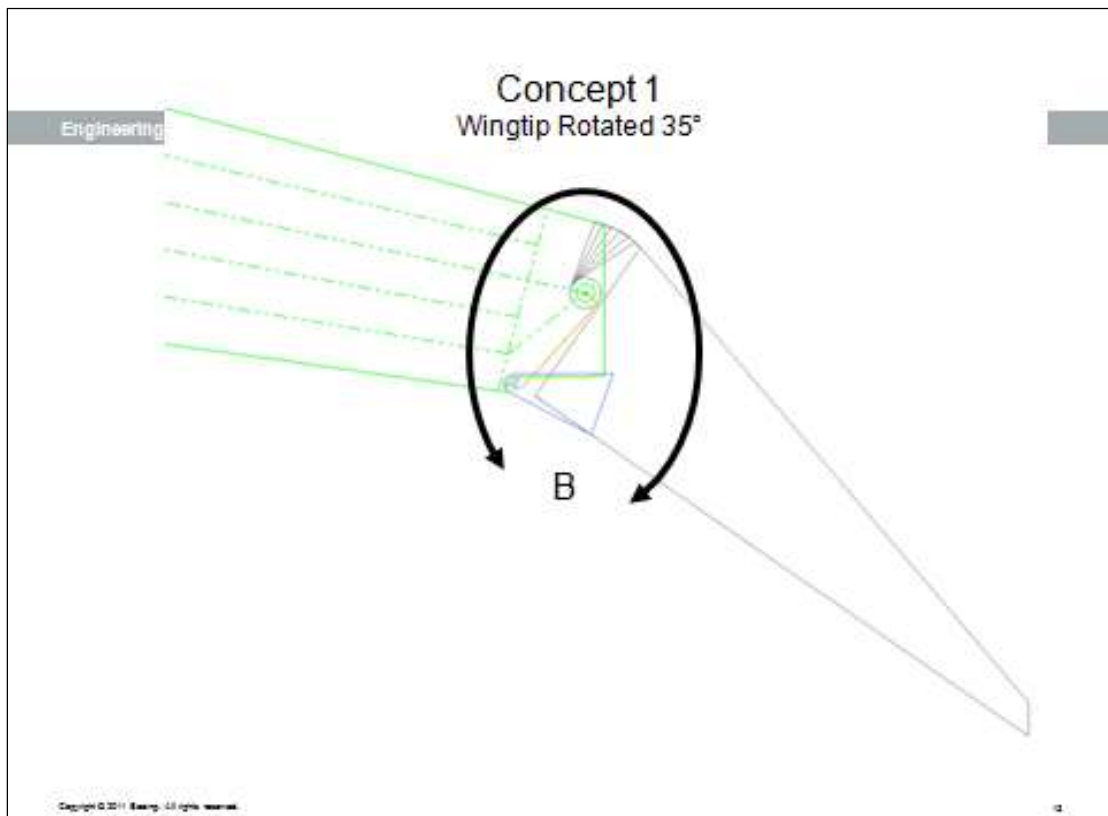
### Un-rotated Wingtip

Engineering



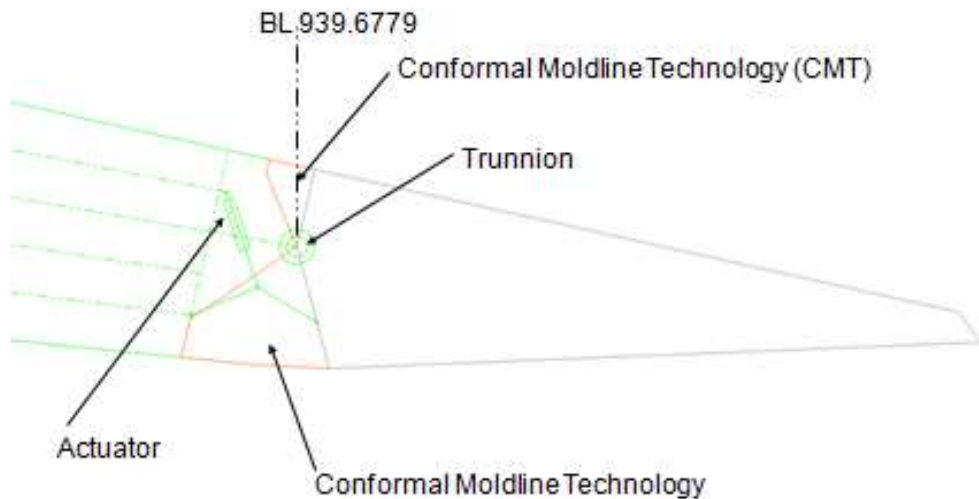
Copyright © 2011 Boeing. All rights reserved.

12



## Concept 2 Un-rotated Wingtip

Engineering, Operations & Technology

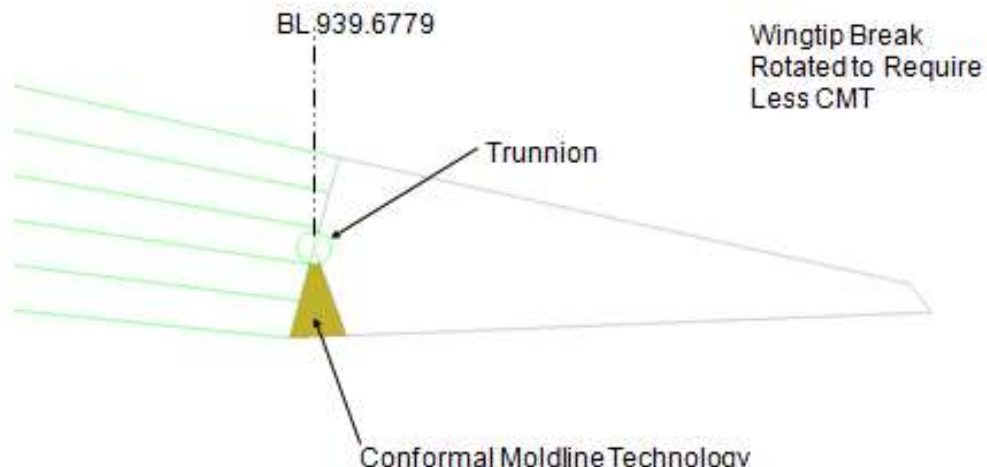


Copyright © 2011 Boeing. All rights reserved.

12

## Concept 3 Un-rotated Wingtip

Engineering, Operations & Technology



Copyright © 2011 Boeing. All rights reserved.

13

## Concept 3 Rotated Wingtip

Engineering, Operations & Technology

BL 939.6779

Conformal Moldline Technology

Copyright © 2011 Boeing. All rights reserved.

14

Engineering

NO STEP

CLOSER

PUSH IN 1°

DAMP DOWN

DOWN 1°

UP 1°

DAMP UP

UP 1°

DOWN 1°

DAMP DOWN

DOWN 1°

UP 1°

DAMP UP

UP 1°

DOWN 1°

DAMP DOWN

DOWN 1°

UP 1°

DAMP UP

UP 1°

DOWN 1°

DAMP DOWN

DOWN 1°

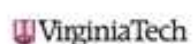
UP 1°

DAMP UP

UP 1°

DOWN 1°

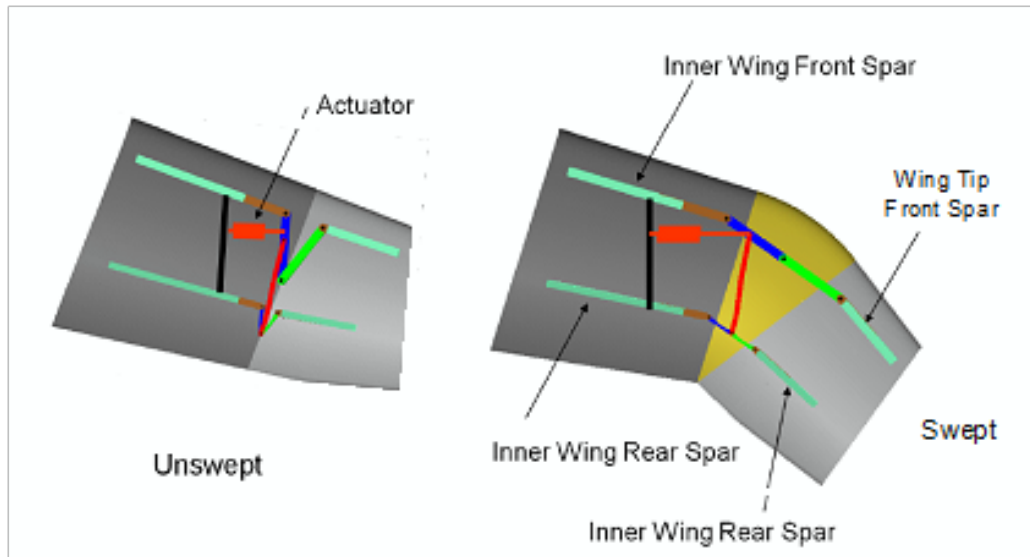
Joe Scheite  
2/4/11



Copyright © 2011 Boeing. All rights reserved.

## Multiple or complex pivots

Engineering, Operations & Technology



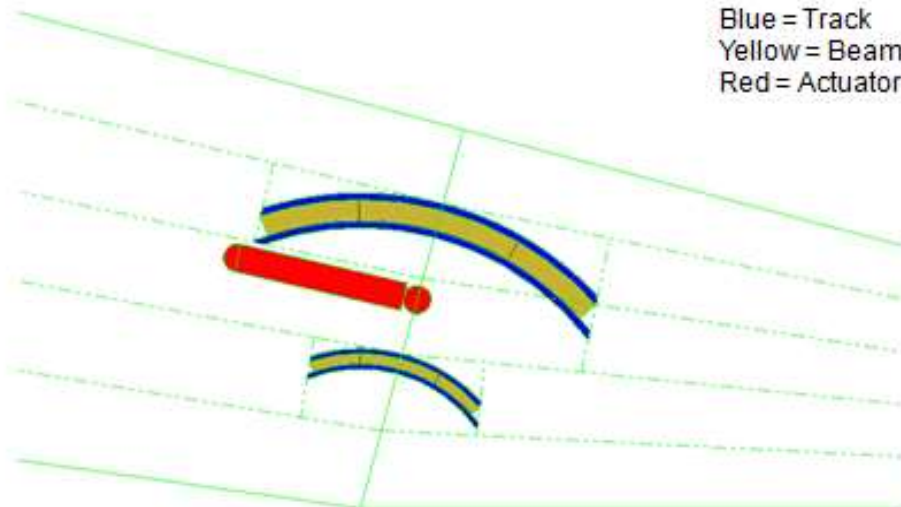
Copyright © 2011 Boeing. All rights reserved.

2

## Split Track Concept

Engineering, Operations & Technology

Blue = Track  
Yellow = Beam  
Red = Actuator

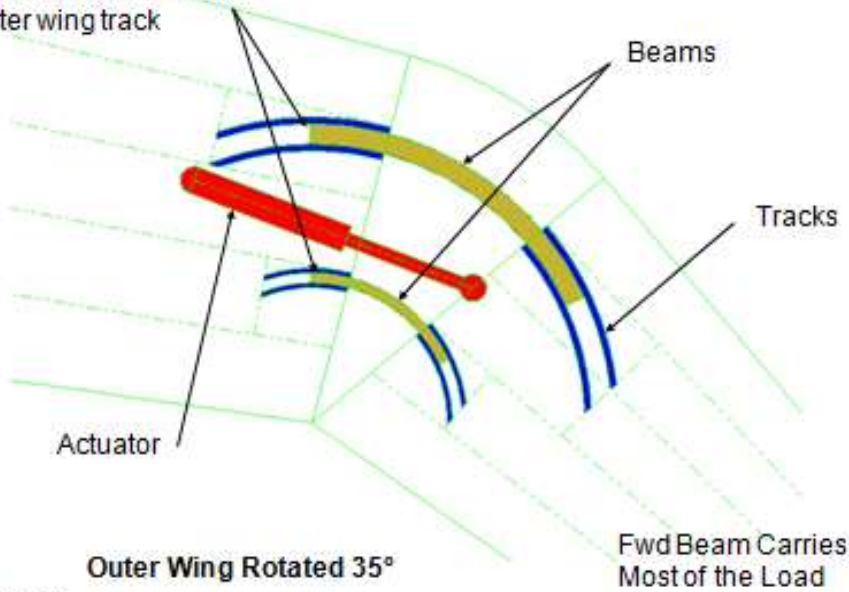


Copyright © 2011 Boeing. All rights reserved.

## Split Track Concept

Engineering, Operations & Technology

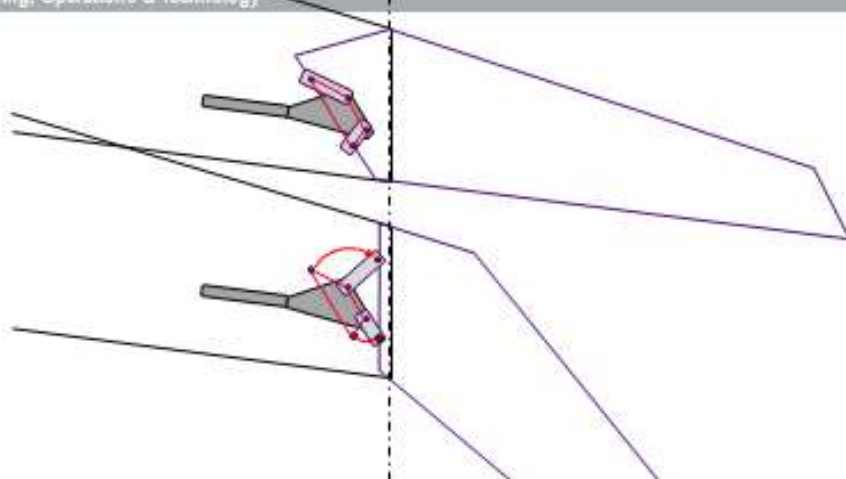
Stops here, after which actuator drives beam in outer wing track



Copyright © 2011 Boeing. All rights reserved.

## 4-Bar Linkage – 2 Bars Carry Loads

Engineering, Operations & Technology



NEXTGEN AERONAUTICS

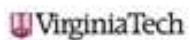
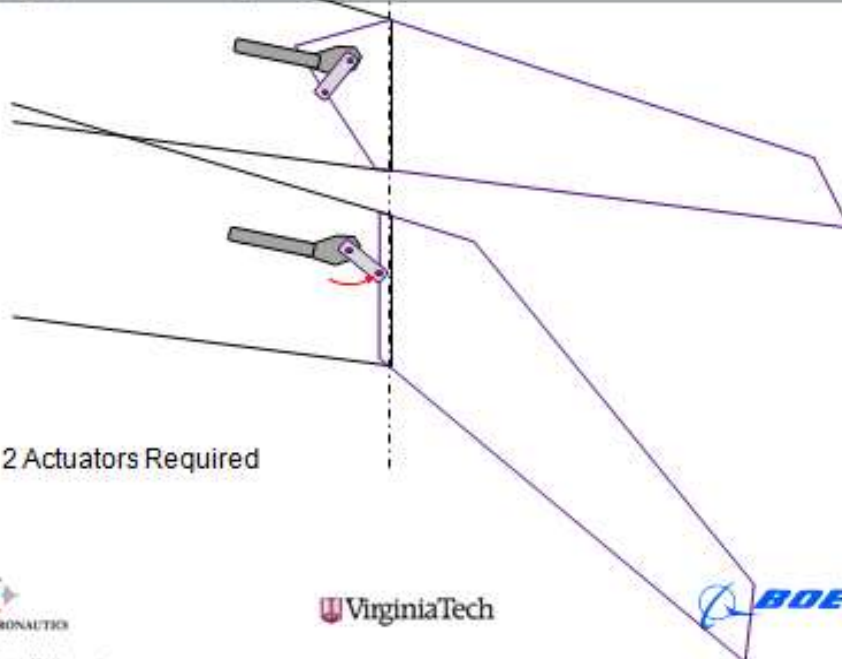
Virginia Tech

BOEING

Copyright © 2011 Boeing. All rights reserved.

## 4-Bar Linkage – 1 Bar Carry Loads

Engineering, Operations & Technology



## Simple Morphing Concept

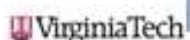
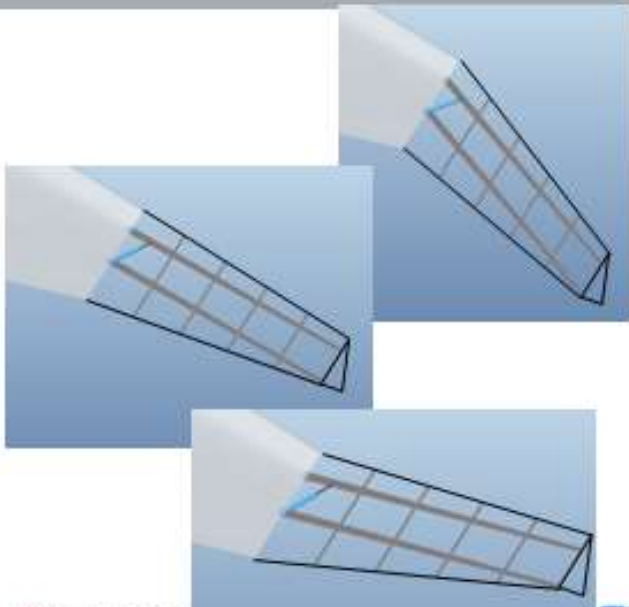
Engineering, Operations & Technology

• Features:

- Rigid telescoping leading and trailing edges

Pros:

- Minimized shear deflection if using flexible skin
- Solid spars with simple pivot joints
- Fixed location LE and TE attachment points
- Simple actuation
- Rigid TE can incorporate continuous or rigid control surface



Copyright © 2011 Boeing. All rights reserved.

## Hybrid Morphing/Rigid Concept

Engineering, Operations & Technology

• Features:

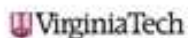
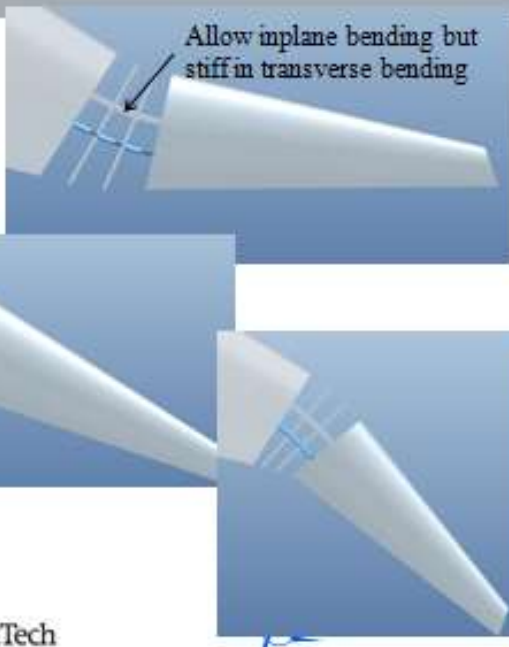
- Rigid outboard wingtip
- Morphing inboard section
- Relatively smooth continuous LE and TE

Pros:

- Uses conventional control surfaces on outboard section
- Can use flexible or nesting skin types

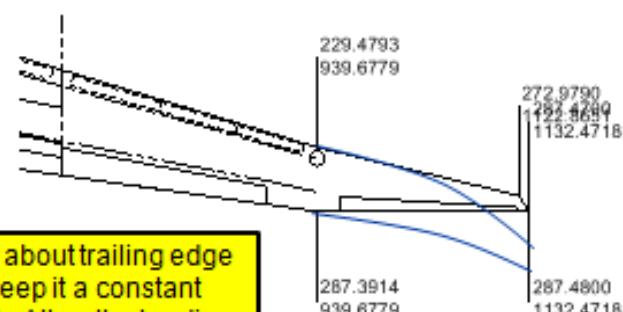
• Cons:

- More complex load path through spar joints



## Don't Rotate But "Bend"

Engineering, Operations & Technology



## Features of Proposed Flex Spar Concept



Engineering, Operations & Technology

- Rigid aft spars for wing & wingtip attached with vertical hinge at the pivot location.
- Rigid fwd spars for wing & wingtip attached with section of spar free to flex in fore/aft direction. This flex spar is attached by a vertical hinge at the wingtip – and is guided through the outbd end of the rigid wing spar. (The flex spar may have multiple leaves stacked in the chordwise direction.)
- A single actuator located along the fwd wing spar (inbd of the fex spar) will actuate the wingtip sweep motion.
- A section of the wing extending inbd & outbd of the pivot location will incorporate skins & core elements with significant flexibility in the spanwise extensive & fore/aft bending directions.
- Under-expanded (UE) honeycomb core elements will provide additional torsional stiffness across the flexible portion of the wing, & additional out-of-plane stiffness support for the skins.
- The UE honeycomb can be attached (bonded) to the end ribs, TE spars, & upper/lower skins for the wing & wingtip.



VirginiaTech



## Features of Proposed Flex Spar Concept



Engineering, Operations & Technology

- Rigid aft spars for wing & wingtip attached with vertical hinge at the pivot location.
- Rigid fwd spars for wing & wingtip attached with section of spar free to flex in fore/aft direction. This flex spar is attached by a vertical hinge at the wingtip – and is guided through the outbd end of the rigid wing spar. (The flex spar may have multiple leaves stacked in the chordwise direction.)
- A single actuator located along the fwd wing spar (inbd of the fex spar) will actuate the wingtip sweep motion.
- A section of the wing extending inbd & outbd of the pivot location will incorporate skins & core elements with significant flexibility in the spanwise extensive & fore/aft bending directions.
- Under-expanded (UE) honeycomb core elements will provide additional torsional stiffness across the flexible portion of the wing, & additional out-of-plane stiffness support for the skins.
- The UE honeycomb can be attached (bonded) to the end ribs, TE spars, & upper/lower skins for the wing & wingtip.



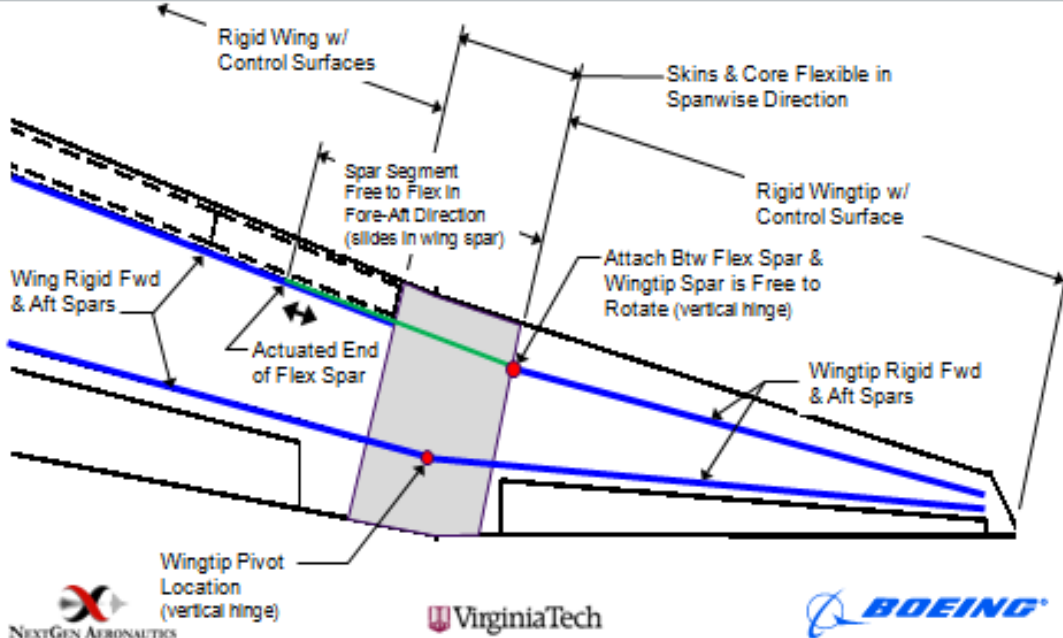
VirginiaTech



## Flex Spar Concept Layout (fwd position)



Engineering, Operations & Technology



NEXTGEN AERONAUTICS

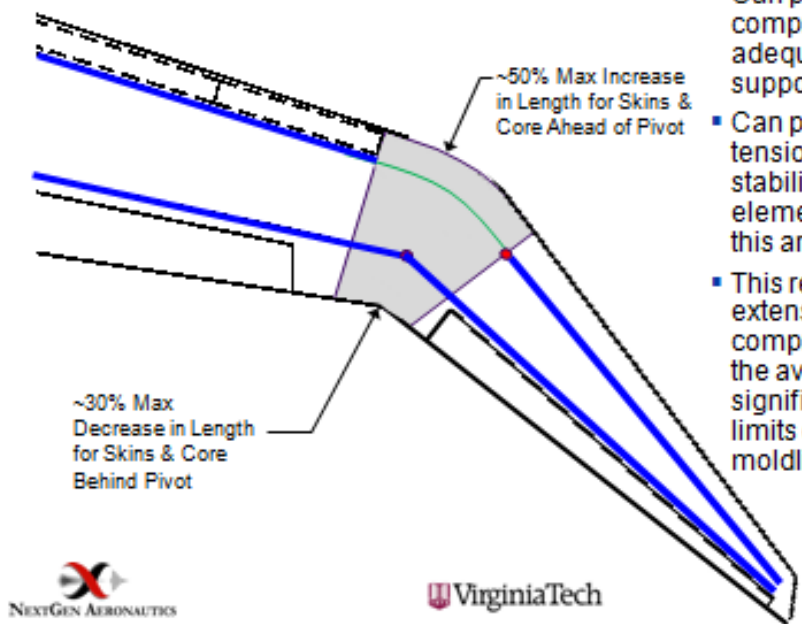
VirginiaTech

BOEING®

## Flex Spar Concept Layout (swept position)



Engineering, Operations & Technology



NEXTGEN AERONAUTICS

VirginiaTech

- Can pre-stress LE skins in compression by 10% (with adequate out-of-plane support from core elements)
- Can pre-stress TE skins in tension by 20% (to help stabilize – since core elements extremely thin in this area)
- This results in a max skin extension of ~40%, & a max compression of ~10% – with the averages being significantly less (within limits of current continuous moldline technology)

BOEING®

## Wing Cross-section

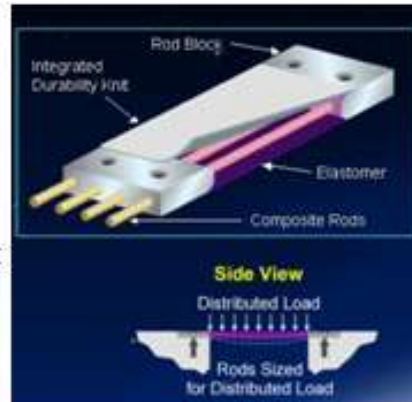


Engineering, Operations & Technology



### Skin Options:

1. Mod continuous moldline concept to increase out-of-plane stiffness. Replace rods with vertical webs. Longest web dim'n spanwise, next longest vertical (parallel to pivot axis), shortest dim'n chordwise (to minimize force req'd to bend in fore-aft direction).
2. Support existing continuous moldline concept skins with under-expanded honeycomb – which will provide significant torsional & shear stiffness while being extremely flexible for fore-aft bending. (Ref. next chart)



VirginiaTech

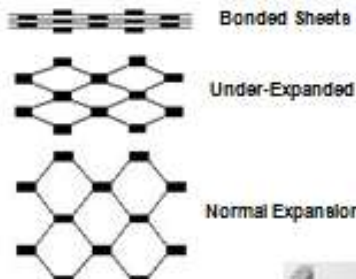
BOEING

## Under-Expanded Honeycomb Core



Engineering, Operations & Technology

- Under-expanded (UE) honeycomb is extremely flexible for in-plane & out-of-plane bending – even if it is not flexcore.
- UE honeycomb has significant torsional & out-of-plane shear stiffness due to the full-airfoil-height webs.
- All or part of the core for the section of the wing that must flex could be filled with UE honeycomb to increase torsional stiffness & support the skins against out-of-plane deflection.
- UE honeycomb could be bonded to the TE spars, ribs at either end of the flexible section, & the upper/lower skins.



VirginiaTech

BOEING

Copyright © 2011 Boeing. All rights reserved.

## Advantages, Biggest Risk, & Additional Option For the Proposed Flex Spar Concept



Engineering, Operations & Technology

- **Structurally Efficient:**

- Provides direct transfer of both the fwd & aft spar loads btw the wing & wingtip.
- Avoids inefficiencies associated with transferring loads to/from link hardware (minimizes hardware required to transfer loads & motion).
- Makes max use of spar height for transferring lift loads.
- Only requires one actuator to sweep wingtip.

- **Allows Use of Continuous Moldline Technology Skins With:**

- Max deflections within currently achievable limits
- Reduced in-plane stiffness & increase out-of-plane stiffness through replacing rods w/ webs, or by supporting skins with under-expanded honeycomb.

- **Biggest Risk: Long-term reliability of skins for section that must flex**

- **Additional Option: Use the flex spar at the fwd spar location combined with nested (non-flexible) skins in the transition area.**



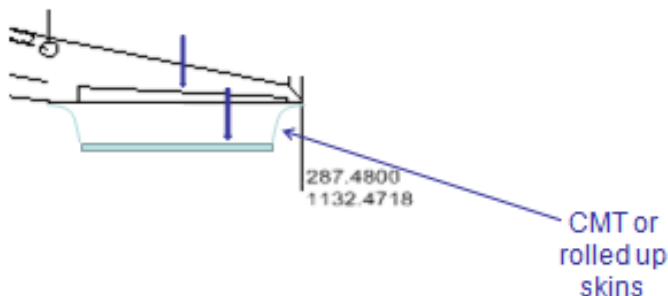
VirginiaTech



Copyright © 2011 Boeing. All rights reserved.

## Extend only aileron portion of the wing

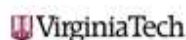
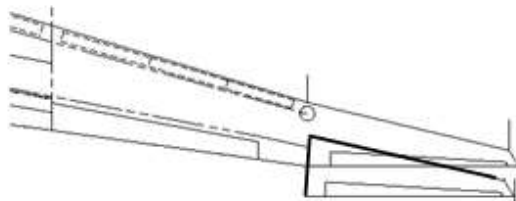
Extend the rear portion of wing tip that has aileron attached.



VirginiaTech



## Translate/Slide Tip Aft



## Concept Categorization

- Single, simple pivot. Several contributors suggested a simple pivot. Variations mostly had to do with chordwise location of the pivot and the means to address the surface area changes associated with the pivots.
- Multiple pivots. Generally variations on a 4-bar linkage type of mechanism that allows more freedom in the motion of the wing tip. A major variation is a multi-pivot (at LE/TE/spars) concept extending the kinematics into the entire wing tip with flexible skins.
- Selectively flexible primary load carrying members, e.g., flexible spars. This concept differs in that in the other concepts the primary load carrying members are "rigid" and the motion is achieved through kinematics.
- Other



36

## APPENDIX B. AEROELASTIC ANALYSIS EQUATIONS OF MOTION

The aeroelastic analysis has been performed as shown below. Thin airfoil theory as presented in [13] has been used to perform the aerodynamic analysis. We will use the principle of virtual work to obtain the equations of equilibrium.

Let us obtain our external virtual work  $\delta W_{\text{ext}}$  due to rigid and elastic forces for virtual plunge and pitch displacements  $\delta w$  and  $\delta \theta$  measured at the elastic axis of the wing as,

$$\begin{aligned} \delta W_{\text{ext}} = & \int_0^L L(x) \delta w(x) dx + \int_0^L M(x) \delta \theta(x) dx + \int_0^L L_{r-\text{wing}}(x) \delta w(x) dx + \\ & \int_0^L M_{r-\text{wing}}(x) \delta \theta(x) dx + \\ & \int_0^{L_{cs}} L_{r-cs}(x) \delta w(x) dx + \int_0^{L_{cs}} M_{r-cs}(x) \delta \theta(x) dx \end{aligned} \quad (34)$$

Where,

$$L(x) = q_d c \frac{\partial C_L}{\partial \alpha} \cos^2(\Lambda) \{\theta - w' \tan(\Lambda)\} \quad (35a)$$

$$M(x) = q_d c e \frac{\partial C_L}{\partial \alpha} \cos^2(\Lambda) \{\theta - w' \tan(\Lambda)\} + q_d c^2 \frac{\partial C_M}{\partial \alpha} \cos^2(\Lambda) \{\theta - w' \tan(\Lambda)\} \quad (35b)$$

$$L_{r-\text{wing}} = q_d c \frac{\partial C_L}{\partial \alpha} \cos^2(\Lambda) \alpha_r \quad (35c)$$

$$M_{r-\text{wing}} = q_d c e \frac{\partial C_L}{\partial \alpha} \cos^2(\Lambda) \alpha_r + q_d c^2 \frac{\partial C_M}{\partial \alpha} \cos^2(\Lambda) \alpha_r \quad (35d)$$

$$L_{r-cs} = q_d c_{cs} \frac{\partial C_L}{\partial \beta} \cos^2(\Lambda) \beta_r \quad (35e)$$

$$M_{r-cs} = q_d c_{cs} e_{cs} \frac{\partial C_L}{\partial \beta} \cos^2(\Lambda) \alpha_r + q_d c_{cs}^2 \frac{\partial C_M}{\partial \alpha} \cos^2(\Lambda) \beta_r \quad (35f)$$

The strain energy of a beam undergoing both bending and torsion with the elastic axis as the reference points can be written as,

$$U = \frac{1}{2} \int_0^L EI(x) w''(x)^2 dx + \frac{1}{2} \int_0^L GJ(x) \theta'(x)^2 dx \quad (36)$$

From the first variation of the strain energy, we can obtain our internal virtual work  $\delta W_{\text{int}}$ , due to elastic restoring forces generated due to bending and torsion forces as,

$$\delta W_{\text{int}} = \delta^{(1)} U = \int_0^L EI(x) w''(x) \delta(w''(x)) dx + \int_0^L GJ(x) \theta'(x) \delta(\theta'(x)) dx \quad (37)$$

Let us now assume our approximate solution as follows,

$$\theta(x) = \sum_{i=1}^n a_i \psi_i(x), \quad w(x) = \sum_{i=1}^m b_i \phi_i(x) \quad (38)$$

Then, let us have the following test functions

$$\delta\theta(x) = \delta a_i \psi_i(x), \quad i = 1, \dots, n \quad (39a)$$

$$\delta w(x) = \delta b_i \phi_i(x), \quad i = 1, \dots, m \quad (39b)$$

We also have,

$$\delta(\theta'(x)) = \delta a_i \psi'_i(x), \quad i = 1, \dots, n \quad (40a)$$

$$\delta(w''(x)) = \delta b_i \phi''_i(x), \quad i = 1, \dots, m \quad (40b)$$

Thus, substituting equations (39) and (40) in equation (34) and using equations (35a) - (35f), we can write,

$$\begin{aligned} \delta W_{\text{ext}} = & \left( \sum_{j=1}^n \left[ \int_0^L q_d c \frac{\partial C_l}{\partial \alpha} \cos^2(\Lambda) \psi_j(x) \phi_i(x) dx \right] a_j \right. \\ & - \sum_{j=1}^m \left[ \int_0^L q_d c \tan(\Lambda) \frac{\partial C_l}{\partial \alpha} \cos^2(\Lambda) \phi'_j(x) \phi_i(x) dx \right] b_j \\ & + \left. \int_0^L q_d c \frac{\partial C_l}{\partial \alpha} \cos^2(\Lambda) \alpha_r \phi_i(x) dx + \int_0^{L_{cs}} q_d c_{cs} \frac{\partial C_L}{\partial \beta} \cos^2(\Lambda) \beta_r \phi_i(x) dx \right) \delta b_i, i \\ & = 1, \dots, m + \\ & \left( \sum_{j=1}^n \left[ \int_0^L q_d c e \frac{\partial C_l}{\partial \alpha} \cos^2(\Lambda) \psi_i(x) \psi_i(x) dx \right] a_j - \right. \\ & \sum_{j=1}^n \left[ \int_0^L q_d c e \tan(\Lambda) \frac{\partial C_l}{\partial \alpha} \cos^2(\Lambda) \phi'_j(x) \psi_i(x) dx \right] b_j + \\ & \sum_{j=1}^n \left[ \int_0^L q_d c^2 \frac{\partial C_m}{\partial \alpha} \cos^2(\Lambda) \psi_j(x) \psi_i(x) dx \right] a_j - \\ & \sum_{j=1}^n \left[ \int_0^L q_d c^2 \tan(\Lambda) \frac{\partial C_m}{\partial \alpha} \cos^2(\Lambda) \phi'_j(x) \psi_i(x) dx \right] b_j + \int_0^L q_d c e \frac{\partial C_l}{\partial \alpha} \cos^2(\Lambda) \alpha_r \psi_i(x) dx + \\ & \int_0^L q_d c^2 \frac{\partial C_m}{\partial \alpha} \cos^2(\Lambda) \alpha_r \psi_i(x) dx + \int_0^{L_{cs}} q_d c_{cs} e_{cs} \frac{\partial C_l}{\partial \beta} \cos^2(\Lambda) \beta_r \psi_i(x) dx + \\ & \left. \int_0^{L_{cs}} q_d c_{cs}^2 \frac{\partial C_m}{\partial \beta} \cos^2(\Lambda) \beta_r \psi_i(x) dx \right) \delta a_i, i = 1, \dots, n \end{aligned} \quad (41)$$

Similarly, substituting equations (39) and (40) in equation (37), we can write,

$$\begin{aligned} \delta W_{\text{int}} = & \sum_{j=1}^m \left( \left[ \int_0^L EI(x) \phi_i''(x) \phi_j''(x) dx \right] b_j \right) \delta b_i, i = 1, \dots, m + \\ & \sum_{j=1}^n \left( \left[ \int_0^L GJ(x) \psi'_i(x) \psi'_j(x) dx \right] a_j \right) \delta a_i, i = 1, \dots, n \end{aligned} \quad (42)$$

Now, if we equate the internal virtual work to the external virtual work for each test function, we can obtain our equations of static equilibrium as follows,

For bending:

$$\begin{aligned}
& \sum_{j=1}^m \left[ \int_0^L EI(x) \phi_i''(x) \phi_j''(x) dx \right] b_j = \\
& \sum_{j=1}^n \left( \left[ \int_0^L q_d c \frac{\partial C_l}{\partial \alpha} \cos^2(\Lambda) \psi_j(x) \phi_i(x) dx \right] a_j \right) \\
& - \sum_{j=1}^m \left( \left[ \int_0^L q_d c \tan(\Lambda) \frac{\partial C_l}{\partial \alpha} \cos^2(\Lambda) \phi_j'(x) \phi_i(x) dx \right] b_j \right) + \\
& \int_0^L q_d c \frac{\partial C_l}{\partial \alpha} \cos^2(\Lambda) \alpha_r \phi_i(x) dx + \int_0^{L_{cs}} q_d c_{cs} \frac{\partial C_l}{\partial \beta} \cos^2(\Lambda) \beta_r \phi_i(x) dx, \delta b_i \neq 0, \delta a_i = 0, i = 1, \dots, m
\end{aligned} \tag{43}$$

For torsion:

$$\begin{aligned}
& \sum_{j=1}^n \left[ \int_0^L GJ(x) \psi_i'(x) \psi_j'(x) dx \right] a_j = \\
& \sum_{j=1}^n \left( \left[ \int_0^L q_d c e \frac{\partial C_l}{\partial \alpha} \cos^2(\Lambda) \psi_j(x) \psi_i(x) dx \right] a_j + \left[ \int_0^L q_d c^2 \frac{\partial C_m}{\partial \alpha} \cos^2(\Lambda) \psi_j(x) \psi_i(x) dx \right] a_j \right) \\
& - \sum_{j=1}^m \left( \left[ \int_0^L q_d c e \tan(\Lambda) \frac{\partial C_l}{\partial \alpha} \cos^2(\Lambda) \phi_j'(x) \psi_i(x) dx \right] b_j \right. \\
& \left. + \left[ \int_0^L q_d c^2 \tan(\Lambda) \frac{\partial C_m}{\partial \alpha} \cos^2(\Lambda) \phi_j'(x) \psi_i(x) dx \right] b_j \right) \\
& + \int_0^L q_d c e \frac{\partial C_l}{\partial \alpha} \cos^2(\Lambda) \alpha_r \psi_i(x) dx + \int_0^L q_d c^2 \frac{\partial C_m}{\partial \alpha} \cos^2(\Lambda) \alpha_r \psi_i(x) dx \\
& + \int_0^{L_{cs}} q_d c_{cs} e_{cs} \frac{\partial C_l}{\partial \beta} \cos^2(\Lambda) \beta_r \psi_i(x) dx \\
& + \int_0^{L_{cs}} q_d c_{cs}^2 \frac{\partial C_m}{\partial \beta} \cos^2(\Lambda) \beta_r \psi_i(x) dx, \delta a_i \neq 0, \delta b_i = 0, i = 1, \dots, n
\end{aligned} \tag{44}$$

These can be written down in matrix form once we replace the test functions by finite element shape functions and assemble them for the whole structure as shown below,

$$\begin{bmatrix} K_t & \mathbf{0} \\ \mathbf{0} & K_b \end{bmatrix} \{ \mathbf{a} \} = \begin{bmatrix} K_{a-tt} & K_{a-tb} \\ K_{a-bt} & K_{a-bb} \end{bmatrix} \{ \mathbf{b} \} + \{ Q_{m-wing} \} + \{ Q_{m/cs} \} \tag{45}$$

$$\Rightarrow \mathbf{K}_s \mathbf{q} = \mathbf{K}_{aero} \mathbf{q} + \mathbf{Q}_{r-wing} + \mathbf{Q}_{r/cs} \tag{46}$$

## APPENDIX C. STRUCTURAL MODES COMPARISON FOR SUGAR VGRWT

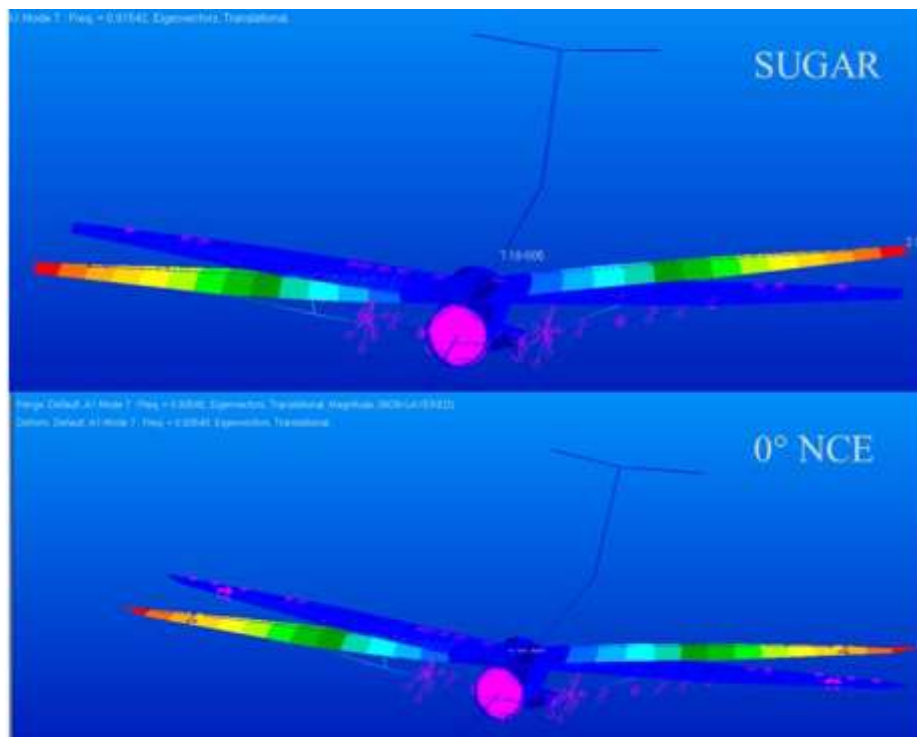


Figure C-1. Full-fuel: Structural mode 7 for baseline SUGAR (0.92 Hz) and 0-deg NCE (0.94) Hz.

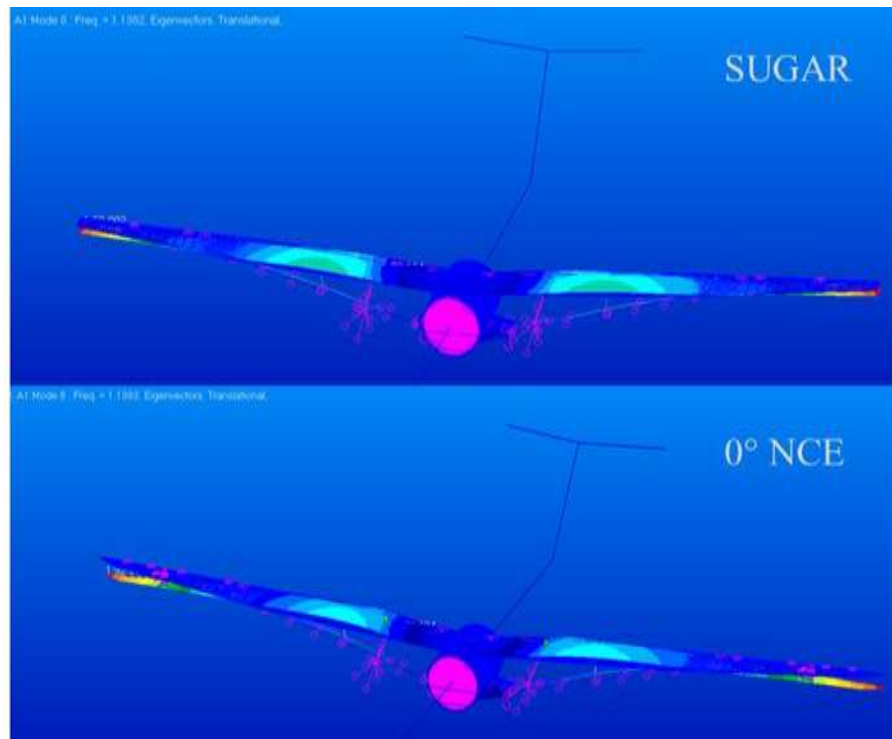
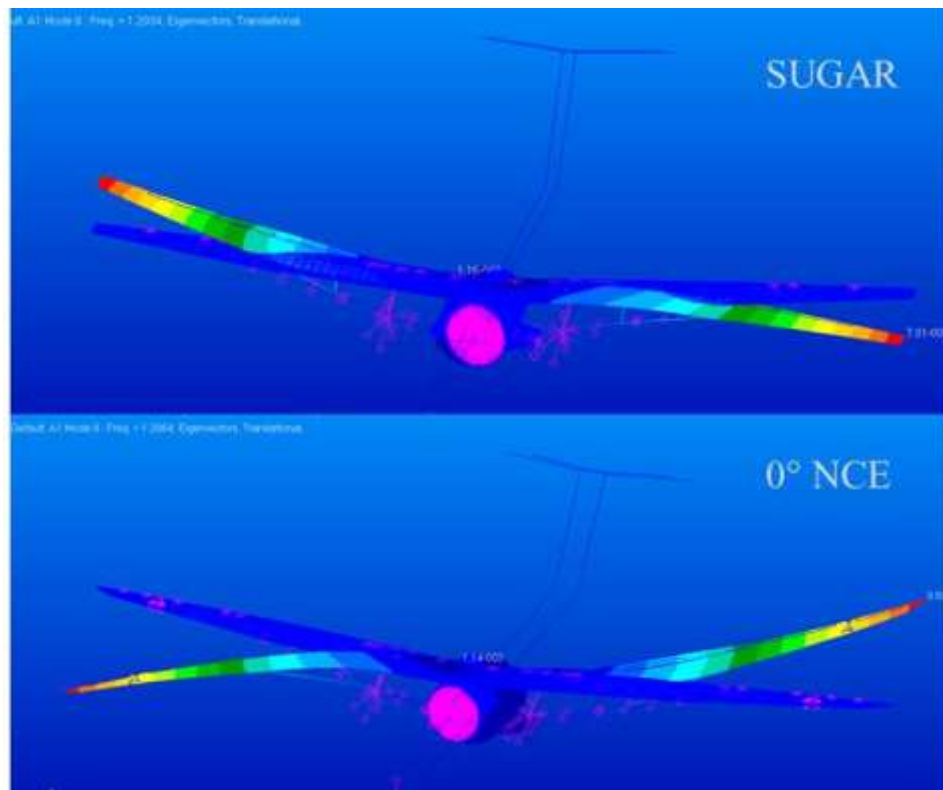
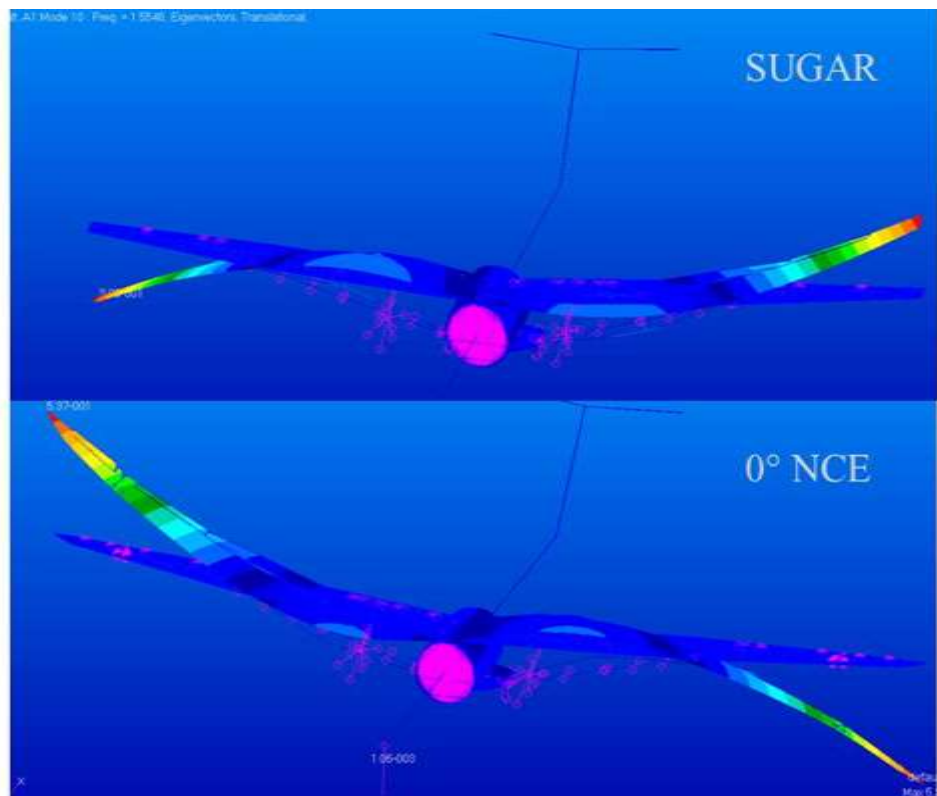


Figure C-2. Full-fuel: Structural mode 8 for baseline SUGAR (1.14 Hz) and 0-deg NCE (1.14) Hz.



**Figure C-3. Full-fuel: Structural mode 9 for baseline SUGAR (1.20 Hz) and 0-deg NCE (1.21) Hz.**



**Figure C-4. Full-fuel: Structural mode 10 for baseline SUGAR (1.66 Hz) and 0-deg NCE (1.64) Hz.**

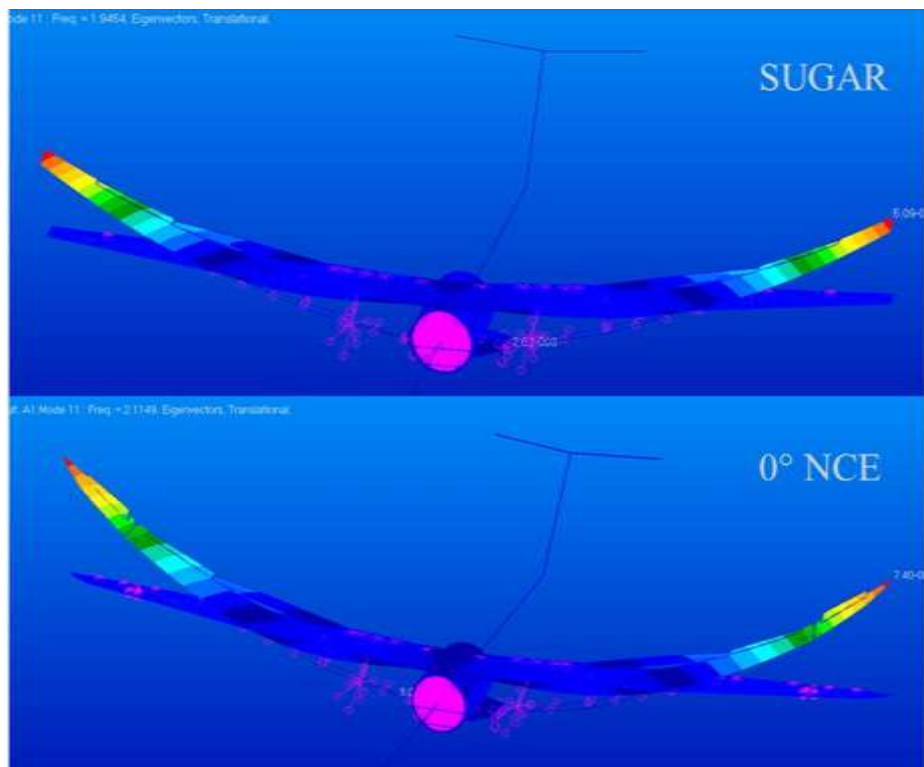


**Figure C-5.** Full-fuel: Structural mode 11 for baseline SUGAR (1.95 Hz) and 0-deg NCE (2.11) Hz.

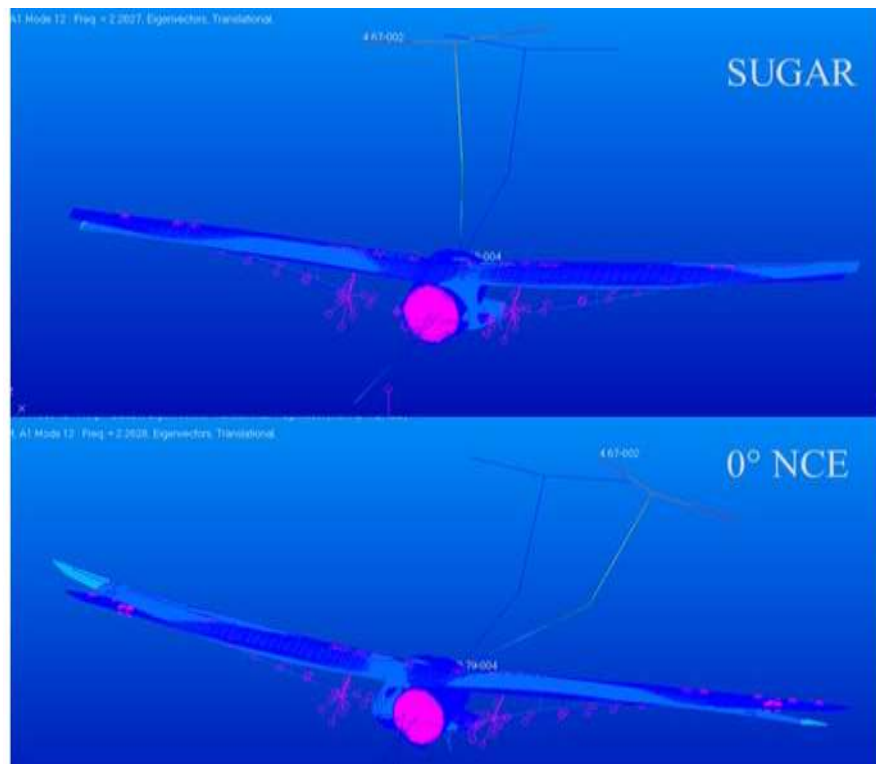


**Figure C-6.** Full-fuel: Structural mode 12 for baseline SUGAR (2.26 Hz) and 0-deg NCE (2.26) Hz.

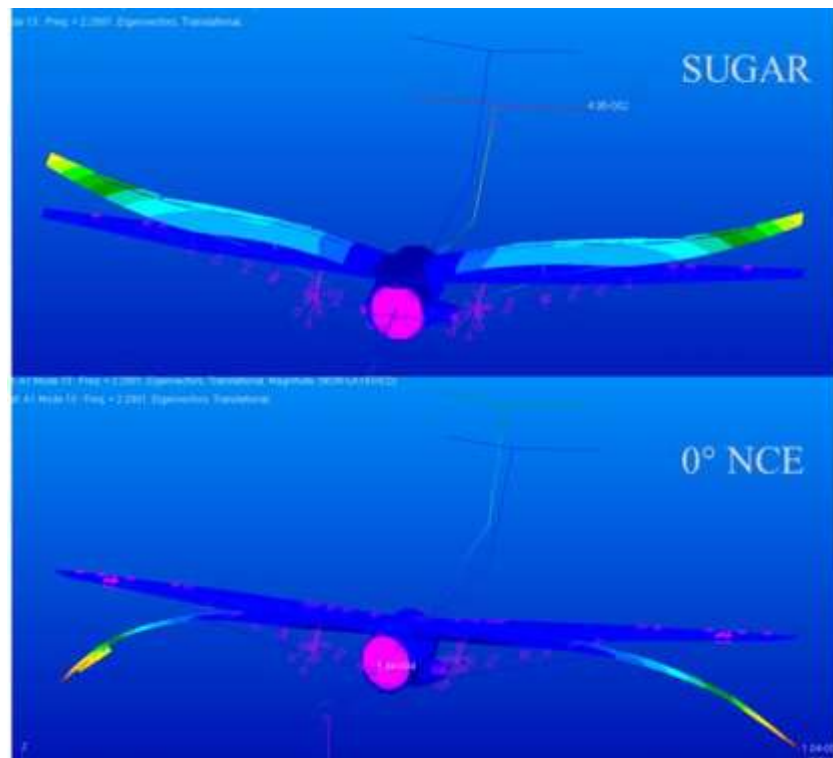


**Figure C-7. Full-fuel: Structural mode 13 for baseline SUGAR (2.28 Hz) and 0-deg NCE (2.29) Hz.**

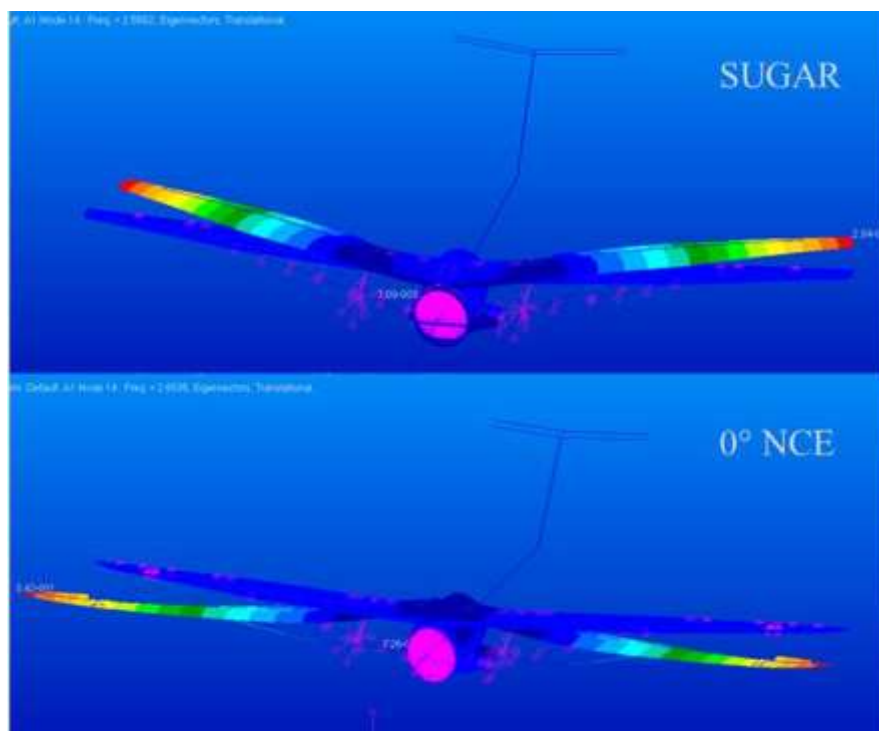


**Figure C-8. Full-fuel: Structural mode 14 for baseline SUGAR (2.66 Hz) and 0-deg NCE (2.65) Hz.**

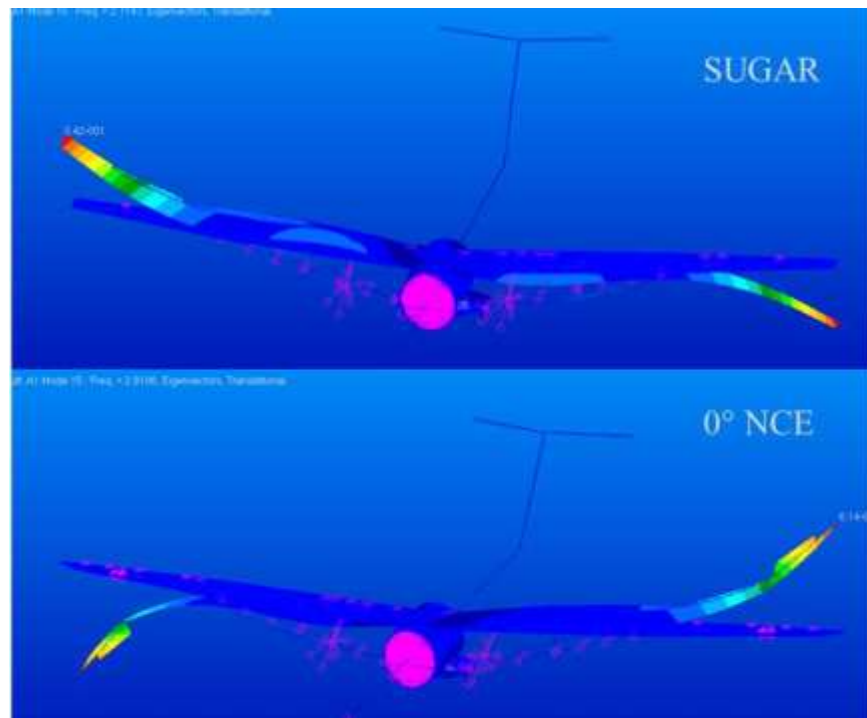


**Figure C-9. Full-fuel: Structural mode 15 for baseline SUGAR (2.71 Hz) and 0-deg NCE (2.81) Hz.**

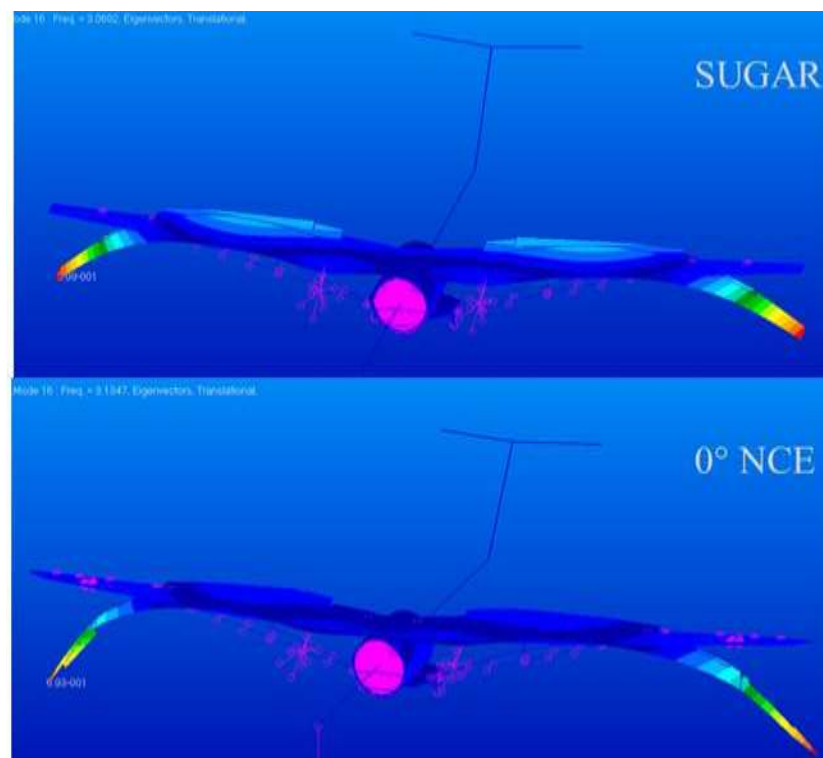


**Figure C-10. Full-fuel: Structural mode 16 for baseline SUGAR (3.06 Hz) and 0-deg NCE (3.13) Hz.**

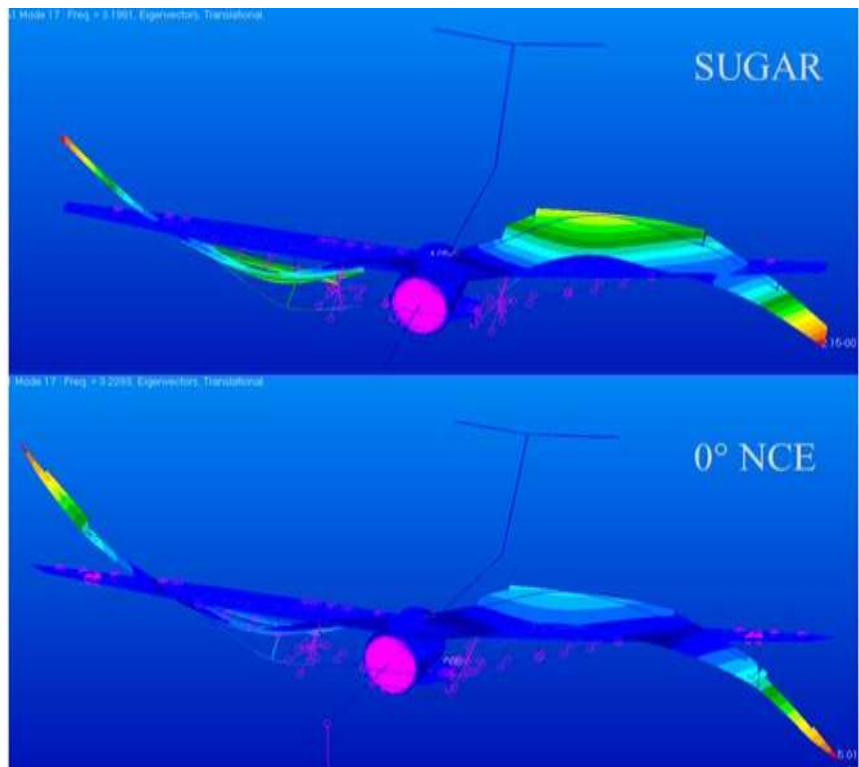


**Figure C-11.** Full-fuel: Structural mode 17 for baseline SUGAR (3.20 Hz) and 0-deg NCE (3.23) Hz

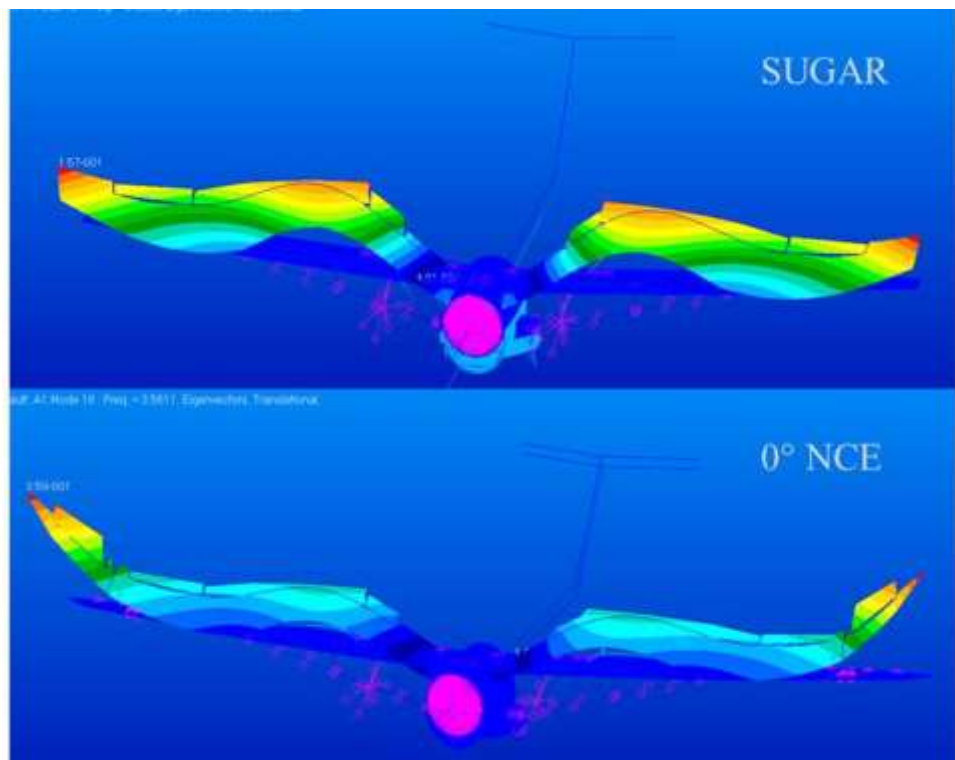


**Figure C-12.** Full-fuel: Structural mode 18 for baseline SUGAR (3.54 Hz) and 0-deg NCE (3.56) Hz.

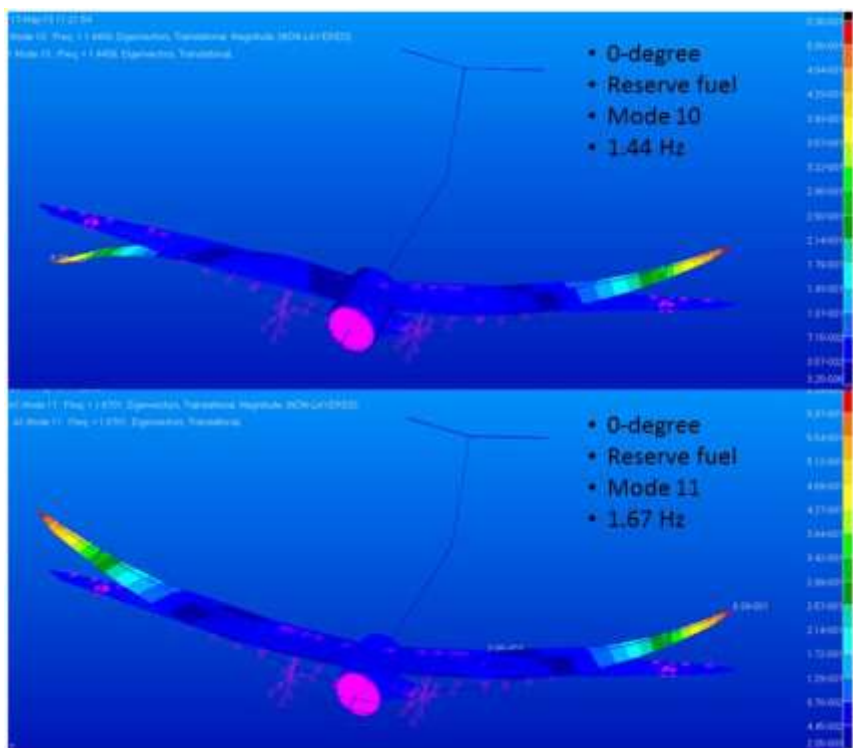


**Figure C-13.** Reserve-fuel: Structural mode 10 and 11 for 0-deg NCE.

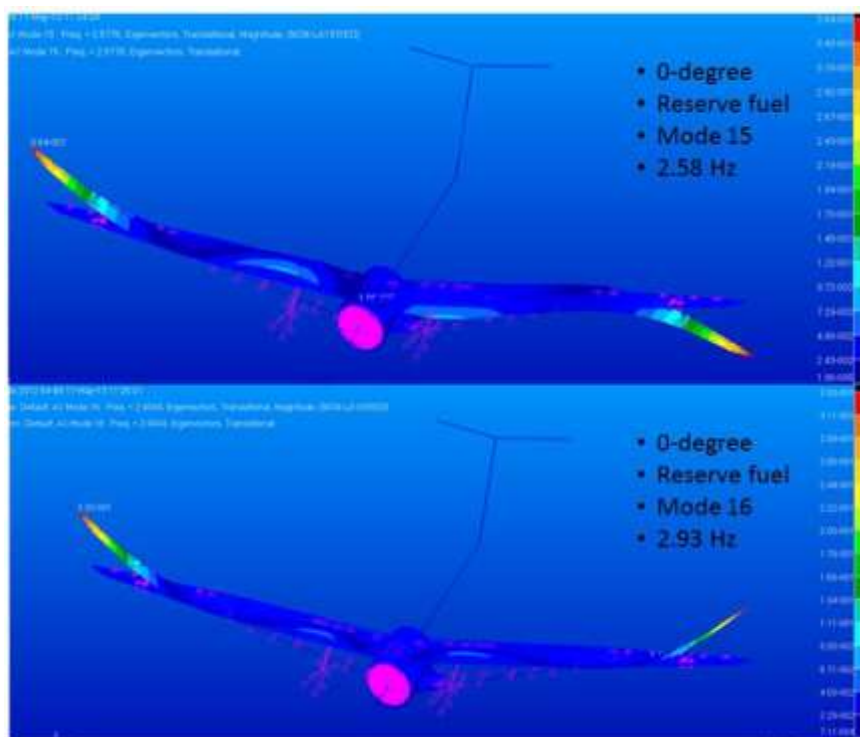


**Figure C-14.** Reserve-fuel: Structural mode 15 and 16 for 0-deg NCE.

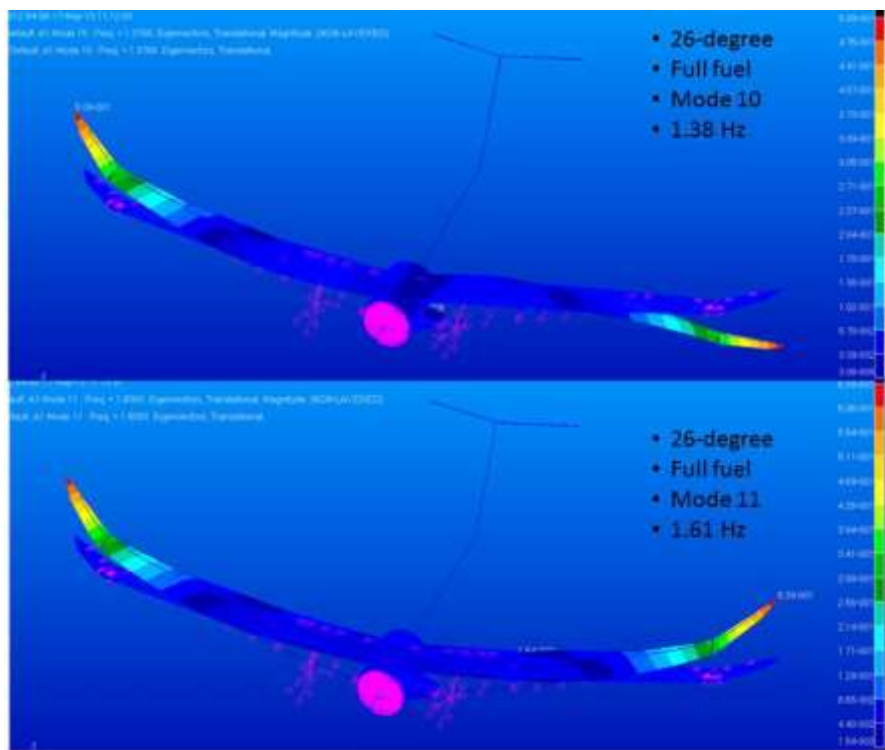


**Figure C-15. Full-fuel: Structural mode 10 and 11 for 26-deg NCE.**

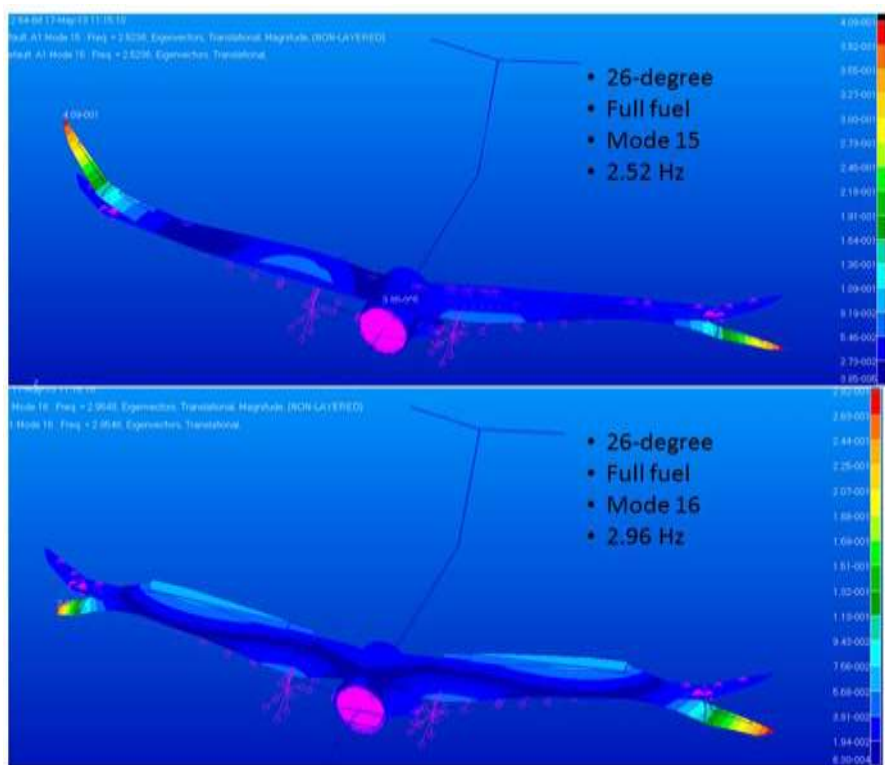


**Figure C-16. Full-fuel: Structural mode 15 and 16 for 26-deg NCE.**

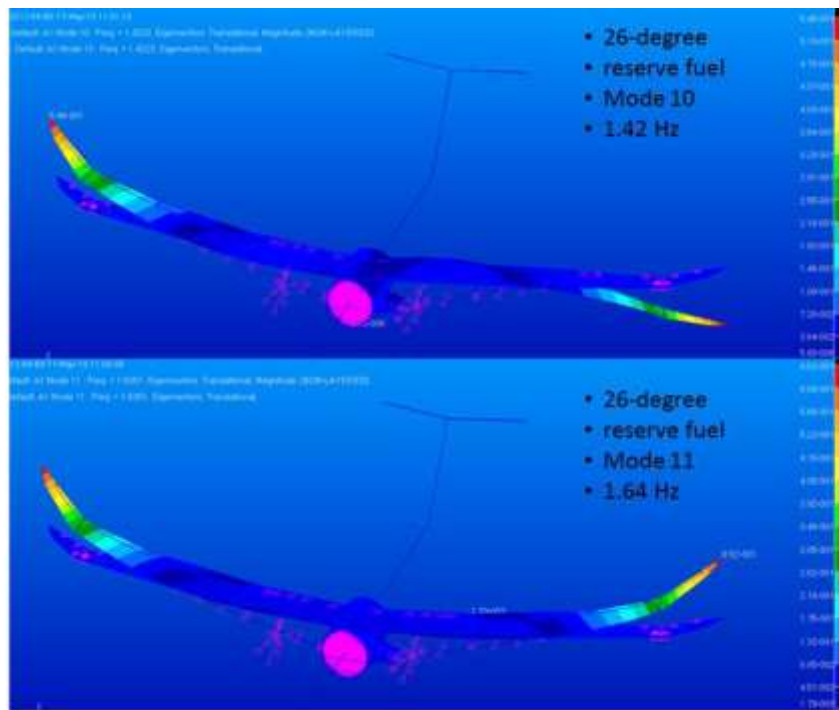


**Figure C-17.** Reserve-fuel: Structural mode 10 and 11 for 26-deg NCE.

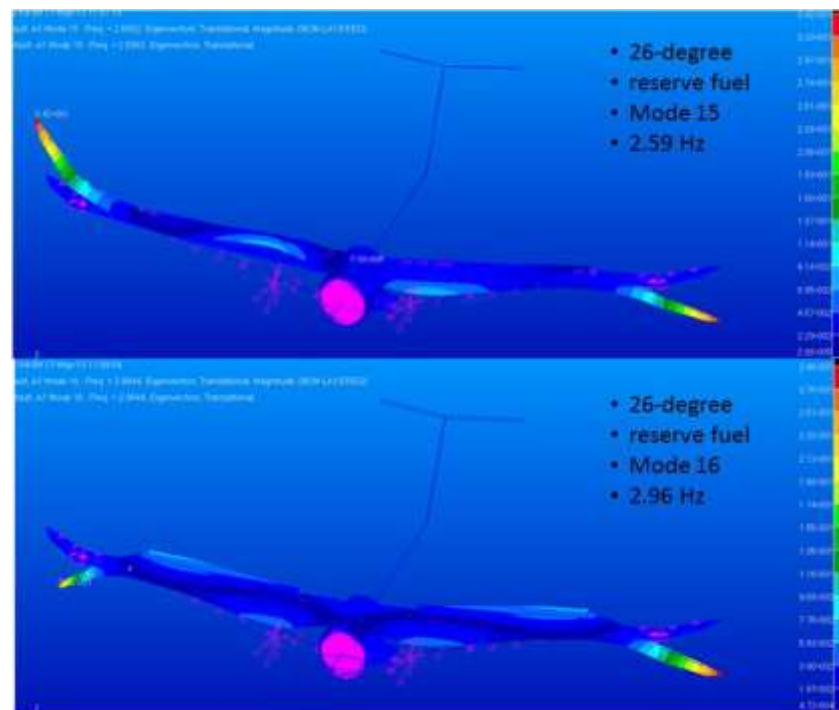


**Figure C-18.** Reserve-fuel: Structural mode 15 and 16 for 26-deg NCE.

REPORT DOCUMENTATION PAGE				Form Approved OMB No. 0704-0188	
<p>The public reporting burden for this collection of information is estimated to average 1 hour per response, including the time for reviewing instructions, searching existing data sources, gathering and maintaining the data needed, and completing and reviewing the collection of information. Send comments regarding this burden estimate or any other aspect of this collection of information, including suggestions for reducing this burden, to Department of Defense, Washington Headquarters Services, Directorate for Information Operations and Reports (0704-0188), 1215 Jefferson Davis Highway, Suite 1204, Arlington, VA 22202-4302. Respondents should be aware that notwithstanding any other provision of law, no person shall be subject to any penalty for failing to comply with a collection of information if it does not display a currently valid OMB control number.</p> <p><b>PLEASE DO NOT RETURN YOUR FORM TO THE ABOVE ADDRESS.</b></p>					
1. REPORT DATE (DD-MM-YYYY)	2. REPORT TYPE		3. DATES COVERED (From - To)		
01-08 - 2015	Contractor Report		21 September 2011 - 27 February 2015		
4. TITLE AND SUBTITLE			5a. CONTRACT NUMBER NNL10AA00B 5b. GRANT NUMBER  5c. PROGRAM ELEMENT NUMBER  5d. PROJECT NUMBER  5e. TASK NUMBER NNL11AC32T 5f. WORK UNIT NUMBER 081876.02.07.02.01.01		
Novel Control Effectors for Truss Braced Wing					
6. AUTHOR(S)			5d. PROJECT NUMBER  5e. TASK NUMBER NNL11AC32T 5f. WORK UNIT NUMBER 081876.02.07.02.01.01		
White, Edward V.; Kapania, Rakesh K.; Joshi, Shiv					
7. PERFORMING ORGANIZATION NAME(S) AND ADDRESS(ES)				8. PERFORMING ORGANIZATION REPORT NUMBER	
NASA Langley Research Center Hampton, Virginia 23681-2199					
9. SPONSORING/MONITORING AGENCY NAME(S) AND ADDRESS(ES)				10. SPONSOR/MONITOR'S ACRONYM(S)	
National Aeronautics and Space Administration Washington, DC 20546-0001				NASA	
				11. SPONSOR/MONITOR'S REPORT NUMBER(S)	
				NASA/CR-2015-218792	
12. DISTRIBUTION/AVAILABILITY STATEMENT					
Unclassified Subject Category 08 Availability: NASA STI Program (757) 864-9658					
13. SUPPLEMENTARY NOTES					
Langley Technical Monitor: Daniel D. Moerder					
14. ABSTRACT					
<p>At cruise flight conditions very high aspect ratio/low sweep truss braced wings (TBW) may be subject to design requirements that distinguish them from more highly swept cantilevered wings. High aspect ratio, short chord length and relative thinness of the airfoil sections all contribute to relatively low wing torsional stiffness. This may lead to aeroelastic issues such as aileron reversal and low flutter margins. In order to counteract these issues, high aspect ratio/low sweep wings may need to carry additional high speed control effectors to operate when outboard ailerons are in reversal and/or must carry additional structural weight to enhance torsional stiffness. The novel control effector evaluated in this study is a variable sweep raked wing tip with an aileron control surface. Forward sweep of the tip allows the aileron to align closely with the torsional axis of the wing and operate in a conventional fashion. Aft sweep of the tip creates a large moment arm from the aileron to the wing torsional axis greatly enhancing aileron reversal. The novelty comes from using this enhanced and controllable aileron reversal effect to provide roll control authority by acting as a servo tab and providing roll control through intentional twist of the wing. In this case the reduced torsional stiffness of the wing becomes an advantage to be exploited. The study results show that the novel control effector concept does provide roll control as described, but only for a restricted class of TBW aircraft configurations. For the configuration studied (long range, dual aisle, Mach 0.85 cruise) the novel control effector provides significant benefits including up to 12% reduction in fuel burn.</p>					
15. SUBJECT TERMS					
Braced; Novel; Truss; Wing					
16. SECURITY CLASSIFICATION OF:			17. LIMITATION OF ABSTRACT	18. NUMBER OF PAGES	19a. NAME OF RESPONSIBLE PERSON
a. REPORT	b. ABSTRACT	c. THIS PAGE	UU	236	STI Help Desk (email: <a href="mailto:help@sti.nasa.gov">help@sti.nasa.gov</a> )
U	U	U			19b. TELEPHONE NUMBER (Include area code) (757) 864-9658